Creep and Microstructures of Slurry Die Cast Al-Si-Mg Alloy

Keren Shi

A Thesis Submitted in Fulfillment of the Requirements for the Degree of

Doctor of Philosophy in Materials Engineering

Prince of Songkla University

2017

Copyright of Prince of Songkla University

Thesis Title Creep and Microstructures of Slurry Die Cast Al-Si-Mg Alloy
Author Mr. Keren Shi
Major Program Materials Engineering

Major Advisor	**Examining Committee:**
…….	……..……Chairperson
(Asst. Prof. Dr. Thawatchai Plookphol)	(Dr. Suchart Chantaramanee)
	……..……...Committee
Co-advisor	(Asst. Prof. Dr. Thawatchai Plookphol)
……..…	……..……...Committee
(Dr. Somjai Janudom)	(Dr. Somjai Janudom)
	……..……...Committee
	(Dr. Phairote Sungkhaphaitoon)

The Graduate School, Prince of Songkla University, has approved this thesis as fulfillment of the requirements for the Doctor of Philosophy Degree in Materials Engineering

……
(Assoc. Prof. Dr. Teerapol Srichana)
Dean of Graduate School

This is to certify that the work here submitted is the result of the candidate's own investigations. Due acknowledgement has been made of any assistance received.

……Signature

(Asst. Prof. Dr. Thawatchai Plookphol)
Major Advisor

……Signature

(Dr. Somjai Janudom)
Co-advisor

……Signature

(Mr. Keren Shi)
Candidate

I hereby certify that this work has not been accepted in substance for any other degree, and is not being currently submitted in candidature for any degree.

……Signature

(Mr. Keren Shi)
Candidate

ชื่อวิทยานิพนธ์ การคืบและโครงสร้างจุลภาคของอลูมิเนียมผสม Al-Mg-Si ที่หล่อขึ้นรูปด้วยกรรมวิธีสเลอรีไดคาสต์

ผู้เขียน Mr. Keren Shi

สาขาวิชา วิศวกรรมวัสดุ

ปีการศึกษา 2559

บทคัดย่อ

ในงานวิจัยนี้ได้ใช้เทคนิคการทำโลหะกึ่งของแข็งโดยวิธีการปล่อยฟองแก๊ส หรือ กีส (Gas Induced Simi-Solid หรือ GISS) สำหรับเตรียมสเลอรีโลหะกึ่งของแข็ง ซึ่งประกอบด้วยเฟสของแข็งปริมาณน้อย ๆ และเฟสของโลหะเหลว โลหะอลูมิเนียมผสมชนิด Al-Si-Mg-Fe (AC4C) ถูกนำมาใช้ในการศึกษาวิจัยนี้ สเลอรีของโลหะอลูมิเนียมผสม AC4C ถูกเตรียมขึ้นโดยเทคนิคกีสก่อน จากนั้นสเลอรีจะถูกนำไปหล่อขึ้นรูปเป็นแผ่นชิ้นงานโดยใช้เครื่องหล่อโลหะแบบไดคาสต์ วัตถุประสงค์ของงานวิจัยนี้ เพื่อศึกษาโครงสร้างจุลภาคและสมบัติเชิงกลของโลหะอลูมิเนียมผสมเกรด AC4C ที่หล่อขึ้นรูปจากสเลอรี่โดยวิธีการหล่อไดคาสต์ (GISS-DC) และเปรียบเทียบกับโครงสร้างจุลภาคและสมบัติเชิงกลของชิ้นงานหล่อขึ้นรูปโดยวิธีการหล่อไดคลาสต์แบบทั่ว ๆ ไป ซึ่งหล่อจากโลหะหลอมเหลว (CL-DC) การศึกษาวิจัยแบ่งเป็น 5 ส่วน ดังนี้

การศึกษาวิจัยส่วนที่ 1 เป็นการศึกษาโครงสร้างจุลภาคและความแข็งแรงดึงของชิ้นงานภายหลังการหล่อไดคลาสต์ โดยศึกษาจากตัวอย่างชิ้นทดสอบที่เตรียมจากตำแหน่งต่าง ๆ ของชิ้นงานหล่อ ผลการศึกษาพบว่า ชิ้นทดสอบที่เตรียมจากส่วนล่างสุดใกล้กับทางไหลเข้าของโลหะเหลวและชิ้นทดสอบที่เตรียมจากส่วนกลางของแผ่นชิ้นงานหล่อมีความแข็งแรงและความเหนียวมากกว่าชิ้นทดสอบที่เตรียมจากส่วนบนสุดของแผ่นชิ้นงานหล่อ สาเหตุเนื่องมาจากบริเวณตำแหน่งบนสุดของแผ่นชิ้นงานหล่อประกอบด้วยรอยบกพร่อง เช่น โพรงขนาดเล็กที่เกิดจาการหดตัวของโลหะเหลวขณะเปลี่ยนสภาพเป็นแข็งตัวในระหว่างการหล่อไดคาสต์ รอยบกพร่องจากโพรงหดตัวนี้เป็นสาเหตุหลักที่ทำให้ชิ้นงานหล่อมีความแข็งแรงดึงและความเหนียวลดลง

การศึกษาวิจัยส่วนที่ 2 เป็นการศึกษาสมบัติความต้านทานแรงดึงและโครงสร้างจุลภาคของตัวอย่างชิ้นงานหล่อโลหะอลูมิเนียมผสม AC4C ที่หล่อขึ้นรูปแบบกิสไดคาสต์ ภายหลังการบ่มแข็งแบบ T6 (GISS-DC-AC4C-T6) และเปรียบเทียบกับตัวอย่างชิ้นงานหล่อโลหะอลูมิเนียมผสม AC4C ที่หล่อขึ้นรูปโดยการหล่อไดคาสต์ปรกติทั่วไป ภายหลังการบ่มแข็งแบบ T6 (CL-DC-AC4C-T6) ในตัวอย่างชิ้นทดสอบภายหลังหล่อแบบกิสไดคลาสต์ (GISS-DC-AC4C) และตัวอย่างชิ้นทดสอบภายหลังหล่อแบบไดคลาสต์ทั่วไป (CL-DC-AC4C) โดยไม่ผ่านการบ่มแข็ง T6 พบโครงสร้างจุลภาคที่ประกอบด้วยเฟสของสารประกอบเชิงโลหะที่มีลักษณะคล้ายตัวอักษรจีน (π-Chinese script) และเฟส β ภายหลังการบ่มแข็งแบบ T6 พบว่าเฟสยูเทคติกซิลิกอนจะเปลี่ยนไปเป็นรูปทรงกลม และพบเฟส β เฟสยังคงเหลืออยู่ การทดสอบความแข็งแรงดึงที่อุณหภูมิ 25, 100, 175 และ 250 ^{o}C พบว่าความแข็งแรงดึงสูงสุด (UTS) ความแข็งแรงคราก (YS) และการยืดตัว (elongation) ของตัวอย่างชิ้นทดสอบ GISS-DC-AC4C-T6 และ CL-DC-AC4C-T6 มีค่าลดต่ำลงเมื่อใช้อุณหภูมิสูงขึ้น ที่อุณหภูมิ 25^{o}C โลหะผสม GISS-DC-AC4C-T6 มีค่า UTS และ YS เท่ากับ 300.9 MPa และ 244.5 MPa ตามลำดับ เมื่อเพิ่มอุณหภูมิสูงขึ้นลักษณะของรอยแตกหักเปลี่ยนจากรอยแตกหักแบบเปราะไปเป็นรอยแตกหักแบบเหนียว ค่ายกกำลังสเตรนฮาดเดนนิง (n) มีค่าลดลงเมื่อความเครียดเพิ่มขึ้นที่อุณหภูมิ 250 ^{o}C พบการอ่อนตัวเวิร์คซอฟเทนนิง และพบรอยบุ๋ม (dimples) บนผิวของรอยแตกหัก การเปลี่ยนแปลงจากการแตกหักแบบเปราะไปเป็นการแตกหักแบบเหนียวเกิดขึ้นทั้งในชิ้นงานทดสอบโลหะผสมแบบ GISS-DC-AC4C-T6 และแบบ CL-DC-AC4C-T6 และยังพบว่าอนุภาคของสารประกอบเชิงโลหะและรูพรุนขนาดเล็กเป็นตัวกำหนดสมบัติการต้านทานแรงดึงของโลหะอลูมิเนียมผสมหล่อไดคาสต์ทั้งสองแบบ

การศึกษาวิจัยส่วนที่ 3 เป็นการศึกษาโครงสร้างจุลภาคและสมบัติการคืบของชิ้นงานทดสอบ GISS-DC-AC4C-T6 ที่ช่วงอุณหภูมิ 300-360 ^{o}C และช่วงความเค้น 20-40 MPa และเปรียบเทียบกับโครงสร้างจุลภาคและสมบัติการคืบของชิ้นงานทดสอบ CL-DC-AC4C-T6 ภายหลังการบ่มแข็งแบบ T6 พบว่า เฟสยูเทคติดซิลิกอนเปลี่ยนเป็นรูปทรงกลมและมีขนาดโตขึ้น เฟส α-Al ในตัวอย่าง GISS-DC-AC4C-T6 มีลักษณะเป็นรูปทรงคล้ายกลีบกุหลาบ (Rosette) ส่วนใน

ตัวอย่าง CL-DC-AC4C-T6 มีลักษณะเดนไดรต์ ค่ายกกำลังความเค้นการคืบ (n) และค่าพลังงานกระตุ้นการคืบ (Q_C) ของตัวอย่าง GISS-DC-AC4CT6 และ CL-DC-AC4C-T6 ถูกประมาณค่าจากผลการทดลอง พบว่า n ของตัวอย่าง CL-DC-AC4C-T6 ที่อุณหภูมิ 300, 330 และ 360 °C มีค่าเท่ากับ 3.95, 3.66 และ 4.94 ในขณะที่ n ของตัวอย่าง GISS-DC-AC4C-T6 มีค่าเท่ากับ 3.52, 4.82 และ 5.74 ตามลำดับ เมื่อพิจารณาจากค่า n ของตัวอย่างทั้งสองกลุ่ม สามารถบ่งชี้ได้ว่า กลไกการคืบอาจจะถูกควบคุมโดยกระบวนการไถลและการปีนของดิสโลเคชัน ค่าพลังงานกระตุ้นการคืบโดยเฉลี่ยมีค่าเท่ากับ 257.8 kJ/mol ซึ่งสูงกว่าค่าพลังงานกระตุ้นของการแพร่ในตัวเองของโลหะอลูมิเนียมบริสุทธิ์ (143 kJ/mol)

การศึกษาวิจัยส่วนที่ 4 เป็นการวิเคราะห์ข้อมูลจากการทดสอบการคืบแตกหัก (Creep rupture) โดยใช้โมเดลมองค์แมน-แกรนต์ (Monkman-Grant model) ค่าพารามิเตอร์ความทนทานต่อการเสียหาย (The damage tolerance parameter) และวิธีเธตาโปรเจ็คชัน (The theta projection method) เพื่อใช้ในการทำนายอายุการคืบ พบว่าความสัมพันธ์ระหว่างอัตราการคืบและเวลาแตกหักมีความสัมพันธ์เชิงเส้นและสอดคล้องกับโมเดลมองค์แมน-แกรนต์ และข้อมูลเส้นโค้งการคืบที่ได้จากการศึกษาวิจัยครั้งนี้สามารถสร้างเป็นสมการโมเดลการคืบด้วยวิธีเธตาโปรเจ็คชัน

การศึกษาวิจัยส่วนสุดท้าย ส่วนที่ 5 เป็นการทดสอบการคืบแบบเปลี่ยนค่าความเค้นที่อุณหภูมิ 25, 250, 280 และ 300 °C ของตัวอย่างโลหะผสม GISS-DC-AC4C-T6 และ CL-DC-AC4C-T6 การทดสอบการคืบโดยการลดค่าความเค้น (Stress-dip test) การลดลงของความเค้นมีผลทำให้เกิดความเค้นภายในย้อนกลับ (Internal backstress) ในกรณีที่ความเค้นลดลงมีค่าน้อยมาก ๆ ค่าความเค้นภายในย้อนกลับจะเข้าสู่จุดสมดุลกับค่าความเค้นกระทำ ในสภาวะเช่นนี้จะเกิดเส้นโค้งการคืบแบบปรกติ ในการศึกษาครั้งนี้การตอบสนองต่อการลดความเค้นเกิดขึ้นอย่างรวดเร็วมากเกินกว่าความสามารถของเครื่องเก็บข้อมูลที่จะบันทึกไว้ได้ สำหรับในการทดสอบลดความเค้นลงในปริมาณมาก ๆ จะมีทำให้โครงสร้างจุลภาคเปลี่ยนแปลงอย่างรวดเร็วไปสู่จุดสมดุล ดังนั้น การเปลี่ยนรูปย้อนกลับ (Back flow) และความเค้นย้อนกลับภายในมีส่วนเกี่ยวข้องกับการเปลี่ยนแปลงโครงสร้างจุลภาค เช่น การเกิดเกรนย่อย (Subgrain formation)

Thesis Title Creep and Microstructures of Slurry Die Cast Al-Si-Mg Alloy
Author Mr. Keren Shi
Major Program Materials Engineering
Academic Year 2016

ABSTRACT

In this research work, Gas Induced Simi-Solid (GISS) technique was used for preparing a slurry of semi-solid metal alloy which contains a low solid fraction and liquid phases. Al-Si-Mg-Fe aluminum alloy (AC4C) was used in the study. The slurry of AC4C alloy was prepared by GISS technique then cast into a simple plate product using a conventional die casting machine. The purposes of this research work were to investigate microstructures and mechanical properties of GISS die casting (GISS-DC) AC4C alloy and compare with those of conventional die casting (CL-DC) one. The studies were divided into five parts.

In the first part, the microstructures and tensile properties of as-cast specimens from different locations of die cast plates were studied. The results show that the specimens from the bottom location, near the gate section and from the middle location of die cast plates are stronger and more ductility than those from the top one. The top location of die cast plates contains more defects, such as shrinkage pores than those from other locations. The shrinkage porosity defects are resulted in a lower strength and ductility of the as-cast product.

The second part, the tensile properties and microstructures of GISS die-cast AC4C alloy after T6 heat treatment (GISS-DC-AC4C-T6) were studied and compared with those of conventional die cast AC4C alloy (CL-DC-AC4C-T6). In the as-cast GISS-DC and CL-DC specimens, π-Chinese script and β phases were generally observed. After T6 heat treatment, the eutectic-Si particles were spheroidized and β phase was remained. Tensile tests were performed at 25, 100, 175 and 250 °C. The UTS, YS and elongation of GISS-DC-AC4C-T6 and CL-DC-AC4C-T6 decreased with increasing temperatures. At 25 °C, the GISS-DC-AC4C-T6 alloy gained UTS and YS of 300.9 MPa and 244.5 MPa, respectively. With increasing temperature, the fracture changed from brittle to ductile mode. Work hardening exponent (*n*) decreases with increasing strain. Work softening and dimples on fracture surfaces were observed at

250 °C. The transition from brittle to ductile fracture was observed in both GISS-DC-AC4C-T6 and CL-DC-AC4C-T6 alloys. The intermetallic particles and micro voids are responsible for tensile properties of the alloys.

The third part, the microstructures and creep behavior of GISS-DC-AC4C-T6 alloy were investigated at temperature range of 300-360 °C and stress range of 20-40 MPa and compared with those of CL-DC-AC4C-T6 alloy. After T6 heat treatment, spheroidization and coarsening of eutictic-Si particles occured. Shapes of primary α-Al phases in GISS-DC-AC4C-T6 alloy are rosette while those in CL-DC-AC4C-T6 alloy are dendritic. Creep stress exponents (n) and apparent activity energy (Q_c) for creep of GISS-DC-AC4CT6 and CL-DC-AC4C-T6 alloys were evaluated. The stress exponents n of CL-DC-AC4C-T6 alloy at 300 °C, 330 °C and 360 °C are 3.95, 3.66 and 4.94, while n of GISS-DC-AC4C-T6 are 3.52, 4.82 and 5.74, respectively. Based on the stress exponents n, creep mechanism of both alloys may be governed by the dislocation glide-climb process. The average activation energy for creep (Q_c) are about 257.8 kJ/mol which is higher than the activation energy for self-diffusion of pure aluminum (143 kJ/mol).

The fourth part, the analysis of creep rupture data using the Momkman-Grant model, the damage tolerance parameter and the theta projection method for predicting creep life was studied. The creep rate and rupture time are linear relationship and well fitted to the Monkman-Grant model. The creep damage tolerance parameter was analyzed for predicting creep life and creep fracture mechanisms. Based on creep curve data from the present work, constitutive models for fitting creep curves were created by using the theta projection procedure.

In the final fifth part, the stress-change creep tests were peformed at temperatures of 25, 250, 280 and 300 °C on GISS-DC-AC4C-T6 and CL-DC-AC4C-T6 alloys. The result of stress-dip (or stress decrease) is responsible for an action of the internal backstress. If the stress reduction is very small, the internal backstress will quickly be in equilibrium with the applied stress. This situation gives a normal creep curve. In the present study, the responds of stress-dip are too fast to be detected. For the large stress-dip test, the stress reduction is too large to allow the microstructures to change quickly into a balance situation. So, the back flow and internal backstress are associated with the evolution of microstructures such as subgrains fromation.

ACKNOWLEDGEMENT

First, I want to thank my academic supervisor, Asst. Prof. Dr. Thawatchai Plookphol, for giving me the opportunity to join his research group and for the patient supervision of this work.

Many thanks also to Dr. Suchart Chantaramanee for the suggestions and corrections on the written work and for his help with the sample casting, the tensile test and creep experimentation.

Special thanks to Dr. Phairote Sungkhaphaitoon for his help with the sample casting and the creep experimentation and for the numerous reviews of the draft thesis and the draft papers.

Thanks to Dr. Somjai Janudom for his help with the sample casting and for the suggestion of research, work the draft thesis and the draft papers.

Thanks to Assoc. Prof. Dr. Sirikul Wisutmethangoon for helping with the Transmission Electron Microscopy analysis.

Special thanks to Mr. Sangop Thanabumrungkul for his valuable support, advices and his help for qualify examination preparation.

Special thanks to Mr. Sukrit Songkuea and Mr. Saravut Thongkam for his help with the creep experimentation and the metallographic preparation and etching of the Al alloys samples.

Thanks also to all staff in scientific equipment center of help for giving me the opportunity to use X-ray Diffractometer, Differential Scanning Calorimeter, the Scanning Electron Microscopy and Transmission Electron Microscopy.

Thanks to the president office in Prince of Songkla University for giving me a scholarship.

Thanks to the graduate school in Prince of Songkla University for giving me the financial support to support this work.

Thanks to all my beloved friends that supported me with their smiles and words through the sunny and the stormy days of my stay in Thailand.

Thanks to my family, especially to my dear father and mother, at the other side of the computer and telephone, during the long way of this work from the very beginning to the very end.

Finally, I want to thank my wife, Dr. Huiqin Yao, for her motivation through the years and for her strong patience and love.

This work is dedicated to all my love to two my children, Xiangyao Shi and Xiangchen Shi, who were the final motivation to end it.

Keren Shi

CONTENT

COVER i

APPROVAL PAGE ii

CERTIFICATION iii

ABSTRACT v

ACKNOWLEGEMENT x

CONTENT xii

LIST OF TABLES xv

LIST OF FIGURES xvi

CHAPTER 1. INTRODUCTION 1

1.1 Background 1

1.2 Objectives 5

1.3 Significance of the study 5

1.4 Scope of the study 6

1.5 Financial support 6

1.6 Research places 6

CHAPTER 2. REVIEW OF LITERATURE AND THEORY 7

2.1 Aluminum alloy 7

2.1.1 Aluminum 7

2.1.2 Designation system for aluminum alloys 7

2.1.3 Casting Al-Si Alloy 8

2.1.4 The heat treatment of aluminum alloy 9

2.1.5 AC4C aluminum alloy 10

2.1.6 Reviews of Al-Si-Mg alloy 11

2.2 Semi-Solid Metal Casting 11

2.2.1 Theory 12

2.2.2 SSM process technology 14

2.2.3 GISS process technique 14

2.3 Mechanical behavior of Al-Si-Mg 21

2.3.1 Microstructure of aluminum silicon eutectic alloys 21

2.3.2 T6 Heat treatment 21

2.3.3 Tensile test 23
2.3.4 Creep behavior 24
CHAPTER 3. MATERIALS AND EXPERIMENTS 38
3.1 Overview 38
3.2 Materials 38
3.3 Casting 38
3.4 Heat treatment 40
3.5 Tensile test 41
3.6 Creep test 41
3.7 Microstructure characterization 47
3.7.1 Microstructure characterization by OM and SEM 47
3.7.2 Microstructure characterization by XRD and DSC 47
3.7.3 Microstructure characterization by TEM 48
CHAPTER 4. RESULTS AND DICUSSION 50
4.1 Overview 50
4.2 T6 heat treatment 50
4.2.1 Microstructure examination results by OM 50
4.2.2 Microstructure examination results by SEM 52
4.2.3 Microstructure examination results by DSC 62
4.2.4 Microstructure examination results by XRD 63
4.2.5 Microstructure examination results by TEM 65
4.3 Effect of position of as casting AC4C 66
4.3.1 Microstructures 66
4.3.2 Mechanical properties 67
4.3.3 Fracture surfaces of AC4C aluminum alloys tensile specimens were examined using SEM and OM. 71
4.3.4 Conclusions 77
4.4 The Effects of Temperature on mechanical properties after T6 78
4.4.1 Mechanical properties 78
4.4.2 Fractography of GISS-DC and CL-DC AC4C after T6 85
4.4.3 Conclusions 89
4.5 Power law creep behavior after T6 90

4.5.1 Creep behavior 91
4.5.2 Rupture of creep 98
4.5.3 Conclusions 104
4.6 Theta projection method 105
4.6.1 Estimated the yield stress at 573K, 603K and 633K 107
4.6.2 Calculation primary creep constitutive model parameters of semi-solid AC4C alloys 108
4.6.3 Calculation tertairy creep constitutive model parameters of semi-solid AC4C alloys 110
4.6.4 The creep damage tolerance 116
4.6.5 Conclusions 117
4.7 The stress-change creep 117
4.7.1 Stress change creep at room temperature and 220, 250, 280 and 300°C 118
4.7.2 Fracture of stress change creep 131
4.7.3 Conclusions 134
CHAPTER 5. CONCLUSIONS AND SUGGESTIONS 135
5.1 Conclusions 135
5.2 Suggestions 138
REFERENCES 139
APPENDIX A 152
APPENDIX B 157
VITAE 169

LIST OF TABLES

Table 1 The AA designation system for aluminum alloys. 8
Table 2 Chemical composition standard of AC4C 10
Table 3 AC4C properties by die casting 10
Table 4 AC4C properties by sand casting 11
Table 5 The AA designation system for aluminum alloys. 15
Table 6 Chemical composition of ingot of AC4C alloy 38
Table 7 Chemical composition of semi-solid GISS-die casting AC4C alloys and CL-DC AC4C alloys 38
Table 8 Data of load calibration 43
Table 9 The data of the calibration of LVDT 45
Table 10 Semi-quantitative SEM-EDS analysis of Si and Mg content in a-Al phase 59
Table 11 Tensile properties of GISS-DC AC4C speciemens prepared from different parts of die cast plate. 69
Table 12 Mechanical properties of Al-Si-Mg alloys by different semi-solid forming processes, test at strain rate of $1*10^{-2}$ s^{-1} are included for comparison. 82
Table 13 Creep stresses and minimum creep rates of GISS-DC AC4C-T6 and CL-DC AC4C-T6 (N.R. = no rupture) 94
Table 14 Yield stress at high temperatures 108
Table 15 The values of θ_1 andθ_2 109
Table 16 The values of σ/σ_y and ln θ_1 109
Table 17 The values of Ln $\theta_2$exp(Q/RT) 109
Table 18 The values of θ_3 andθ_4 111
Table 19 The values of σ/σ_y and ln θ_3 111
Table 20 The values of Ln $\theta_4$exp(Q/RT) 111
Table 21 The exponents of increase test, dip test and creep test 130

LIST OF FIGURES

Fig. 1. Schematic of dendrite multiplication for fragmentation mechanism. 13
Fig. 2. Schematic of the experimental setup used, not to scale. 15
Fig. 3. Schematic diagrams of GISS forming processes: (a) GISS die casting; (b) GISS squeeze casting; (c) GISS rheo-extrusion; (d) GISS low pressure casting. 16
Fig. 4. A representative micrograph showing different types of particles found: (a) rosette; (b) dendrite; (c) globular. 16
Fig. 5. Schematic diagram of GISS 18
Fig. 6. schematic diagram of GISS die casting 18
Fig. 7. Schematic of GISS sand casting process 20
Fig. 8. Schematic of GISS squeeze casting process 20
Fig. 9. Schematic drawing of rheo-extrusion system 20
Fig. 10. Creep curve. 24
Fig. 11. Weertman-Climb model (Weertman Pill-Box Model) 30
Fig. 12. The top edge dislocation of crystals. 30
Fig. 13. The edge-dislocation. 31
Fig. 14. Schematic drawing of GISS technique 39
Fig. 15. Schematic diagram of GISS die casting process 40
Fig. 16. Drawing of casting part. 40
Fig. 17. Designation of tensile specimens prepared from different parts of die cast plate. 41
Fig. 18. Dimensions of tensile specimen. 41
Fig. 19. The extensometer and holder system. 42
Fig. 20. Pictures of (a) tensile creep test machine and (b) temperature control and data acquisition system. 42
Fig. 21. Load cell 43
Fig. 22. The curve of load versus true force. 44
Fig. 23. Data acquisition system (DAQ) 45
Fig. 24. The curve of micrometer Millimeter vs. DC voltage 45
Fig. 25. The temperture program. 46
Fig. 26. Optical micrographs showing the microstructure of (a), (c) as-cast GISS and

(b), (d) GISS-T6. 52
Fig. 27. Elemental mapping of polished section of as cast GISS-DC AC4C alloys. 53
Fig. 28. Microstructure of as cast GISS-DC AC4C alloy (a) SEM micrograph, (b), (c) and (d) are spectra of EDS point scanning corresponding to point 1, 2 and 3 marked in (a). 54
Fig. 29. Element mapping of polished section of as cast CL-DC AC4C alloys 54
Fig. 30. Microstructure of as cast CL-DC AC4C alloy (a) SEM micrograph, (b), (c) and (d) are spectra of EDS point scanning corresponding to point 1, 2 and 3 marked in (a). 55
Fig. 31. Element mapping of polished section of CL-DC-AC4C-T6 alloys 57
Fig. 32. Element mapping of polished section of GISS-DC-AC4C-T6 alloys 57
Fig. 33. Microstructure of CL-DC-AC4C-T6 alloy (a) SEM micrograph, (b), (c) and (d) are spectra of EDS point scanning corresponding to point 1, 2 and 3 marked in (a). 58
Fig. 34. Microstructure of GISS-DC-AC4C-T6 alloy (a) SEM micrograph, (b), (c) and (d) are spectra of EDS point scanning corresponding to point 1, 2 and 3 marked in (a). 58
Fig. 35. Microstructure of as cast CL-DC AC4C alloy (a) SEM micrograph, (b), (c) and (d) are spectra of EDS point scanning corresponding to point 1, 2 and 3 marked in (a). 60
Fig. 36. Microstructure of CL-DC-AC4C-T6 alloy (a) SEM micrograph, (b), (c) and (d) are spectra of EDS point scanning corresponding to point 1, 2 and 3 marked in (a). 60
Fig. 37. Microstructure of as cast GISS-DC AC4C alloy (a) SEM micrograph, (b), (c) and (d) are spectra of EDS point scanning corresponding to point 1, 2 and 3 marked in (a). 61
Fig. 38. Microstructure of GISS-DC-AC4C-T6 alloy (a) SEM micrograph, (b), (c) and (d) are spectra of EDS point scanning corresponding to point 1, 2 and 3 marked in (a). 61
Fig. 39. DSC curves of CL-DC-AC4C-T6 alloys 62
Fig. 40. DSC curves of GISS-DC-AC4C-T6 alloys 63
Fig. 41. XRD of CL-DC-AC4C-T6 alloys 64
Fig. 42. XRD of GISS-DC-AC4C-T6 alloys 65

Fig. 43. TEM of GISS-DC-AC4C-T6 alloys 65
Fig. 44. Optical micrographs showing microstructures of AC4C alloy prepared from (a) part 1 (bottom) and (b) part 4 (top) of die cast plate. 67
Fig. 45. Stress-strain curves from tensile tests, (a), (b), (c) and (d) corresponding to specimens prepared from parts 1, 2, 3, and 4 of the die cast plate. 70
Fig. 46. (a) Ultimate tensile strength (UTS), (b) Yield strength (YS) and (c) Elongation of specimens prepared from different parts of die cast plate. 70
Fig. 47. Comparison of UTS of GISS-DC AC4C alloy from this study (meshed pattern) with those from the literatures (blank) 71
Fig. 48. Comparison of UTS of GISS-DC AC4C alloy from this study (meshed pattern) with those of GISS-DC A356 (blank). 71
Fig. 49. SEM fractographs of specimens after tensile tests. (a) and (b) corresponding to specimens prepared from parts 1 and 4 of die cast plate, respectively. 74
Fig. 50. SEM fractographs of specimens after tensile tests, showing shrinkage pores and micro voids. (a) and (b) corresponding to specimens prepared from parts 1 and 4 of die cast plate, respectively. 74
Fig. 51. SEM fractograph of specimen after tensile test, prepared from part 4 of die cast plate. 75
Fig. 52. (a) SEM fractograph of specimen after tensile test, prepared from part 1 of die cast plate and (b) EDX spectrum along the line marked in (a). 75
Fig. 53. (a) SEM fractograph of specimen prepared from part 4 of die cast plate, (b), (c) and (d) are EDS spectra from point scan corresponding to points 1, 2 and 3 marked in (a), respectively. 76
Fig. 54. Optical micrographs showing microstructures near fracture surface of specimens after tensile tests. (a) and (c) specimen prepared from part 1, and (b) and (d) from part 4 of die cast plate. 76
Fig. 55. Engineering stress-strain curves of CL-DC-AC4C-T6 alloy at 25 °C, 100 °C, 175 °C and 250 °C. 82
Fig. 56. The UTS, Yield Strength and Ductility of GISS-DC-AC4C-T6 alloy at 25 °C, 100 °C, 175 °C and 250 °C. 83
Fig. 57. The UTS, Yield Strength and Ductility of CL-DC-AC4C-T6 alloy at 25 °C, 100 °C, 175 °C and 250 °C. 83

Fig. 58. Ultimate tensile strength (UTS), elongation and reduction of area of AC4C by GISS at different temperature compared with GISS squeeze casting A356. (Last two data from paper) 84
Fig. 59. Ultimate tensile strength (UTS), elongation and reduction of area of GISS-DC AC4C alloy compared with A356 by GISS sand cast, Squeeze cast and Thixoform casting at 25 ^{o}C. 84
Fig. 60. Curve of n-ε of GISS-DC-AC4C-T6 Al alloys. 85
Fig. 61. SEM fractographs of fracture surface of GISS-DC-AC4C-T6 Al alloys show cracking of Si particles and incipient cavitation in the surrounding matrix tested at room temperature and EDX results of the pot scanning of fracture particles. (a) SEM micrograph, (b), (c) and (d) are spectra of EDS point scanning corresponding to point 1, 2 and 3 marked in (a). 87
Fig. 62. SEM fractographs of fracture surface of GISS-DC-AC4C-T6 alloy showing cracking of intermetallic particles and incipient cavitation in the surrounding matrix. (a), (b), (c) and (d) corresponding to the specimens are tested at room temperature, 100 °C 175 °C and 250 °C, respectively 88
Fig. 63. SEM fractographs of fracture surface of CL-DC-AC4C-T6 alloy showing cracking of intermetallic particles and incipient cavitation in the surrounding matrix. (a), (b), (c) and (d) corresponding to the specimens are tested at room temperature, 100 °C 175 °C and 250 °C, respectively. 89
Fig. 64. Creep curves of the GISS-DC and CL-DC AC4C Al alloys after T6 heat treatment at (a) 300 °C, (b) 330 °C and (c) 360 °C. 94
Fig. 65. Minimum creep rate versus rupture time for GISS-DC and CL-DC AC4CAl alloys. 95
Fig. 66. The variations of pressures (20 MPa, 30 MPa and 40 MPa): the creep strain with normalized time of (a) CL-DC and (b) GISS-DC AC4C Al alloy and the creep strain rate with normalized time of (c) CL-DC and GISS-DC (d) AC4C Al alloy at 330 °C. 95
Fig. 67. The variations of pressures (300 °C, 330 °C and 360 °C): the creep strain with normalized time of (a) CL-DC and (b) GISS-DC AC4C Al alloy and the creep strain rate with normalized time of (c) CL-DC and GISS-DC (d) AC4C Al alloy at 30 MPa. 96

Fig. 68. Minimum creep rate versus stress of (a) CL-DC and (b) GISS-DC AC4C Al alloys, at temperature of 300 °C, 330 °C and 360 °C. 96
Fig. 69. Minimum creep rate versus temperature of (a) CL-DC and (b) GISS-DC AC4C Al alloy at stresses of 20, 30 and 40 MPa. 97
Fig. 70. Minimum creep rate$^{1/4.5}$ versus stress of CL-DC and GISS-DC AC4C Al alloy at (a) 300 °C, (b) 330 °C and (c) 360 °C. 97
Fig. 71. Minimum creep rate versus stress of (a) CL-DC and (b) GISS-DC AC4C Al alloys, at 300 °C, 330 °C and 360 °C. 98
Fig. 72. Rupture surface for the (a) CL-DC and the GISS-DC (b) AC4C Al alloy at 20 MPa and 360 °C. 100
Fig. 73. OM microstructures of (a) the CL-DC and (b) the GISS-DC AC4C Al alloy longitudinal sections specimens after creep tests at 20 MPa and 360 °C. 100
Fig. 74. SEM microstructures of (a) the CL-DC and (b) the GISS-DC AC4C Al alloy longitudinal sections specimens after creep tests at 20 MPa and 360 °C. 101
Fig. 75. Schematic illustration of longitudinal sections fracture mechanism of alloy at creep temperature of the CL-DC AC4C-T6 Al alloy and the GISS-DC AC4C-T6 Al alloy: (a) Formation of micropores; (b) Growth of micropores; (c) Formation of cracks between micropores; (d) Rupture. 101
Fig. 76. The rupture surface element mapping of GISS-DC AC4C Al alloy at 20 MPa and 360 °C. 102
Fig. 77. The rupture surface element mapping of DC-DC AC4C Al alloy at 20 MPa and 360 °C. 102
Fig. 78. Rupture surface of GISS-DC AC4C Al alloy at (a) 20 MPa, (b) 30 MPa and (c) 40 MPa and 330 °C. 103
Fig. 79. Rupture surface of the GISS-DC AC4C-T6 Al alloy at 30 MPa and (a) 300 °C, (b) 330 °C and (c) 360 °C. 103
Fig. 80. OM microstructures of specimens after creep tests at (a) 20 MPa, (b) 30 MPa and (c) 40 MPa at 330 °C, (d) 30 MPa at 300 °C and (e) 30 MPa at 360 °C for GISS-DC AC4C. (Note that the direction of applied stress was in the vertical direction of the micrographs.) 104
Fig. 81. Rupture time versus applied stress for CL-DC AC4CAl alloys. 106
Fig. 82. Rupture time versus applied stress for GISS-DC AC4CAl alloys. 106

Fig. 83. The YS vs temperautres of semi-solid AC4C alloys 108
Fig. 84. The relationships of Ln θ_1 and σ/σ_y 110
Fig. 85. The relationships of σ/RT and Ln $\theta_2$exp(Q/RT) 110
Fig. 86. The relationships of Ln θ_3 and σ/σ_y 112
Fig. 87. The relationships of σ/RT and Ln $\theta_4$exp(Q/RT) 112
Fig. 88. Schematic representation of the physical significance of the primary and tertiary stages. 114
Fig. 89. The relationships of minimum creep rate and θ_3 θ_4. 115
Fig. 90. The relationships of normal stresses and Ln $\theta_3\theta_4$exp(Q/RT) 115
Fig. 91. The relationships of Ln($1/t_r$) and σ/σ_y 115
Fig. 92. The relationships of Ln($1/t_r$) and σ/σ_y 116
Fig. 93. The curve of creep damage tolerance parameter 117
Fig. 94. The stress increase change creep curve of GISS-DC-T6 at 25°C 121
Fig. 95. The stress-dip change creep curve of GISS-DC-T6 at 25°C 121
Fig. 96. The stress increase change creep curve of CL-DC-T6 at 25°C 122
Fig. 97. The stress-dip change creep curve of CL-DC-T6 at 25°C 122
Fig. 98. Minimum creep rate versus stress of CL-DC and GISS-DC AC4C Al alloys, at temperature of 25 °C. 123
Fig. 99. The stress increase change creep curve of GISS-DC-T6 at 250°C 123
Fig. 100. The stress change-dip creep curve of DC-DC-T6 at 250°C 123
Fig. 101. The stress change increase creep curve of DC-DC-T6 at 250°C 123
Fig. 102. The stress change-dip creep curve of DC-DC-T6 at 250°C 124
Fig. 103. Minimum creep rate versus stress of CL-DC and GISS-DC AC4C Al alloys, at temperature of 250 °C. 124
Fig. 104. The stress-increase change creep curve of GISS-DC-T6 at 220°C 125
Fig. 105. The stress-increase change creep curve of CL-DC-T6 at 220°C 125
Fig. 106. The stress-increase change creep curve of GISS-DC-T6 at 280°C 126
Fig. 107. The stress-increase change creep curve of CL-DC-T6 at 280°C 126
Fig. 108. Minimum creep rate versus stress of CL-DC and GISS-DC AC4C Al alloys, at temperature of 220 °C, 250 °C and 280 °C. 127
Fig. 109. The stress increase change creep curve of GISS-DC-T6 at 300°C 127
Fig. 110. The stress-dip change creep curve of GISS-DC-T6 at 300°C 128

Fig. 111. The stress-increase change creep curve of CL-DC-T6 at 300°C 128
Fig. 112. The stress-dip change creep curve of CL-DC-T6 at 300°C 128
Fig. 113. Minimum creep rate versus stress of CL-DC and GISS-DC AC4C Al alloys, at temperature of 300 °C. 129
Fig. 114. Exponents of CL-DC and GISS-DC AC4C Al alloys versus temperatures. 129
Fig. 115. The stress-dip change creep curve of CL-DC-T6 at 300°C with small stress and large stress deduction. 130
Fig. 116. The stress-dip change creep curve of GISS-DC-T6 at 300°C small stress and large stress deduction. 130
Fig. 117. Rupture surface for the CL-DC AC4C Al alloy (a) at 25 °C, (b) 250 °C, (c) at 280 °C and (d) at 300 °C. 133
Fig. 118. Rupture surface for the GISS-DC AC4C Al alloy (a) at 25 °C, (b) 250 °C, (c) at 280 °C and (d) at 300 °C. 134

CHAPTER 1. INTRODUCTION

1.1 Background

Prices of energy and the need of environmental protection lead to the use of light metals for the reduction of weight and consumption of energy. The net effect of automotive and aviation industry was increased toward increasing use of AC4C Al alloys. Die casting which is the near net shape manufacturing process provided the more competitive advantage than other casting. Al-Si aluminum alloys have some advantages such as great castablility, low thermal expansion coefficient, corrosion resistance and high strength to weight ratio which result in the demand in automotive industry increased for reduction of fuel consumption at a wide range of temperatures [1, 2].

Semi-solid metallurgy (SSM) is now more than 40-years-old in terms of time for its produce in the laboratory. During these years, there has been a steadily growing of research on the subject and the beginning of significant industrial applications [3]. Semi solid processing in which there is a two phase region (liquid and solid) is the net shape manufacturing of alloys. There are two major types for SSM processing: thixocasting and rheocasting. Thixocasting is a process that starts from a special billet that is carefully reheated to a semi-solid temperature range until the SSM has about 50% liquid fraction and then it is formed into parts. Rheocasting is a process that uses molten metal from the start and then produces it into semi-solid slurry by a special method. When it has about 50% solid fraction, the SSM is then formed into products [4]. A considerable amount of research work has been focused on semi-solid metal processing as a unique manufacturing method to form near-net-shape products of various industrial applications, such as for the automotive and electronic industries. As a semi-solid slurry an alloy has a much higher viscosity than when fully liquid, thereby retaining laminar flow and filling a die more evenly, facilitating the near-net shape forming with a single processing step [5].

GISS (Gas Induced Simi-Solid), which was being developed at the Department of Mining and Materials Engineering, Prince of Songkla University is a novel rheocasting process which has been invented and published in 2006 by a Thai

researcher and his US co-workers to refine the size of grains and improve the mechanical properties of machining and applications. GISS semi-solid die casting process and its heat treatment will be widely used in Metallurgical process in the expectable future. A lot of research work has been focused on semi-solid metal processing as a way to form near-net-shape products [6]. A novel approach, gas induced semi-solid (GISS) technique, has been proposed by the Innovative Metal Technology (IMT) team at the Prince of Songkla University. Gas induced semi-solid (GISS) process technique, which is a simple, economical and efficient process as novel approach been invented by the Innovative Metal Technology (IMT) team at the Prince of Songkla University. This technique has succeeded to produce globular structure in Al-Si alloy [7]. This technique involves the flow of very fine inert gas bubbles out of porous graphite to the liquid aluminium. It has since been proven a simple, economical and efficient process. Additionally, this technique has succeeded to produce globular structure in A356 alloy [7].

The components which produce by high pressure die casting could have more minimal air entrapment and oxide inclusions and higher mechanical properties, because there is the less turbulent flow during the mold filling. The cost of components production by GISS die processing is lower than of those by conventional liquid die-casting (CL-DC). However, Al-Si casting Al alloys also have poor ductility and toughness. So the microstructural effect such as dendrite and Si particles shape and size have been studied extensively [8]. So, many processing want to control the shape and size of Si particles to improve the mechanical behavior, such as solidification [9], additions of modifying elements [10] and heat treatments [11]. T6 heat treatment is sample and produces maximum strength for Al-Si alloys [12, 13]. In the AC4C that is one kind of Al-Si alloys, addition of Mg can increase strength but decreased ductility [14], so addition of Fe to increase the ductility. However, no work has focused on the microstructure of semi-solid Al-Si-Mg-Fe alloys after T6.

The study of creep properties at high temperatures has received little attention on Al-Si alloys and a few research work focus on semi-solid Al-Si at lower temperature [15] or element effect on impression creep [14]. The creep is of considerable importance of designing structural components that are required to maintain dimensional stability over a long period while in service. Some structural

materials are used at various temperatures; therefore, temperature plays a major role in creep deformation. Usually, these structures operate in temperatures higher than 0.5 T_m (T_m being the melting temperature) under loads which would not cause plastic deformation at room temperature (loads or stresses below the yield point).

Low-temperature creep at or below 0.5T_m is believed to be governed by non-diffusion controlled mechanisms, whereas high-temperature creep, above 0.5Tm, is diffusion controlled. Under the constant load, most Al alloys display normal creep strain/time curves at temperature about over 0.5 T_m which are widely considered to have three stages, primary, secondary and tertiary [16]. Steady-state creep is often emphasized on primary or tertiary creep due to the relatively large fraction of creep life within this regime. The importance of steady state is evidenced by the empirical Monkman-Grant relationship [17]. So the most studies ignore the primary and tertiary stages and only focus on the minimum or secondary creep rate, the creep life (t_f) and the total creep strain to failure using the power law equation [18]. The constant structure is assumed during the steady state creep; however, actually it is not constant. At the temperatures from 0.6 T_m to T_m, from 1957 up to now, it is accepted that activity energy of creep is equal to self-diffusion coefficient of pure alloy or single-phase alloys, which was found by Luthy and Sherby and Miller. Therefore, Mukherjee suggested that the power low equation could change into the new equation [19]. But, the stress exponent, for particle-hardening or precipitation hardening Al alloys sometimes n values are higher than 5 due to the precipitation to block the move of dislocation or dislocation–particle interaction. Therefore, the stress exponent was higher than that in pure aluminum (≈4.5). At high temperature, the creep behavior is not driven by the applied stress, but rather by effective stress, which is $\sigma_e = \sigma - \sigma_{th}$. [20] Under this condition, the rate- controlling equations for high-temperature creep, regardless of the nature of the rate controlling mechanism, may be represented by the following form which is called the Mukherjee–Bird–Dorn expression (modified power law creep) [21]. The n=4.4 was also used in semi-solid 7075 Al alloys at 300 °C [22]. This equation has been widely used recently to explain the higher creep exponents [23-25].

However, the studies on creep of semi-solid die casting Al-Si-Mg-Fe alloys are very less in recent years. Wilshire [26] described and predicted the steady state creep phenomenology at a very widely regimes of temperatures and stresses. They

did not think that the Harper-Dorn creep, five-power-law creep, power law breakout (PLB) are transitions from one steady state rate to another. Weertman [27] suggested that the three-power-law or natural law are basically consequence, so the five-power-low which is still many researcher recognize that the five-power-law is very fairly fitted for the creep behavior for the pure metals or Class M alloys at a greatly range of stress. Although the value always is not 5 to varies from 4-8 or higher. Weertman also told that five-power-law is transition from natural law to PLB. The element solid solutions are intentional or impurity. The addition of element for alloys will be lead to hardening or softening and change the steady state exponents and activation energy of creep during the creep test at different regime of temperatures and stresses.

In recent years, there a few researchers who worked on the Al alloys. Liu [28] et al. studied on the creep aging of Al-Cu-Mg alloys. Lin group modeled the creep behavior of 2024, 2124, 7075 and Al-Cu-Mg Al alloys [18, 28-30]. Abdu [20] et al. studied the creep characteristics and microstructure of nano-particle strengthened AA6082 Al alloys. Du [31] et al. studied the microstructural evolution after creep of Al alloy 2618. Yu [32] et al. studied effect of temperature on creep behavior of 2024 aluminum alloy. Esgandari [14] et al. studied the effect of Mg and semi-solid processing on microstructure and creep properties of A356 Al alloy. Mahathaninwong [22] et al. studied creep behavior of semi-solid cast 7075-T6 Al alloy.

There many researchers who worked on the Mg and other alloys. Wan [33] et al. studied the creep and microstructure of Mg-Zn-Al alloys. Zhu [34] et al. studied the creep behaviour of die-cast Mg–3Al–1Si alloy. Yoshihiro [35, 36] et al. focused on the creep life of die cast Mg alloys. In this work, the microstructure of semi-solid AC4C Al alloys by the Gas Induced Semi-Solid (GISS) die casting process were studied and compared with commercial liquid die casting CL-DC AC4C Al alloys after T6 heat treatment, and the creep behavior of semi-solid AC4C Al alloys by the Gas Induced Semi-Solid (GISS) die casting process were investigated and compared with commercial liquid die casting CL-DC AC4C Al alloys at temperature of 300 °C, 330 °C and 360 °C and pressures of 20, 30 and 40 MPa.

Although there are many people who have studied on the tensile test and creep behavior of the aluminum alloys [37], only a few of them study on the heat treatment effect on tensile properties of the high Si aluminum alloys, but none of them

worked on GISS in the comparison with CLC. However, GISS semi-solid process and its heat treatment will be widely used in Metallurgical process in expectable future. All above motivated us to study on microstructure, the tensile test and the creep behavior of the AC4C aluminum alloys. In my work, combination of GISS and die casting will be studied by using the AC4C aluminum alloys.

1.2 Objectives

1.2.1 To investigate effect of location of specimens on tensile properties and microstructures of as cast AC4C produced by the GISS die-casting and compared with CL-DC AC4C alloys at room temperature.

1.2.2 To investigate tensile properties and microstructures of AC4C produced by the GISS die-casting and compared with CL-DC AC4C alloys at room and high temperature.

1.2.3 To investigate creep and microstructures of the AC4C alloys produced by GISS die-casting and compared with CL -DC AC4C alloys at T6 heat treatment.

1.2.4 To analyze creep data using the θ projection method.

1.3 Significance of the study

1.3.1 Understand the influence of locations of specimens on tensile properties and microstructures of GISS-DC Al alloy.

1.3.2 Obtain tensile properties and microstructures of GISS-DC-T6 and CL-DC-T6 Al alloy at high temperatures.

1.3.3 Gain knowledge of creep and microstructures of GISS-DC-T6 and CL-DC-T6 Al alloy.

1.3.4 Establish a constitutive equation for semi-solid Al alloy to describe primary and tertiary creep using the θ projection method.

1.4 Scope of the study

1.4.1 The position effect on GISS die casting process of AC4C aluminum alloys which compared with CLC, will be studied in this research.

1.4.2 The tensile property of the GISS die casting AC4C alloys at various temperature with a range from room temperature to 250^{o}C has been studied.

1.4.3 The creep property of the SSM AC4Caluminum alloy by the GISS die casting process after T6 heat treatment will be evaluated compared with the CL-DC.

1.4.4 Microstructure characterizations of the AC4C produced by GISS and CLC process after heat treatment and as-casting and creep test are examined by Optical Microscopy (OM), Scanning Electron Microscopy (SEM), and Transmission Electron Microscopy (TEM).

1.4.5 The constitutive equation of semi-solid Al alloys to describe and prediction the primary stage and tertiary stage of creep is established using the θ projection method.

1.5 Financial support

This work was supported by the Higher Education Research Promotion and National Research University Project of Thailand, Office of the Higher Education Commission and research scholarship from Graduate School of Prince of Songkla University. The writer was funded by the president scholarship from president office of Prince of Songkla University.

1.6 Research places

1.6.1 Department of Mining and Materials Engineering, Faculty of Engineering, Prince of Songkla University.

1.6.2 Scientific Equipment Center, Prince of Songkla University, Hat Yai, Songkhla, Thailand.

CHAPTER 2. REVIEW OF LITERATURE AND THEORY

2.1 Aluminum alloy

2.1.1 Aluminum

The human civilizations are linked with materials and the stage of era uses some kinds of metals to name. Aluminum plays a very important role in our time. Aluminum comprises approximately 8% of the earth's crust [38]. Due to no natural aluminum and aluminum alloy, the Hall-Heroult process was developed to produce aluminum commercially. The higher specific strength of aluminum alloys, higher corrosion resistance of the formation of a stable oxide layer and ease of working lead to that aluminum alloys are competitive with ferrous alloys in engineering applications of industry.

2.1.2 Designation system for aluminum alloys

There are different designation systems for aluminum alloys at different country. Aluminum alloys are used the Aluminum Association (AA) system of the United States commonly all over the world[39]. There are casting alloys and wrought alloys (e.g. rolled, pressed and forged) after alloying process, as shown in Table 1 [39].

The Aluminum Association system (International Alloy Designation System), a Unified Numbering System (UNS) numbering system developed by the Society of Automotive Engineers, the American Society for Testing of Materials (ASTM) and the International Organization for Standardization (ISO) makes an international agreement on the standard notation and description of wrought alloys [40]. However, for casting alloys, in the ASM Specialty Handbook there is no similar international agreement on the standard notation and description [40].

Table 1 The AA designation system for aluminum alloys.

Wrought Alloys		Cast Alloys	
1xxx	≥99% pure Aluminum	1xx.x	≥99% pure Aluminum
2xxx	Aluminum-Copper	2xx.x	Aluminum-Copper
3xxx	Aluminum-Manganese	3xx.x	Aluminum-Silicon-Copper-Magnesium
4xxx	Aluminum-Silicon	4xx.x	Aluminum-Silicon
5xxx	Aluminum-Magnesium	5xx.x	Aluminum-Magnesium
6xxx	Aluminum-Magnesium-Silicon	6xx.x	Aluminum-Silicon-Magnesium
7xxx	Aluminum-Zinc	7xx.x	Aluminum-Zinc
8xxx	Aluminum-Other elements	8xx.x	Aluminum-Tin alloys
9xxx	Unused series	9xx.x	Aluminum-Other elements

2.1.3 Casting Al-Si Alloy

Al-Si aluminum alloys have some advantages such as great castablility, low thermal expansion coefficient, corrosion resistance and high strength to weight ratio which result in the demand in automotive industry increased for reduction of fuel consumption at a wide range of temperatures [1, 2]. However, Al-Si casting Al alloys also have poor ductility and toughness. So the microstructural effect such as dendrite and Si particles shape and size have been studied extensively [8].

There are three different types of aluminum production, namely super purity, commercial purity and alloys. Alloys include castings and wrought products. The amount of additions in casting alloys is commonly greater than those wrought ones[40].

Cast Aluminum alloys are widely used, because they possess many desirable qualities which include high fluidity, low melting points, lightweight, rapid heat transfer and good surface finish [41]. Using Alloy additions enhance some special properties, such as the most common addition silicon. Other alloying additions also are used to improve the mechanical properties of the casting, or other reasons. The AC4C is focused in present work. So a list of some elements presents in AC4C alloys, as follows.

Silicon. The addition of silicon can increase fluidity, decrease the melting temperature, and reduce hot tearing. The percentages of silicon can depend on the specific casting process. Slow cooling processes can use alloys with lower silicon

compositions of 5% to 7%, such as sand and investment casting. Fast cooling processes need higher silicon contents of 8% to 12%, such as die-casting. Because fast cooling processes need a higher fluidity and lower melting temperature than lower. These advantages result in most common commercial casting aluminum alloys containing higher percentages of silicon.

Magnesium. The small additions of magnesium lead to increase tensile and fatigue strength, and decrease ductility and impact strength. The containing Mg precipitation formation is very large to effect the mechanical properties.

Iron. Iron usually is an impurity in aluminum alloys to decreases the mechanical properties of the alloy due to formation of phases such as $FeAl_3$ and $\beta AlFeSi_2$. Iron increases hot tear resistance and reduces die soldering, but decreases flowability and feeding characteristics.

Manganese. When manganese presents in casting alloys, most of it comes from recycled scrap wrought alloys. Manganese barely effects on the mechanical properties of cast aluminum silicon alloys. If alloys contain iron element, manganese will form into α Al (Mn, Fe) Si "Chinese script" precipitates instead of more brittle β $AlFeSi_3$ plates [42].

2.1.4 The heat treatment of aluminum alloy

In 1903, Alfred Wilm, a German, made an accidental discovery of Duralumin, as well as the age hardening of Al alloy [43]. The discovery of age hardening by Alfred Wilm 100 years ago was the most important metallurgical development during the 20^{th} century. Although this method has been associated with special aluminum alloys, more and more alloys may be strengthened by this method of heat treatment. As Martin said, “the gradual realization that age hardening has its origin in complex precipitation processes provides a good example of the transition of metallurgy from an art to a science” [44]. The process or structures that was invisible in an optical microscope in the past can now be resolved at an atomic level using the modern scientific analysis technology, such as scanning electron microscope (SEM) [45], transmission electron microscope (TEM) [46], Energy Dispersive X-ray Detector (EDX) [47], electro-probe microanalyzer (EPMA) [48] and so on.

The designations of heat treatment and temper as follows. **F,** means no

special heat treatment or working applied to them. **H** is used to the wrought products with undergoing strain hardening without regard to heat treatment. **O** is annealed state which is nominally the lowest strength, highest ductility state. **W,** is solution heat treatment without the age hardening treatment. **T** is also heat treatment with (e.g. a few weeks) naturally or artificially (i.e. at an elevated temperature) aging hardening.

The number digit designations after letter indicates more specific details about the heat treatment. For example, 2024 T4 indicates an aluminum-copper alloy that has been solution heat treated and naturally aged at room temperature. 2024 T6 indicates an aluminum-copper alloy with heat treatment and artificially aging[49].

Present work focus on the tensile test, creep property and Microstructures of Al Alloys of GISS-DC AC4C as casting and T6 heat treatment.

2.1.5 AC4C aluminum alloy

The AC4C (Al-Si-Mg-Fe) series aluminum alloy is developed by the United States in the 1970s to the late 1970s for the automotive industry[50]. The AC4C is JIS standard designation due to the lack of AA standard to describe the Al-Si-Mg-Fe. With the rapid development of automobile industry, the AC4C aluminum alloy in the late 1980s has been widely applied in the automotive industry[50]. In Table 2, the composition standard of AC4C is showed, there are Si, Mg, Cu, Mn, Fe and Zn elements in AC4C. In Table 3 and Table 4, the mechanical properties of die and sand casting AC4C is shown. It is noted that the mechanical properties of die casting are better than sand casting and the highest tensile stress is 230 N/mm^2.

Table 2 Chemical composition standard of AC4C [50]

Si	Mg	Cu max	Mn max	Fe max	Zn max	Ti max	other (each) max	others (total) max	Al
6.5 to 7.5	0.20 to 0.4	0.20	0.6	0.5	0.3	0.20	0.05	0.15	Bal.

Table 3 AC4C properties by die casting [50]

Alloys	Heat Treatment	Tensile Test		HBW
		Tensile stress (N/mm^2)	Elongation (%)	
AC4C	F	150 above	3 above	55
	T5	170 above	3 above	65
	T6	230 above	2 above	85

Table 4 AC4C properties by sand casting [50]

Alloys	Heat Treatment	Tensile Test		HBW
		Tensile stress (N/mm^2)	Elongation (%)	
AC4C	F	130 above	-	45
	T6	220 above	-	80

2.1.6 Reviews of Al-Si-Mg alloy

In recent years, there are some of the studies focusing on Al-Si-Mg Al alloy [51-65]. In particular, the research group of PSU in Thailand carried out a series of studies around the Al-Si-Mg alloy [51-53, 56, 66], The GISS gravity sand casting.[66] and GISS extrusion process [56] is studied and both succeed. A new approach to evaluate fluidity of AC4C is developed to analysis the casting process and calculate the fraction of solid in the semi-slurry [53]. Effects of primary phase morphology on mechanical properties of AC4C alloy are studied [4].

In other countries, there many researches focus on different casting process of Al-Si-Mg, such as Gravity Die Castings [65], high pressure die casting [67], Rotary-die equal-channel angular pressing [68, 69], Gravity Castings [70, 71], rotary-die equal channel angular pressing [68, 72], ultrasonic insert casting [73] and squeeze castings [74]. The cooling rate is an important parameter during casting process, which strongly effect the microstructure and mechanical properties casting production during the casting process [65, 67]. Others parameter during the casting process of AC4C alloy is studied, such as, crack [62], mechanical vibration, [64, 65] filling model [70] and so on.

Al-Si-Mg alloys, which is used as matrix into composite material, widely cause concerns [58, 61, 75-77]. The other mechanical behavior of AC4C is studied, such as cyclic [78] fatigue [79, 80] welding [54, 81, 82], creep behavior [83-85] and so on.

2.2 Semi-Solid Metal Casting

In 1971, Spencer invented semi-solid metal (SSM) [86, 87] processing which is a metal forming process that fills partially solidified metal with globular

structure in a mold at Massachusetts Institute of Technology.

The benefit of SSM is lower heat content than liquid metal, partially solidified metal at the time of mold filling, higher viscosity than liquid metals, flow stress lower than that of solid metals [86].

A fine equiaxed microstructure is better than a coarse dendritic structure. Because of improved metal fluidity, finer dispersed porosity and second phases, improved resistance to hot tearing, greater fatigue strength, and better pressure tightness [88].

Methods to obtain the non-dendritic structure: Agitation to a molten metal to achieve grain multiplication by dendrite fragmentation. It has been proposed that the convection produced during solidification causes dendrite arms to ‘melt’ off or ‘break’ off which then act as ‘‘secondary nuclei’’ particles. The high density of particles allows non-dendritic growth and results in grain-refined microstructures. Mechanical stirring, electromagnetic stirring, low-temperature casting, and ultrasonic vibrations. These techniques use different media or means to achieve agitation. In mechanical stirring, the media is solid impellers or cylindrical rods. In the other processes, electromagnetic force, convection from fluid flow, and vibrations are the means to apply agitation [89].

2.2.1 Theory

There are two main kinds of mechanism: Nucleation and fragmentation. Some researchers proposed that the globular grains form directly through direct nucleation and growth. Others proposed that the grains come from fragmented dendrite arms [86].

1. Nucleation mechanism

The rapid and continuous heat extraction and melt convection will result in the nucleation and growth to obtain the numerous grains or particles [90]. Researchers [90] proposed the crystal separation theory, explaining that the granular crystals nucleate and grow on the chill mold wall and separate from it due to the fluid motion. Others proposed that the globular form directly through direct nucleation and grown [91].

2. Fragmentation mechanism

Dendrite fragmentation is the formation of SSM metal structure [92]. The convection of melt during the solidification causes dendrite arms to ‘melt’ off or ‘break’ off, so ‘secondary nuclei’ particles shown in Fig. 1 is producted. Then, a large number of the particles from the fragmentation have make to non-dendritic or ‘particles’ growth [92].

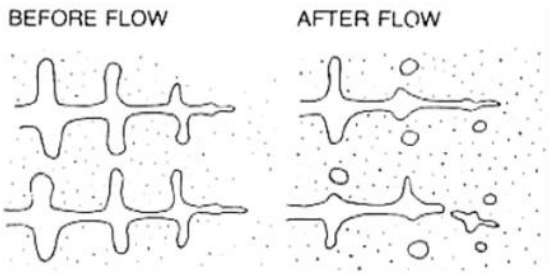

Fig. 1. Schematic of dendrite multiplication for fragmentation mechanism [92].

The mechanism for SSM structure formation is still unclear and disputed [86]. It is well accepted that the globular microstructure is obtained when a great large number of solid grains is formed during the early stages of solidification[93]. The high density of the solid grains results in non-dendritic growth and globular microstructure [93]. In semi-solid microstructure [83, 94, 95], there is the globular microstructure is. However, most of them cannot explain it perfectly, so it is important to study the microstructure evolution at the early stages [96, 97].

The real time or in-situ is a good way to analysis the microstructure and get some accurate information about the solid particle evolution in the slurry [98, 99]. But the real time or in situ is difficult and complicated. Therefore, a new approach to evaluate the solid fraction of semi-solid slurries is produced [100]. This method is easy and simple, so it is used to explain the evolution mechanism during the GISS process [91, 101]. However, the results cannot strongly explain the evolution mechanism during the GISS process.

The fluidity of semi-solid slurries is very important for the uniform distribution of microstructure during the semi-solid process due to the liquid part in semi-solid slurry [53]. Therefore, the effect of fluidity on the semi-solid process is studied. With the increase of solid fraction, the rheological behavior of the semi-solid

slurries turned from turbulence flow to laminar flow. The turbulence flow is considered to be responsible for the worse tensile properties and fracture [52].

2.2.2 SSM process technology

Semi-solid metal (SSM) processing has been continuously developed for about 40 years. SSM metal parts have uniform microstructure and improve mechanical properties to use into various applications [102].

There are two types of SSM processing: **Thixocasting** and **rheocasting** SSM processing routes. **Thixocasting** is a process which starts from a special billet. The billet will be reheated then be formed into parts. The cost of Thixocasting is higher, so the recent trend in SSM processing is focused on the rheocasting. **Rheocasting** is the SSM processing which starts from the molten metal and then is going to be turned into the semi-solid slurries before forming into parts [45, 51, 103].

Today several processes are being used worldwide, including the New Rheo Casting process (NRC) [104], , the Sub Liquidus Casting (SLC) [105], the Slurry-On-Demand process (SOD) [106], the Semi-Solid Rheocasting (SSR) [6] and so on.

2.2.3 GISS process technique

The new technology of GISS process is invented and developing [89]. It was the first time that the new bubbling method was reported in 2006 [89]. J. Wannasin used aluminum alloy A357 and achieved grain refinement using bubbles to agitate a molten metal during the solidification. The alloy was melted and heated to 630 °C. Then it was slowly cooled down to 625 °C with the cooling rate of about 1°C/min, and the diffuser immersed. When the metal temperature reached 610 °C and 612 °C (about 45% solid fraction), removed the crucible and quenched in water.

In 2008, J. Wannasin studied the feasibility of preparing A356, Al-4.4%Cu, and ADC12, semi-solid metal slurry using GISS shown in Fig. 2. He got some data from the cooling curves and show them in Table 5. According this, he succeeded to produce SSM A356 and Al-4.4 percentage Cu with the fine non-dendritic and globular structure using the GISS. However, he failed to get the SSM ADC12 because of eutectic reaction during solidification [93].

The current focus of the GISS process is on the SSM slurries with low fraction solid (<0.25). Because it needs the little modification to the conventional machines and processing steps. So die casting, squeeze casting, gravity casting, and rheo-extrusion of GISS processes are carried out shown in Fig. 3 on some commercial alloys include: A356, A380, A383, 5052, 6061, 2024, 7075, and ZAMAK-3 using the GISS processes [4, 56, 63, 93, 107-109].

The representative micrographs of SSM are the primary α particles (in Fig. 4) are dispersed in a matrix of finer secondary particles and eutectic structure. Three types of primary α particle are observed in semi-solid parts. According the fragmentation mechanism, the mother dendrites are formed and then are partially remelted, so the surviving fragments are formed the different shapes of primary α particle [110].

Table 5 The AA designation system for aluminum alloys.

Aluminum alloy	Liquidus temperature (°C)	Eutectic temperatures (°C)
A356	612	574
Al-4.4%Cu	646	571
ADC12		569

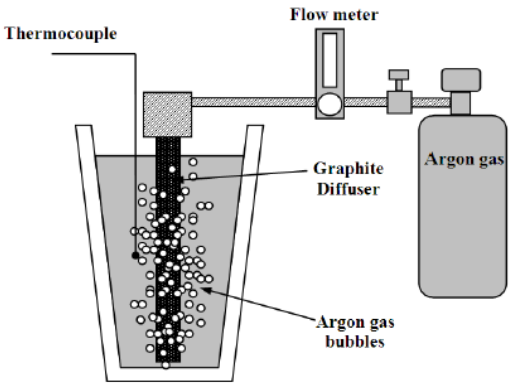

Fig. 2. Schematic of the experimental setup used, not to scale. [93]

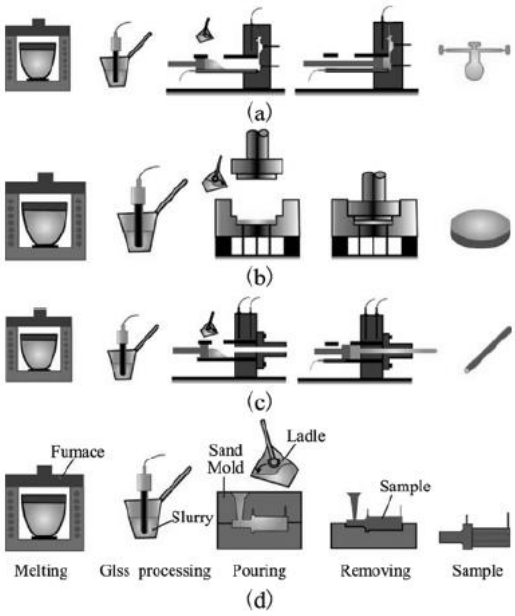

Fig. 3. Schematic diagrams of GISS forming processes: (a) GISS die casting; (b) GISS squeeze casting; (c) GISS rheo-extrusion; (d) GISS low pressure casting. [63, 114, 56]

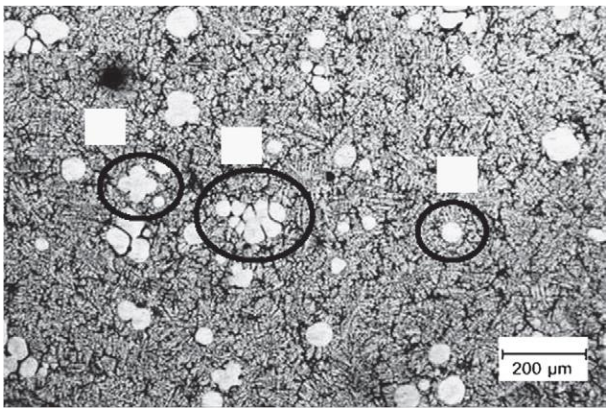

Fig. 4. A representative micrograph showing different types of particles found: (a) rosette; (b) dendrite; (c) globular [89].

2.2.3.1 GISS die casting

The parts produced by high-pressure die-casting, have high quality because of the less turbulent flow during the mold filling [52]. Fig. 5 and Fig. 6 show the GISS die casting process. So the parts have minimal air entrapment and oxide

inclusions and higher mechanical properties. The production cost of parts produced by SSM processing is lower than of those processing by conventional liquid pressure die-casting [7, 51, 52]. Because SSM slurry cast into a die requires significantly less heat to flow into the die than the liquid process. So the operates of the die needs a lower temperature and the die life increase. In addition, less heat result in the shorter cycle time. It can increase the productivity. In addition, SSM processing need less heat, that allow thick and large components to be cast with SSM die-casting [93].

In 2008, J. Wannasin reported a new approach to evaluate the solid fraction of semi-solid slurries in a rheocasting aluminum die casting alloy AC4C rapid quenching method [100]. It was important during the GISS slurries production to control the solid fractions. He also had been making effort to scale the process up for high pressure die casting applications [93]. But, there still have been some problem to solve, such as hot tearing and shrinkages [93]. The appropriate T6 heat treatment for GISS die casting A365 was studied in 2008 [111]. The condition of the heat treatment is : solubilizing at 520 and 540 °C for 4hr. aging at 135, 165 and 195 °C for 4, 8, 12 and 16hr [111].

In 2010, S. Janudom, et al studied the ADC12 using GISS die casting [107]. It is feasible to produce SSM ADC12 parts using GISS DC with the appropriate plunger speed and solid fractions of the slurry. The porosity and shrinkage defects in the alloys can be reduced by increasing the solid fraction of the slurry. In 2010, S. Thanabumrungkul, et al studied that the GISS DC is feasible to produce the Al 7075 tube adapt casting parts and Al A356 automotive casting parts and the automatic GISS DC system is developed by GISSCO Co., Ltd. in Thailand[108]. The parts by GISS-DC have less prosity than that of LDC. The UTS of LDC, GISS-DC and GISS-DC T6 are 162.1, 235.3 and 293.3 MPa, the elongations of them are 2.08, 7.35 and 10.21%.

In general, the low solid fraction had been used for producing the casting and minor machine modifications. The small size of the primary α(Al), the SSM alloys produced with the low solid fraction have got the excellent mechanical properties especially the elongation [51].

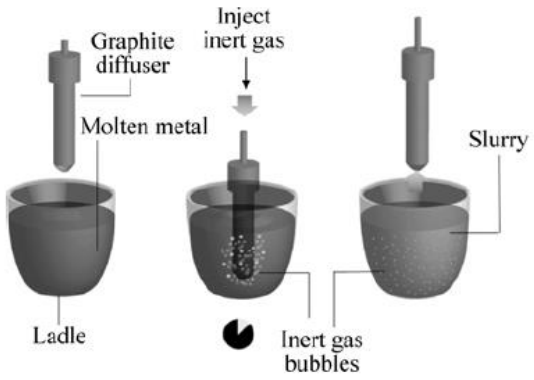

Fig. 5. Schematic diagram of GISS[93]

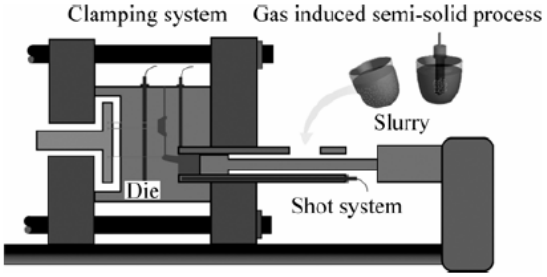

Fig. 6. schematic diagram of GISS die casting [93]

2.2.3.2 Other GISS casting processes

The SSM gravity casting with low solid fractions has been reported[112]. SSM slurries with high solid fraction have the lower fluidity to make the gravity casting impossible [113]. Although they have some advantages in small lot, complex parts and big pars. However, shrinkage and gas porosity are the major disadvantages of the gravity casting [113]. So recently, a few numbers of SSM gravity casting studies that have been carried out [91]. In 2008, Wannasin, J reported that the GISS gravity casting of Al-Cu alloys reduced the hot tearing tendency compared with liquid casting and allowed lower production costs compared with the high pressure machines[93].

In 2010, T. Chucheep et al. studied the AC4C using GISS gravity casting (Fig. 7) at a low solid fraction [63] in Fig. 8. The UTS of GISS-GC is 268.0MPa which higher than 254.0 MPa of conventional casting, and the elongation of SSM are slightly 5.4 higher than 4.0 of CVC. Nevertheless, the casting yield of GISS GC is higher than that of the conventional casting due to the elimination of a big riser [63]. In 2010, R. Burapa, et al studied the effects of primary phase morphology on the mechanical

properties of GISS squeeze casting AC4C alloys [4]. A schematic of GISS process is shown in Fig. 8. The schematic of GISS squeeze casting process is shown in Fig. 8. The SSM AC4C alloys with globular and finer primary α (Al) have got the highest ultimate tensile strength and elongation which are 203.8 MPa and 10.1%, respectively [4].

In 2012, N. Mahathaninwong at el. studied the T6 heattreatment of SSM 7075-T6 using GISS squeeze casting [22, 114] in Fig. 8. In the same year, N. Mahathaninwong at el. researched and explained the creep rupture behavior of SSM 7075-T6 using GISS squeeze casting. These alloys have a better creep resistant than that of liquid squeeze casting at stress ranges of 120-140 MPa, but the contrary in the case of 180 MPa and the activation energy was 95.827 J/mol [114]. In 2012, S. Wisutmethangoon at el studied precipitation hardening of A356 Al alloy using the GISS squeeze casting. She suggested that maximum hardness and tensile strength at 165 ^{o}C for 18h and the activation energy was 128.717 J/mol [7] .

Extrusion is one of the various forming processes that is used to produce long and straight metal products with constant cross section, such as bars, solid and hollow sections, tubes, and wires [115, 116]. The parts from this procession are in a near net shape, which require high pressure to force the slurry in the solid state. In the products, there are many defects such as surface cracking, oxide inclusion and piping defect [112]. SSM extrusion process has some advantages such as lower extrusion force, good flowability, and less friction between the dies and materials [112]. Thixo-extrusion has achieved high quality products with good surface and high ultimate tensile strength. Nevertheless, during this process, it has a problem of using a billet and non-recycled scraps. Therefore, researchers are focused on rheo-extrusion [112, 115, 116]. However, most of them need high temperature and low ram speed because of the high solid fractions. In 2010, it is with low solid fraction that T. Rattanochaikul studied the AC4C Al alloys using GISS extrusion casting (Fig. 9) so they used lower temperatures and higher speeds [56]. Only the parts produced by the conditions of 5% solid fraction at 4 and 6 cm/s plunger speeds and 10% solid fraction at 6 cm/s plunger speed can reach the expected length. There is a liquid layer at the outer of the parts. The highest UTS and YS of AC4C after T6 are 276.5 MPa and 208.4 MPa, and the elongation is 12.4% [56].

Several commercial casting parts are being developed using GISS

process such as an automotive rotor cover, a prosthesis tube adaptor, and a prosthesis foot adaptor by GISSCO, Co. Ltd [53, 109].

Although there are many people who have studied on the tensile test and creep behavior of the SSM aluminum alloys, only a few of them study on the heat treatment effect on tensile properties of the high Si aluminum alloys, but none of them works on GISS in the comparison with CLC. Although there are many works were studied on the tensile test and creep behavior of the aluminum alloys, only a few on the heat treatment effect on tensile properties of the high Si aluminum alloys, but none of them work on rheo-die casting at room temperature and elevated temperatures. However, GISS semi-solid process and its heat treatment will be widely used in industrial production in expectable future, all above motivated us to study on microstructure, the tensile test behavior of the AC4C.

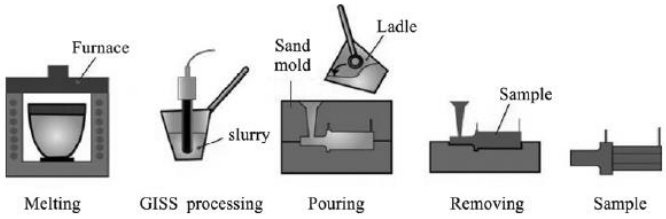

Fig. 7. Schematic of GISS sand casting process [63]

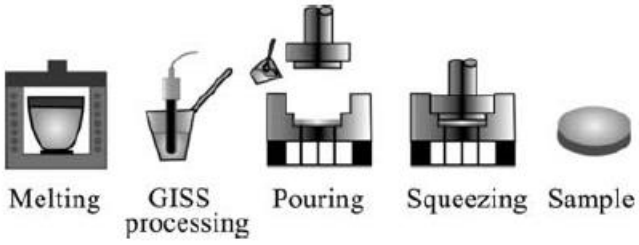

Fig. 8. Schematic of GISS squeeze casting process [114]

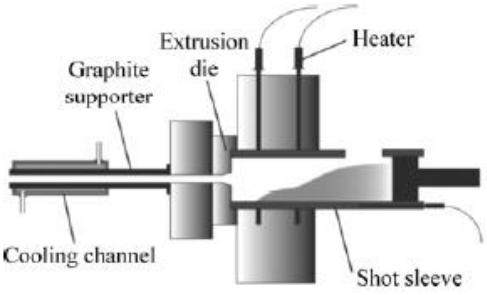

Fig. 9. Schematic drawing of rheo-extrusion system [56]

2.3 Mechanical behavior of Al-Si-Mg

2.3.1 Microstructure of aluminum silicon eutectic alloys

The three major kinds of the microstructure constituents of Al-Si eutectic alloys are the primary phases; the aluminum silicon eutectic structure; minor inclusions or particles resulting from reactions between the major and minor constituents in the melt [5, 11, 13, 15, 117-120]. These constituents and structures are mostly dependent on the the cast or wrought processing, element content and the cooling rate during solidification and heat treatment and aging [5, 11, 13, 15, 117-120].

Primary Phase. In almost all commercial castings of the aluminum silicon eutectic alloy, the major primary phase is Al, in the form of dendrites or rosettes or round [117]. Primary silicon can form in regions of the bulk casting where the cooling rates are slower or the local alloy content is more favorable towards primary silicon formation[4]. The form of the primary silicon is usually large faceted blocks [5].

Eutectic Phase. The most microstructural feature of Al-Si eutectic alloys is the morphology of the silicon in the eutectic [121]. The silicon structure in the eutectic represents the major modification of the strengthening mechanism in the alloy. The microstructure of the silicon in the eutectic can be generally described as either unmodified (acicular, massive, rod, angular, faceted, flake), partially or fully modified (fibrous, modified angular), or over modified[117, 122-124].

Inclusions. In the Al-Si eutectic alloys, there are the types of inclusions [11, 97, 124, 125]. Al-Si alloys add elements, such as titanium, manganese and magnesium, iron [13]. A common example is the undesirable β AlFeSi plates, which form in commercial Al-Si alloys, especially at the boundaries of the eutectic colonies [95, 121, 126]. Traditionally, manganese has been added to change the morphology from a plate structure to a rounded dendritic structure (Chinese script), associated with α Al (Mn, Fe) Si [46, 95, 127].

2.3.2 T6 Heat treatment

The T6 heat treatment is the most common heat treatment that contains a precipitate hardening constituent [128, 129]. Solution heat-treated and then artificially

aged: Applies to products which are not cold worked after solution heat-treatment, or in which the effect of cold work in flattening or straightening may not be recognized in applicable specifications. The eutectic structure, which forms easily spherodizes during solution treatment. This change in eutectic morphology is responsible for the improved ductility of both dendritic and SSM components, and in the T6 even strength is improved [130].

The primary reason for the solution treatment, however, is to insure that the in the aluminum matrix solute (in the case of A356, magnesium and silicon) is at its maximum solubility [131]. This solution treatment also helps maximally eliminate any coring segregation, which may have taken place [132]. After the solution treatment, components are removed from the furnace and quenched. The quenching treatment must carefully avoid creating residual stresses or distortion by cooling too quickly, which is enough to insure that incoherent precipitates do not form. Another important consequence of quenching is the retention of vacancies from the elevated solution temperature, which can promote higher rates of diffusion later on [131].

Solution heat treatment at a relatively high temperature to dissolve Si- and Mg-rich particles formed during solidification to achieve a high and homogeneous concentration of the alloying elements in solid solution. The eutectic Si particles are spheroidized [2]. The temperature of Quenching is usually room temperature, to obtain a supersaturated solid solution of solute atoms and vacancies [11]. Parts are subsequently artificially aged to accelerate the nucleation and growth of the precipitate hardening phases. At this point, it is believed clusters of aging atoms begin to form GP (Guinier-Preston zones) zones [133]. Age hardening causes precipitation from the supersaturated solid solution at an elevated temperature [11].

For Mg-Si-Mg, solution treatment was performed at 540 degree Celsius for 4 hours, followed by a water quench at room temperature [7]. The samples were then artificially aged at 195 degrees Celsius for 3 hours. The optimum aging condition of the alloy after solution heat treatment at 540 ◦C for 4 h was 165 ◦C for 18 h at which the highest hardness of 96 HRE and the average tensile strength of 312 MPa with elongation of 7.6% were obtained at this condition [7]. Nevertheless, we need more ductility because our specimen is small and thin. The optimum aging condition at 165 ◦C for 18 h exhibited higher yield strength and ulti- mate tensile strength but slightly

lower ductility than the aged specimens at 195 ˚C for 3 h and 225 ˚C for 15 min. Therefore, we chose the 195 ˚C for 3 h.

The Al-Si-Mg cast alloys are widely used in the automotive industry due to good formability, corrosion and weldability [134]. The precipitation sequence and the chemical element and structure in 6xxx and Al are difficulties to identification.

There are still some arguments in the sequence of structural change during the aging processing [135]. For Al-Si alloys without excess Si (balanced alloys). The sequence of precipitation is following:

SSS - GP zones (spheres or needles) –β" (needles)- β'(rods)- β (plates, Mg_2Si or nonstoichiometric Mg_xSi_y)

Many works focus on the heat treatment and aging processing [4, 46, 133, 136-138]. In the case of AI-7Si-0.3Mg alloy, the most common heat treatment is the T6, which consists of a solution heat treatment, water quenching and artificial aging, and it is carried out at about 540 for 4 h to dissolve the hardening elements Mg and Si in the Al matrix [138]. Hence, T6 heat treatment is used in present work.

2.3.3 Tensile test

Tensile test or tension test is a fundamental test of materials, in which a sample is subjected to uniaxial tension until failure. The results from the test are commonly used to select a material for an application, quality control. The tensile properties include ultimate tensile strength (UTS), elongation and reduction of area which can also determine the following properties: Young's modulus, Poisson's ratio, yield strength, and strain-hardening exponent.

There are many works on tensile test of Al-Si-Mg alloys [51, 104, 138, 139]. For semi-solid Al alloys, the UTS, YS and ductility is different at different temperatures [140-143] and different heat treatment [144, 145] or different casting processing [4, 56, 111, 146]. For example, Zhou Yi [140] studied on high-temperature tensile properties of semi-solid aluminium alloy A356-T6 produced by the GISS process. The results indicate that, at room temperature, the SSM A356-T6 alloy gained the UTS and 0.2% yield strength of 291 MPa and 233 MPa respectively with elongation of 11%; both the UTS and 0.2% yield strength were decreased with increasing temperature; the ductility of the SSM A356-T6 was decreased with increasing

temperatures from 25 ^{o}C to 150 ^{o}C.

2.3.4 Creep behavior

2.3.4.1 Creep theories

Creep is an important part in this thesis, so creep theories are also very important. In practical application, some materials are required to survive for long periods under fixed or no fixed load at room or relative high temperatures, example for the turbine blades of jet engineering [16].

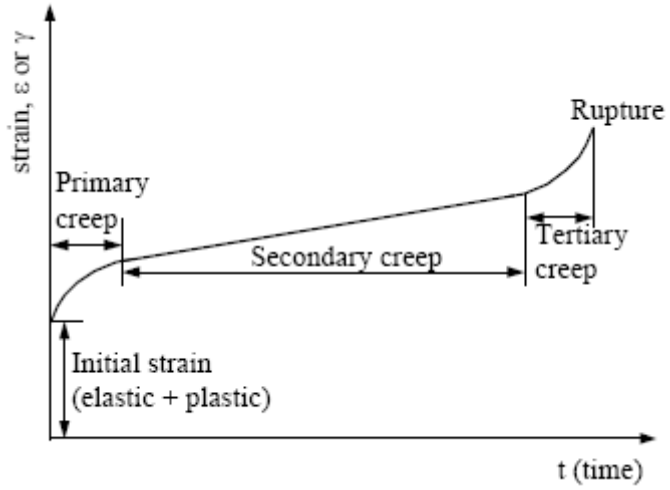

Fig. 10. Creep curve [16].

Under the constant load, most Al alloys display normal creep strain/time curves at temperature about over 0.5 T_m which are widerly considered to have three stages, primary, secondary and tertiary. In classic creep curve (Fig. 10), there are three creep stages. They are the primary (initial, transient) creep stage, the secondary (steady-state) stage and the accelerating (tertiary) creep stage [16]. However, the most studies ignore the primary and tertiary stages and only focus on the minimum or secondary creep rate, the creep lifeand the total creep strain to failure using the power law equation, as follow:

$$\dot{\varepsilon} = \frac{d\varepsilon}{dt} = A\sigma^{n} exp - \left({Q_C}/{RT}\right) \quad (1)$$

Where $\dot{\varepsilon}$ is called the rate for creep, ε is the time-dependent or creep strain, σ is the nominal stress on the specimen, A is a constant, Q_C is called the 'activation energy' for creep and has units of Jmol-1, R is the universal gas constant (8.314 Jmol-1K-1). However, the studies on creep of semi-solid die casting Al alloys are very less in recent years.

When power law relationships are used to describe steady state creep behavior, the values of n and Q_c can vary in different stress/temperature regimes. Some structural materials are used at various temperatures; therefore, temperature plays a major role in creep deformation. Usually, these structures operate at temperatures higher than 0.5 T_m (T_m being the melting temperature) under loads which would not cause plastic deformation at room temperature (loads or stresses below the yield point). Low-temperature creep at or below $0.5T_m$ is believed to be governed by non-diffusion controlled mechanisms, whereas high-temperature creep, above $0.5T_m$, is diffusion controlled. In most metals and alloys, diffusion mechanism is the dominant in the vacancy movement, in a pure metal, which is called self-diffusion. The activation energy of self-diffusion is called the activation energy for self-diffusion, Q_{SD}. The activation energy for creep Q_C is frequently found to be equal to that for self-diffusion at high creep temperatures, Q_C values significantly less than Q_{SD} are often reported at creep temperature of around 0.4 to 0.6 T_m [16].

There are many numerous factors involving material costs, ease of component manufacture, material density, resistance to environmental attack and the ability to resist serious distortion or failure during service that must be considered when selecting materials for high temperature service [18, 28, 33]. A phenomenon known a "creep" must be given to particular attention, which is the resistance of materials to deformation or failure over long time under load at relative high temperatures and the creep is of considerable importance in designing structural components that are required to maintain dimensional stability over a long period of time while in service [35]. At low temperatures, dimensional changes are usually extremely small and failure rarely occurs due to creep. In contrast, at high temperatures, creep deformation can cause considerable changes in dimensions and failure generally occurs after some time, t_F. The time to fracture, t_F, decreases with increasing temperature and with increasing applied stress. So, it would be important to avoid creep by selecting materials of high

melting point and maintaining operating temperatures at low temperature always less than about 0.3Tm [147]. Unfortunately, this simple answer is insufficient to all the industry applications.

Although for different applications maybe need specified operation conditions, all of them need know the required operating life to avoid excessive, creep distortion or creep failure [35, 36, 148]. Therefore a detail of the creep behavior of materials is essential for safe and economic design of critical components and structures which must operate for long periods under load at high temperatures.

The study of creep properties at high temperatures has received little attention for Al-Si alloys and a few research work focus on semi-solid Al-Si at lower temperature [15] or element effect on impression creep [14]. The creep is of considerable importance in designing structural components that are required to maintain dimensional stability over a long period while in service. Some structural materials are used at various temperatures; therefore, temperature plays a major role in creep deformation. Usually, these structures operate at temperatures higher than 0.5 T_m (T_m being the melting temperature) under loads which would not cause plastic deformation at room temperature (loads or stresses below the yield point).

Low-temperature creep at or below 0.5T_m is believed to be governed by non-diffusion controlled mechanisms, whereas high-temperature creep, above 0.5Tm, is diffusion controlled. Under the constant load, most Al alloys display normal creep strain/time curves at temperature about over 0.5 T_m which are widely considered to have three stages, primary, secondary and tertiary [16]. Steady-state creep is often emphasized over primary or tertiary creep due to the relatively large fraction of creep life within this regime. The importance of steady state is evidenced by the empirical Monkman-Grant relationship [17]:

$$\dot{\varepsilon}_{ss} \times t_r = k \quad (2)$$

Where $\dot{\varepsilon}_{ss}$ is steady state creep rate, t_r is time of rupture, k is a constant. So the most studies ignore the primary and tertiary stages and only focus on the minimum or secondary creep rate, the creep life (t_f) and the total creep strain to failure using the power law equation [18], as follow:

The constant structure is assumed during the steady state creep; however, actually it is not constant. At the temperatures from 0.6 T_m to T_m, from 1957 up to now,

it is accepted that activity energy of creep is equal to self-diffusion coefficient of pure alloy or single-phase alloys, which was found by Luthy and Sherby and Miller. Therefore, Mukherjee suggested that the power low equation could change into [19]:

$$\dot{\varepsilon} = A_2(\frac{D_{sd}Gb}{kT})(\frac{\sigma}{G})^n \quad (3)$$

Where $\dot{\varepsilon}$ is called the rate for creep, σ is the nominal stress on the specimen, A_2 is a constant, D_{sd} is the lattice self-diffusion coefficient, T is creep temperature, G is shear modulus, k is Boltzmann constant, b is Burgers vector.

But, the stress exponent, for particle-hardening or precipitation hardening Al alloys sometimes n values are higher than 5 due to the precipitation to block the move of dislocation or dislocation–particle interaction. Therefore, the stress exponent was higher than that in pure aluminum (≈4.5). At high temperature, the creep behavior is not driven by the applied stress, but rather by effective stress, which is $\sigma_e = \sigma - \sigma_{th}$. [20] Under this condition, the rate- controlling equations for high-temperature creep, regardless of the nature of the rate controlling mechanism, may be represented by the following form which is called the Mukherjee–Bird–Dorn expression (modified power law creep) [21].

$$\dot{\varepsilon} = A_3 \frac{DGb}{kT}(\sigma - \sigma_{th})^n \quad (4)$$

In AC4C Al alloys at a constant temperature here, the above equation can be simplified to [24]:

$$\dot{\varepsilon}_m = A_4(\sigma - \sigma_{th})^{n_m} \quad (5)$$

Where σ_{th} is the threshold stress and n_m is the stress exponent of the matrix (the pure Al n_m ≈4.5). The n=4.4 was also used in semi-solid 7075 Al alloys at 300 °C [22]. This equation has been widely used recently to explain the higher creep exponents [23-25].

However, the studies on creep of semi-solid die casting Al-Si-Mg-Fe alloys are very less in recent years. Wilshire [26] described and predicted the steady state creep phenomenology at a very widely regimes of temperatures and stresses. They did not think that the Harper-Dorn creep, five-power-law creep, power law breakout (PLB) are transitions from one steady state rate to another. Weertman [27] suggested that the three-power-law or natural law are basically consequence, so the five-power-low which is still many researcher recognize that the five-power-law is very fairly fitted

for the creep behavior for the pure metals or Class M alloys at a greatly range of stress. Although the value always is not 5 to varying from 4-8 or higher. Weertman also told that five-power-law is transition from natural law to PLB. The element solid solutions are intentional or impurity. The addition of element for alloys will be lead to hardening or softening and change the steady state exponents and activation energy of creep during the creep test at different regime of temperatures and stresses.

In recent years, there a few researchers who worked on the Al alloys. Liu [28] et al. studied on the creep aging of Al-Cu-Mg alloys. Lin group modeled the creep behavior of 2024, 2124, 7075 and Al-Cu-Mg Al alloys [18, 28-30]. Abdu [20]et al. studied the creep characteristics and microstructure of nano-particle strengthened AA6082 Al alloys. Du [31] et al. studied the microstructural evolution after creep of Al alloy 2618. Yu [32] et al. studied effect of temperature on creep behavior of 2024 aluminum alloy. Esgandari [14] et al. studied the effect of Mg and semi-solid processing on microstructure and creep properties of A356 Al alloy. Mahathaninwong [22] et al. studied creep behavior of semi-solid cast 7075-T6 Al alloy.

There many researchers who worked on the Mg and other alloys. Wan [33] et al. studied the creep and microstructure of Mg-Zn-Al alloys. Zhu [34] et al. studied the creep behaviour of die-cast Mg–3Al–1Si alloy. Yoshihiro [35, 36] et al. focused on the creep life of die cast Mg alloys. In this work, the microstructure of semi-solid AC4C Al alloys by the Gas Induced Semi-Solid (GISS) die casting process were studied and compared with commercial liquid die casting CL-DC AC4C Al alloys after T6 heat treatment, and the creep behavior of semi-solid AC4C Al alloys by the Gas Induced Semi-Solid (GISS) die casting process were investigated and compared with commercial liquid die casting CL-DC AC4C Al alloys at temperature of 300 °C, 330 °C and 360 °C and pressures of 20, 30 and 40 MPa.

The dislocation is a crystallographic defect, or irregularity, in a crystal structure. The presence of dislocations strongly influences many of the properties of materials.

Up to now, some researchers try to establish the dislocation substructure evolution processing using some techniques [149-154]. During the plastic deformation in the creep steady stage the dislocation density or misorientation angles are important to explain the microstructural changes during the creep test. The misorientation angle

is defined that the minimum rotation to bring two lattices or grains into coincidence. At the elevated temperatures, the misorientation angles are lower than 1 which are difficulty to detect using the selected area electron diffraction (SAED) [31, 115] or the electron backscattered patterns (EBSP) [127, 155] which are widely used. However, the lower misorientation angles may comprise a widely numbers of subgrain boundaries, this is the reason which it is difficult that the subgrain is difficult to find in some specimens. The dislocation density has two definitions by using the TEM, one is in the section surface, the number of dislocation line intersections per unit surface area of selected thin foil and another is the dislocation line length per unit volume. Actually, the latter one always is double of the former [18].

In the past years, the researchers used the polarized light optical microscopy (PLOM) or etch pit analysis to detect dislocation and dislocation density [156]. Now it is very clearly that the former technique is always unreliable for detecting the subgrain size due to being difficult to detect the lower misorientation angles. The latter may be unreliable due to being no able to detect the dislocation density when material has higher density at very small areas.

However, for TEM, there also have some short coming. First, the result is dependent on the small given thin foil which transparent to the electron beam. Secondly, some FCC metals such as Al have high stacking fault energy, so dislocation will recovery very quickly in the thin foil [150, 157]. It is easy to lead to be difficult to find the dislocation at elevated temperature or underestimate the dislocation density. Thirdly, at the elevated temperatures, the misorientation angles are lower than 1 which is difficulty to detect by TEM, which may comprise a main subgrain boundaries. Fourthly, the dislocation has some different set in FCC metal and tilt, twist and mixed, or called edge or screw or mixed of Burger vectors. Howerver only the tilt angle by Kikuchi shift using the TEM is accurately got, but detect the accurate misorientation angles need the single orientation, the twist or mixed can not accurately get. Therefore, examination of total subgrain boundaries or subgrain structure is impossible [158-161] .

2.3.4.2 θ projection

From Weertman-Climb model, the relation of stress and temperature will be revealed combining with other creep theory and equations [162].

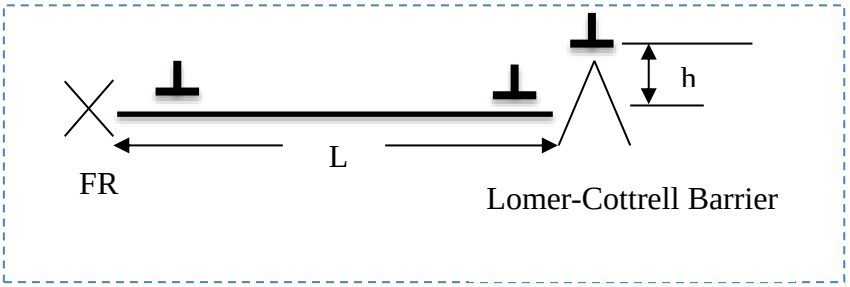

Fig. 11. Weertman-Climb model (Weertman Pill-Box Model)

L = Average distance a dislocation glides

t_g = Time for glide motion

h = Average distance a dislocation climbs

t_c = Time for climb

$$\Delta\gamma = \Delta\gamma_g + \Delta\gamma_c \quad (6)$$

$\Delta\gamma$ = Strain during glide-climb event

$\Delta\gamma_c$ = Strain during climb event

$\Delta\gamma_g$ = Strain during climb event

$$\Delta\gamma_g \gg \Delta\gamma_c$$

So

$$\Delta\gamma \approx \Delta\gamma_g = \rho bL \quad (7)$$

Orowan equation[163]:

$$\dot{\varepsilon} = \rho bv \quad (8)$$

b = Type of dislocation

ρ = Density of dislocation as function of stress

v = Velocity of dislocation as function of stress

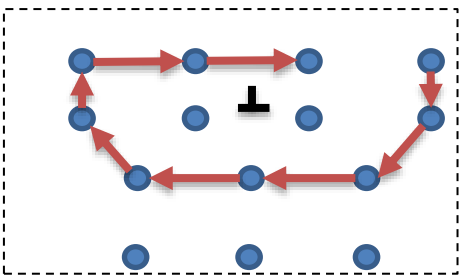

Fig. 12. The top edge dislocation of crystals.

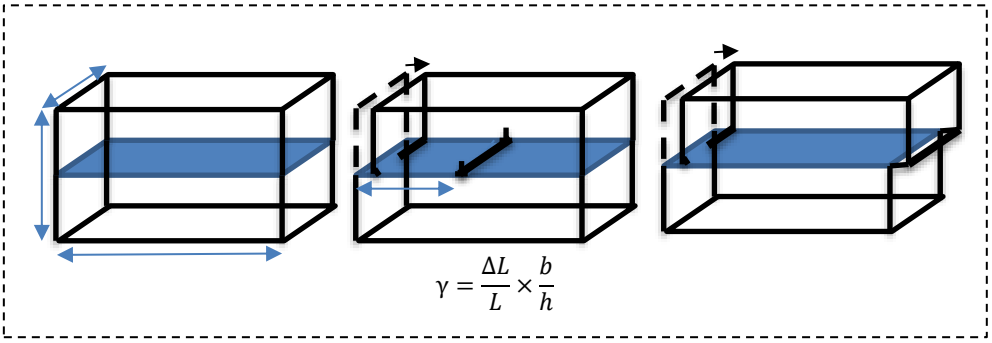

Fig. 13. The edge-dislocation.

$$V = Lhl \tag{9}$$

If one dislocation glides through part of the crystal the added shear strain is (in Fig. 12 and Fig.13.):

$$\gamma = \frac{\Delta L}{L} \times \frac{b}{h} \tag{10}$$

If N dislocation glide through part of the crystal the added shear strain is:

$$\gamma = N \times \frac{\Delta L}{L} \times \frac{b}{h} = \frac{Nl}{l} \times \frac{\Delta L}{L} \times \frac{b}{h} = \frac{Nl\Delta Lb}{V} \tag{11}$$

Dislocation density is defined by:

$$\rho = \frac{Nl}{V} \Leftrightarrow \gamma = \rho \Delta L b \tag{12}$$

So strain rate by:

$$\dot{\gamma} = \frac{\partial \gamma}{\partial t} = \frac{\partial(\rho \Delta L b)}{\partial t} = \rho b \frac{\partial(\Delta L)}{\partial t} \Leftrightarrow \dot{\gamma} = b\rho v \tag{13}$$

$$t = t_g + t_c \tag{14}$$

t = Strain during glide-climb event

t_c = Strain during climb event

t_g = Strain during glide event

$$t_c \gg t_g$$

So

$$t \approx t_c$$

so

$$\dot{\gamma} = \frac{\partial \gamma}{\partial t} \approx \frac{\Delta \gamma}{t} = \frac{\rho b L}{h/v_c} = \rho b (\frac{L}{h}) v_c \quad (15)$$

Where $v_c \propto \Delta C_v e^{-E_m/kT}$, E_m = activation energy of vacancy for vacancy migration [164].

Here, $\Delta C_v = C_v^+ - C_v^- = C_v^0 e^{\sigma V/kT} - C_v^0 e^{-\sigma V/kT} = C_v^0 \times 2 \times \sinh(\frac{\sigma V}{kT})$ (16)

So

$$v_c = B \times C_v^0 \times 2 \times e^{-E_m/kT} \times \sinh(\frac{\sigma V}{kT})$$

$$\dot{\varepsilon} = C\dot{\gamma}$$

We use content B and C, then content $\alpha = B \times C$

$$\dot{\varepsilon} = C\dot{\gamma} = \alpha\rho b \left(\frac{L}{h}\right) v_c = \alpha\rho b \left(\frac{L}{h}\right) \times C_v^0 \times 2 \times e^{-E_m/kT} \times \sinh(\frac{\sigma V}{kT})$$

When low stresses, $\sinh(\frac{\sigma V}{kT}) \approx \frac{\sigma V}{kT}$

So

$$\dot{\varepsilon} = \alpha\rho b \left(\frac{L}{h}\right) \times C_v^0 \times 2 \times e^{-E_m/kT} \times \sinh\left(\frac{\sigma V}{kT}\right) = 2\alpha\rho b \left(\frac{L}{h}\right) \times C_v^0 \times e^{-E_m/kT} \times \frac{\sigma V}{kT}$$

When $A_1 = \frac{2\alpha b V}{k}$ and $D = C_v^0 \times e^{-E_m/kT}$

$$\dot{\varepsilon} = 2\alpha\rho b \left(\frac{L}{h}\right) \times C_v^0 \times e^{-E_m/kT} \times \frac{\sigma V}{kT} = A_1 \rho\sigma \left(\frac{L}{h}\right) D(\frac{1}{T})$$

Dislocation density [165]: From theory and experiment we know that the density of dislocations is mainly a function (Taylor equation) of:

$$\rho = \alpha(\frac{\sigma}{b})^2 \quad (17)$$

α = Material constant

weertman : $\frac{L}{h} \propto \sigma^{1.5}$

so

$$\dot{\varepsilon} = ADf(T)\sigma^{4.5} \quad (18)$$

Like the experimentally observed in Al

In general: Power law

$$\dot{\varepsilon} = f(T)\sigma^n \quad (19)$$

When high stresses, $\mathrm{Sinh}(x) \approx e^x$

$$\dot{\varepsilon} = A_H D \mathrm{e}^{B\sigma}$$

$$\dot{\varepsilon} = A_2 \mathrm{e}^{B\sigma} \exp\left(-Q_C/_{RT}\right) \quad (20)$$

If the rate of stress is constant

$$\dot{\varepsilon} \exp\left(Q_C/_{RT}\right) = A_2 \, \mathrm{e}^{B\sigma} \quad (21)$$

$$\sigma = \frac{Q_C}{RT} + C \quad (22)$$

$$\sigma \propto \frac{1}{T} \quad (23)$$

This equation looks like to reveal some relationship between stress and temperatures; actually, this relationship does not exist. The normal stress is one of ways to consider effect of temperature [29, 166].

This talk about the creep researcher recently works. R. W. Evans and B. Wilshire proposed θ projection concept to describe the creep behavior. This method has already described the some creep behavior of metals and alloys [29, 166]. This work investigates the creep behavior of semi-solid Al alloys at elevated temperatures. The constitutive equation of semi-solid al alloys is established to describe and prediction the primary stage and tertiary stage of creep using the θ projection method. Many researchers try to use the θ projection method to predict the long term creep curves or fracture time or rupture life [28, 166-168].

Creep curves consist with three parts such as primary stage, secondary stage and tertiary stages. Wilshire and Evans established the θ projection concept to describe the creep behavior. This method has already described the some creep behavior of metals and alloys.

The total energy required will be defined as F. The necessary activation energy is q. The local stress is σ. If the engergy required the barrier. So:$F = q$ and $\sigma = 0$. If the barrier stress is σ_b, so $q = F \times \frac{(\sigma_b - \sigma)}{\sigma_b}$. So:

$$\frac{d\varepsilon}{dt} = B \times e^{\frac{-q}{kT}} = B \times e^{\frac{-F}{kT} \times \frac{(\sigma_b - \sigma)}{\sigma_b}}$$

B is the term including the dislocation density. The energy par is the process about the barrier which is important.

$$d\sigma == \frac{\partial \sigma_b}{\partial \varepsilon} \times d\varepsilon + \frac{\partial \sigma_b}{\partial t} dt$$

$$\frac{d\sigma_b}{dt} = f(\varepsilon, t) = \frac{\partial \sigma_b}{\partial \varepsilon} \times \frac{d\varepsilon}{dt} + \frac{\partial \sigma_b}{\partial t}\frac{dt}{dt}$$

So, $\sigma_b - \sigma = h\varepsilon - rt$ and $F = \sigma_b ba$, b is Burgers vector and a is the areas of activation to overcome the obstacle.

$$\frac{d\varepsilon}{dt} = B \times exp\left[-\frac{ba}{kT} \times (h\varepsilon - rt)\right]$$

Because $\sigma_b - \sigma$ is small, so using Taylor lead to:

$$f(0) = B,\ \dot{f(0)} = B \times \left[-\frac{ba}{kT} \times (h\varepsilon - rt)\right]$$

$$\frac{d\varepsilon}{dt} = B \times \left[1 + \frac{rbat}{kT}\right] - \frac{Bbah}{kT}$$

When $\varepsilon = 0$ at $t = 0$,

$$\int_0^{\varepsilon} \frac{d\varepsilon}{dt} = \int_0^{\varepsilon} \left\{B \times \left[1 + \frac{rbat}{kT}\right] - \frac{Bbah}{kT}\right\}$$

$$\varepsilon = \frac{kT}{Bbah} \times \left(B + \frac{r}{h}\right) \times \left[1 - exp\left(\frac{-rbat}{kT}\right)\right] + \frac{rt}{h}$$

So,

$$\varepsilon = \theta_1\left(1 - e^{-\theta_2 t}\right) + \frac{rt}{h}$$

$$d\sigma = \frac{\partial \sigma_b}{\partial \varepsilon} \times d\varepsilon + \frac{\partial \sigma_b}{\partial t} dt$$

At the steady stage, $d\sigma = 0$, so:

$$0 = \frac{\partial \sigma_b}{\partial \varepsilon} \times d\varepsilon + \frac{\partial \sigma_b}{\partial t} dt$$

$$\frac{d\varepsilon}{dt} = \dot{\varepsilon}_s = \frac{\partial \sigma / \partial t}{\partial \sigma / \partial \varepsilon} = \frac{r}{h}$$

$$\varepsilon = \theta_1\left(1 - e^{-\theta_2 t}\right) + \frac{rt}{h}$$

Cosidering the sharp of ceep curve, the first part is the primary stage and second will connect to the tertiary. So the relation between the steady creep rate and the tertiary creep rate. So:

$$\begin{cases} \frac{d\varepsilon_t}{dt} = \dot{\varepsilon}_t = \dot{\varepsilon}_s(1 + \omega) \\ \dot{\omega} = C \times \frac{d\varepsilon_t}{dt} \end{cases} \quad (24)$$

Integration of all above equation, we will get the equqtion:

$$\varepsilon = \theta_1\left(1 - e^{-\theta_2 t}\right) + \theta_3\left(e^{\theta_4 t} - 1\right) \quad (25)$$

According the some creep works[159], so the eqution is got as follows:

$$\begin{cases} \varepsilon = \theta_1\left(1 - e^{-\theta_2 t}\right) + \theta_3\left(e^{\theta_4 t} - 1\right) \\ \theta_1 = G_1 exp H_1\left(\frac{\sigma}{\sigma_Y}\right) \\ \theta_2 = G_2 exp\left[-\frac{Q - H_2\sigma}{RT}\right] \\ \theta_3 = G_3 exp H_3\left(\frac{\sigma}{\sigma_Y}\right) \\ \theta_4 = G_4 exp\left[-\frac{Q - H_4\sigma}{RT}\right] \end{cases} \quad (26)$$

Where ε is creep strain; θ_1 is the primary strain-like parameters, θ_2 is the primary rate constant, θ_3 is the tertiary strain-like parameters, θ_4 is the primary rate constant, G_i and H_i are constants of the alloys, R is the universal gas constant (8.31 $Jmol^{-1}K^{-1}$), T is the creep absolute temperature (K), Q si the activation energy of creep (kJ/mol), σ is applied stress of creep, σ_y is the rapid yield stress at the creep temperatures.

2.3.4.3 Creep fracture

Low-temperature creep at or below $0.5T_m$ is believed to be governed by non-diffusion controlled mechanisms, whereas high-temperature creep, above 0.5Tm, is diffusion controlled. Under the constant load, most Al alloys display normal creep strain/time curves at temperature about over 0.5 T_m which are widely considered to have three stages, primary, secondary and tertiary [16]. Steady-state creep is often emphasized over primary or tertiary creep due to the relatively large fraction of creep life within this regime. The importance of steady state is evidenced by the empirical Monkman-Grant relationship [17]:

$$\dot{\varepsilon}_{ss} \times t_r = k$$

$$\dot{\varepsilon} = \frac{d\varepsilon}{dt} = A_1\sigma^n exp - \left({}^{Q_C}/_{RT}\right) \quad (27)$$

$$\frac{1}{t_r} = \frac{d\varepsilon}{dt} = A_2\sigma^n exp - \left({}^{Q_C}/_{RT}\right) \quad (28)$$

The strain in or after the rupture is important for creep behavior. The concentrations of stains will occur the concentrations of stress [159]. During this process, the ability of a material to resistant the damage or rupture should be depend on

the plastic and rupure strain [169]. The Monkman-Grant relationship will be show the ability of creep behavior. The very useful measure may be introduced by the creep damage tolerance parameter defined as [170, 171]:

$$\lambda = \frac{(\varepsilon_f - \varepsilon_p)}{\dot{\varepsilon}_{ss} \times t_r} \tag{29}$$

When values betwen 1 to 2.5, the fracture of creep should be attributable to cavitation. If the value is higher than 2.5, the fracture of creep should begin as necking. If the value is higher than 5, the fracture of creep should begin as precipitate coarsening [170].

If the fructure strain is very larger than plastic strain, the equaion will be change to be like as [172]:

$$\lambda = \frac{(\varepsilon_f - \varepsilon_p)}{\dot{\varepsilon}_{ss} \times t_r} \cong \frac{\varepsilon_f}{\dot{\varepsilon}_{ss} \times t_r} \tag{30}$$

.

2.3.4.4 Creep change test

The constant structure are difficult to exist in different specimens due to the different cast processing and different heat treatment suffering. So the sensitivity of materials for creep behavior can be obtained using two ways. One is the strain rate change test, most of which are increase strain rate tests [24, 29, 148] . Other is the stress change test, most of which are decrease stain, also say, stress-drop [173] or dip stress test [174-176].

The stress change creep test originated by Gibbs and nix 40 years ago [173] . Recently, some researcher still focus on it [173-175]. There are two kinds of this test, one is large stress used. Firstly the elastic and inelastic reduce quickly, then inelastic part reduce slowly gradually. Next the inelastic increase slowly like some kinds of backflow [151] . However, the very small stress reductions work during creep test. After the elastic and inelastic reduce quickly, then inelastic part increase slowly gradually. This results of stress-dip test partially should be responsible for action of the internal stress of inter backstress. If the stress reduction is very small, the internal backstress will quickly be equal to the applied stress in the balance situation, that shows like normal creep curve shapes [175]. But if the stress reduction is too large to change

the microstructure too quickly into balance situation. So, the back flow and internal back stress are associated the microstructure defect such as dislocation or subgrain. Recently, some researcher focus on the internal stresses using modern analysis methods including the X-ray diffraction [176] or convergent bean electron diffraction (CBED) [177] and electron back-scattered diffraction (EBSD) [178, 179] to try to find some relationship between the internal stress and microstructure defects. Unfortunately most results of these works could not fit commonly for all materials and less strong math constitution equations or others powerful evidences were obtain to clearly explain the mechanism of affection of microstructure defects.

CHAPTER 3. MATERIALS AND EXPERIMENTS

3.1 Overview

The materials and experiments in this work will be introduced in this chapter. In chapter 3, the process of casting and heat treatment will be introduced too. This chapter will attempt to describe the design and operation of die casting machine and the creep test machine. The processes of creep test and tensile test included in this part. This chapter reviews the microstructure characterization of Al alloys.

3.2 Materials

Commercial AC4C aluminum alloy used in this study was obtained from Daiki Aluminium Industry (Thailand) Co., Ltd., Chonburi, Thailand. The chemical compositions of alloy were shown in Table 6. The chemical composition of as-cast alloy employed in this work was examined by Science equipment's center. Using optical emission spectrometer (OES) and show in the Table 7 in weight percent. The AC4C ingots were produced following the JIS H 5202-1999 standard.

Table 6 Chemical composition of ingot of AC4C alloy

Elements	Si	Fe	Cu	Mn	Mg	Zn	Ti	Al
Ingot	7.01	0.43	0.05	0.04	0.34	0.05	0.02	Bal.

Table 7 Chemical composition of semi-solid GISS-die casting AC4C alloys and CL-DC AC4C alloys

Elements	Si	Fe	Cu	Mn	Mg	Zn	Ti	Cr	Ni	Pb	Al
GISS-DC	7.54	0.46	0.06	0.06	0.38	0.09	0.02	0.01	0.01	0.00	Bal.
CL-DC	8.00	0.49	0.06	0.04	0.36	0.09	0.01	0.01	0.01	0.00	Bal.

3.3 Casting

At first, an aluminum alloy ingot was melted in the graphite crucible in

an electrical furnace at above the liquids temperature (700˚C). Then, about 200 g was taken from the graphite crucible by a ladle cup. Next, the nitrogen gas from a graphite diffuser was injected into the ladle cup at the temperature of about 616 ˚C. The times of injecting the gas were 10 s. The schematic diagram of the GISS process is shown in Fig. 14 [56].

The aluminum slurry was filled into the shot sleeve of die casting machine. The die pressures capacities of the die-casting machine is 80 tons. After the slurry was poured into the shot sleeve at same temperature, the plunger shoved it into the die at the speed of 0.20 m/s. The shot sleeve and die were preheated to temperatures of 250 and 200 ˚C, respectively. The die temperature was 200 ˚C. The schematic diagram of the GISS die casting process is illustrated in Fig. 15 [107].

The ingots were bought in commercial manufacturers. The casting parts were manufactured with dimension of width 70mm, length 100mm, and thickness 8mm with gate thickness 6mm by GISSCO, Co. Ltd. shown in Fig. 16.

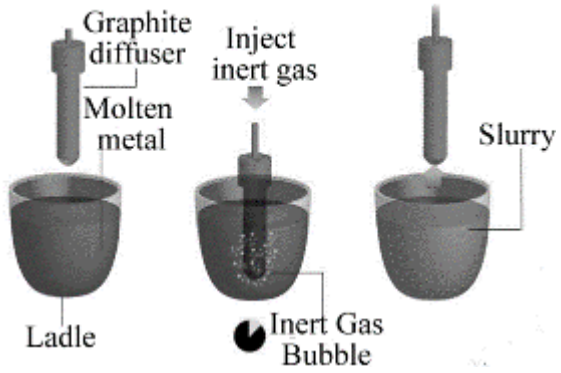

Fig. 14. Schematic drawing of GISS technique [56]

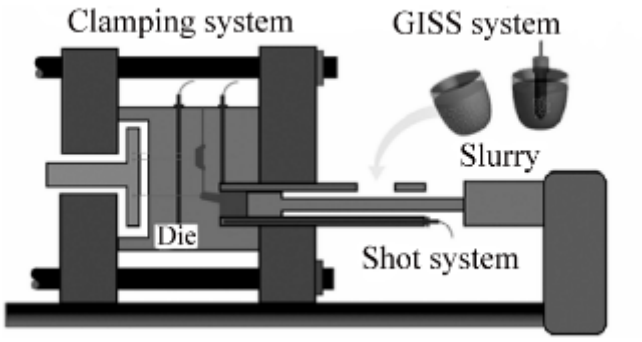

Fig. 15. Schematic diagram of GISS die casting process [107]

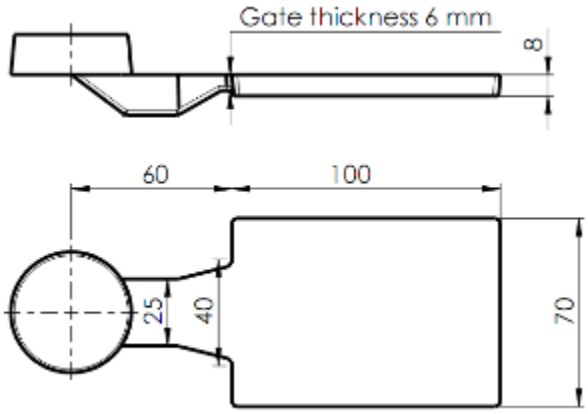

Fig. 16. Drawing of casting part.

3.4 Heat treatment

Al-Si-Mg alloys are usually subject to the T6 heat treatment including the solution heat treatment at higher temperature and aged at lower temperature. The Mg and Si elements are decomposed and dissolved into Al matrix during the solution heat treatment at higher temperature about 540 °C, and then precipitated during aging. During solution heat treatment, the π Fe-bearing intermetallic particles can be transformed into β phase by releasing Mg into Al matrix [1], because the rich Mg particles formed during the solidification are completely decomposed and dissolved into Al matrix after 1h solution treatment at 538 °C, which revealed by the electron microprobe analysis [181]. The as cast AC4C aluminum alloy was aged at 195 ºC for 3 h after solution heat treatment at 540 ºC for 4h is more ductility [3].

3.5 Tensile test

The tensile test machine was HOUNSFILELD Model H100KS, Serial No. 0068. The operation crosshead speed of the tensile test will be 1.5 mm/min, or the strain of the tensile test is 1×10^{-3} 1/s at room temperature. The tensile specimens with a 4mm×4mm cross section and 25mm gauge length were machined from the top location and bottom locations of the plates, as shown in Fig. 17 and Fig. 18. Tensile testing was carried out at 25, 100, 175 and 250 ºC.

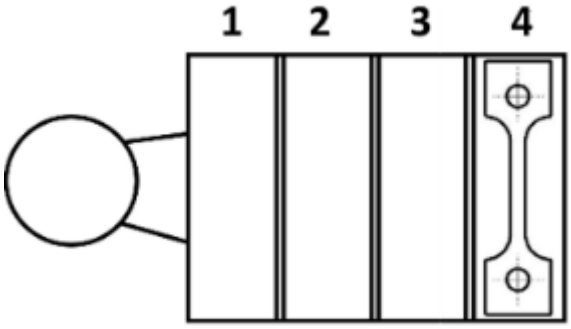

Fig. 17. Designation of tensile specimens prepared from different parts of die cast plate.

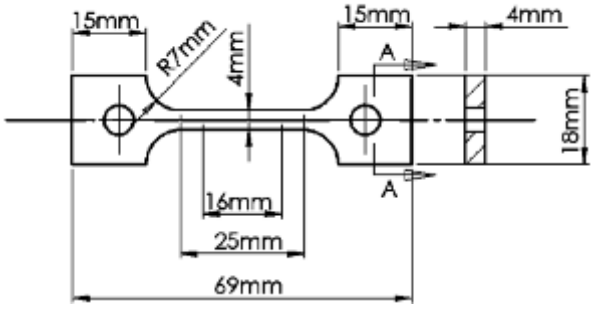

Fig. 18. Dimensions of tensile specimen.

3.6 Creep test

This creep test machine was designed by Dr. Suchart Chantaramanee

(Fig. 19). The extensometer was designed by author (Fig. 20), which was fabricated in workshop in Songkhla city. The tensile specimens of a cross section of 4mm*4mm and 25mm gauge length were machined form the top and bottoms of the plates, as above in tensile test.

Fig. 19. The extensometer and holder system.

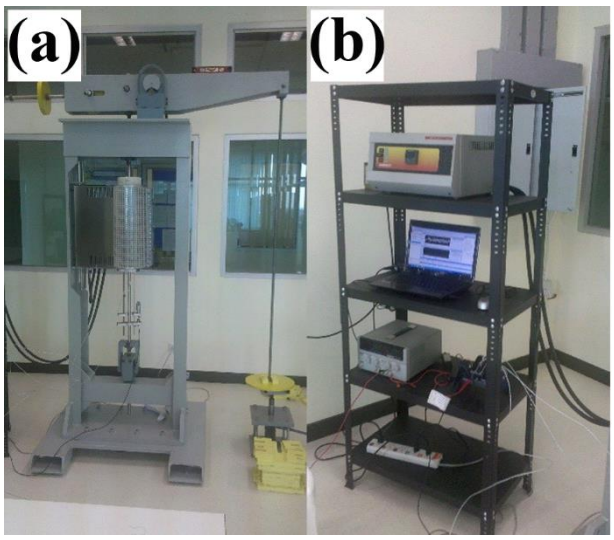

Fig. 20. Pictures of (a) tensile creep test machine and (b) temperature control and data acquisition system.

3.6.1.1 Calibration of Load weight and true force

The true or real tension of the creep machine was calibrated by a load cell (Fig. 21) with precision 0.01kg of 0-99kg and 0.1kg of 100-999kg. Using this, the data of load weight and true force was got in the Table 8.

According the Fig. 22, the linear relation between loads versus true force is got. The linear fitted equation is y=4.8832x which will be used to turn the loads into the true force during the creep test.

Table 8 Data of load calibration

Load (kg)	Load (kg)	True force(kg)	Ture force(kg)
11.662	11.662	54.6	55.2
11.830	23.492	113.0	113.5
11.721	35.213	170.7	171.3
11.793	47.006	228.6	229.3
11.757	58.763	286.3	286.8
7.437	66.200	322.8	323.3
7.473	73.673	359.4	359.9
7.475	81.148	396.0	396.4
7.489	88.637	432.5	433.1
4.193	92.830	453.2	453.5
4.097	96.927	473.2	473.4
4.080	101.007	493.0	493.4
4.088	105.095	513.4	513.2

Fig. 21. Load cell

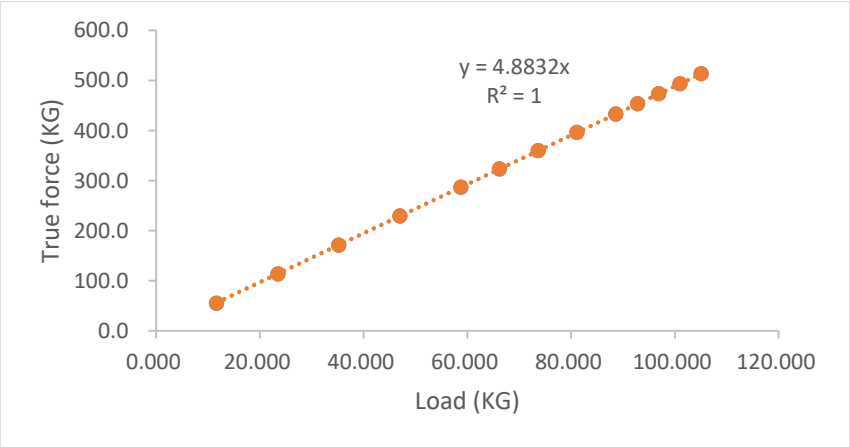

Fig. 22. The curve of load versus true force.

3.6.1.2 Calibration of Linear Variable Differential Transformer (LVDT)

The elongation of the creep samples is recorded by a data acquisition system (DAQ) in Fig. 23 based on a LVDT produced by National Instruments Corporation as it is show in Fig. 24.

Steps of using DAQto test:

A. Using DC Power Supply, he output voltage is adjusted to DC 10 volt;
B. Digital Multimeter is connected with an output terminal connected to detect the volt. The output voltage will be corrected to 10 volt. However, on a display of DC Power Supply it may be value of 9.9.
C. LVDT will be connected with DC Power Supply and Digital Multimeter to measure voltage. When the value of Micrometer is set to 10mm, the LVDT will stop to be adjusted after Multimeter gets the voltage value 0.000 volt.
D. Micrometer is adjusted between +5 mm and -5 mm, meanwhile a DC value is read at intervals of 0.5.
E. The curse of the micrometer Millimeter vs. DC voltage is plotted.

The above steps are used to get the data in Table 9 and then the curve of micrometers versus DC is dawn in the Fig. 25. According to the Fig. 25, the linear relation between micrometers versus DC is got. The linear fitted equation is y=0.5771x which will be used to turn the volt value into the elongation during the creep test.

Table 9 The data of the calibration of LVDT

Micrometer (mm)	Test 1 (Volt)	Test 2 (Volt)	Micrometer (mm)	Test 1 (Volt)	Test 2 (Volt)
5	2.87	2.89	-0.5	-0.28	-0.32
4.5	2.62	2.6	-1	-0.57	-0.6
4	2.32	2.3	-1.5	-0.86	-0.87
3.5	2.05	2.02	-2	-1.14	-1.16
3	1.76	1.72	-2.5	-1.43	-1.45
2.5	1.47	1.45	-3	-1.72	-1.73
2	1.18	1.15	-3.5	-1.99	-2.04
1.5	0.9	0.86	-4	-2.28	-2.32
1	0.61	0.58	-4.5	-2.55	-2.57
0.5	0.33	0.29	0	0	0

Fig. 23. Data acquisition system (DAQ)

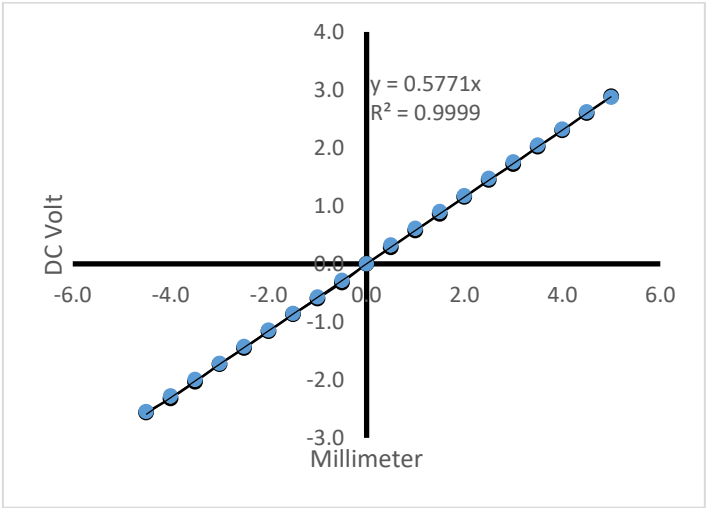

Fig. 24. The curve of micrometer Millimeter vs. DC voltage

3.6.1.3 Calibration of Temperatures

Controlling temperatures is very important in the creep test. Firstly, the appropriate temperature program was established, which is the increasing temperature slowly manual. The different positions in the furnace have the different temperatures. The higher position was used as the location for the creep test. As in Fig. 25, the temperature controlling is very stable for a long time at three different temperatures and the increasing temperature process range is acceptable for present research work.

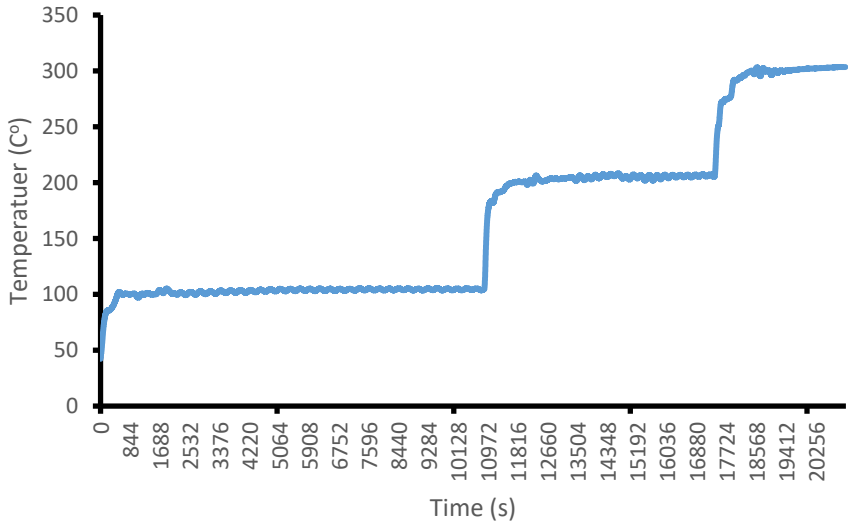

Fig. 25. The temperture program.

3.6.1.1 Ceep test

The creep test of semi-solid AC4C Al alloy produced by the Gas Induced Semi-Solid (GISS) die casting process were investigated at temperature range of 300-360 °C and pressures range of 20-40 MPa and compared with the conventional liquid die casting (CL-DC) one after T6 heat treatment. Stress change creep produced at room temperature and 220 ºC, 250 ºC, 280 ºC and 300°C.

3.7 Microstructure characterization

Microstructures characterization of AC4C were tested by the optical microscope (OM) and scanning electron microscope (SEM) and energy dispersive spectroscopy (EDS), X-ray Diffractomete (XRD), equipment is Differential Scanning Calorimeter (DSC) and Transmission Electron Microscope (TEM).

3.7.1 Microstructure characterization by OM and SEM

The specimens for microscopy were mounted using plastic mounting materials that cured at room temperature and grinded by standard method using silicon carbide (SiC) abrasive paper (from 180-2000 grit) with a rotation speed of 300 rpm/min manually, then two-steps polished using medium-nap cloth with an alumina abrasive suspension in particle sizes of 5 and 1 micron with a rotation speed of 150 rpm/min manually. Keller's reagent was used to reveal the microstructure. The fracture surface SEM analysis coupled was to understand the microscopic failure mode of the material.

Microstructures of AC4C were tested by the optical microscope (OM) and scanning electron microscope (SEM) and energy dispersive spectroscopy (EDS) before and after heat treatment. The test equipment of SEM is Quanta 400, FEI, Czech Republic Scanning Electron Miroscope.

3.7.2 Microstructure characterization by XRD and DSC

XRD equipment is X-ray Diffractometer, X'Pert MPD, PHILIPS, Netherlands in Scientific Equipment Center of Prince of Songkla University. The specimen for XRD is a square shape of 2 cm × 2 cm of as cast GISS-DC and GISS-DC-AC4C-T6 alloys. The scanning scale is chosen a full 2θ angle scanning of 5-90°. The scanning rate is 3 °/min. Work voltage and current are 40kV and 30 mA. The X-ray tube is Cu tube. The step of time and size of 2θ is 1 second and 0.05°. The wavelength of X-ray of CuKα is 0.0154 nm.

DSC equipment is Differential Scanning Calorimeter, DSC7, Perkin Elmer, USA in Scientific Equipment Center of Prince of Songkla University. The coolant is ice. The scanning program is heat from 100 ^{o}C to 400 ^{o}C at 5 ^{o}C/min, then cool from 400 ^{o}C to 100 ^{o}C at 5 ^{o}C/min and heat from 100 ^{o}C to 400 ^{o}C at 5 ^{o}C/min.

3.7.3 Microstructure characterization by TEM

The majority of TEM samples are prepared from bulk AC4C Al alloy in three stages: Disc preparation; Pre-thinning; Ion milling and use the equipment: Precision Ion Polishing System (PIPS) and accessories and type: Gatan Specimen Preparation System. The PIPS can produce high quality and reliable TEM specimens. The PIPS includes high milling rates at shallow angles for double sided low angle milling. It is easy and simple to operate and maintain.

3.7.3.1 Disc Preparation

The thin slice (to get a thin slice about 500 μm was cutted from the bulk specimens using a low speed diamond saw, because the Al alloys are soft metal and will dull the blade without using the low speed diamond saw. The sample diameter requirment are 3.05 mm for all TEMs. The disc punch was used to punch discs without mechanical damage to the central region or tearing of the edges.

3.7.3.2 Mechanical Pre-Thinning

Before the ion polishing, the pre-thinining is important. The mechanical grinding and polishing is always employed for pre-thinning, but sometimes chemical polishing can use too. Pre-thinning can greatly save time for TEM sample preparationIon by comparison of a relatively slow milling process. If pre-thining can well done, the ion-polishing time will be shorter and the TEM sample will be smoother. Although, the michanical grinding and polishing can ger the thin samples to electron transparency. The mechanical thin samples are difficult to clean and the mechanical damage are unsuitable for TEM tests.

The factors of the mechanical damage include the material and polishing compound, and the polishing force. Semiconductors, ceramics, and minerals are free from mechanical damage, so the perfect mechanical pre-thinning thickness can be down to about 5μm. But for metals, after gradully repeated attempts, the optimum value of pre-thinning thickness will be done.

Simple parallel grinding techniques can be used to produce large thin areas but the resulting samples are so weak mechanically that they must be glued to a

support ring or grid to avoid fracture during subsequent handling. Chances of sample fracture during parallel grinding are higher as well.

These problems can be avoided by mechanically pre-thinning the sample in two steps: Disc grinding and Dimple grinding.

Disc Grinding

The thickness of sample will be thined to 40-70 μm using the Gatan Disc Grinder. The samles are grinded with with SiC sandpaper (100 - 240 - 600 grit sizes) and polished witsh Al_2O_3 or diamond suspensions (5 - 1 - 0.1μm).

Dimple Grinding

The purposal of dimple grinding is to get thin area in the center of the sample. The Gatan Dimple Grinder is used for this process.

After disc grinding, the sample is grinded using the 15mm phosphor bronze wheel and 2 μm diamond paste for coarse dimple grinds to a thickness of 20-25 μm under under 15-20 gm load and with form low to medium speed. Then the sample is polished for 5 min using the felt wheel and 2 μm diamond paste, under 20-25 gm load and with form low to medium speed. The sample is polished with the new felt wheel and 1 μm diamond paste under 20 gm load and with form low to medium speed for 5 min with the medium speed. The sample is polished again with the new felt wheel and 0.05 μm Alumina suspension under 30 gm load and with form low to medium speed for 10 min with the medium speed.

3.7.3.3 Ion-beam Milling

After pre-thinned, the process of ion-beam milling is produced. Set the rpm is the 10 and adjust the ion beam energy is the 45 keV. And use the double ion-beam milling. About 6-8 hours for one samples.

CHAPTER 4. RESULTS AND DICUSSION

4.1 Overview

The heart of this thesis is the development of novel processes for the semi solid casting AC4C Al alloys. The following chapter summarises the experimental results obtained from the position effect on GISS-DCAC4C Al alloys which compared with CLC-DC AC4C Al alloys. The results will be discussed as. In this regard, Chapter 4 is dedicated to study the tensile property of GISS-DCAC4C Al alloys at various temperature with a range from room temperature to 250 ^{o}C. The results are presented as creep test of both alloys with microstructure characterizations and the constitutive equation to describe and prediction the primary stage and tertiary stage of creep is established using the θ projection method.

4.2 T6 heat treatment

The as cast AC4C aluminum alloy was aged at 195 ^{o}C for 3 h after solution heat treatment at 540 ^{o}C for 4h is more ductility [3]. Microstructures characterization of AC4C were tested by the optical microscope (OM) and scanning electron microscope (SEM) and energy dispersive spectroscopy (EDS), X-ray Diffractomete (XRD), equipment is Differential Scanning Calorimeter (DSC) and Transmission Electron Microscope (TEM) after heat treatment.

4.2.1 Microstructure examination results by OM

The as cast microstructure of Al-Si-Mg-Fe alloys (AC4C) is comprised of α-Al dendrites and eutectic Si and Fe-bearing intermetallic particles[180]. Fig. 26 indicates the microstructures of as-cast GISS die casting AC4C aluminum alloys are typically multiply phases comprising α-Al, eutectic Si and numerous intermetallic phases. It is noted that there are needle and plate-like phase in the grainboundary which are composed of the intermetallic and Si particles and some defects also are found like microvoid and impurity particles.

Al-Si-Mg alloys are usually subject to the T6 heat treatment including the solution heat treatment at higher temperature and aged at lower temperature. The Mg and Si elements are decomposed and dissolved into Al matrix during the solution heat treatment at higher temperature about 540 °C, and then precipitated during aging. During solution heat treatment, the π Fe-bearing intermetallic particles can be transformed into β phase by releasing Mg into Al matrix [1], because the rich Mg particles formed during the solidification are completely decomposed and dissolved into Al matrix after 1h solution treatment at 538 °C, which revealed by the electron microprobe analysis [181].

Typical microstructures of an as-cast AC4C aluminum alloy were composed of the rosette or globular structure of primary grain, plate-like or rod-like eutectic Al-Si and plate-like or rod-like intermetallic equilibrium phase in Fig. 26 (a) and (c) [180]. The microstructures of are given in Fig. 26 (b) and (d) and the rosette or globular structure of primary phase and the round eutectic Al-Si and plate-like or rod-like intermetallic equilibrium phase is shown in Fig. 26 (b) and (d). It is noted that from OM photo the shapes of eutectic Al-Si change from plate-like or rod-like to round or spheroidization of eutectic Al-Si is observed. The data from the pictures of microstructure of GISS-DC AC4C alloy: Average size of round eutectic Al-Si of GISS-DC-AC4C-T6: 3.44μm; Average globular primary grain size of GISS-DC-AC4C-T6: 48.7μm; Average globular primary grain size of as-cast GISS-DC AC4C: 47.6μm [63].The particles of Si are easily found in the Fig. 26 due to the existence of intermetallic phase and Si precipitate-free-zone (PFZ) near the interface between eutectic silicon particles and the eutectic aluminum phase matrix. The PFZ is formed from depletioning of silicon near the eutectic regions where the silicon atoms in Al matrix near eutectic region diffuse to surrounding eutectic silicon particles and the Si particles are grown up and round. It is confirmed to be the Silicon particles precipitate during aging which are reported in the literatures [182]. However, the large grains are softer and the transmission of slip is easy across the grain boundary compared with the small one, but the area fraction and the clustering level of the primary aluminum grain effect the mechanical properties more seriously. Additionally, due to the different solidified rate of semi solid slurry in the shot sleeve, the bottom’s the grains size increased.

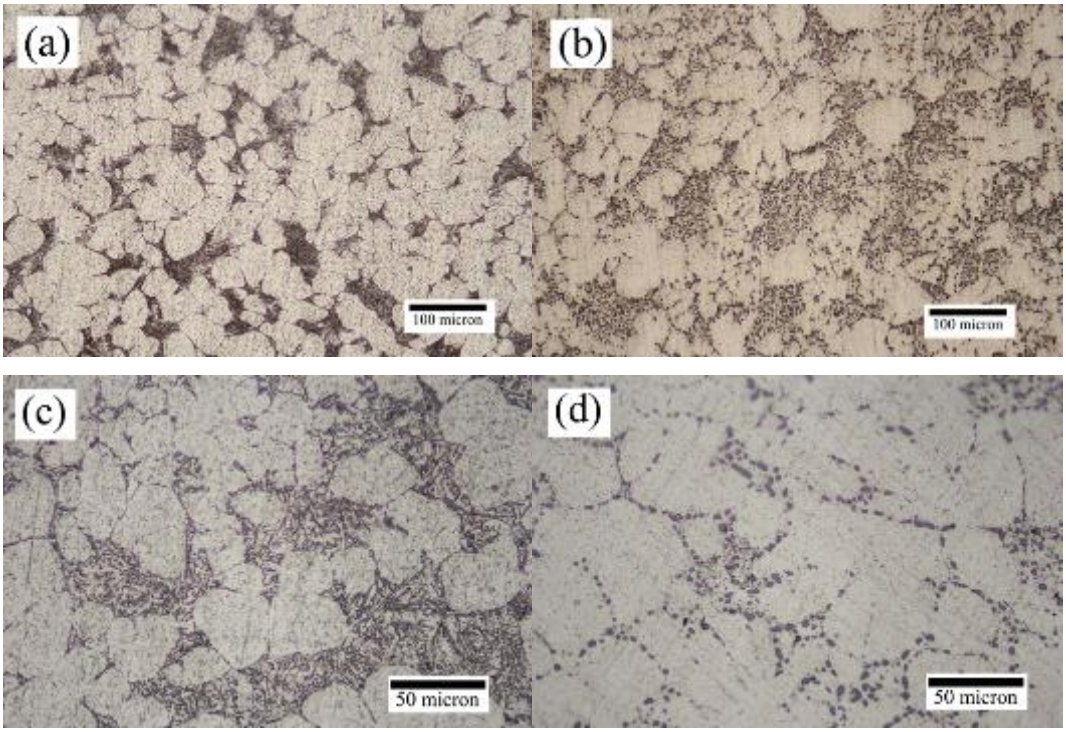

Fig. 26. Optical micrographs showing the microstructure of (a), (c) as-cast GISS and (b), (d) GISS-T6.

4.2.2 Microstructure examination results by SEM

4.2.2.1 Intermetallic in As cast AC4C alloys

As shown in Fig. 26, in as cast GISS-DC the dark phase is rosotte α (Al) primary phase and the large rod-shaped precipitates are white and rich Fe and some of them have the rich Mg. It noted that the white areas contain a large number of elements: Fe, Mg and Si which constitute the intermetallic particles. The gray areas contain only the Si particles which are needle and plate-like. The dark areas are α (Al) primary phase where almost every element precipited in.

As shown in Fig. 27, in as cast GISS-DC AC4C, there are rosette or globular α (Al) primary phase, eutectic Si and the large rod-shaped rich Fe and Mg intermetallic. It noted that the white areas contain a large number of elements: Fe, Mg and Si which constitute the intermetallic particles. The gray areas contain only the Si

particles which are needle and plate-like. The dark areas are α (Al) primary phase where almost every element precipitated in. the Fig. 28, it is noted that there are many different composition of intermetallic particle including: SiMgFe, SiMgFeMn. However the intermetallic composition in the Al-Si-Mg alloys is a hot research topic still. These evidents show that the intermetallic composition is not one but complex and include elements of Si, Fe, Mg, Si, Mn.

However, the large grains are softer and the transmission of slip is easy across the grain boundary compared with the small one, but the lower area fraction and the higher clustering of the primary aluminum grain effect the mechanical properties more seriously. Additionally, the partial solidified semi solid slurry from the shot sleeve of the bottoms also increased the grains size and quantities.

Fig. 29 and Fig. 30 show that the dark phase is dendritic α (Al) primary phase, the gray areas are Si, and white areas are intermetallic particles that include a large number of elements: Fe, Mg and Si in CL-DC AC4C Al alloys. It noted that the white areas contain a large number of elements: Fe, Mg and Si which constitute the intermetallic particles. The gray areas contain only the Si particles which are needle and plate-like. The dark areas are α (Al) primary phase where almost every element precipited in.

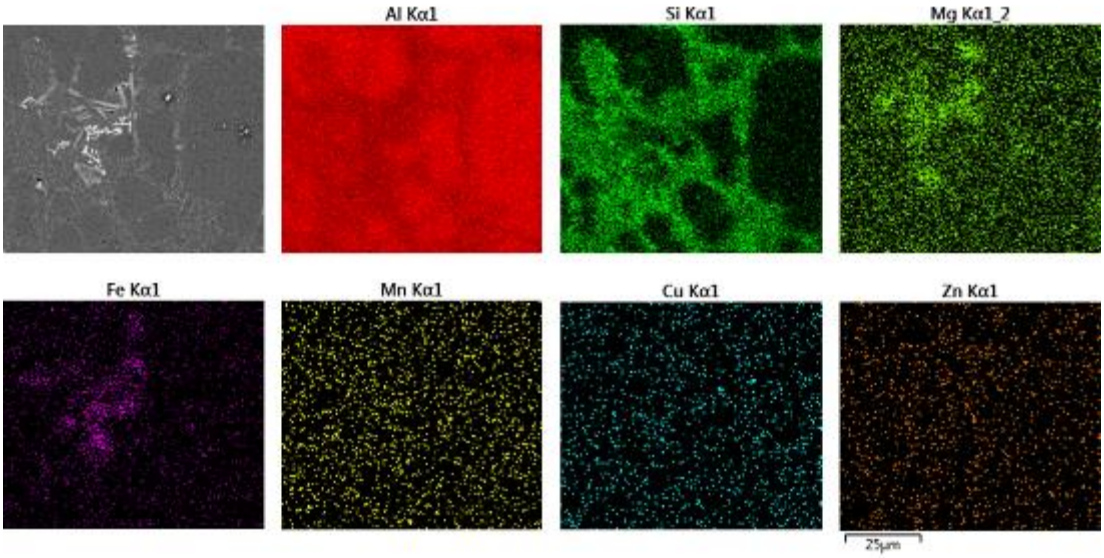

Fig. 27. Elemental mapping of polished section of as cast GISS-DC AC4C alloys.

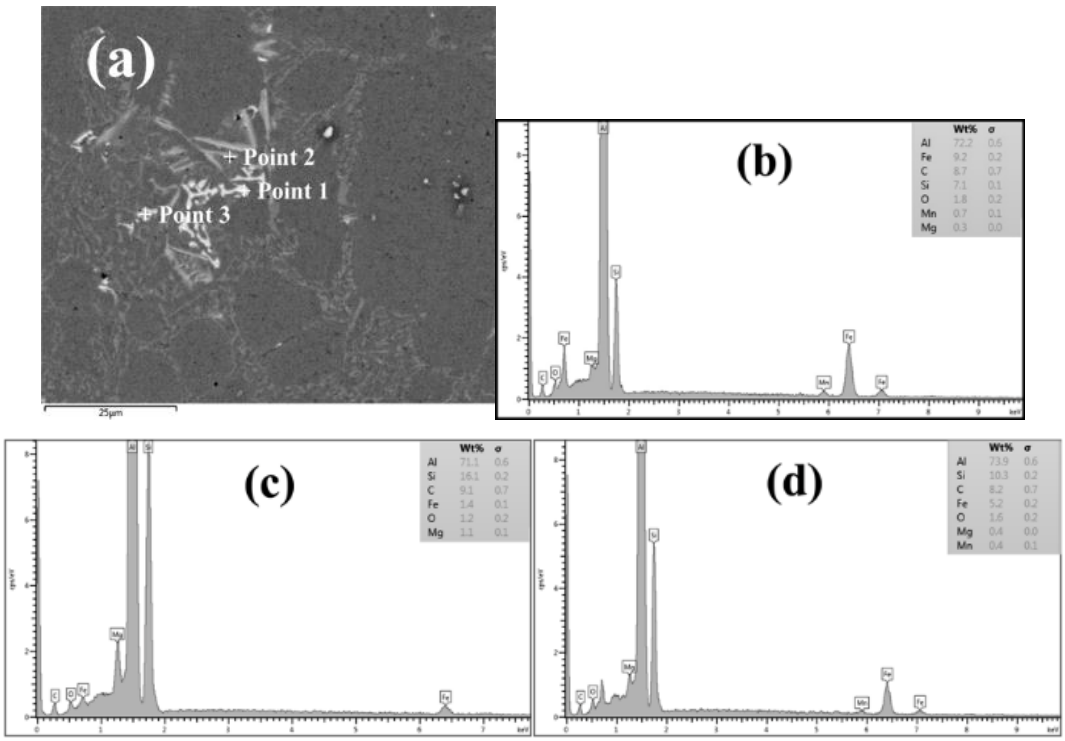

Fig. 28. Microstructure of as cast GISS-DC AC4C alloy (a) SEM micrograph, (b), (c) and (d) are spectra of EDS point scanning corresponding to point 1, 2 and 3 marked in (a).

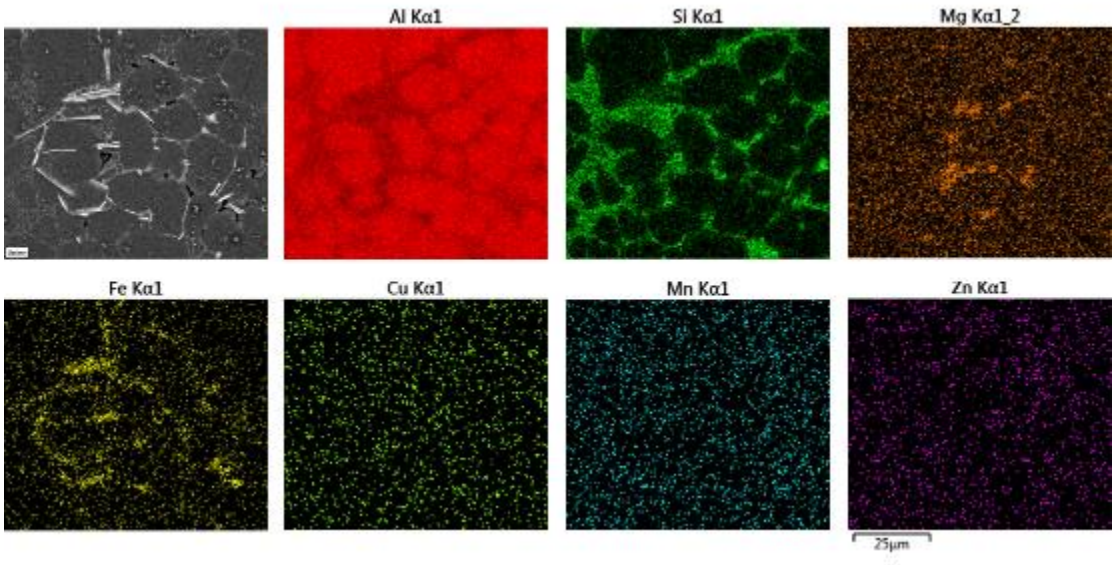

Fig. 29. Element mapping of polished section of as cast CL-DC AC4C alloys

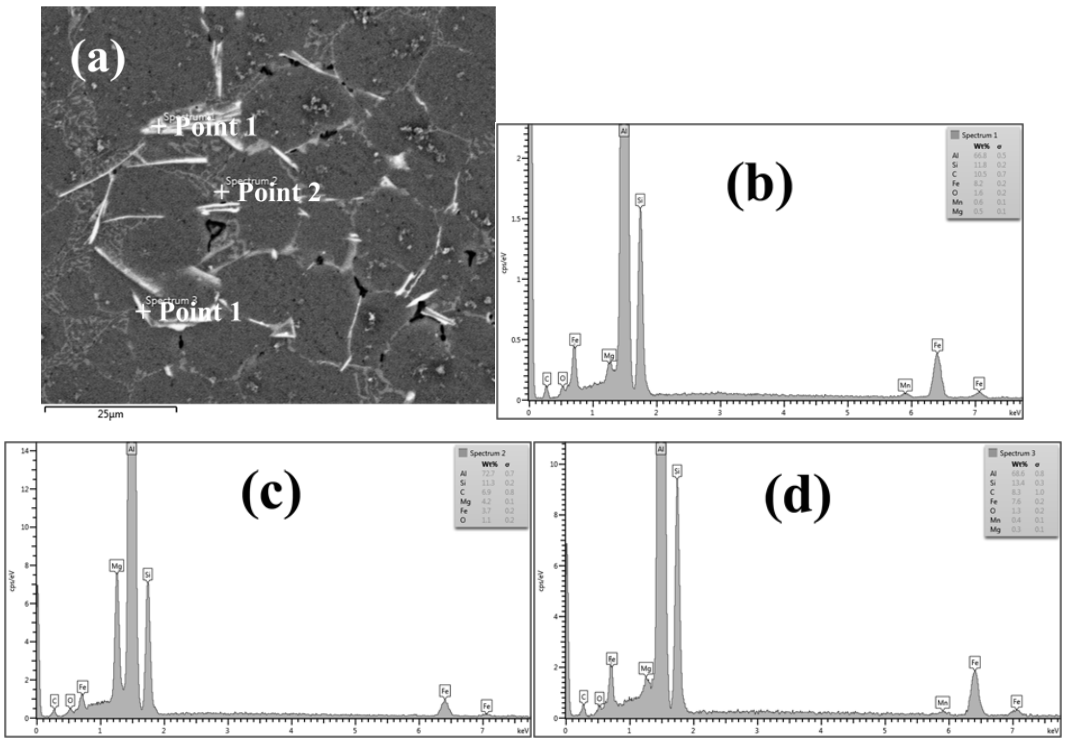

Fig. 30. Microstructure of as cast CL-DC AC4C alloy (a) SEM micrograph, (b), (c) and (d) are spectra of EDS point scanning corresponding to point 1, 2 and 3 marked in (a).

4.2.2.2 Intermetallic after T6 heat treatment

After T6 heat treatment, Fig. 31 and Fig. 32 show that the dark phase is dendritic and rosette α (Al) primary phase that did not change, however, the gray areas are Si which changed to be around and spherical, and white areas are intermetallic particles that include a large number of elements: Fe and Si, no Mg, in GISS-T6 and CL-DC-AC4C-T6 Al alloys. The spherical and around gray areas contained only the Si particles are larger and more size-uniform in GISS-T6 than CL-DC-AC4C-T6 Al alloys. The dark areas, α (Al) primary phase, where almost every element precipitated in are bigger in GISS-T6 than CL-DC-AC4C-T6 Al alloys. Fe distribution is more concentrated in GISS-T6 than CL-DC-AC4C-T6 Al alloys in intermetallic, and other element distribution is same in GISS-T6 and CL-DC-AC4C-T6 Al alloys.

In the Fig. 33 and 34, it is seen that there is one kinds of intermetallic particle including AlSiFe (include Mg=0.3% which is same detected in α (Al) primary phase) due to the precipitation of Mg which show in the Fig. 33 and 34. This result is

very different with others work [2, 94, 183] which include some Chinese script and Mg_2Si particles. These evidences show that the intermetallic composition is not Mg_2Si, because the excess Si exists, so there only the AlSiFe intermetallic component and the excess Si should be considered. The Mg can be found in α (Al) primary phase or α (Si) primary phase.

Therefore, AC4C Al alloys are usually subject to the T6 temper including the solution heat treatment at higher temperature and aged at lower temperature. The Mg and Si are decomposed and dissolved into Al matrix during the solution heat treatment, and then precipitated during aging. During solution heat treatment, the π Fe-bearing intermetallic particles can be transformed into β phase by releasing Mg into Al matrix [1], and the Mg_2Si particles formed during the solidification are completely decomposed and dissolved into Al matrix after 1h solution treatment at 538^{o}C, which revealed by the electron microprobe analysis [181]. However, in this work, Mg2Si particles not find and no rich Mg in rich Fe intermetallic particles or in Si particles. Mg content is about 0.3% and uniformly contributed in the GISS-T6 and CL-DC-AC4C-T6 Al alloys.

All above, the spheroidisation eutectic Si occurred after T6 heat treatment, and in the as cast GISS and CL die casting AC4C alloys there are some π-Chinese script phase ($Al_8Mg_3FeSi_6$) that contains Mg or π-Chinese script phase (AlMgFeSiMn) and β(Al_5FeSi) phase. But after T6 heat treatment, only β(Al_5FeSi) phase can be found in the GISS-T6 and CL-DC-AC4C-T6 Al alloys.

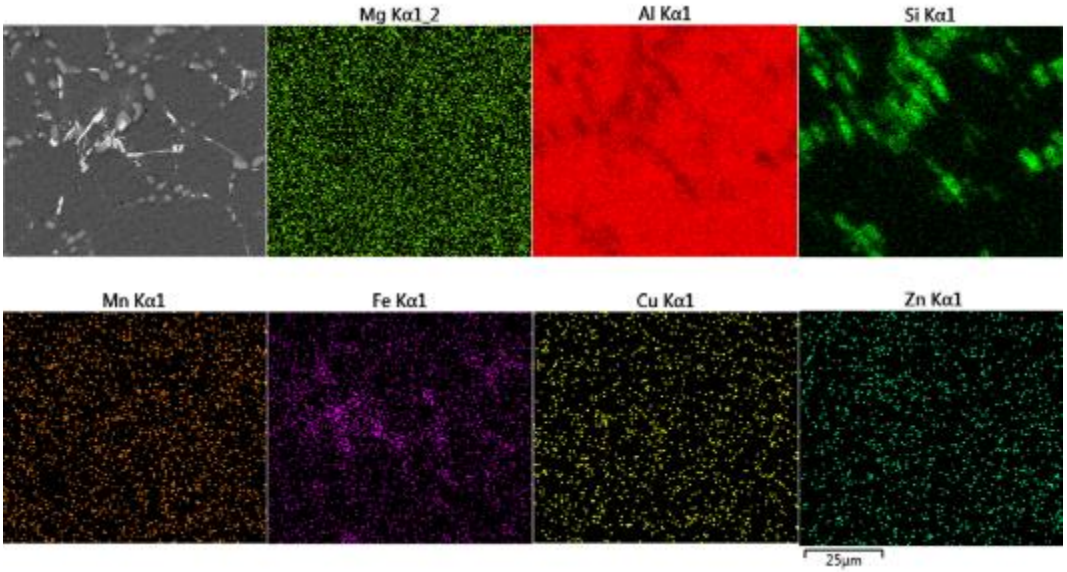

Fig. 31. Element mapping of polished section of CL-DC-AC4C-T6 alloys

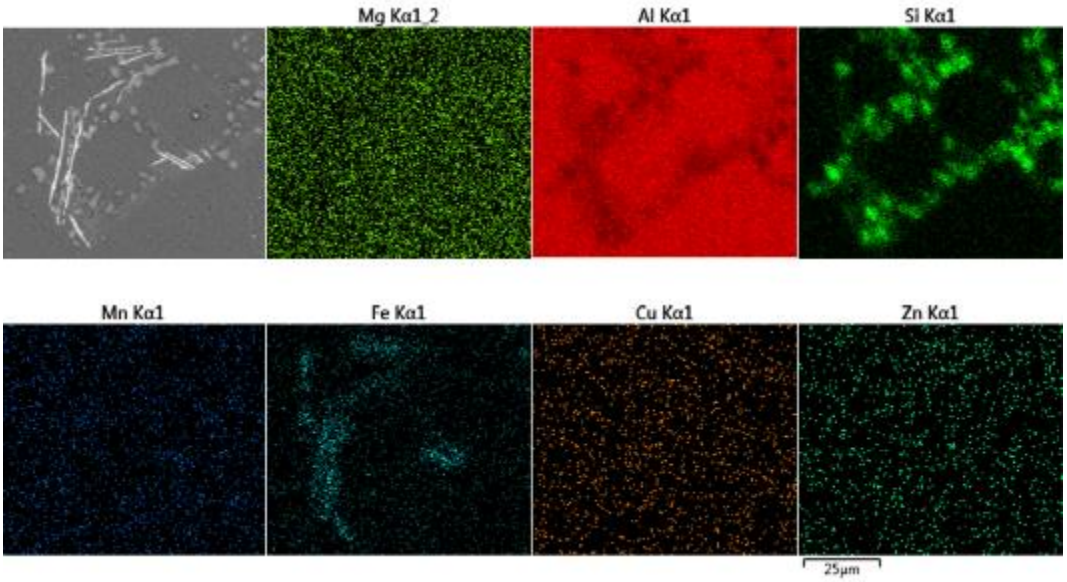

Fig. 32. Element mapping of polished section of GISS-DC-AC4C-T6 alloys

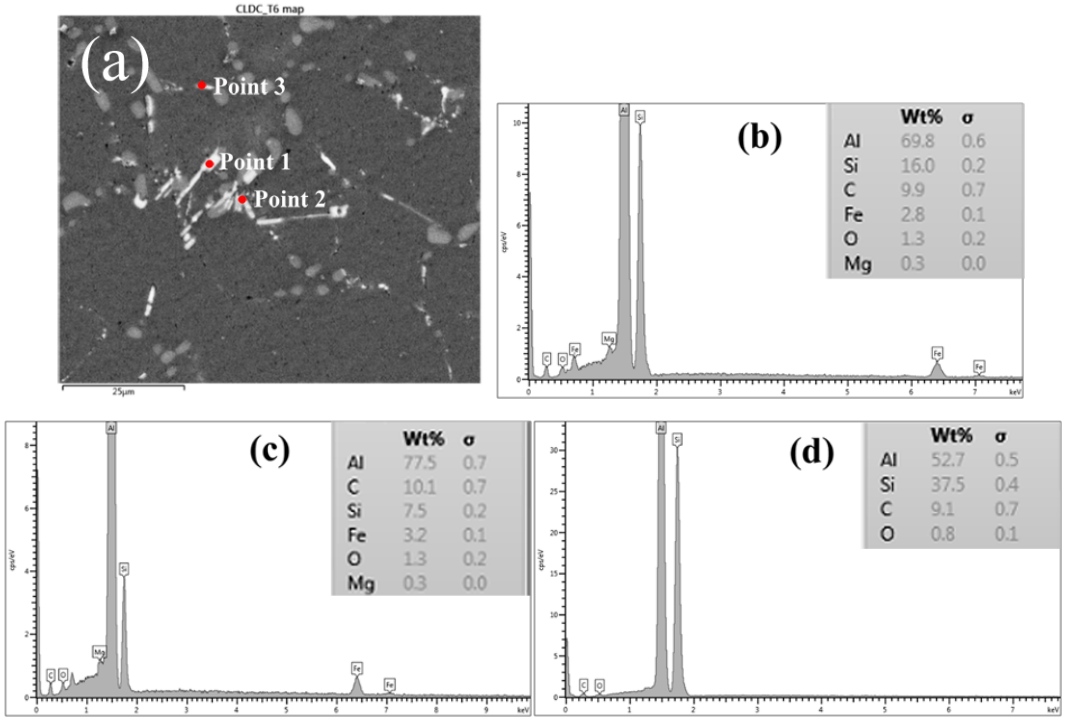

Fig. 33. Microstructure of CL-DC-AC4C-T6 alloy (a) SEM micrograph, (b), (c) and (d) are spectra of EDS point scanning corresponding to point 1, 2 and 3 marked in (a).

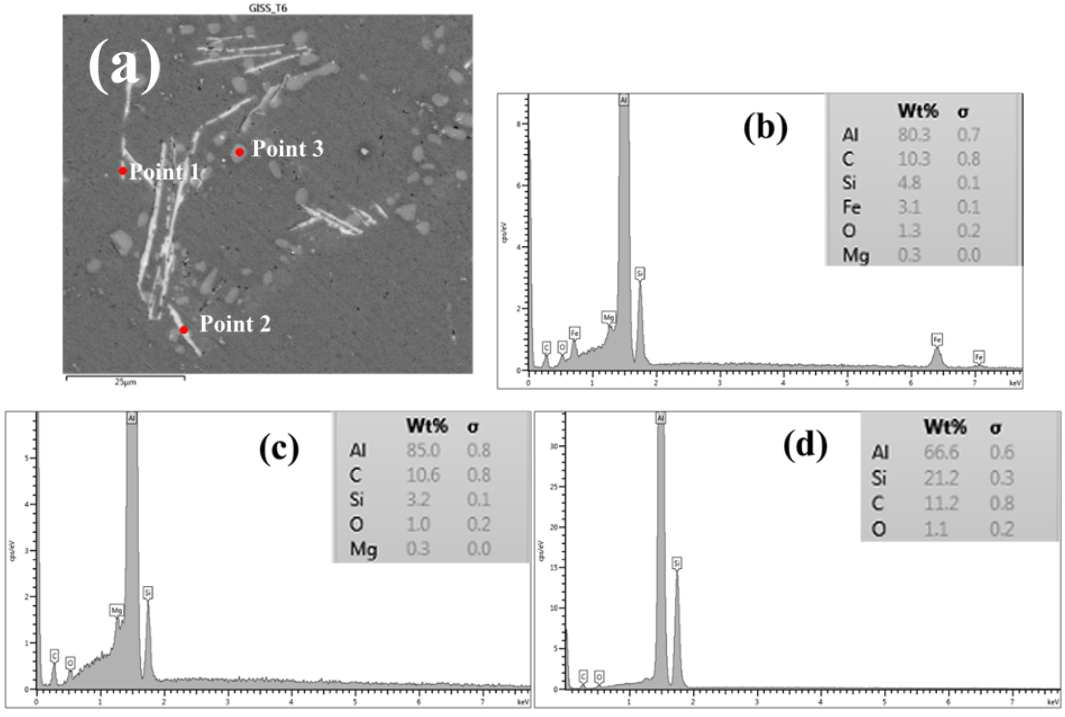

Fig. 34. Microstructure of GISS-DC-AC4C-T6 alloy (a) SEM micrograph, (b), (c) and (d) are spectra of EDS point scanning corresponding to point 1, 2 and 3 marked in (a).

4.2.2.3 The Mg and Si in Al matrix before and after T6 heat treatment

The segregation of Mg and Si were observed in Al matrix in the Fig. 35-38 and listed in Table 10 , in both of the GISS and CL-DC AC4C Al alloys the Mg percentages increase after T6 heat treatment due to the Mg element dissolvent in Al matrix phase uniformly. The Si percentages in CL-DC AC4C Al alloys increased after T6 heat treatment, however, the Si percentages in GISS-DC AC4C Al alloys decreased after T6 heat treatment. Because during the CL-DC cast processing, the parts cooled very quickly to be formed the solid phase and during the GISS-DC cast processing, the slurry with solid fraction was hold to form the semi-solid and was stirred by the N_2 gas both of which helped to dissolved high Si percentages in the GISS-DC AC4C alloys due to the exceed Si.

Table 10 Semi-quantitative SEM-EDS analysis of Si and Mg content in a-Al phase

	CL-DC						GISS-DC					
	As cast			T6			As cast			T6		
Mg (%)	0.1	0.1	0.1	0.4	0.3	0.3	0.1	0.0	0.1	0.3	0.3	0.3
Si (%)	2.2	2.1	2.6	3.5	3.5	3.9	2.8	2.9	2.9	2.6	2.5	2.5

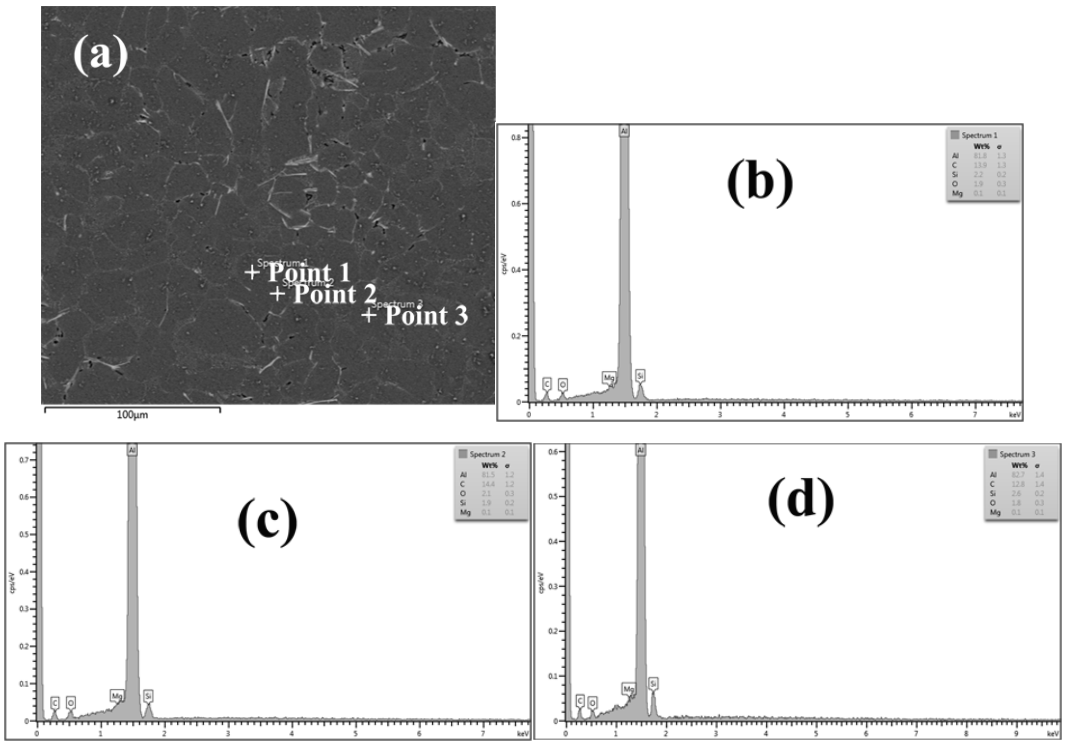

Fig. 35. Microstructure of as cast CL-DC AC4C alloy (a) SEM micrograph, (b), (c) and (d) are spectra of EDS point scanning corresponding to point 1, 2 and 3 marked in (a).

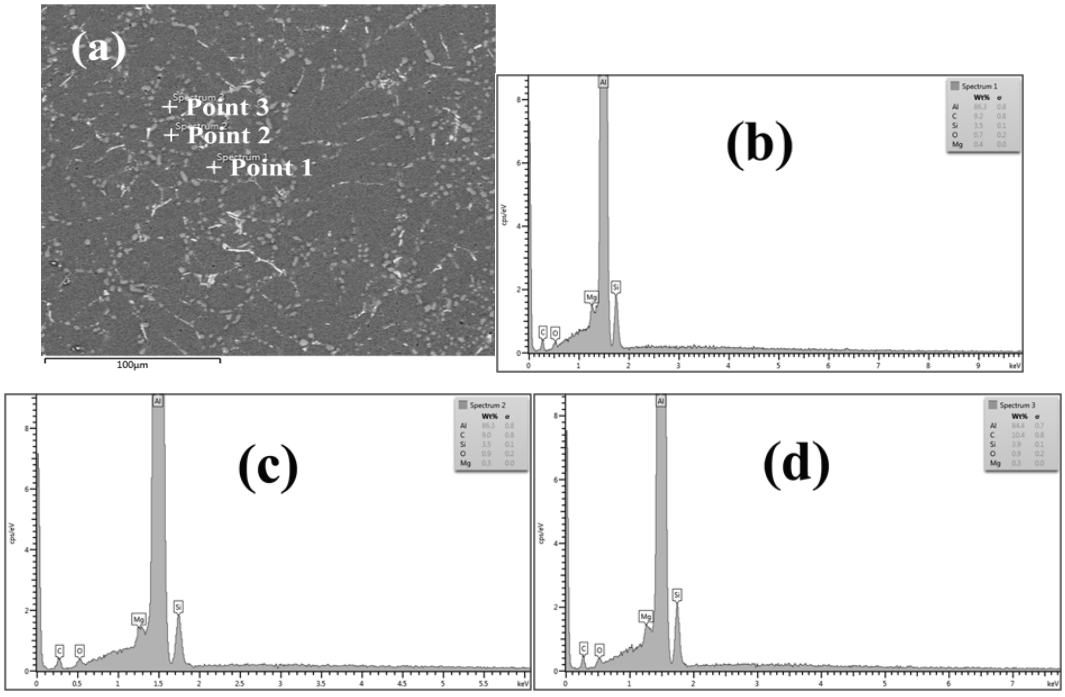

Fig. 36. Microstructure of CL-DC-AC4C-T6 alloy (a) SEM micrograph, (b), (c) and (d) are spectra of EDS point scanning corresponding to point 1, 2 and 3 marked in (a).

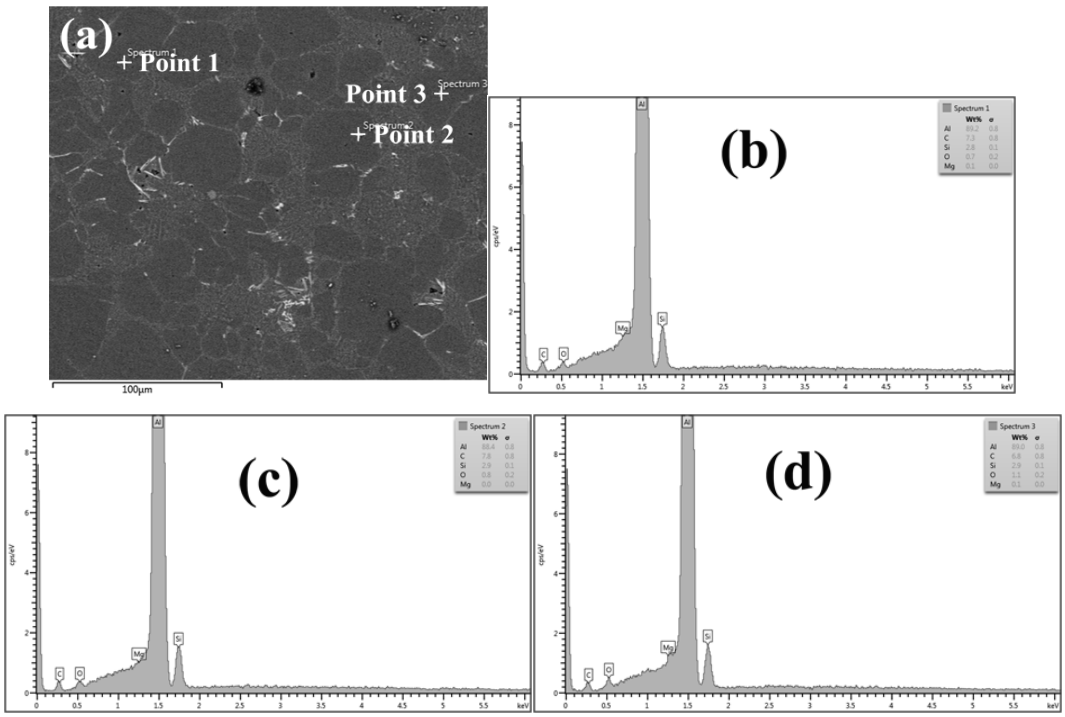

Fig. 37. Microstructure of as cast GISS-DC AC4C alloy (a) SEM micrograph, (b), (c) and (d) are spectra of EDS point scanning corresponding to point 1, 2 and 3 marked in (a).

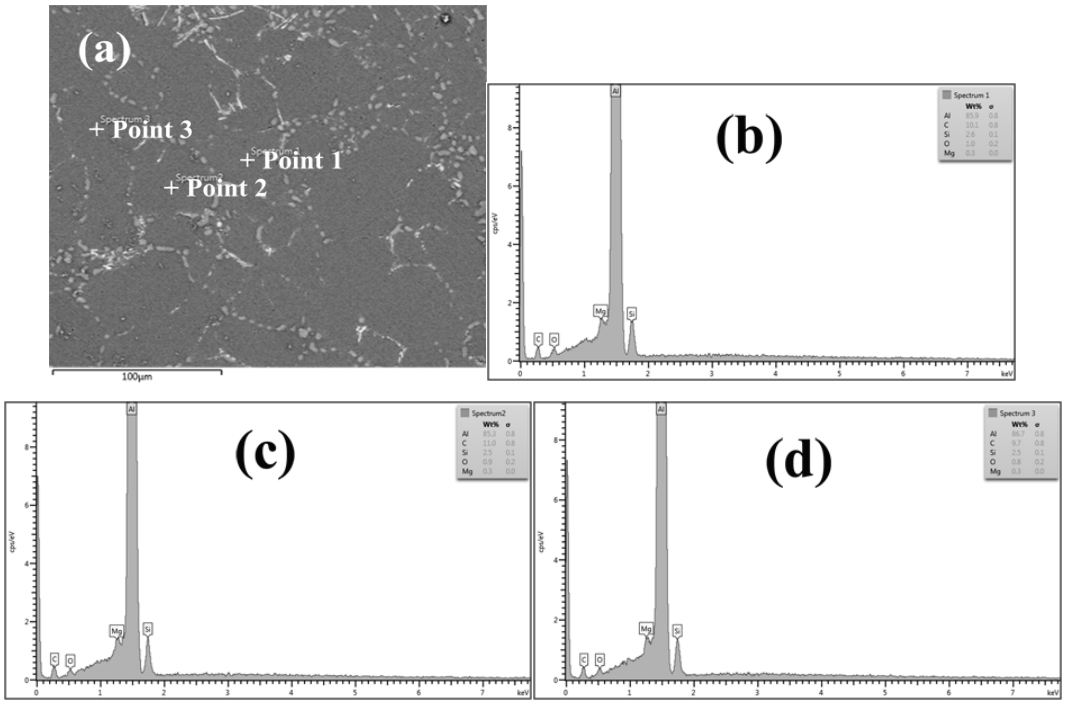

Fig. 38. Microstructure of GISS-DC-AC4C-T6 alloy (a) SEM micrograph, (b), (c) and (d) are spectra of EDS point scanning corresponding to point 1, 2 and 3 marked in (a).

4.2.3 Microstructure examination results by DSC

The Fig. 39 and 40 looks similar, which maybe mean the same reaction during the T6 heat treatment in the GISS-T6 and CL-DC-AC4C-T6 Al alloys. The literature[135] affirms that peak 1 (at 221.19 ^{o}C in CL-DC-T6 and 221.21 ^{o}C in GISS-DC-T6) is an unresolved one of two superimposed peaks, due to the formation of GP-I or fine precipitates and GP-II / (β”), no evidence of the combination of two peaks was detected in our DSC in Fig. 39 and 40 in the GISS-T6 and CL-DC-AC4C-T6 Al alloys. However, the heating rate used in this investigation is same (5 min/^{o}C) but the excess amount of Si will accelerate the precipitation rate. In general, some authors [184, 185] associate the peak 2 (occurring approximately at 253.75 $^{\circ}$C in CL-DC-T6 and 262.83 °C in GISS-DC-T6) with precipitation. However, the DSC traces in this peak also seem to be the result of the superimposition of two peaks, and this is in accordance with TEM observations [183, 184] reporting that there is the formation of two phases, B’ and β’ with hexagonal crystal structure. It is noted that there is a peak at about 170 °C during decreasing the temperature. That maybe some phase decomposed. Therefore, secondary cycle there are also smaller similar peaks at the same temperatures.

It is noted that there is a peak at about 170 ^{o}C during decreasing the temperature. That maybe some phase decomposed. Therefore, secondary cycle there are also smaller similar peaks at the same temperatures.

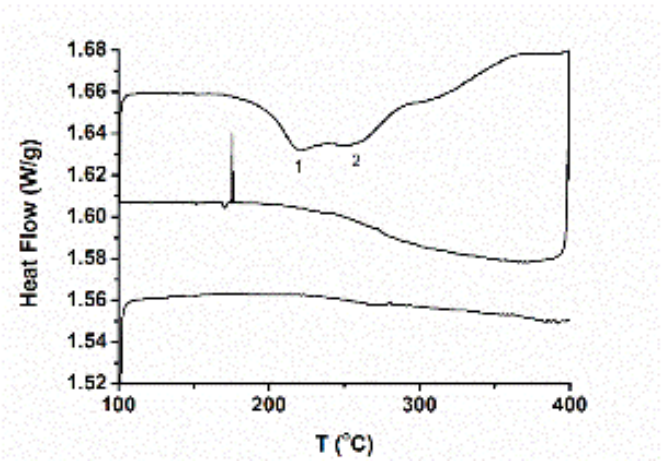

Fig. 39. DSC curves of CL-DC-AC4C-T6 alloys

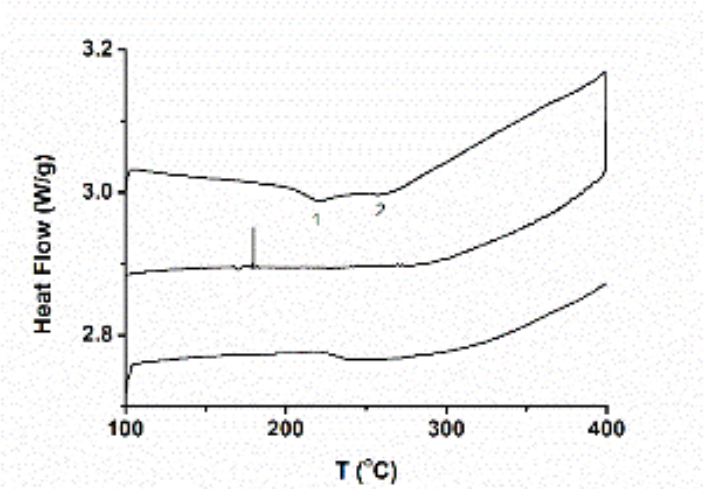

Fig. 40. DSC curves of GISS-DC-AC4C-T6 alloys

4.2.4 Microstructure examination results by XRD

The XRD results of the GISS-T6 and CL-DC-AC4C-T6 Al alloys are showed in Fig. 41 and 42. The peak 1 may be AlMgSi and peak 3 and peak 2 may be the AlMnSi or AlFeSi [82, 122]. Because previous work which revealed that there are some AlFeSi in the metallic. So AlFeSi crystal is comfirmed in the metallic of the GISS-T6 and CL-DC-AC4C-T6 Al alloys.

Therefore, AC4C Al alloys are usually subject to the T6 temper including the solution heat treatment at higher temperature and aged at lower temperature. The Mg and Si are decomposed and dissolved into Al matrix during the solution heat treatment, and then precipitated during aging. During solution heat treatment, the π Fe-bearing intermetallic particles can be transformed into β phase by releasing Mg into Al matrix [1], and the Mg_xSi_y particles formed during the solidification are completely decomposed and dissolved into Al matrix after 1h solution treatment at 538°C , which revealed by the electron microprobe analysis [2, 128, 181, 186]. However, in this work, Mg_2Si particles not find and no rich Mg in rich Fe intermetallic particles or in Si particles. Mg content is about 0.3% and uniformly contributed in the GISS-T6 and CL-DC-AC4C-T6 Al alloys.

All above, the spheroidization of eutectic Si occurred after T6 heat treatment and in the as cast GISS-DC and CL-DC AC4C alloys there are some π-Chinese script phase (AlMgFeSi or AlMgFeSiMn) and β(AlFeSi) phase. But after T6

heat treatment, only β (AlFeSi) phase can be found in the GISS-T6 and CL-DC-AC4C-T6 Al alloys. In both of the GISS and CL-DC AC4C Al alloys the Mg percentages increase after T6 heat treatment due to the Mg element dissolvent in the Al phase uniformly. The Si percentages in CL-DC AC4C Al alloys increased after T6 heat treatment, however, the Si percentages in GISS-DC AC4C Al alloys decreased after T6 heat treatment due to the GISS process.

The composites and the major microstructures features including the volume fraction of porosity, morphology and the intermetallic phases such as Si precipitates hugely effected on the mechanical properties of the AC4C Al alloys in practice. The interface between brittle intermetallic particles and the easily plastically deformed Al matrix restricted the ductility property of this alloy through the stress inhomogeneity. These intermetallic particles will be easily cracked on load finally.

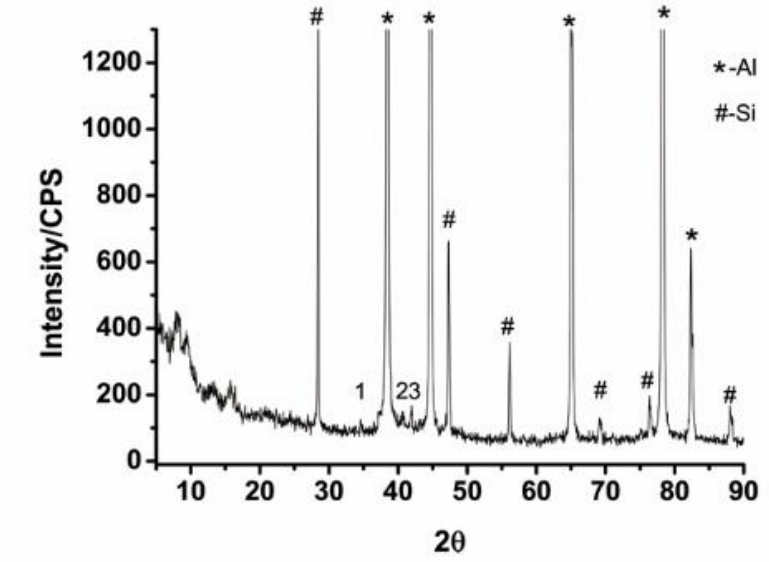

Fig. 41. XRD of CL-DC-AC4C-T6 alloys

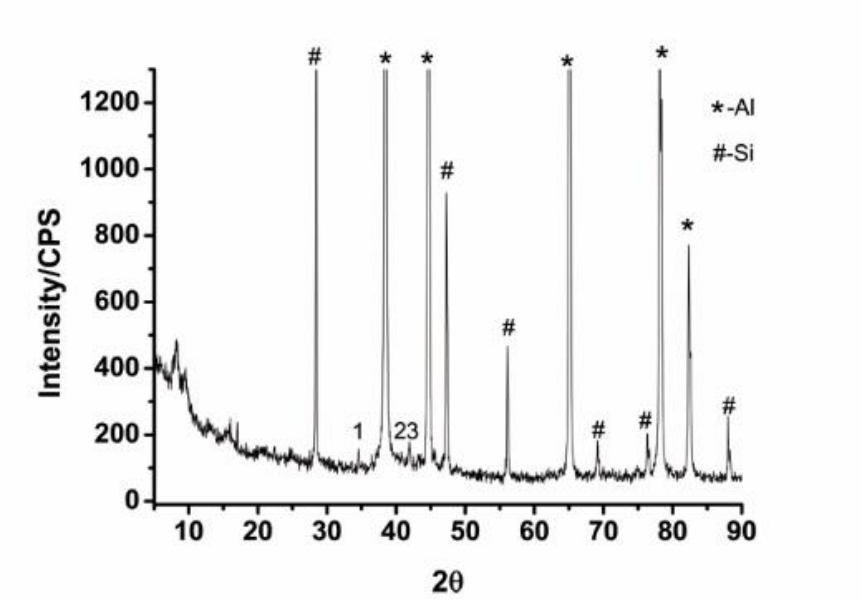

Fig. 42. XRD of GISS-DC-AC4C-T6 alloys

4.2.5 Microstructure examination results by TEM

The TEM results of the GISS-T6 AC4C Al alloys is showed in Fig. 43. The precipitate particles in the primary Al phase are found in Fig. 43 [187]. The size of particle is about 80nm. Acording the lattice parameter, the calculate data equate to the data from the TEM diffraction pattern.

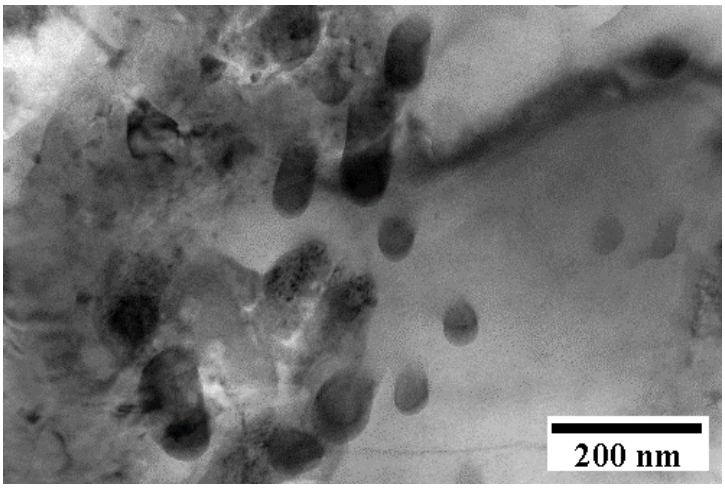

Fig. 43. TEM of GISS-DC-AC4C-T6 alloys

4.3 Effect of position of as casting AC4C

In this part, impact on tensile test results was presented and explained for the GISS-DC AC4C alloy. The effect of position of microstructures and tensile properties of specimens of as casting AC4C Al alloy from different locations of cast plates was studied. The results show that the specimens from bottom location, near the gate section and the middle location of cast plates are stronger and more ductility than those from the top location. The microstructures of this alloy were studied by OM, SEM and EDS. The fractures of alloy were characterized by OM, SEM and EDS.The microstructural examination reveals that the specimens from top location of cast plates contain more defects, such as shrinkage pores than those from the other locations. These defects are resulted in lower strength and ductility of the cast product.

4.3.1 Microstructures

The as cast microstructure of Al-Si-Mg-Fe alloys (AC4C) is known widely that it is comprised of dendritic primary Al grain and eutectic Al-Si and Fe-bearing intermetallic phases phase [180] . Fig. 44 indicates the microstructures of as-cast GISS-DC AC4C aluminum alloys are typically multiply phases comprised of circular or rosette primary Al grain, eutectic Al-Si and numerous intermetallic phases. The precipitates are distributed in primary Al grain and some research reported that there are the large rod-shaped Mg_2Si compounds and intermetallic around primary Al grains phase [128]., As shown in Fig. 44, it is evident that primary Al grain size and quantities in location 1 compared with location 4 increased due to the slower cooling rate and the different flow behavior of location 4 region compared with others during the die cast processing. However, the large grains are softer and the transmission of slip is easy across the grain boundary compared with the small one, but the lower area fraction and the higher clustering of the primary Al grain effect the mechanical properties more seriously. Additionally, the partial solidified semi solid slurry from the shot sleeve of the others location also increased the grains size and quantities.

As shown in Fig. 29, it is evident that the primary grain phase is Al elment where the large rod-shaped precipitates are distributed almost uniformly to increase the strength of metals [128]. It noted that the areas between primary grain

contain a large number of elements: Fe, Mg and Si which constitute the intermetallic particles or eutectic Al-Si which are needle or plate-like.

In the Fig. 32, it is noted that there are many different comlocation of rich Fe element intermetallic particle including: FeSiMn, SiFeMg, FeSiMgMn and balance of Al element. However specific comlocation and crystal structure of the intermetallic phases and precipitations in the Al-Si-Mg-Fe alloy is a hot research topic still due to the very difficult acurate determination [128]. These evidents show that the intermetallic comlocation is not one but complex and include elements of Al, Fe, Mg, Si, Mn.

However, the large grains are softer and the transmission of slip is easy across the grain boundary compared with the small one, but the lower area fraction and the higher clustering of the primary Al grain effect the mechanical properties more seriously. Additionally, the partial solidified semi solid slurry from the shot sleeve of the others than location 4 also increased the grains size and quantities.

Besides the different microstructures, at location 4, AC4C also had some typical defects, such as gas porosity which is always near the surface from the die-casting process. It is intended to have some big blisters more near the end of the specimen corresponding to area with the more porosities near the gate overflow during manufacture, when a worst case happens only.

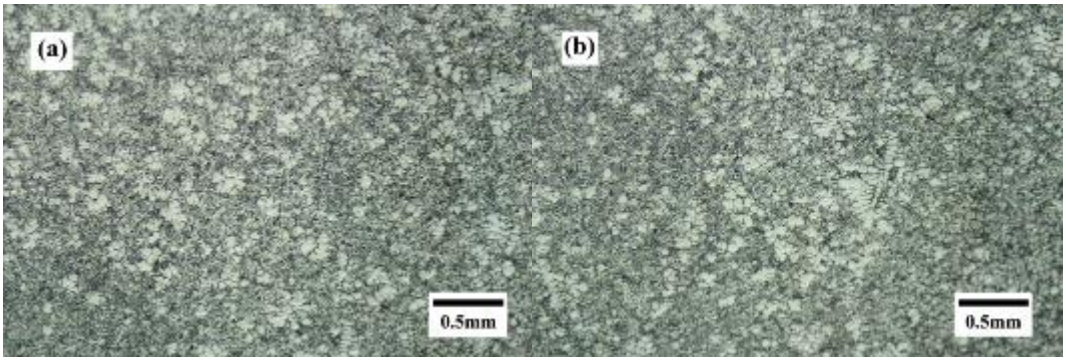

Fig. 44. Optical micrographs showing microstructures of AC4C alloy prepared from (a) part 1 (bottom) and (b) part 4 (top) of die cast plate.

4.3.2 Mechanical properties

The Fig. 45 show the stress versus strain curves of different locations of

4 specimens. Necking and yield point was not obvious during the tensile test. Therefore, the proof strength (0.2%) was used. Both the location 4 and other cases showed a similar trend of deformation but the differences of the strain hardening behavior. The location 4 specimens show a lower strain hardening rate compared to the other three specimens. Additionally, significant decreased strain to fracture is observed from the location 4 to others, due to some multiple reasons of the strain hardening and other defects such as the arrangement of micro porosity and the shrinkages.

The YS and UTS at different locations of the alloys are shown in the Fig. 46. Significant differences in these curves about the different locations are observed. The YS and UTS in different locations show a different trend. The average YS values of all locations are same and around 100 MPa. The UTS enormously decreases from around 200 MPa of the other locations to 140 MPa of the location 4. The location impact on the UTS is higher than YS and elongation. The strain hardening also increases significantly in the location 4 compared to others. The multiple defects would be responsible for the higher UTS of the bottom specimens than location 4. Fig. 46 also shows the strain of fracture in the specimens. The location impact on the fracture strain is higher than YS and UTS, in other words, the elongation of location 4 is the lower than others. The average elongations of the location 4 and others are 6.7 % and 11.8 %, separately.

This study concludes that the mechanical properties and ductility are increasing form location 4 to the others. From some literatures, it showed that the different solidification time on different locations extremely affects the final microstructures and mechanical properties. Fig. 44 show that the microstructural difference is expected on account of faster solidification time of skin and location 4 region than the others of the casting in the mold. This would be the reason for the obtained changes of mechanical properties with location impact in the specimens. Besides, the higher area fraction percentages of porosity and higher probability of crack and the propagations of the eutectic and primary Al grains are also the multiply reasons of the different stains hardening of different locations due to the effect of some microstructures as follow on the mechanical properties.

The comparison of the tensile properties with the reported literature data of A356 by GISS-DC is presented in the Fig. 47. The UTS value presented in the present

work is higher than commercial liquid die-casting (CL-DC) as it is different to use the different processing due to the semi-solid microstructure of the finer and circular Al primary phase which will hinder the slid or dislocation to traverse. However, it is slightly lower than GISS-DC A356 the other, because the Fe contain in AC4C is a little higher than A356 but have good castability and less erosion and shrinkage [128].

The comparison of the tensile properties of GISS-DC AC4C with some data by GISS-squeeze casting AC4C is presented in the Fig. 48. The UTS values of GISS-squeeze casting AC4C at GISS time of 620 °C are little better than presented in the present work by GISS-die casting processing.

The comparisons are complicated by the characteristic of the manufacturing defects previously and latterly discussed. However it is worth to note that the comparison of the properties without considering the processing conditions.

Table 11 Tensile properties of GISS-DC AC4C speciemens prepared from different parts of die cast plate.

Location No.	YS 0.2% (MPa)	UTS (MPa)	Elongation (%)
1	105.4±1.9	203.2±9.4	11.2±2.0
2	103.1±3.3	189.9±23.8	10.4±2.1
3	100.3±4.3	205.6±9.2	12.2±2.0
4	96.6±5.8	149.1±15.3	6.9±1.0

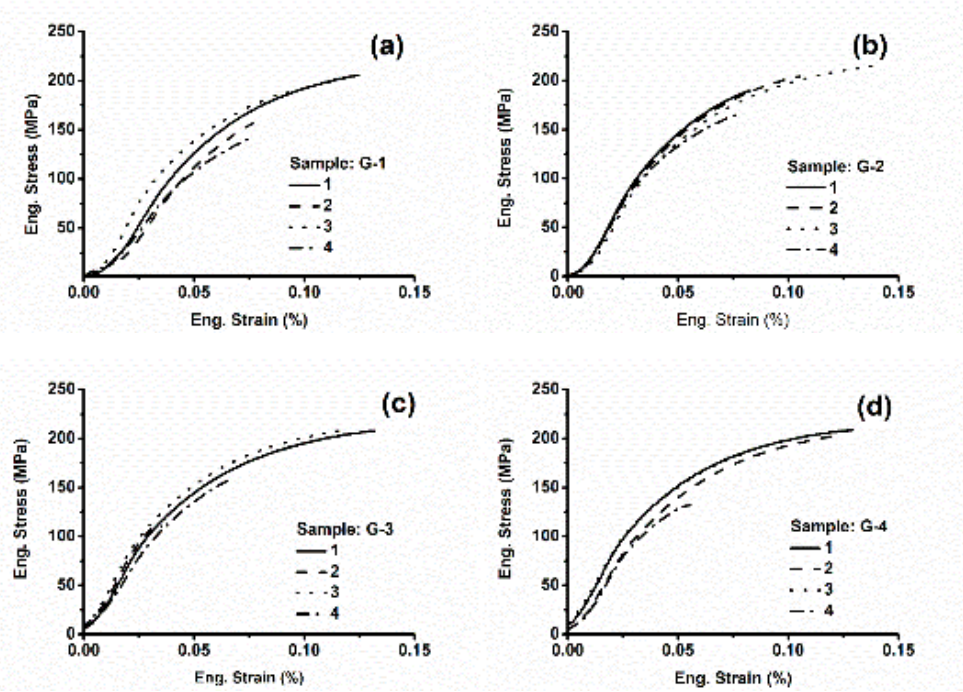

Fig. 45. Stress-strain curves from tensile tests, (a), (b), (c) and (d) corresponding to specimens prepared from parts 1, 2, 3, and 4 of the die cast plate.

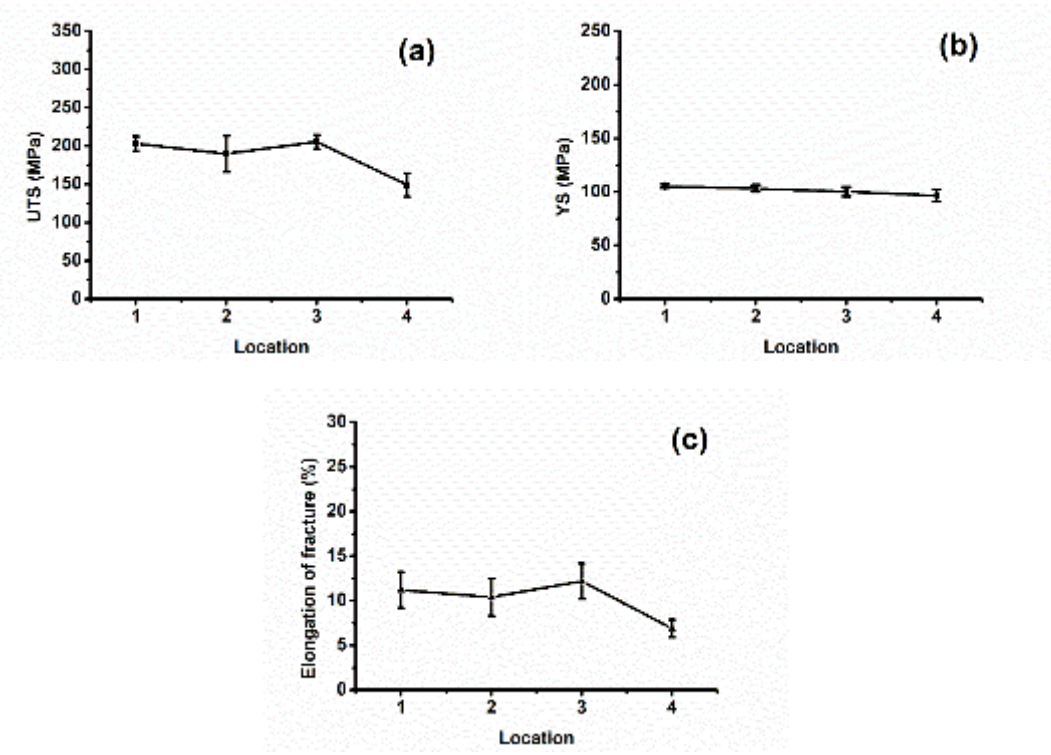

Fig. 46. (a) Ultimate tensile strength (UTS), (b) Yield strength (YS) and (c) Elongation of specimens prepared from different parts of die cast plate.

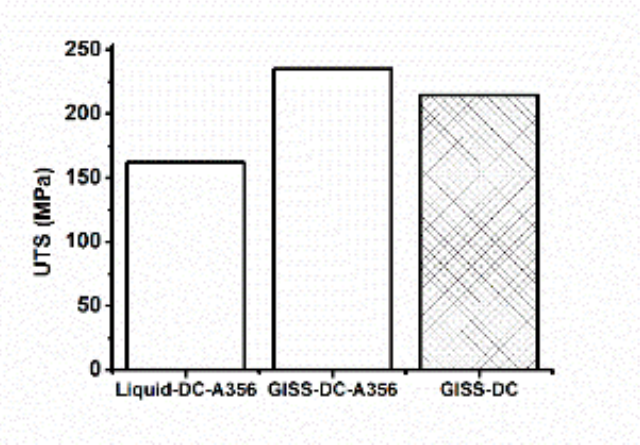

Fig. 47. Comparison of UTS of GISS-DC AC4C alloy from this study (meshed pattern) with those from the literatures (blank)

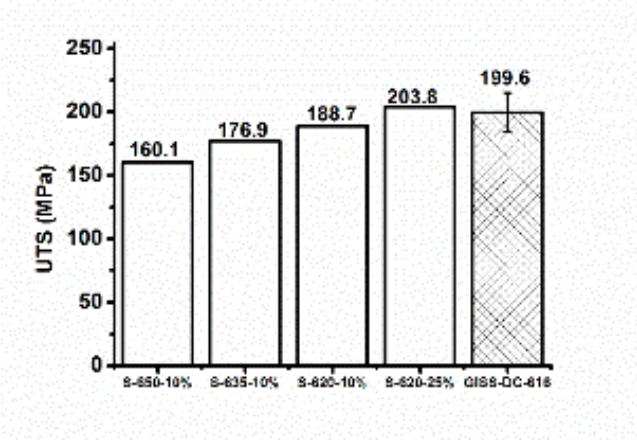

Fig. 48. Comparison of UTS of GISS-DC AC4C alloy from this study (meshed pattern) with those of GISS-DC A356 (blank).

4.3.3 Fracture surfaces of AC4C aluminum alloys tensile specimens were examined using SEM and OM.

The macroscopic observation of the tensile test fracture by naked eyes reveals the brittle nature features of this alloy. From observations of SEM in Fig. 49, it is showed that the fracture surfaces of AC4C aluminum alloy tensile samples at different locations display a clearly brittle fracture, and the quasi-cleavage feature can be observed. The fracture surfaces of GISS-DC AC4C Al alloy tensile samples don't show a dimple-like morphology. The dimple-like fracture surfaces reveal the ductile characteristics of the samples and show the micro-necking crack around dimples. The quasi-cleavage morphology of AC4C aluminum alloy tensile samples at location 4 is

same as at other locations, so the location impact don’t effect fracture.

Moreover, the more shrinkage defects and micro voids can also be observed at location 4 than location 1, as shown in Fig. 50 (a) and (b). The mechanical properties of location 4 decreased due to some defects such as shrinkages during the die cast process or gas babble during the GISS process. The shrinkage pore is easy to cluster and harmful to tensile properties in die casting components. It is also confirmed that the clustering characteristics of pores and the eutectics are higher in location 4 than others. The fracture path preferentially goes through the shrinkage porosity in the case of the existence of excessive shrinkage defects, which results in the significant decrease of mechanical properties. In addition, there are no pores which are found to exist in the edge region of all locations.

From Fig.51, the big crack is observed in the location 4, which is resposible for the reduce of the tensile property of location 4. It is so big that must generate before the tensile test, but the crack lines located in the center of the specimens so it is difficult to observed before the tensile test.

The EDX of AC4C Al alloys at different location in Fig. 52 and 53 show that the silicon distributions at different locations are observed using line and point scanning. Some precipitated silicon particles embedded in an eutectic matrix consisting of continuous of Al and Si. The shrinkage in the location 1 observed along the grain boundary which the silicon particles centralized showed in Fig. 26. The fractures of all specimens were brittle and intra-granular with no evidence of necking. Cavity coalescence and crack growth were deduced as the failure mechanism. In Fig. 53, the same trend is also observed but the point scanning is used. The porosity could be the effect the crack propagations and reduced the material mechanical properties when the tensile test is carried out, the porosities would be contracted around internal stresses, and then the fracture would begin at this field. After that, the propagations of the cracks could lead to speed up to failure, which reduce the mechanical properties, especially to a loss of ductility as above. The crack from shrinkage pores also is observed in Fig. 49, 50 and 51.

From the OM after tensile test in Fig. 54, some secondary phase areas after the tensile test at the all location is always larger than before fracture, because the big primary phase may be broke and generate the new secondary phase during the

tensile test. There are three parts during the damage process: particle cracking and deboning, micro crack formation and growth in the cracking and debonding particles, and local linkage of microcracks [1]. Fig. 54 show the OM fracture surfaces on longitudinal sections of all locations, the damage process can be observed. Moreover, the OM fractography reveal that the crack is observed along the grain boundary and is stopped by the eutectic particles or clusters. It was said that the existence of the silicon particles, especially in the presence of other defects, would increasingly degrade tensile properties. Fig. 54 is showed that the fracture mainly goes through the eutectic region.

The eutectic of the AC4C is characterized by phases containing Si, Fe and Mg embedded in Al. The primary silicon particles can be correlated to the tensile performance. The shape of these constituents is elongated and irregular as in a typical eutectic structure. This elongated and irregular eutectic particles are more brittle and fracture faster than the round particles which can generate in the T6 heat treatment, but the as cast GISS-DC shows more brittle behavior. So analysis of micrographs of tensile test samples revealed that the fractures were susceptible to brittle tensile fracture. In the Al alloys, silicon is added to increase the hardness, for improving wear resistance and castability. However, the rupture of silicon particles damages the formability of these alloys. The defects are pre-existing and grown during tensile test, which makes the fracture to be lower and to be more difficult to prediction the strains. The tensile properties could be increased through refinement of the primary silicon particles in our further study, the creep resistance was degraded with increased silicon particle size seen in some literatures [15]. And the fracture and debonding of eutectic Si particles play an important role. In general, the formation of the microcracks in the eutectic silicon particles is mainly normal to the applied stresses similar to results in literatures. In the Fig. 49-54, multiple cracks are observed on the fracture surface. During the tensile test, the deformation in eutectic Al-Si and Fe-bearing intermetallic phases could induce the internal stress to carry out and aggregate and increase [49]. When the internal stresses approach the critical value of fracture stress in some areas, the crack will occur. Therefore, the fracture of particles depends on the stress and mirostructure features such as the size and shape [42].

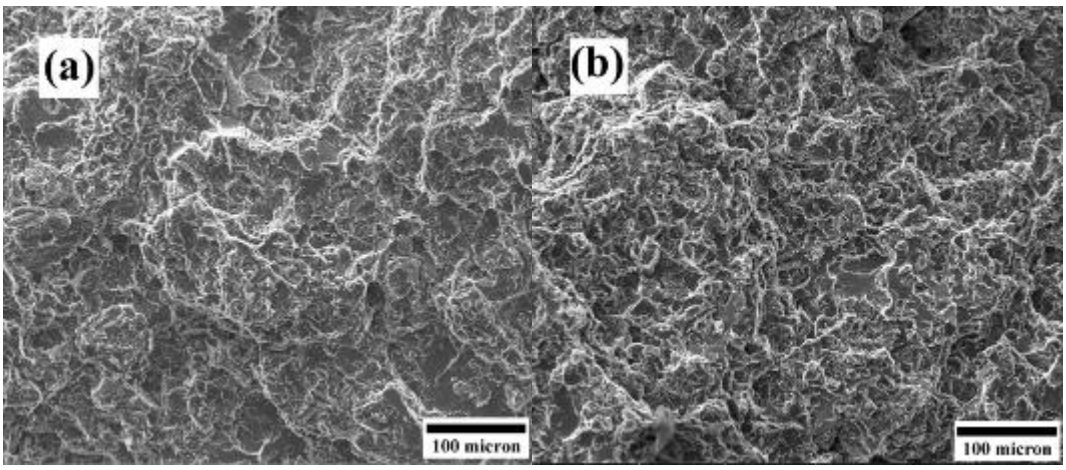

Fig. 49. SEM fractographs of specimens after tensile tests. (a) and (b) corresponding to specimens prepared from parts 1 and 4 of die cast plate, respectively.

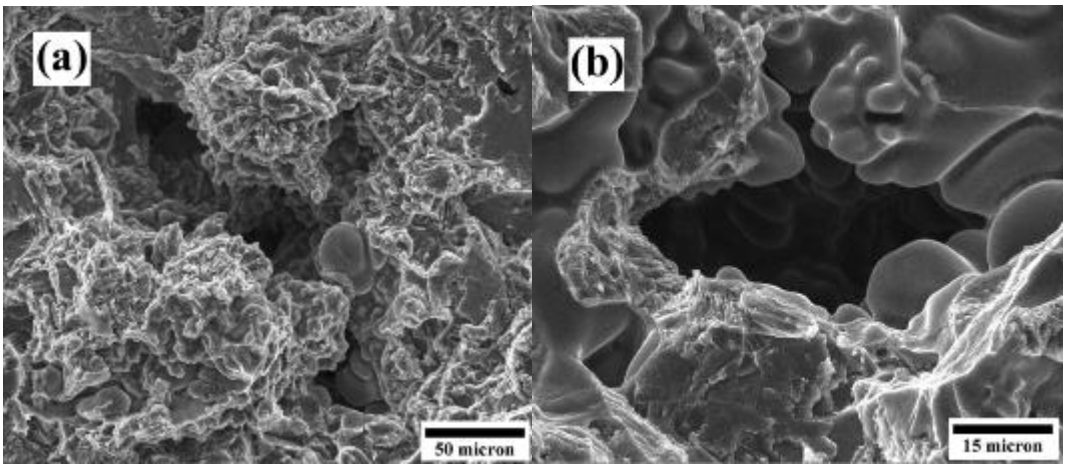

Fig. 50. SEM fractographs of specimens after tensile tests, showing shrinkage pores and micro voids. (a) and (b) corresponding to specimens prepared from parts 1 and 4 of die cast plate, respectively.

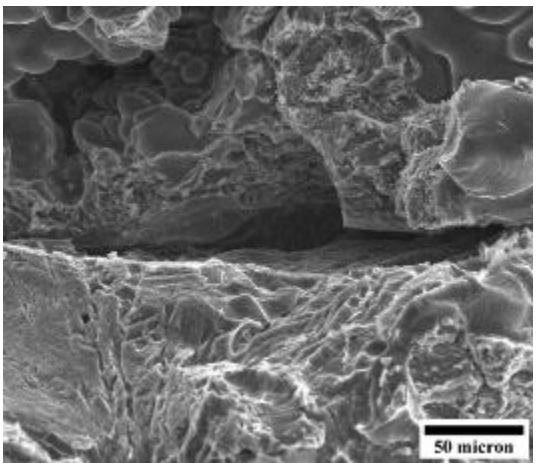

Fig. 51**.** SEM fractograph of specimen after tensile test, prepared from part 4 of die cast plate.

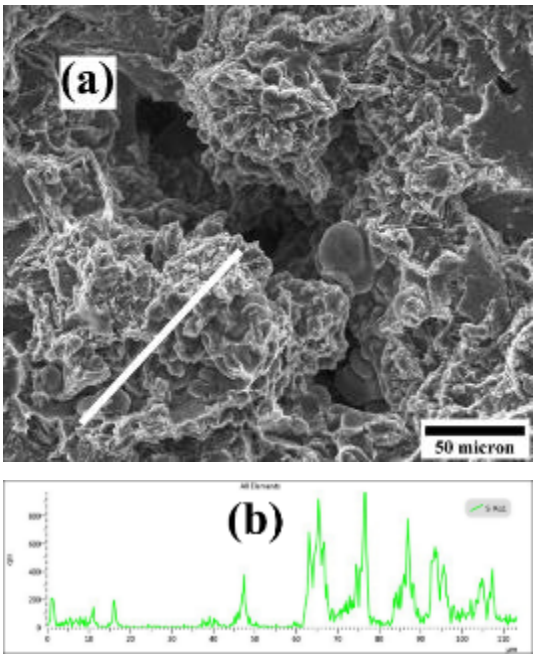

Fig. 52**.** (a) SEM fractograph of specimen after tensile test, prepared from part 1 of die cast plate and (b) EDX spectrum along the line marked in (a).

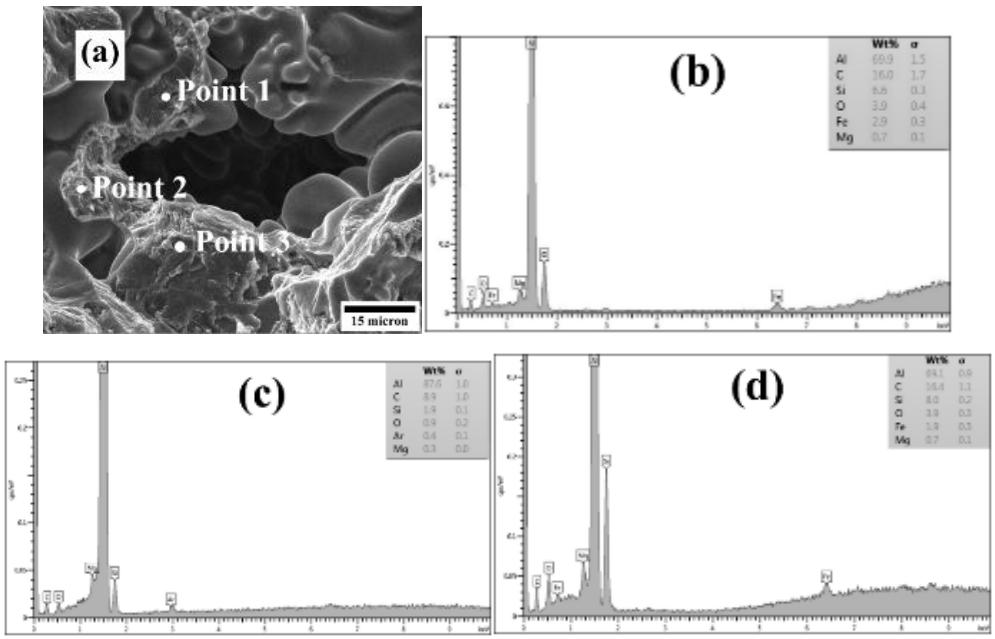

Fig. 53. (a) SEM fractograph of specimen prepared from part 4 of die cast plate, (b), (c) and (d) are EDS spectra from point scan corresponding to points 1, 2 and 3 marked in (a), respectively.

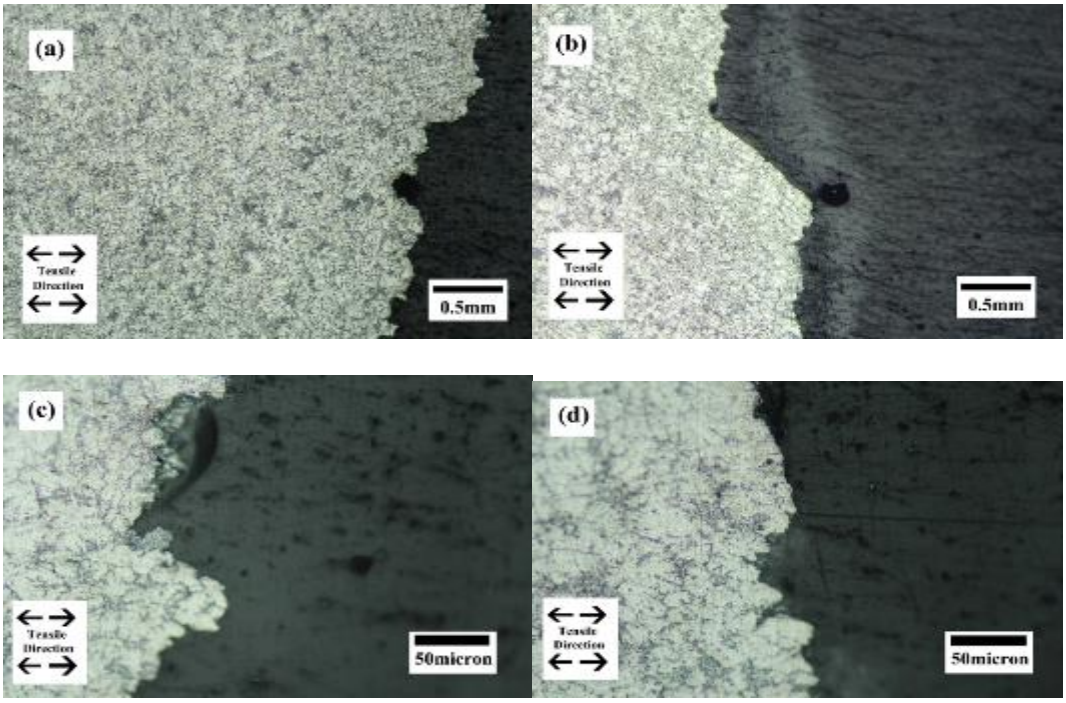

Fig. 54. Optical micrographs showing microstructures near fracture surface of specimens after tensile tests. (a) and (c) specimen prepared from part 1, and (b) and (d) from part 4 of die cast plate.

4.3.4 Conclusions

In present study, location impact on constant tensile test results was presented and explained in the GISS-DC AC4C alloy. The microstructure of this alloy is studied by OM and SEM and EDX. The fractures of GISS-DC AC4C alloys were performed by using SEM and EDX. The complex defects of different geometry of microstructural features are non-uniform and, however, have some spatial correlations with locations. The features which have different spatial arrangement, size distribution and shape cause different fracture mechanisms and strongly affect the fracture path and mechanical properties. The results illustrate the location impact on the microstructure and mechanical properties. The location impact on tensile properties of semi-solid die cast AC4C Al alloy is confirmed and the fracture mechanism is also discussed. It can be concluded that.

1. The primary Al grain size and quantities in location 1 compared with location 4 increased due to the slower cooling rate and the different flow behavior of location 4 region compared with others during the GISS-DC processing.

2. Between primary Al grain contain a large number of elements: Fe, Mg and Si which constitute the intermetallic particles and eutectic Al-Si. The comlocations of rich Fe element intermetallic particle includs FeSiMn, SiFeMg, FeSiMgMn and balance of Al element in GISS-DC AC4C alloys.

3. Significant differences of the YS and UTS and Elongation about the different locations are observed. The UTS and Elongation of location 4 is lower than in other locations. The average YS values of all locations are same and around 100 MPa. The UTS and elongation enormously decreases from around 200 MPa and 11.8 % of the other locations to 140 MPa and 6.7 % of the location 4, separately. The location impact on the UTS is higher than YS and elongation. The strain hardening also increases significantly in the location 4 compared to others.

4. The mechanical properties of GISS-DC are competitive with CL-DC. The UTS value of GISS-DC AC4C is higher than CL-DC A356. However, it is slightly lower than GISS-DC A356.

5. The quasi-cleavage morphology of AC4C aluminum alloy tensile samples at location 4 and other locations are observed. Moreover, the more shrinkage

defects and micro voids can also be observed at location 4 than location 1. In addition, in the edge region there are no pores which are found to exist in all locations and the big crack is observed in the location 4.

6. The crack and fracture from shrinkage pores also is observed in the specimens at all location. These will decrease the mechanical properties and ductility of GISS-DC AC4C alloy.

4.4 The Effects of Temperature on mechanical properties after T6

The effects of temperature on the tensile strengths and ductility of rheo-die cast GISS-DC-AC4C-T6 alloy were investigated. The microstructure of AC4C observed by Optical microscope, SEM and EDX will be presented and discussed. It was found that the tensile properties of GISS-DC and CL-DC AC4C alloys were decreased with increasing of temperatures. The fractographs revealed that fractures of GISS-DC and CL-DC AC4C alloys changed from brittle to ductile with temperatures increasing.

4.4.1 Mechanical properties

According the result from T6 heat treatment, the spheroidization of eutectic Si occurred after T6 heat treatment and in the as cast GISS-DC and CL-DC AC4C alloys there are some π-Chinese script phase (AlMgFeSi or AlMgFeSiMn) and β(AlFeSi) phase. But after T6 heat treatment, only β (AlFeSi) phase can be found in the GISS-T6 and CL-DC-AC4C-T6 Al alloys. In both of the GISS and CL-DC AC4C Al alloys the Mg percentages increase after T6 heat treatment due to the Mg element dissolvent in the Al phase uniformly. The Si percentages in CL-DC AC4C Al alloys increased after T6 heat treatment, however, the Si percentages in GISS-DC AC4C Al alloys decreased after T6 heat treatment due to the GISS process.

The composites and the major microstructures features including the volume fraction of porosity, morphology and the intermetallic phases such as Si precipitates hugely effected on the mechanical properties of the AC4C Al alloys in practice. The interface between brittle intermetallic particles and the easily plastically deformed Al matrix restricted the ductility property of this alloy through the stress inhomogeneity. These intermetallic particles will be easily cracked on load finally.

The GISS-T6 can produce a complex structure SSM Al alloy with high mechanical performances [19-21]. At room temperature, the GISS-DC-AC4C-T6 gained the UTS and YS of 300.9 MPa and 244.5 Mpa, the CL-DC-AC4C-T6 is 307.7MPa and 258.6MPa. At high temperature of 100, 175 and 250 °C, the results of the UTS of GISS-DC-T6 are similar to those of CL-DC-T6. Both the UTS and YS were slightly decreased with increasing temperature, which trend is similar to the other GISS Al alloys [102] and other Al alloys [188]. Tensile properties are shown in Fig. 55-59. The reduction of UTS values of semi-solid AC4C and CL-DC alloys are 53%, 57% up to 250 °C compared with room temperature, respectively. Otherwise, the YS of GISS-DC-T6 and CL-DC-T6 are 51% and 49%. All above are due to the Si particles which annihilate the deformation during tensile test changed with different temperatures. Yet, the alloy ductility is relatively lower at the 25 °C, 100 °C and 175 °C. At high temperature, the ductility was decreased slightly. From these, it shows that that the intermetallic particles are dominant to limit plastic which leading to work hardening at the 25 °C, 100 °C and 175 °C. The dislocation which gathers in deformation areas could result in that the stress increases at the interfaces between intermetallic particles and matrix. Therefore, due to the annihilation of dislocation, climbing and cross-slip at 250 ^{o}C, it is well known that the stress inhomogeneity at the interfaces between intermetallic particles and matrix will be reduced at the higher temperature. So the stress relaxation of matrix should be dominant at 250 ^{o}C leading to the work softening companied with effect on the formation of subgrain within the Al matrix. The voids at high temperatures formed at the boundary between the grains or intermetallic particles will lead to the necking. Therefore, the reduction of ductility is due to the grain boundary cavitation where the segregation of impurities such as intermetallic compound and particles including the iron elements caused the brittleness fractures with increasing temperatures. Additionally, the plastic flow curves are serrated Considère d by the development of the Potenvin-Le Chatelier (PLC) effect. It is sometimes described as “hopping” and the serrations are more irregular with small amplitudes at a medium to high strain rates. It is well known that the PLC effect in Al alloys can limit or improve the alloys ductility.

From Table 12, satisfactory tensile strength (300.9MPa) was obtained by the GISS process at room. The ultimate tensile strength (UTS), Elongation and 0.2%

yield strength of the rheo-die SSM alloy by GISS-DC-T6 from the present work were compared with those data from the tensile properties of the A356 and AC4C alloys in selected literatures which are listed alongside in Table 12. Though the average tensile strength and the yield strength by GISS-DC-T6 are not the highest, these UTS values are higher than those of thixoformed and SSM sand cast-T6 separately by 12.26% and 12.73%; UTS are lower than those of SSM squeeze cast-T6 SSM die cast-T6 separately by 1.36% and 2.26%. The elongation of SSM Die cast-T6 was lower than that of Thixoformed-T6 and SSM Squeeze cast-T6 on account of Fe particles which is higher than 0.4% in former group metal AC4C alloys and less than 2.0% in others of A356.

In Fig. 55, it is compare of the tensile properties between GISS-DC-T6 of AC4C and GISS squeeze casting after T6 [4] at elevated temperatures. The elongation of SSM Die cast-T6 was lower than that of SSM Squeeze cast-T6 on account of Fe particles at elevated temperatures. The peak aging of Al-Si-Mg alloys which is about 190 °C provides higher tensile strength and lower tensile ductility compared to the under aging, it might because the aging provides more precipitates and the precipitates obstruct dislocation moving and sequentially reduced ductility during tensile test. So the ductility of GISS-DC-T6 has a maximize value. Ultimate tensile strength and 0.2% yield strength of AC4C alloy decreased with increasing test temperature. Because the alloy is an FCC alloy which is featured by larger dislocation width and lower peierls stress [188].The critical strain and ductility of GISS-DC-AC4C-T6 alloys was lower than that of others casting process of A356 (Fig. 29) on account of Fe particles too. Iron is deleterious impurity elements to tensile properties such as ductility.

Moreover, the porosity and shrinkage defects of GISS-T6 is smaller than ones of CL-DC-T6. The porosity and shrinkage defects of GISS-as casting and CL-DC-as casting is same as ones of GISS-T6 and CL-DC-T6. GISS-T6 die casting samples produced in this study showed significantly improved tensile properties compared to other cast samples of the same alloy.

After yield point, further plastic deformation requires load or stress to increase, but the rate of the load and area of cross-section of GISS-DC-T6 alloy is decreasing at the same time. The combined effect results in typical load progression curve (see Fig. 55 and Fig. 56). From yield point to the ultimate tensile strength, the

tensile curve shows the work hardening, until the ultimate point, deformation of sample gauge length is considered to be uniform. So the standardized measuring formulae of the strain hardening exponent n at constant strain rate is given as follows [188].

$$n_{\dot{\varepsilon}} = \left(\frac{\partial \lg \sigma}{\partial \lg \varepsilon}\right)\Big|_{\dot{\varepsilon}} \tag{31}$$

However, the true stress strain plot is non-linear, it shows that material does not truly obey the Holloman's equation, and n is not a constant. The strain hardening exponent under tensile deformation has been experimentally proved that strain hardening exponent has very strong sensitivity to structure.

Supposed that there is no effect of electric field, magnetic field and radiant field in the test are constant temperature, stress is only a function of strain and strain rate. So, the equation is simplified into:

$$\sigma = \sigma(\varepsilon, \dot{\varepsilon}) \tag{32}$$

According to above state equation, the mechanical state of tensile deformation of this alloy is determined by strain and stress when strain rate is constant. The work hardening vs strain curve (in Fig. 60) indicates that n is decreasing with the increasing strains at different temperatures at constant strain rate ($0.01s^{-1}$). It is shown that values of n at 25 °C, 100 °C and 175 °C are same and decreasing with the increasing strains and n tends towards zero when necking occurs. At 250 °C, the load is unstable in the superplastic tension, so there does not occur necking. It also noticed that n value at 250 °C not only decreased with the increasing strains but also turn into negative value from position. When the necking occurs, the n tends to zero.

Moreover, the condition of tensile plastic instability resulting in necking can be described by the Considère criterion:

$$\frac{d\sigma}{d\varepsilon} = \sigma \tag{33}$$

The necking starts at a critical plastic strain ε=n, where n is the work hardening exponent. However, the n is not a constant during the tensile test. So the critical plastic strains which are given by Considère criterion are chosen by the maximum one. From the above tensile properties, the alloy cannot reach the onset of necking given by the Considère criterion due to the major structural defects and discontinuities. The brittle intermetallic particles and Si particles always result in significant damage and early fracture at lower elongation which occurred at lower

temperatures, therefore, the Considère criterion was not satisfied in semi-solid AC4C Al alloys for the lower temperatures, as well as the n is not constant, which is different at the high temperature occurred superplastic. Although, S. Wisutmethangoon [3] reported n = 0.158 of the semi-solid squeeze casting A365 alloys, this data may not is available to value the feature of the material in practice.

Table 12 Mechanical properties of Al-Si-Mg alloys by different semi-solid forming processes, test at strain rate of $1*10^{-2}$ s^{-1} are included for comparison.

Process	YS (MPa)	UTS (MPa)	Elongation(%)	Ref
GISS die cast AC4C-T6	244.5±4.1	300.9±9.9	6.4±3.2	This study
GISS sand cast AC4C-T6		262.6±9.7	5.4±0.6	[63]
GISS squeez cast A356-T6	272	305	9.8	[7]
Thixoformed A356-T6	150	264	16	[121]

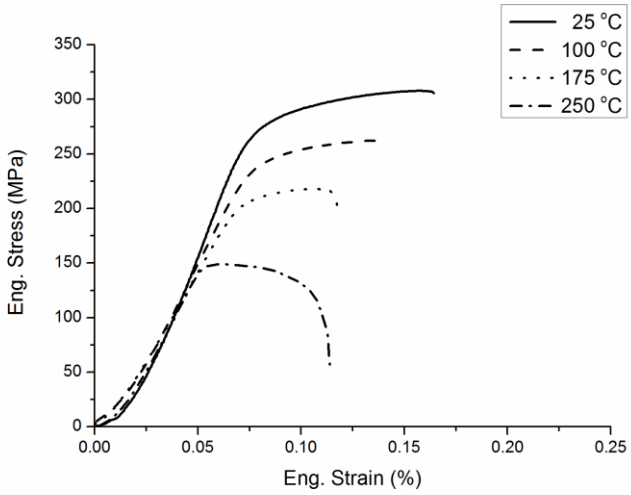

Fig. 55. Engineering stress-strain curves of CL-DC-AC4C-T6 alloy at 25 °C, 100 °C, 175 °C and 250 °C.

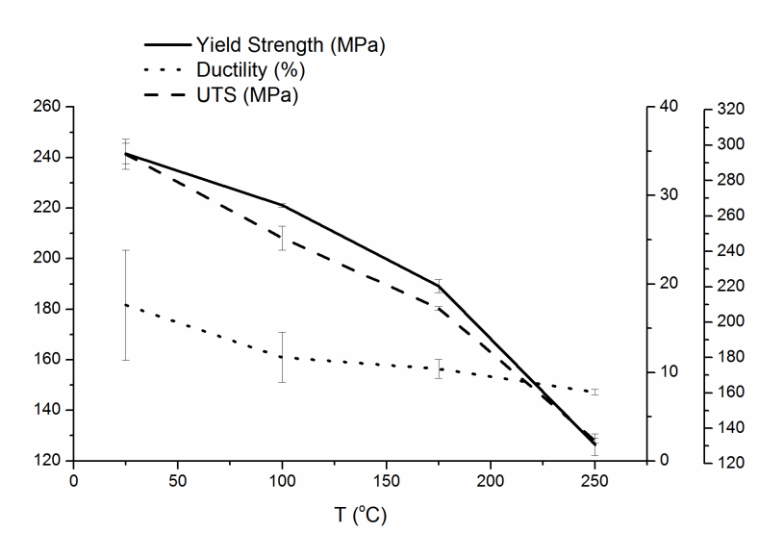

Fig. 56. The UTS, Yield Strength and Ductility of GISS-DC-AC4C-T6 alloy at 25 °C, 100 °C, 175 °C and 250 °C.

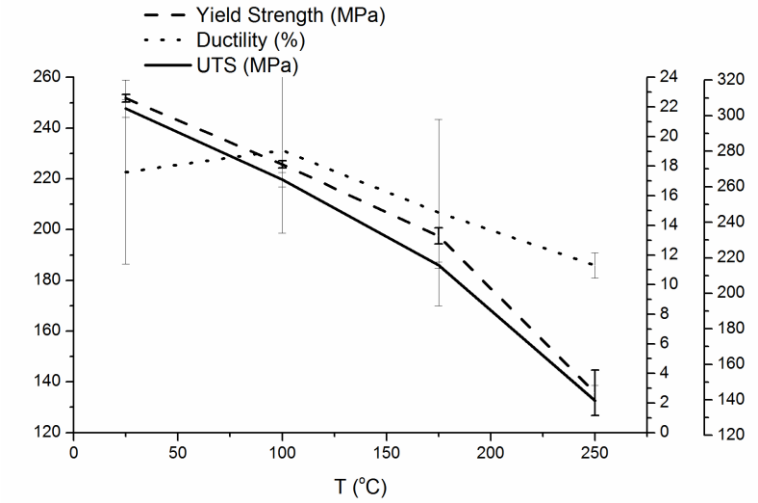

Fig. 57. The UTS, Yield Strength and Ductility of CL-DC-AC4C-T6 alloy at 25 °C, 100 °C, 175 °C and 250 °C.

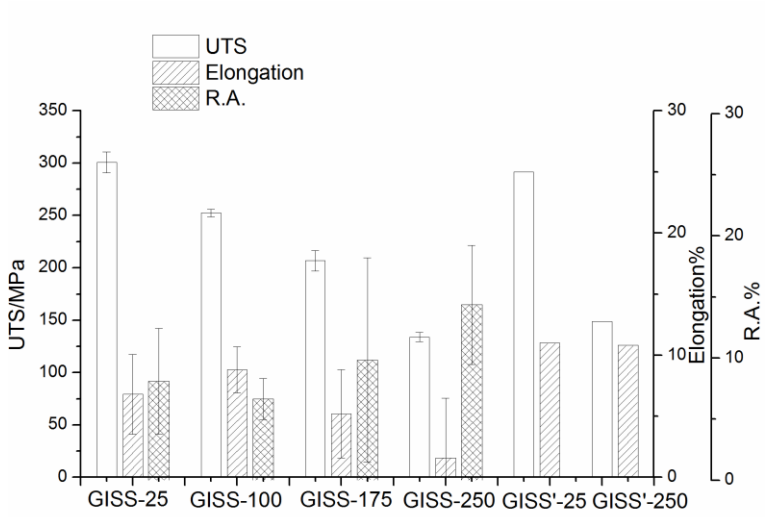

Fig. 58. Ultimate tensile strength (UTS), elongation and reduction of area of AC4C by GISS at different temperature compared with GISS squeeze casting A356. (Last two data from paper [140])

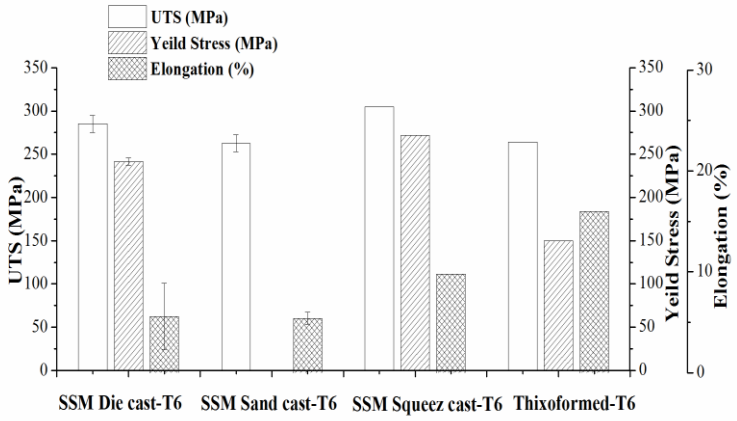

Fig. 59. Ultimate tensile strength (UTS), elongation and reduction of area of GISS-DC AC4C alloy compared with A356 by GISS sand cast, Squeeze cast and Thixoform casting at 25 ^{o}C.

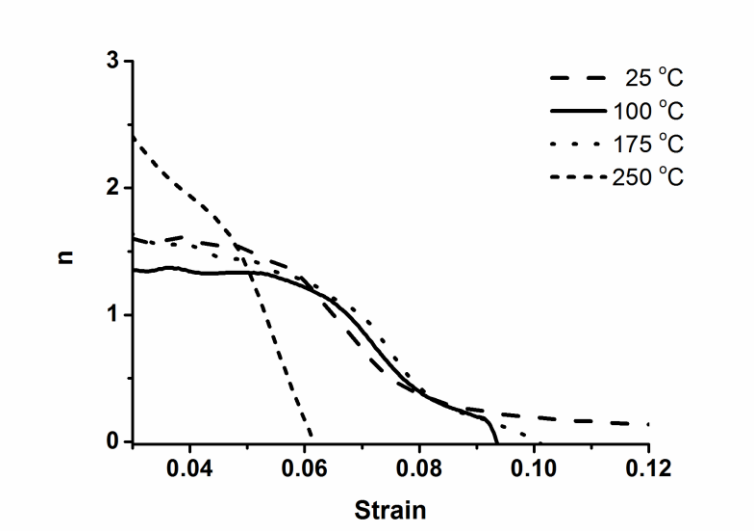

Fig. 60. Curve of n-ε of GISS-DC-AC4C-T6 Al alloys.

4.4.2 Fractography of GISS-DC and CL-DC AC4C after T6

Necking as the local cross section area (CSA) decrease and constriction begins along the gage section after yield point. From this point, inhomogeneity between strain hardening and area decrease arises. As a result, the load required for further progression decreases. This means that load carrying capacity of this alloys decreases. After necking point, practically all plastic deformation is concentrated in the small necked region. Finally failure occurs in the necked region. Regard as the die cast semi-solid AC4C alloy was heat treated by T6, it is expected to exhibit work hardening and the secondary phases which are Si spherical precipitate particles excised in Fig. 61 where the fracture surface comprised of cracking of Si particles on clearage planes. The broken Si particles were found on the fracture surface of the alloys to limit the plasticity of this alloy. No evidence of broken intermetallic was found in this work. The existing of the brittle intermetallic precipitants and Si particles lead to fracture which were found that fracture of Si particles was the dominant feature at the temperature range between room and 250 °C (seen in the Fig. 62). The single dominant cleavage crack observed at low temperature which is seen in Fig. 62. At 175 °C, it is noted that the brittle cleavage fracture with small plastic deformation areas. At 250 °C, the fracture is ductile and it is observed in Fig. 63 where there are ductile dimples due to multiple between the reinforcing intermetallic particles and matrix plastic relaxation and the intermetallic particles dispersed in the small, ductile dimples. However, the fracture of intermetallic

is not found in this work. Notices that these are also the evidences of work hardening exponent n which is not equal to critical stresses satisfied the conditions for Considère criterion. Beyond 250 °C, the brittle cleavage fracture dominant and the surfaces of fracture with some microvoid reveal the transition from brittleness to ductility.

As CL-DC-AC4C-T6 is considered, the dimples are observed in the Fig. 63, therefore, these are evidences that their tensile properties and ductility are better than the semi-solid die casting. In these microscopic, the cracking intermetallic particles are also found in the cavies on the cleavage planes. Apparently, the stress relaxation of Al matrix is dominant which lead the longer ductility and formation of subgrain. At the temperature of 250 °C, it is also the explanation of the work softening like in the semi-solid alloys. It is noted trend from brittle to ductile transition is observed and more cracked intermetallic particles and less micro voids should be reasons for the better tensile properties of CL-DC AC4C Al alloys compared with semi-solid alloys.

The effect of broken Si and intermetallic particles in Al-Si-Mg alloys have been widely studied in some literatures [1, 2, 128, 180] From above, the mode of fractures in both CL-DC and GISS AC4C-T6 alloys during the tensile test is transgranular with quasi-cleavage fracture along grain boundaries.

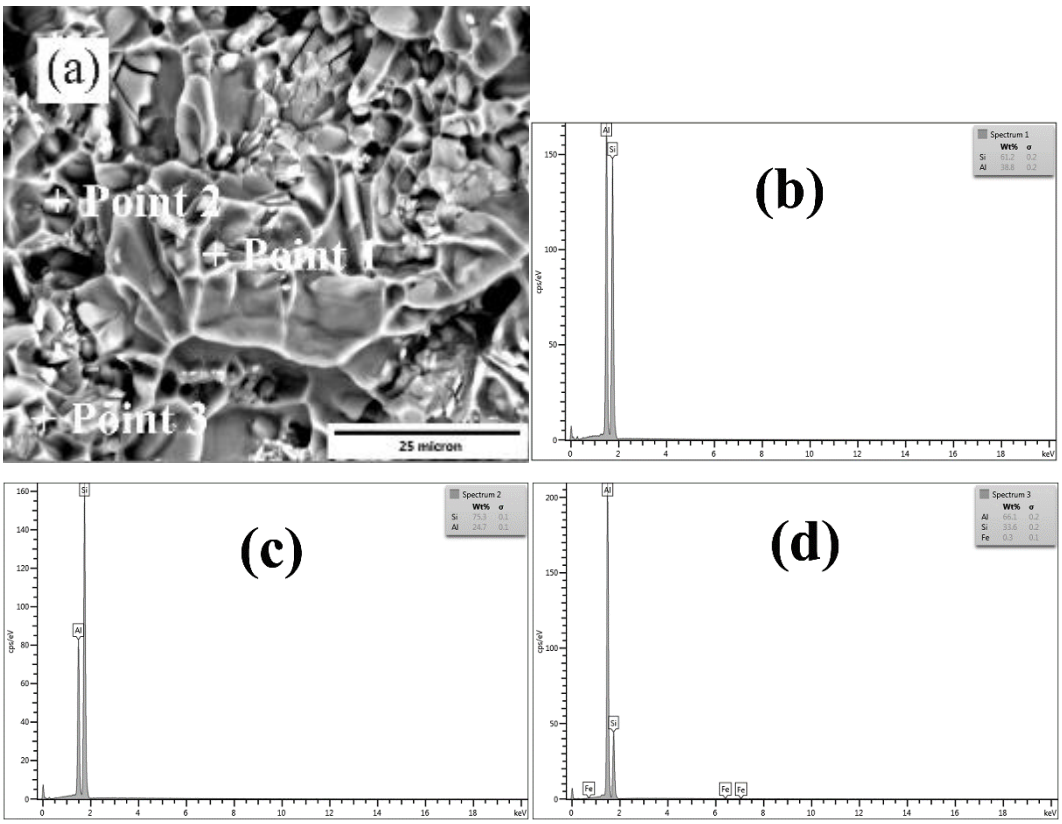

Fig. 61. SEM fractographs of fracture surface of GISS-DC-AC4C-T6 Al alloys show cracking of Si particles and incipient cavitation in the surrounding matrix tested at room temperature and EDX results of the pot scanning of fracture particles. (a) SEM micrograph, (b), (c) and (d) are spectra of EDS point scanning corresponding to point 1, 2 and 3 marked in (a).

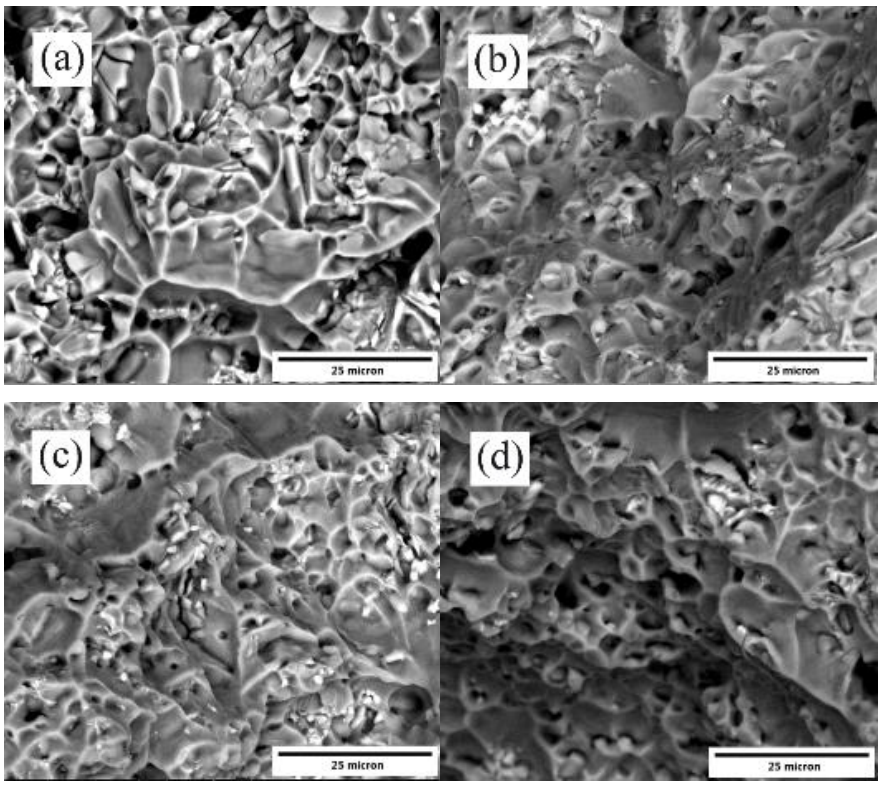

Fig. 62. SEM fractographs of fracture surface of GISS-DC-AC4C-T6 alloy showing cracking of intermetallic particles and incipient cavitation in the surrounding matrix. (a), (b), (c) and (d) corresponding to the specimens are tested at room temperature, 100 °C 175 °C and 250 °C, respectively

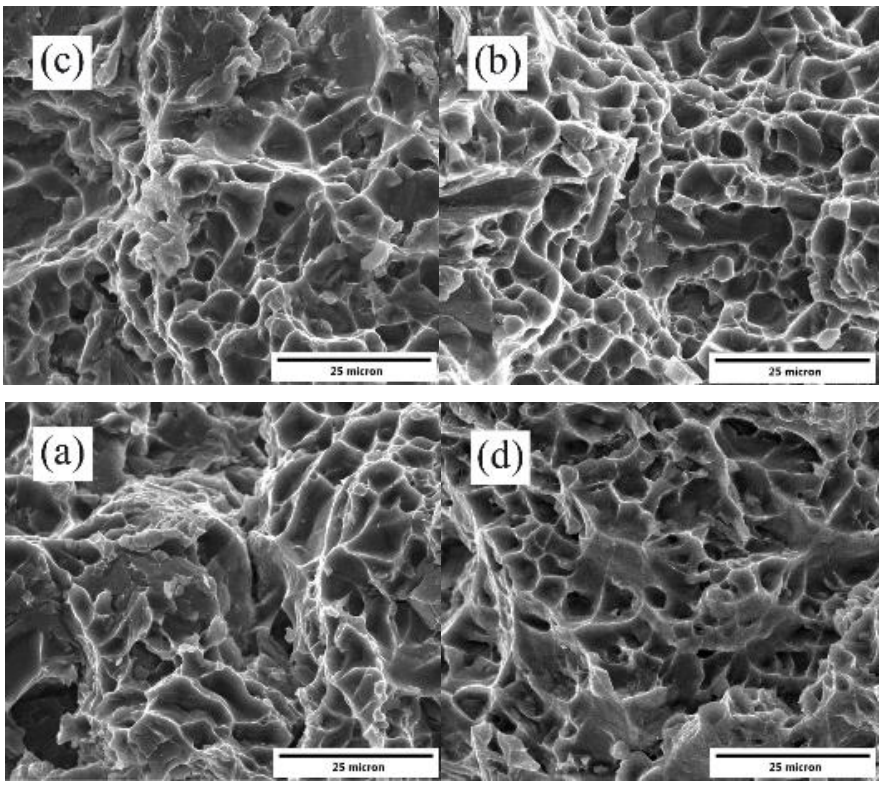

Fig. 63. SEM fractographs of fracture surface of CL-DC-AC4C-T6 alloy showing cracking of intermetallic particles and incipient cavitation in the surrounding matrix. (a), (b), (c) and (d) corresponding to the specimens are tested at room temperature, 100 °C 175 °C and 250 °C, respectively.

4.4.3 Conclusions

The semi-solid die cast AC4C Al alloys were in investigated in this work which focus on the temperatures on the tensile properties and the result was as follows:

1. The spheroidization of eutectic Si occurred after T6 heat treatment and in the as cast GISS-DC and CL-DC AC4C alloys there are some π-Chinese script phase and β phase. But after T6 heat treatment, only β phase can be found in the GISS-T6 and CL-DC-AC4C-T6 Al alloys. In both of the GISS and CL-DC AC4C Al alloys the Mg percentages increase after T6 heat treatment. The Si percentages in CL-DC AC4C Al alloys increased after T6 heat treatment, however, the Si percentages in GISS-DC AC4C Al alloys decreased after T6 heat treatment.

2. In SSM AC4C Alloy conducted by GISS-T6 compared with CL-DC-AC4C-T6 Alloy, it was found that the tensile properties such as UTS, YS and ductility

of GISS-T6 and CL-DC-AC4C-T6 alloys were decreased with increasing of temperatures.

3. At room temperature, the SSM alloy die cast-T6 gained the UTS and YS of 300.9 MPa and 244.5 MPa.The UTS of GISS-T6 AC4C alloys was higher than that of sand cast-T6. The elongation of AC4C alloys was lower than that of A356 on account of Fe particles. The critical strain and ductility of GISS-T6 AC4C alloys was lower than that of others of A356 on account of Fe too. The cracking of intermetallic particles including Si could controlled the failure due to fractures surface observations of the die cast semi-solid AC4C alloys.At temperatures of 25, 100 and 175, the semi-solid AC4C alloy after T6 is brittle to fracture before reaching the maximum calculated by the Considère criterion. The work hardening of semi-solid AC4C is revealed by the curve of n vs. strains, n decreased with the increasing strain. When the necking occurs, n tend to zero. N at 250, can decrease to negative value before necking occurs, due to the superplastic.

4. The microstructures of GISS-T6 compared with CL-DC-T AC4C Alloy showed the different distribution of Si particles and intermetallic particles in different temperatures. The fractographs of these alloys showed that the fracture changed from brittle to ductile behavior with the temperature increasing. At 250, the work softening was observed and ductile due to typical dimple ductile fracture surface of the AC4C alloys. The trend from brittle to ductile transition is observed in both groups' alloys and more cracked intermetallic particles and less microvoids should be responsible for the better tensile properties of CL-DC AC4C Al alloys compared with semi-solid alloys.

4.5 Power law creep behavior after T6

The microstructure and creep behavior of semi-solid AC4C Al alloy produced by the Gas Induced Semi-Solid (GISS) die casting process were investigated at temperature range of 300-360°C and pressures range of 20-40 MPa and compared with the conventional liquid die casting (CL-DC) one after T6 heat treatment. The general trend the strain of steady-state stage of both alloys increases with increasing stress and decreasing temperature. The creep exponents (n) and apparent activity energy

(Qc) of the GISS-DC-T6 and CL-DC-T6 were evaluated. Using the effect stress, n of the CL-DC are about 3.95, 3.66 and 4.94 and 3.52, 4.82 and 5.74 of GISS at 300°C, 330°C and 360°C. Therefore, the mechanism of both alloys was the dislocation glide and climb controlled. Qc increased with the increased pressures in both of CL-DC and GISS-DC AC4C Al alloy after T6 heat treatment. The fracture of creep of both alloys also were studied.

4.5.1 Creep behavior

In constant stress creep curves, the plasticity of GISS-DC AC4C-T6 and CL-DC AC4C-T6 at 300 °C, 330 °C and 360 °C is described under constant stress shown in Fig. 64. The three aspects require some explanations, which delineated three regions, such as Stage I, or primary creep; Stage II, or steady state; Stage III or tertiary creep in Fig. 64, which were class M alloys that have similar creep behavior as pure metals.

First, in Stage I, or primary creep, the creep-rate (plastic strain-rate) is changing with increasing plastic strain and creep time. In Fig. 64, the creep-rate in Stage I decreases with increasing strain. The creep-rate decreases to a constant value over a range of strain, whose area is termed Stage II, secondary, or steady-state creep. Eventually, cavitation and cracking increase the apparent creep-rate. This regime is Stage III, or tertiary creep, and finally leads to fracture.

The rupture time of GISS-DC AC4C-T6 and CL-DC AC4C-T6 decrease with the increase of pressures, however, the elongation changes of GISS-DC AC4C-T6 and CL-DC AC4C-T6 are not regular with the increase of pressures. The rupture time of GISS-DC AC4C-T6 and CL-DC AC4C-T6 decrease with the increase of temperatures, however, the elongation changes of GISS-DC AC4C-T6 and CL-DC AC4C-T6 are not regular with the increase of temperatures, also.

In Fig. 65 reveals that the relationship minimum creep rate and rupture time is linear as the empirical Monkman-Grant relationship to help to predict the service life of materials. Therefore, we focus on the steady state creep rate subsequently. Table 13 shows the general trend the strain of steady-state stage of both alloys increases with increasing stress and decreasing temperature.

It is noted that the curve of the creep stain with normalized time in Fig.

66 (a) and (b) and Fig. 67 (a) and (b) in both alloys show that the stage I is same and the stage III becomes longer with increased stress. In Fig. 66 (c) and (d) and Fig. 67 (c) and (d) show the changes in creep strain rate as normalized time increased, so in tension, a secondary or steady state stage rarely exists in alloys [152] . The minimum creep rate increased with the increased pressures and temperatures, which show in both semi-solid GISS-DC AC4C-T6 and CL-DC AC4C-T6 Al alloys. This same trend was observed in the Table 13 using the traditional mathematic method. The creep curves revealed that 'creep' would be more pronounced at higher temperatures, and less obvious at lower temperatures, since, as will be shown subsequently, work hardening generally diminishes with increasing temperature.

The creep stress exponents of the GISS-DC AC4C-T6 and CL-DC AC4C-T6 are showed in the Fig. 68, respectively. The creep stress exponents of GISS-DC AC4C-T6 alloys are 6.93, 6.81 and 8.63 at temperature of 300 °C, 330 °C and 360 °C. The creep stress exponents of CL-DC AC4C-T6 alloys are 6.96, 9.44 and 11.38 at temperature of 300 °C, 330 °C and 360 °C.

Using the power law, for the secondary stage, the apparent activation energy for creep, Q_c, was derived in the Fig. 69. The apparent activation energy for creeps is extremely higher than the pure Al self-diffusion energy 143 KJ/mol [189] . These results are same as others [15, 190] , these suggested the creep is dislocation climb controlled, but Q_c corresponds to the activation energy for dislocation-pipe diffusion. This reveals that creep of not a diffusion-controlled process, but is controlled by an Orowan bowing process of deformation-controlled process. At 20 MPa, the minimum creep rate of GISS-DC AC4C-T6 is lower than CL-DC AC4C-T6 and the rupture time of GISS-DC AC4C-T6 is longer than CL-DC AC4C-T6, and at 30 and 40 MPa, the minimum creep rate of GISS-DC AC4C-T6 is higher than CL-DC AC4C-T6 and and the rupture time of GISS-DC AC4C-T6 is longer than CL-DC AC4C-T6 in Fig. 66 and Table 13. However, the fracture strain of GISS-DC AC4C-T6 is shorter than CL-DC AC4C-T6 under 20 MPa and 30 MPa, and longer under 40 MPa.

In Fig. 69 showed the apparent activity energy of creep in the GISS-DC AC4C-T6 and CL-DC AC4C-T6 that were calculated by using the power law equation. It is revealed that the activity energy of creep increased with the increased pressures in both of CL-DC and GISS-DC AC4C Al alloy after T6 heat treatment which result like

some literature [15, 190]. According the power law relationship, the activity energy of creep should be constant at above 0.5 T_m temperatures and equal to self-diffusion energy.

CL-DC and of GISS-DC are particle-hardening Al alloys and creep exponent values of them are higher than the stress exponent in pure aluminum (≈ 4.5). The equation (5) is used. Fig. 70 shown plotting the $\dot{\varepsilon}^{1/4.5}$ vs σ of (a) CL-DC and GISS-DC at temperature of 300 °C, 330 °C and 360 °C. The threshold stress, σ_{th} can be calculated by extrapolating linearly to zero creep rate to get as in Fig. 70. The σ_{th} of CL-DC are 12.61 MPa, 11.21 MPa, and 12.57 MPa and the σ_{th} of GISS-DC 11.49 MPa,, 15.77 MPa and 17.70 MPa at temperature of 300 °C, 330 °C and 360 °C, separately.

The new stress exponent, n of CL-DC and GISS-DC can be calculated again shown in Fig. 71. The stress exponents of the CL-DC are about 3.95, 3.66 and 4.94 and 3.52, 4.82 and 5.74 for GISS at temperature of 300 °C, 330 °C and 360 °C. These n values are close to the stress exponent of dislocation glide and climb mechanism in the metal alloy class M or pure aluminum. It is noted that during the creep test it actually is approximately constant stress tensile creep. Therefore, the trend of the effect of temperature and pressures is not as if that is expected.

For pure aluminum, the creep exponent n is 4.5 and for most metals and Class M alloys the creep exponent n is 5, hence these creep is always called ‘five-power' creep or steady state creep at about 0.5 T_m. However, our creep behavior is very like M alloys, and the exponent of creep creep exponent n=5 or closely 5, it is now widely accepted that the activation energy is equal to that of lattice self-diffusion (D_{sd}) , or Q_c = D_{sd}, which actually is not consensus judgment, however, the AC4C alloys is the particle-hardening alloys, so the apparent activity energy is higher than pure Al self-diffusion energy. So, most of the researcher has suggested that the creep mechanism is dislocation climb mechanism [23, 191], some strongly showed the dislocation glide mechanical controlled [14] But others suggest apparent activation energy may be about the activation energy for dislocation-pipe diffusion [19, 20, 192]. Deformation forms the vacancy supersaturation, which will help to explain these changes associated with moving dislocations with jogs. Therefore, this still be dislocation and glide climb control.

Table 13 Creep stresses and minimum creep rates of GISS-DC AC4C-T6 and CL-DC AC4C-T6 (N.R. = no rupture)

Temperature (°C)	Stress (MPa)	Average minimum creep rate (s-1)				Average time to rupture (s)			
		CLC		GISS		CLC		GISS	
300	20	1.10E-08	1.12E-08	6.96E-09	6.55E-09	N.R.	N.R.	N.R.	N.R.
	30	6.48E-08	8.06E-08	5.80E-08	3.67E-08	176820	131403	151319	266725
	40	7.35E-07	1.97E-06	7.56E-07	1.16E-06	13417	7280	3812	9033
330	20	8.78E-08	1.33E-07	6.85E-08	1.35E-07	104246	73379	115656	58005
	30	1.05E-06	8.09E-07	3.70E-06	5.80E-07	18772	15965	3188	17027
	40	7.93E-06	2.16E-05	8.85E-05	6.62E-05	1634	765	176	250
360	20	4.62E-07	4.33E-07	2.89E-07	3.43E-07	11965	21547	17408	14445
	30	4.28E-06	1.31E-04	7.57E-06	2.09E-05	3133	130	2656	142
	40	2.80E-04	1.12E-08	6.96E-09	6.55E-09	62	179	16	43

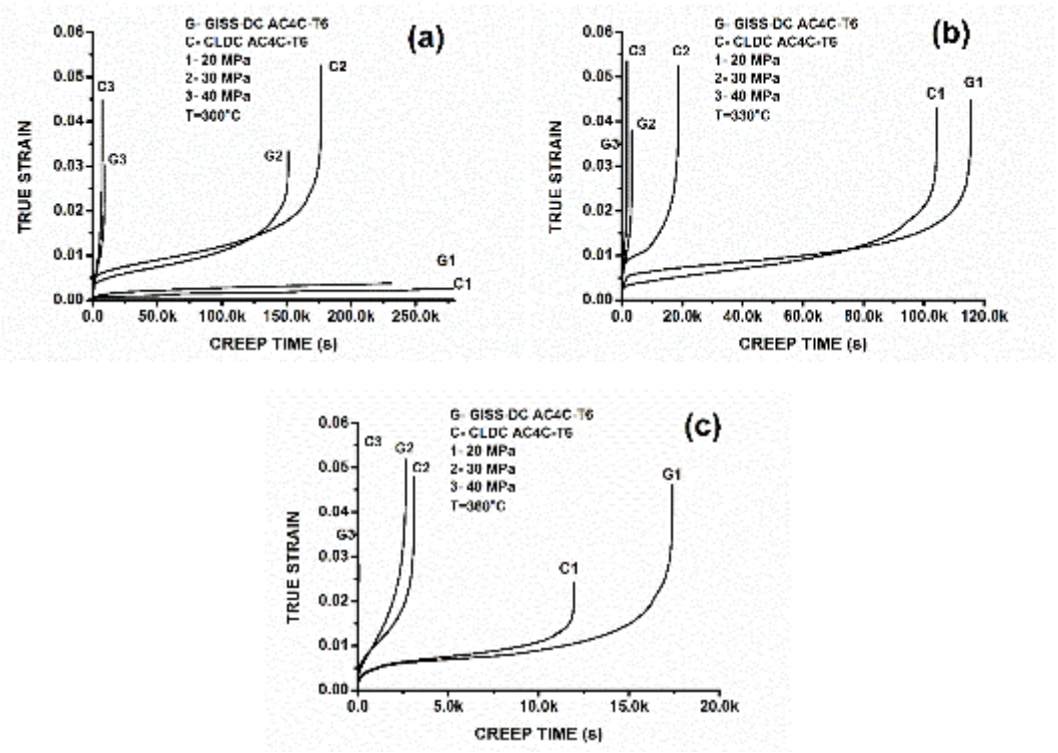

Fig. 64. Creep curves of the GISS-DC and CL-DC AC4C Al alloys after T6 heat treatment at (a) 300 °C, (b) 330 °C and (c) 360 °C.

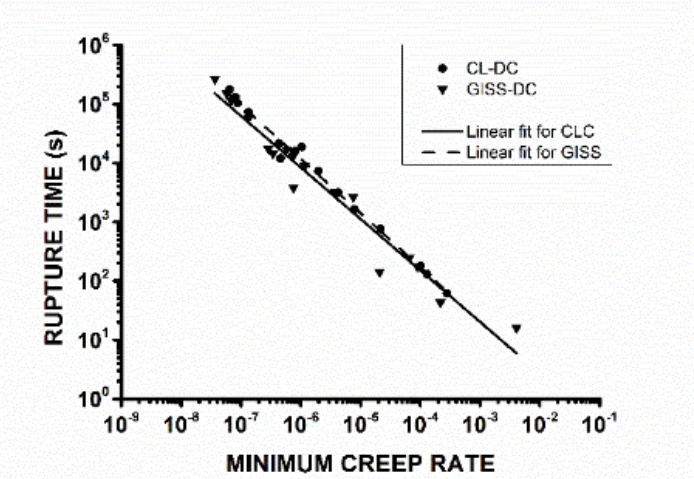

Fig. 65. Minimum creep rate versus rupture time for GISS-DC and CL-DC AC4CAl alloys.

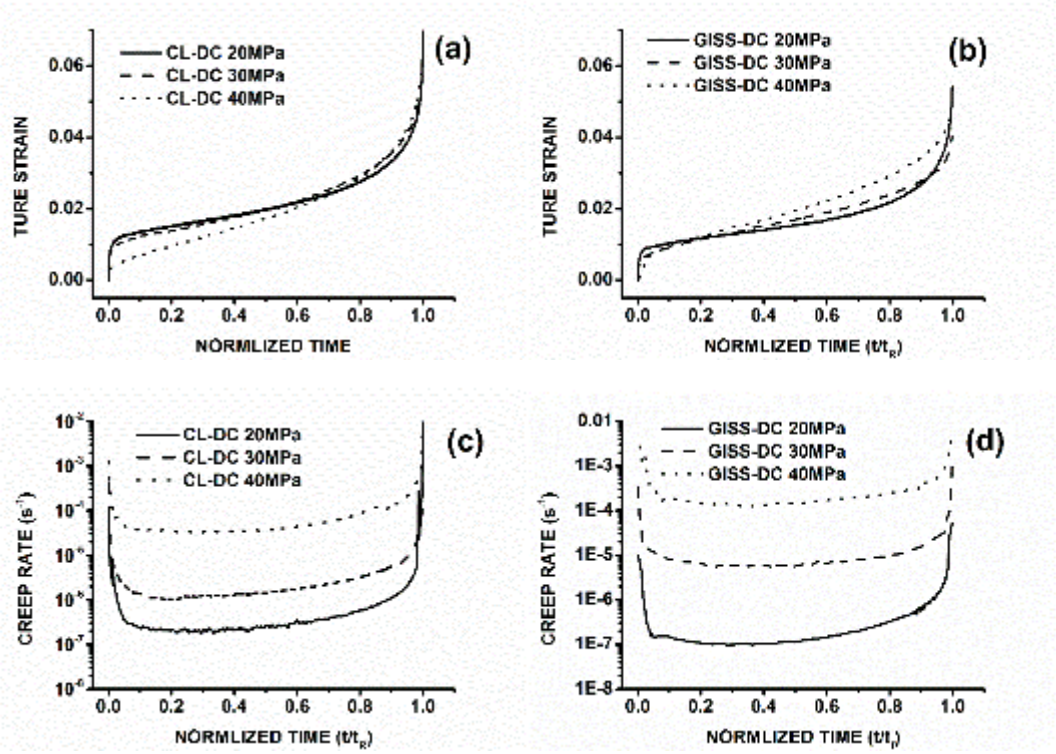

Fig. 66. The variations of pressures (20 MPa, 30 MPa and 40 MPa): the creep strain with normalized time of (a) CL-DC and (b) GISS-DC AC4C Al alloy and the creep strain rate with normalized time of (c) CL-DC and GISS-DC (d) AC4C Al alloy at 330 °C.

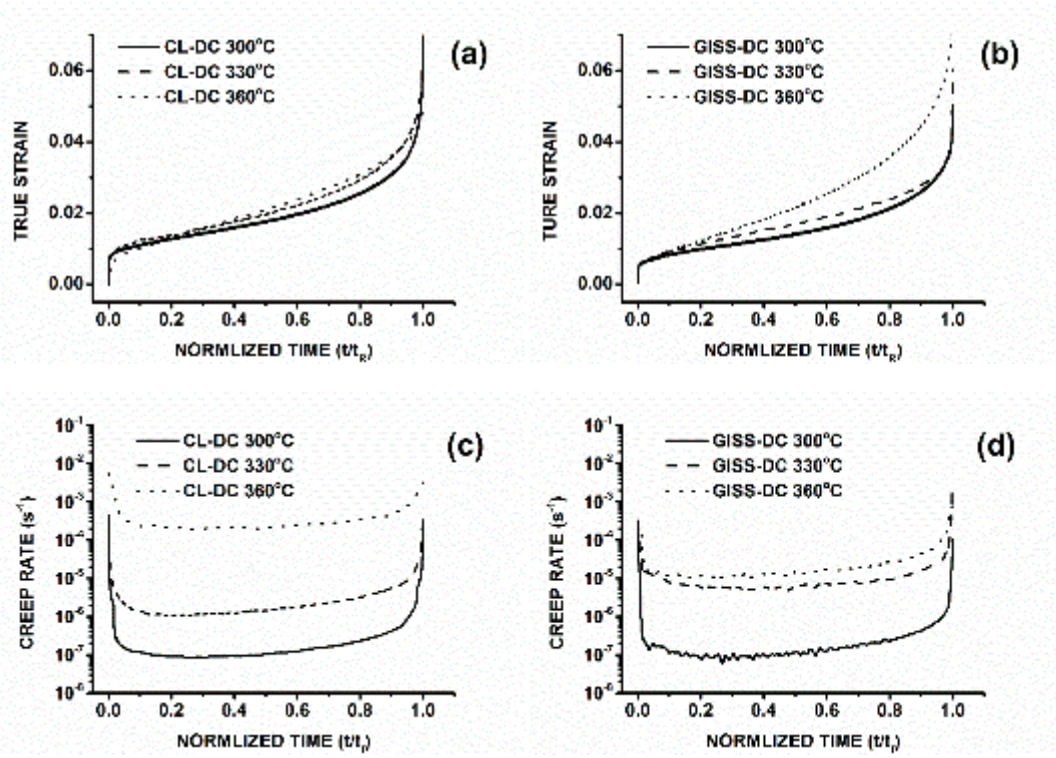

Fig. 67. The variations of pressures (300 °C, 330 °C and 360 °C): the creep strain with normalized time of (a) CL-DC and (b) GISS-DC AC4C Al alloy and the creep strain rate with normalized time of (c) CL-DC and GISS-DC (d) AC4C Al alloy at 30 MPa.

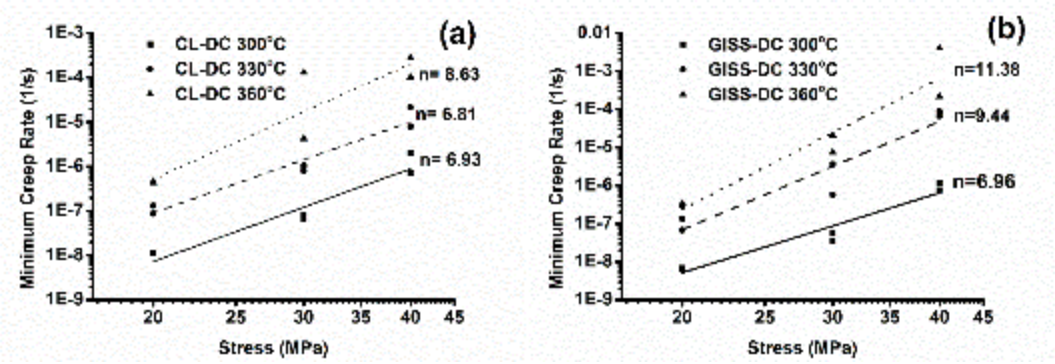

Fig. 68. Minimum creep rate versus stress of (a) CL-DC and (b) GISS-DC AC4C Al alloys, at temperature of 300 °C, 330 °C and 360 °C.

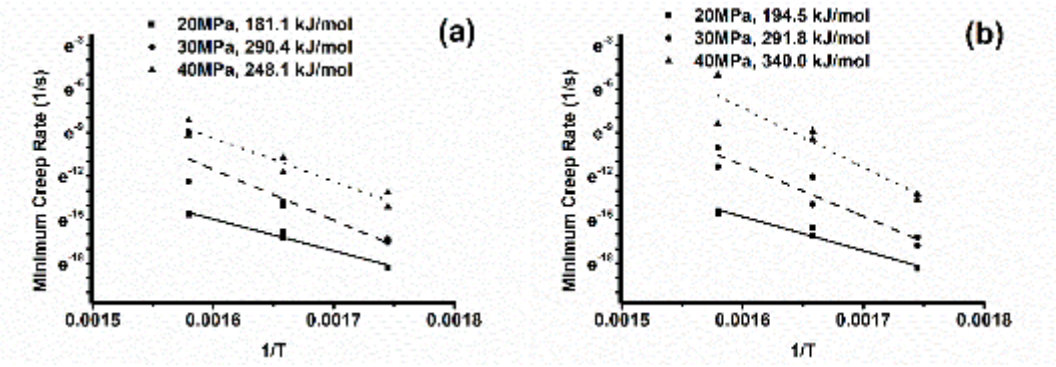

Fig. 69. Minimum creep rate versus temperature of (a) CL-DC and (b) GISS-DC AC4C Al alloy at stresses of 20, 30 and 40 MPa.

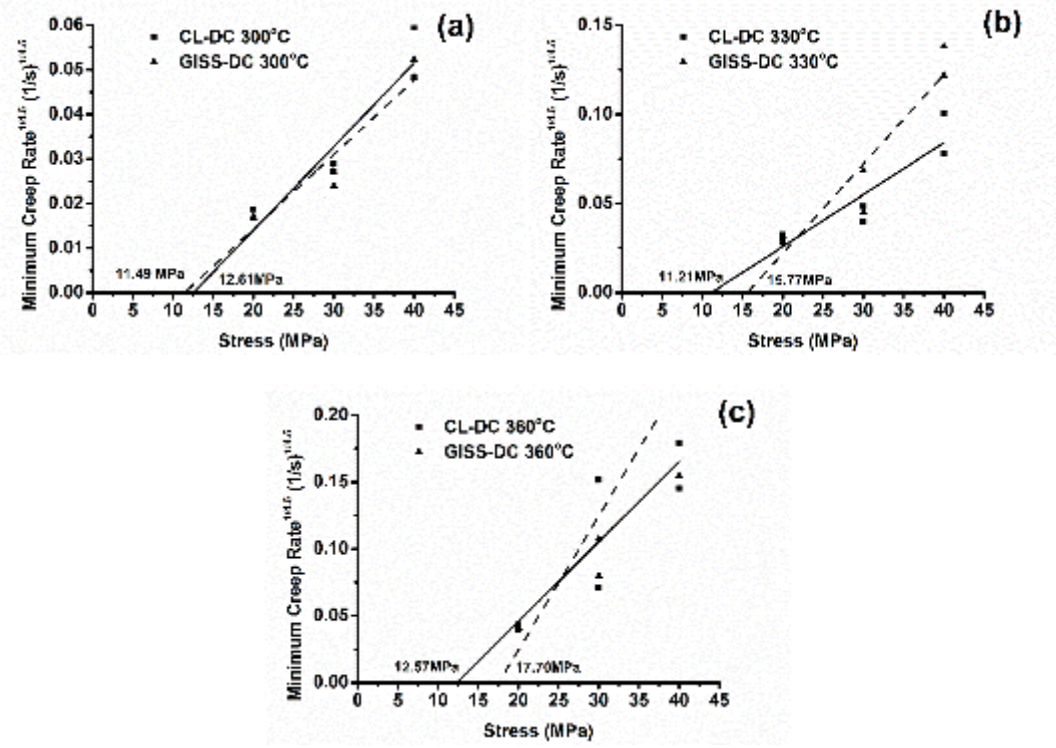

Fig. 70. Minimum creep rate$^{1/4.5}$ versus stress of CL-DC and GISS-DC AC4C Al alloy at (a) 300 °C, (b) 330 °C and (c) 360 °C.

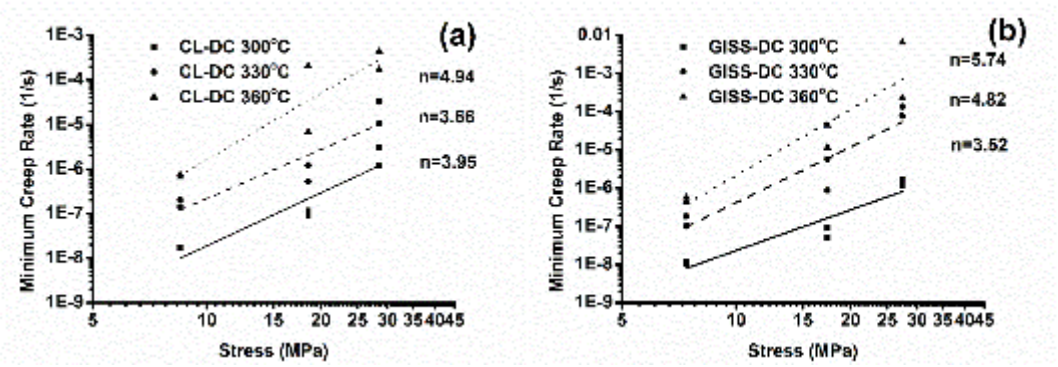

Fig. 71. Minimum creep rate versus stress of (a) CL-DC and (b) GISS-DC AC4C Al alloys, at 300 °C, 330 °C and 360 °C.

4.5.2 Rupture of creep

Fig. 72 shows SEM of rupture surface of both alloys at stress of 20 MPa and the temperature of 360 °C. In the rupture surface of CL-DC, a clearly brittle fracture and the quasi-cleavage feature can be observed and in the rupture surface of GISS, the dimple-like fracture surfaces reveal the ductile characteristics of the samples due to the micronecks of primary aluminum grain. Both of alloys have the clearly visible tear ridges. The GISS-DC AC4C-T6 Al alloy ruptured in more ductile than the fracture surface of the CL-DC AC4C-T6 Al alloy. Fig. 73 and Fig. 74 show OM and SEM of sections of both alloys after creep rupture at stress of 20 MPa and the temperature of 360 °C. Fig. 73 shows that the primary grain of the both is orientation and elongates along paralleled with the stress direction. And the schematic illustration is shown in the Fig. 75 [193]. Some strong evidences in Fig. 73 and 74 to support this mechanism. So the crack or no crack particles can find in the above fracture surfaces of both alloys and the dimple-like surfaces are the main feature of both alloys. The longitudinal sections surface reveal the cavitation mechanical controlled, which the micropores firstly form and grew sometimes with the crack particles or second phases, then the crack between micropores formed and connected the micropore to be a big cave, at last the rupture carried out. Therefore, some crack particles or secondary phase found and the micropores with or without the cracked particles found. The crack between the micropores is found in the longitudinal sections surface of the both alloys.

Element mapping of the rupture surface for the GISS-DC AC4C-T6 Al alloy shows the dimple-like areas are seen in Fig. 76. In contrast, the fracture surface is the clearly brittle fracture and the quasi-cleavage feature in the CL-DC AC4C-T6 Al alloy, as noted in Fig. 77. In the Al alloys, silicon is added to increase the hardness, for improving wear resistance and castability. However, the rupture of silicon particles damages the formability of these alloys. Some rich Si particles are found in tear ridges in the GISS-DC AC4C-T6 Al alloy, the crack particles are rich Si and Fe in the caves of the CL-DC AC4C-T6 Al alloy. These particles were found by point scanning also. The primary silicon particles can be important to the creep fracture. The shape of Si is the round particles which can generate after the T6 heat treatment, so the materials show more ductility after T6 heat treatment.

Fig. 78 show the ductility of GISS-DC decreased with the increase of pressure. The fracture surfaces are simple-like at three pressures at 330 °C. However, Fig. 79 show the ductility of GISS-DC increased and then decreased with increase of temperature at 30 MPa. 330 °C and 300 °C, the fracture surface is dimple like which is ductility, but at 360 °C the fracture surface is brittle and like the quasi-cleavage feature. In tertiary creep, the strain and strain rate increase until fracture occurs. Entering into this stage occurs when there is a reduction in cross-sectional area due to necking or due to internal void formation. Void formation effectively causes a reduction in area. Thus, tertiary creep is important in engineering, because it is often associated with the formation of structural instability, as indicated by voids, crack formation and necking, leading to failure by fracture.

From the OM of AC4C Al alloys after creep in Fig. 80 which shows the OM fracture surfaces on longitudinal sections of AC4C Al alloys. The main crack crossed some dendritic eutectic regions, which are parallel to the main crack profile, the direction of creep is the orientation direction of the primary Al phases which grow longer. During the creep test, the big primary phase may become longer and sometime will be broke. Therefore, the new secondary phase occurred. Moreover, the OM fractography reveal that the crack is observed along the grain boundary and is stopped by the eutectic particles or clusters. There are three parts during the damage process: particle cracking and deboning, micro crack formation and growth in the cracking and debonding particles, and local linkage of microcracks. The cave is found near the

fracture surface. Finally, the cavitation and cracking lead to the fracture of creep test.

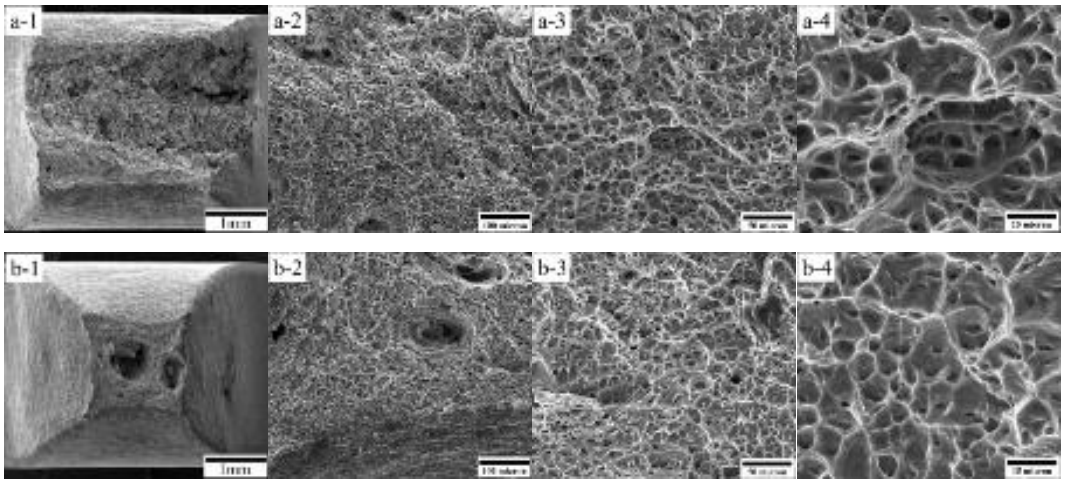

Fig. 72. Rupture surface for the (a) CL-DC and the GISS-DC (b) AC4C Al alloy at 20 MPa and 360 °C.

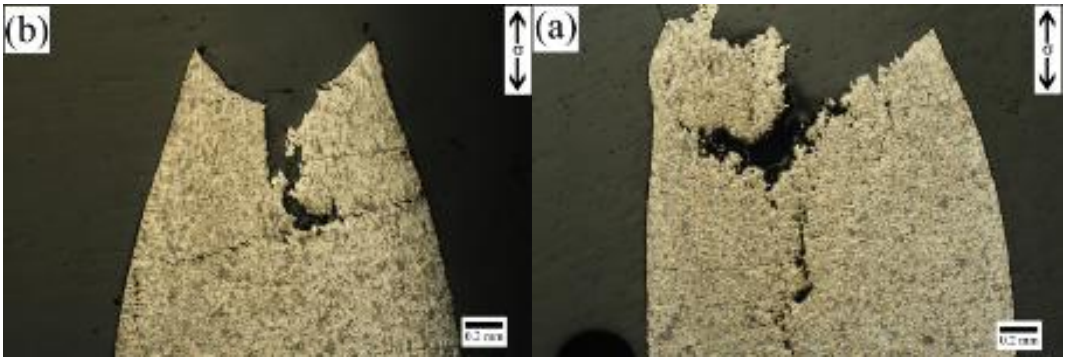

Fig. 73. OM microstructures of (a) the CL-DC and (b) the GISS-DC AC4C Al alloy longitudinal sections specimens after creep tests at 20 MPa and 360 °C.

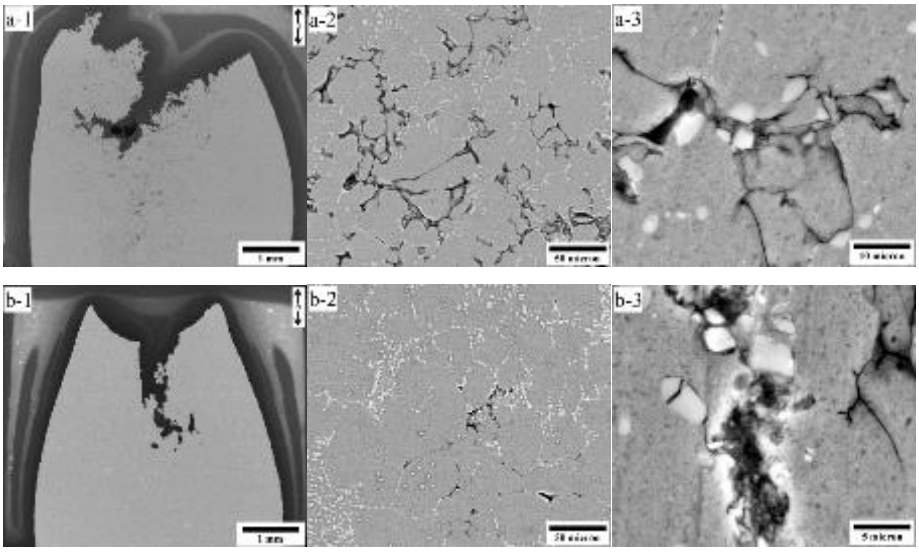

Fig. 74. SEM microstructures of (a) the CL-DC and (b) the GISS-DC AC4C Al alloy longitudinal sections specimens after creep tests at 20 MPa and 360 °C.

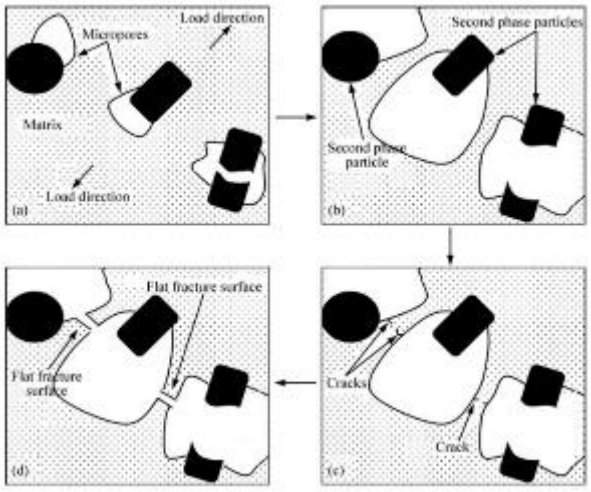

Fig. 75. Schematic illustration of longitudinal sections fracture mechanism of alloy at creep temperature of the CL-DC AC4C-T6 Al alloy and the GISS-DC AC4C-T6 Al alloy: (a) Formation of micropores; (b) Growth of micropores; (c) Formation of cracks between micropores; (d) Rupture[193].

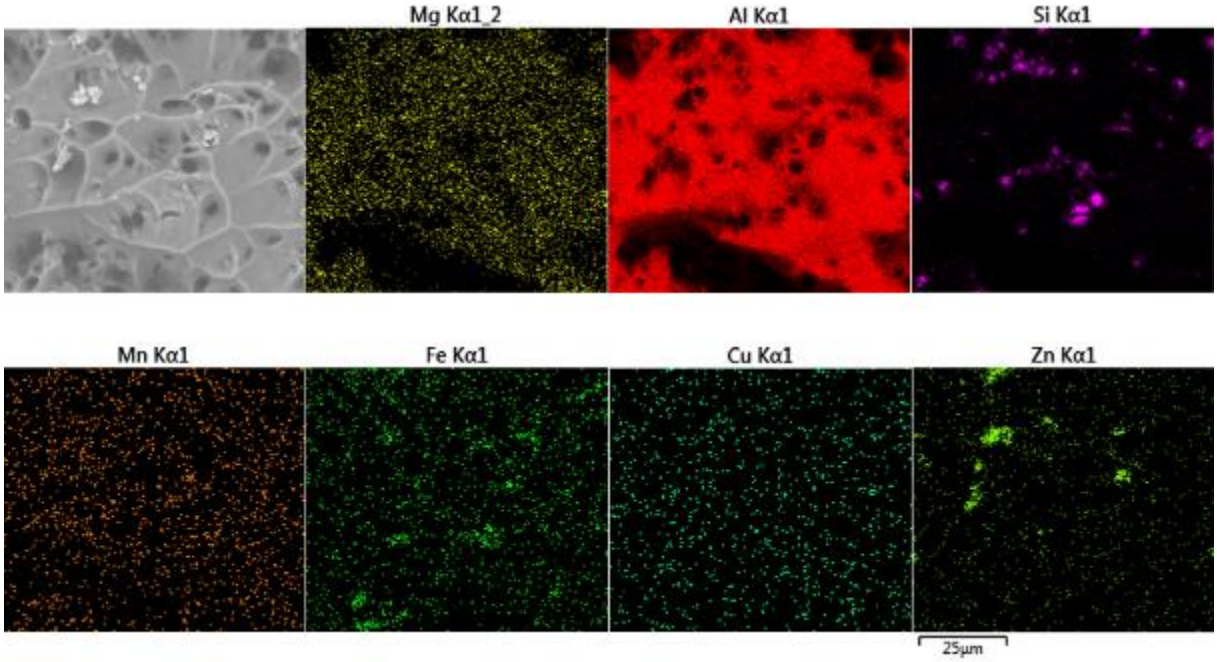

Fig. 76. The rupture surface element mapping of GISS-DC AC4C Al alloy at 20 MPa and 360 °C.

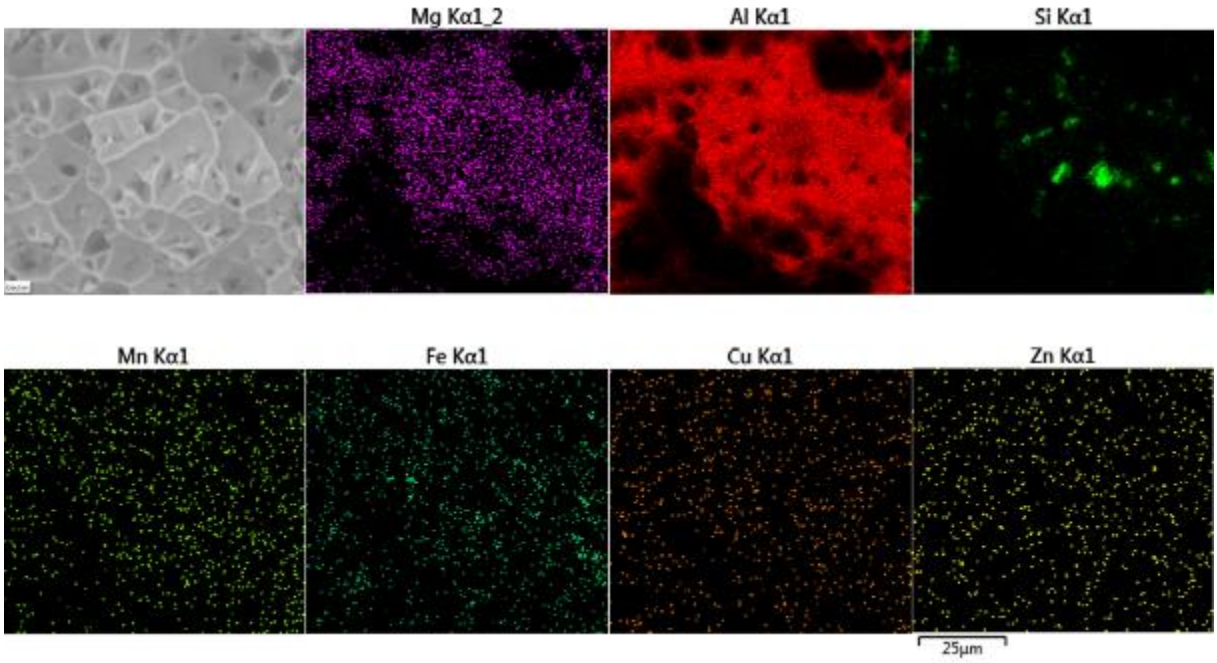

Fig. 77. The rupture surface element mapping of DC-DC AC4C Al alloy at 20 MPa and 360 °C.

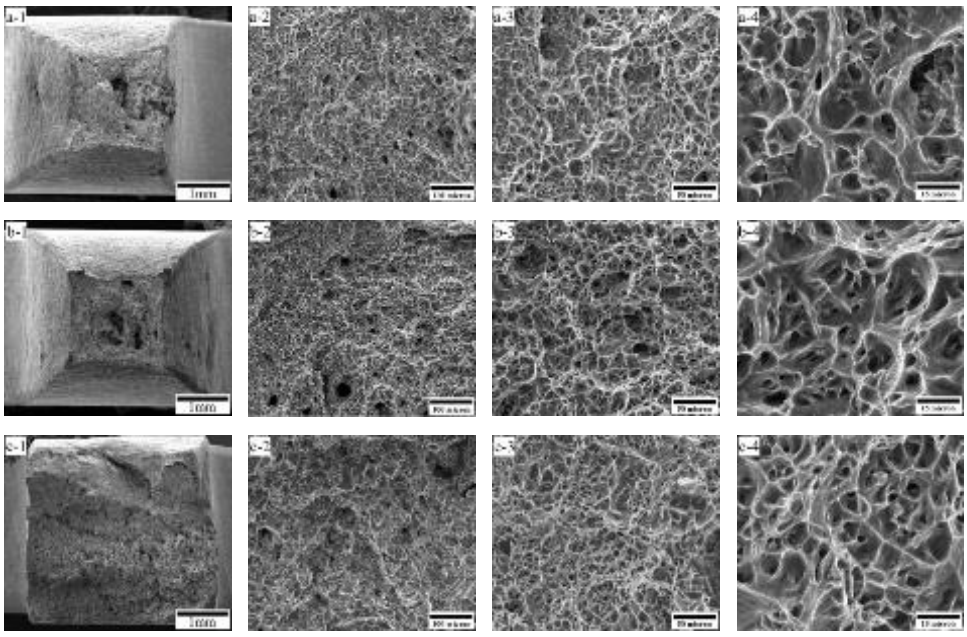

Fig. 78. Rupture surface of GISS-DC AC4C Al alloy at (a) 20 MPa, (b) 30 MPa and (c) 40 MPa and 330 °C.

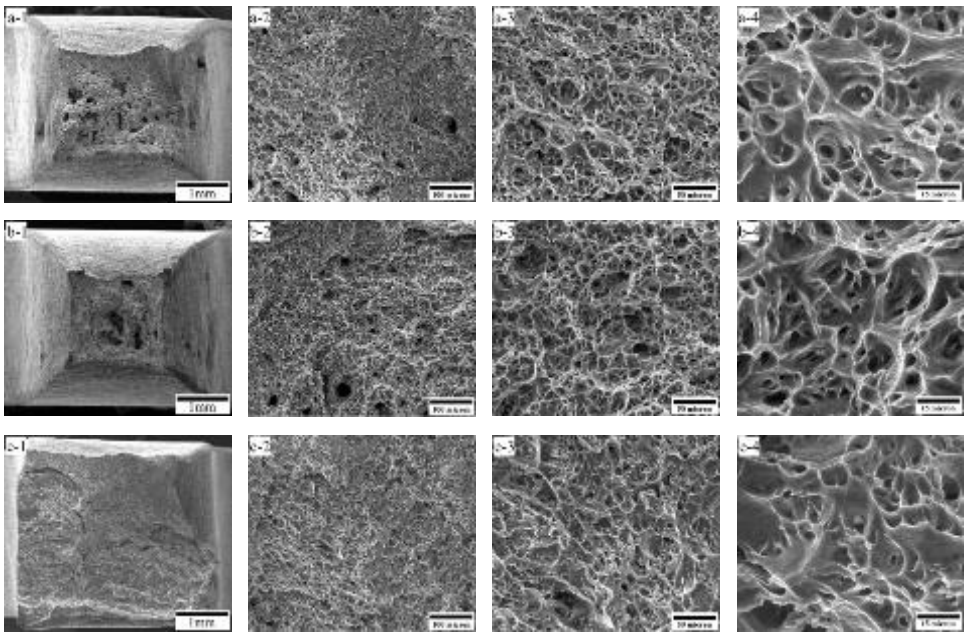

Fig. 79. Rupture surface of the GISS-DC AC4C-T6 Al alloy at 30 MPa and (a) 300 °C, (b) 330 °C and (c) 360 °C.

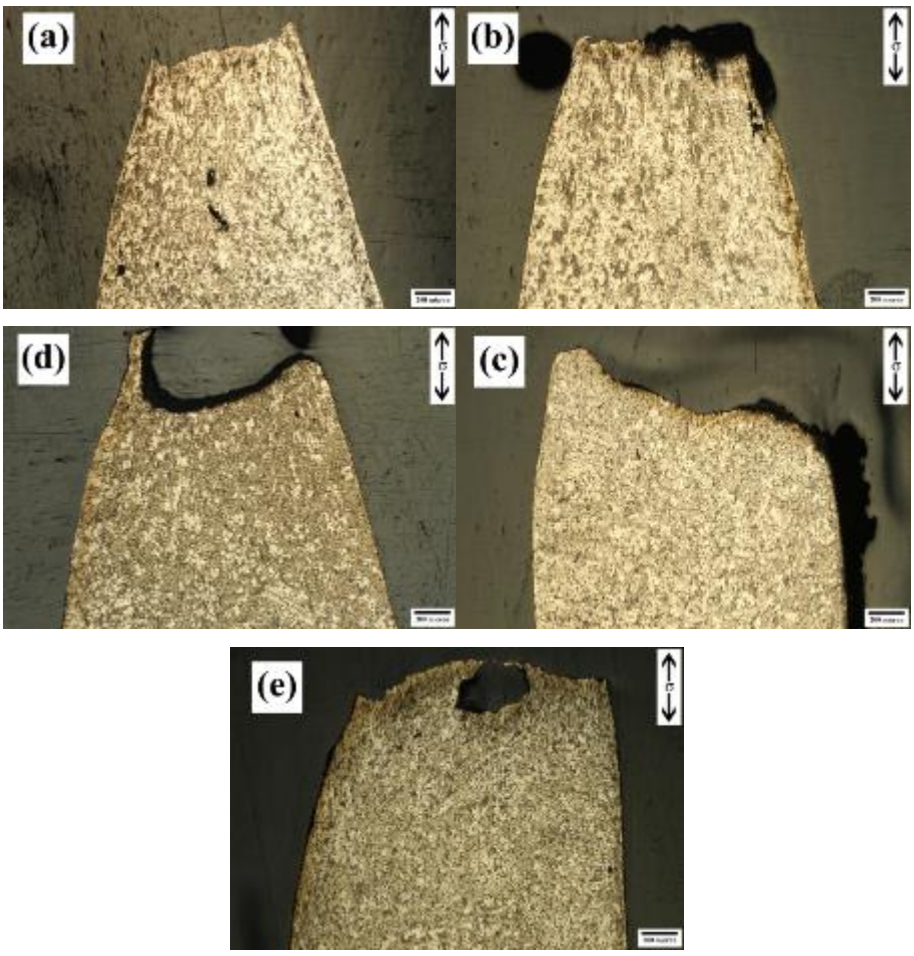

Fig. 80. OM microstructures of specimens after creep tests at (a) 20 MPa, (b) 30 MPa and (c) 40 MPa at 330 °C, (d) 30 MPa at 300 °C and (e) 30 MPa at 360 °C for GISS-DC AC4C. (Note that the direction of applied stress was in the vertical direction of the micrographs.)

4.5.3 Conclusions

The microstructure and creep behavior of semi-solid AC4C Al alloy produced by the Gas Induced Semi-Solid (GISS) die casting process were investigated at temperature range of 300-360 °C and pressures range of 20-40 MPa and compared with the conventional liquid die casting (CL-DC) one after T6 heat treatment. The intermatellic particles of both alloys include a large number of elements: Fe, Mg ang Si after T6 heat treatment. CL-DC-T6 and GISS-DC AC4C alloys have good creep propertity at elevated temperatures. The spheroidization and coarsening of pheutictic Si particles occured after T6 heat treatment and the primary α Al phase in GISS-DC

AC4C alloys which include more rosette morphology are bigger and more round than in CL-DC-AC4C-T6 Al alloys which include more dendritic α (Al) primary phase. The relationship minimum creep rate and rupture time is linear as the empirical Monkman-Grant relationship which proved the good predictive capacity for industrial designers. The creep exponents (n) and apparent activity energy (Q_c) of the GISS-DC-T6 and CL-DC-T6 were evaluated. The stress exponents of the CL-DC are about 3.95, 3.66 and 4.94 at 300 °C, 330 °C and 360 °C. The stress exponents of GISS-DC are 3.52, 4.82 and 5.74 for at 300 °C, 330 °C and 360 °C. These n values are close to the stress exponent of dislocation glide and climb mechanism in the metal alloy class M or pure aluminum. The activity energy of creep increased with the increased pressures in both of CL-DC and GISS-DC AC4C Al alloy after T6 heat treatment. The results reveal both of alloys are the dislocation glide mechanical controlled.

4.6 Theta projection method

Low-temperature creep at or below $0.5T_m$ is believed to be governed by non-diffusion controlled mechanisms, whereas high-temperature creep, above 0.5Tm, is diffusion controlled. Under the constant load, most Al alloys display normal creep strain/time curves at temperature about over 0.5 T_m which are widely considered to have three stages, primary, secondary and tertiary[16]. Steady-state creep is often emphasized over primary or tertiary creep due to the relatively large fraction of creep life within this regime. The importance of steady state is evidenced by the empirical Monkman-Grant relationship [17]:

$$\dot{\varepsilon}_{ss} \times \mathrm{t}_r = \mathrm{k} \tag{34}$$

So, if the empircal MG relationship works very well, then reciprocal of the frature time will be have the relation wih applied stress combining the Power Law relationship, as follow:

$$\dot{\varepsilon} = \frac{\mathrm{d}\varepsilon}{\mathrm{d}t} = \mathrm{A}_1\sigma^n exp - \left({}^{Q_C}/_{RT}\right) \tag{35}$$

$$\frac{1}{\mathrm{t}_r} = \frac{\mathrm{d}\varepsilon}{\mathrm{d}t} = \mathrm{A}_1\sigma^n exp - \left({}^{Q_C}/_{RT}\right) \tag{36}$$

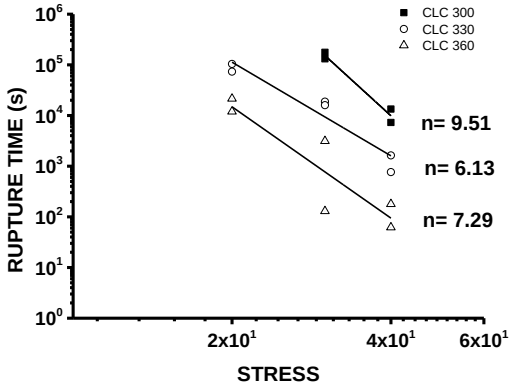

Fig. 81. Rupture time versus applied stress for CL-DC AC4CAl alloys.

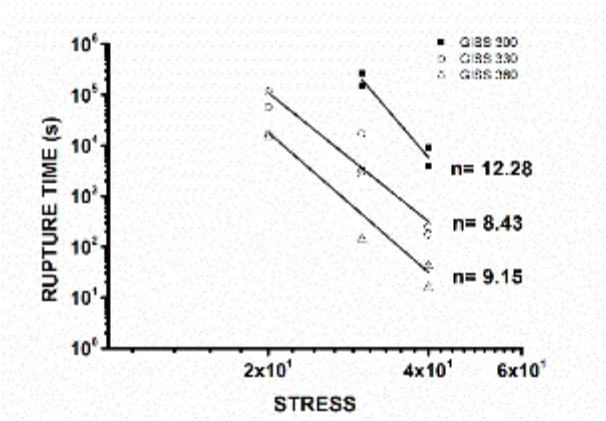

Fig. 82. Rupture time versus applied stress for GISS-DC AC4CAl alloys.

The creep exponents at three temperatures were got from the creep curves at previous work. According the relation above, the creep exponents from the curves of rupture time versus applied stress should be equal to them from the curves of minimum creep rate versus applied stress. However, from Fig 81 and 82, the creep exponents is not equals as in previous work. The different creep exponents at different application were also gotten. If the prediction of long term creep life can work, it is difficult to explain that there are different mechanism in different area of different applied stress and different temperatures. All above, it is reasonable that the theta projection method is used to describe the creep behavior and to predict the long term creep. Because the theta projection method is based on the shape of curve, and most of others methods only focus on the minimum creep rate to predict. In the theta projection method, there are two parts in creep behavior, one is the primary stage and other is tertiary stage, the minimum creep rate is a point of transformation of two stages.

Although, creep curves consist with three parts such as primary stage, secondary stage and tertiary stages. Wilshire and Evans established the θ projection concept to describe the creep behavior according this way. This method has already described the some creep behavior of metals and alloys.

$$\dot{\varepsilon} = \theta_1\left(1 - e^{-\theta_2 t}\right) + \theta_3(e^{\theta_4 t} - 1) \quad (37)$$

$$\theta_1 = G_1 exp H_1(\frac{\sigma}{\sigma_Y}) \quad (38)$$

$$\theta_2 = G_2 exp\left[-\frac{Q - H_2\sigma}{RT}\right] \quad (39)$$

$$\theta_3 = G_3 exp H_3(\frac{\sigma}{\sigma_Y}) \quad (40)$$

$$\theta_4 = G_4 exp\left[-\frac{Q - H_4\sigma}{RT}\right] \quad (41)$$

Where $\dot{\varepsilon}$ is creep strains rate; θ_1 is the primary strain-like parameters, θ_2 is the primary rate constant, θ_3 is the tertiary strain-like parameters, θ_4 is the primary rate constant, G_i and H_i are constants of the alloys, R is the universal gas constant (8.31Jmol-1K-1), T is the creep absolute temperature (K), Q si the activation energy of creep (kJ/mol), σ is applied stress of creep, σ_y is the rapid yield stress at the creep temperatures.

4.6.1 Estimated the yield stress at 573K, 603K and 633K

Because the temperature of our finance limits at no more than 270 °C, the yield stress at temperatures above 270 °C cannot be gotten directly. So, the yield stresses are obtained indirectly. At first, the curve of yield stress and temperatures is drawn in Fig. 83, then the yield stress at high temperatures are gotten by fitting the points and extending to the high temperatures areas. The result is shown in the Table 14.

Table 14 Yield stress at high temperatures

Temperature (K)	20MPa		30MPa		40MPa	
	σy	σ/σy	σy	σ/σy	σ_y	σ/σ_y
573	113.8	0.18	113.8	0.26	113.8	0.35
603	90.2	0.22	90.2	0.33	90.2	0.44
633	65.3	0.31	65.3	0.46	65.3	0.61

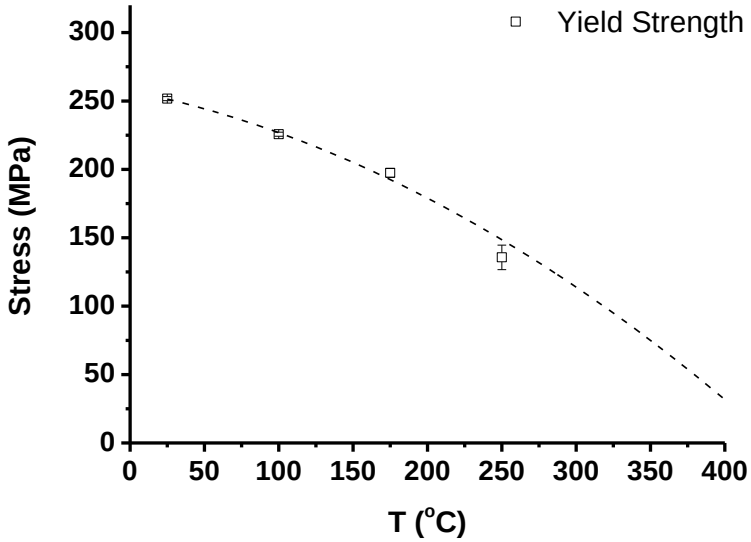

Fig. 83. The YS vs temperautres of semi-solid AC4C alloys

4.6.2 Calculation primary creep constitutive model parameters of semi-solid AC4C alloys

Using the nonlinear least squares fitting method, the value of θ_1 andθ_2 can be gotten. The results of experimental in Table 15. The equation above is taken the natural logarithm, then the equation is gotten.

$$\ln \theta_1 = \ln G_1 + H_1 \times \frac{\sigma}{\sigma_Y} \tag{42}$$

Using above equation, the Table 16 of values of σ/σ_y and ln θ_1 is obtained.. The curve of the relationships of Ln θ_1 and σ/σ_y is obtained too in Fig 84.

$$\ln[\theta_2 \, esp(\frac{Q}{RT})] = \ln G_2 + H_2 \times \frac{\sigma}{RT} \tag{43}$$

Using above equation, the Table 17 of the values of Ln $\theta_2$exp(Q/RT) is obtained The curve of the relationships of Ln θ_1 and σ/σ_y is obtained too in Fig 85. According the Fig. 84 and 85, the constitution equation of primary stage of creep behavior is obtained using the linear least squares. It is noted that the activity energy in

this equation is not the creep activity energy and is associated the primary and tertiary stage to overcome obstacles. The creep activity energy depends on the minimum creep rate and calculated form the minimum creep rate. So, the different activity energy used for the constitution equation establishment.

$$\begin{cases} \varepsilon_1 = \theta_1\left(1 - e^{-\theta_2 t}\right) \\ \theta_1 = e^{[-7.01817+4.8682\times\left(\frac{\sigma}{\sigma_Y}\right)]} \\ 20\ \text{MPa:}\ \theta_2 = e^{\left(57.61773 - \frac{Q}{RT} + \frac{6012.1352\times\sigma}{RT}\right)} \\ 30\ \text{MPa:}\ \theta_2 = e^{\left(73.77114 - \frac{Q}{RT} + \frac{3536.4499\times\sigma}{RT}\right)} \\ 40\ \text{MPa:}\ \theta_2 = e^{\left(96.03709 - \frac{Q}{RT} + \frac{4321.1399\times\sigma}{RT}\right)} \end{cases}$$

Table 15 The values of θ_1 andθ_2

Temperature	20MPa		30MPa		40MPa	
	θ_1	θ_2	θ_1	θ_2	θ_1	θ_2
573	0.00155	0.000130	0.00127	0.00114	0.00298	0.0056
603	0.00858	0.00214	0.00603	0.00433	0.01161	0.09635
633	0.00614	0.00135	0.00663	0.00934	0.01238	0.16847

Table 16 The values of σ/σ_y and ln θ_1

Stress (MPa)	573K		603K		633K	
	σ/σ_y	ln θ_1	σ/σ_y	ln θ_1	σ/σ_y	ln θ_1
20	0.18	-8.20	0.26	-4.83	0.35	-3.49
30	0.22	-6.15	0.33	-4.43	0.44	-2.34
40	0.31	-6.61	0.46	-4.67	0.61	-1.78

Table 17 The values of Ln $\theta_2$exp(Q/RT)

Stress (MPa)	Ln $\theta_2$exp(Q/RT)			
	573K	603K	633K	Average
20	31.88	31.88	31.88	31.88
30	51.43	51.43	51.43	51.43
40	59.42	59.42	59.42	59.42

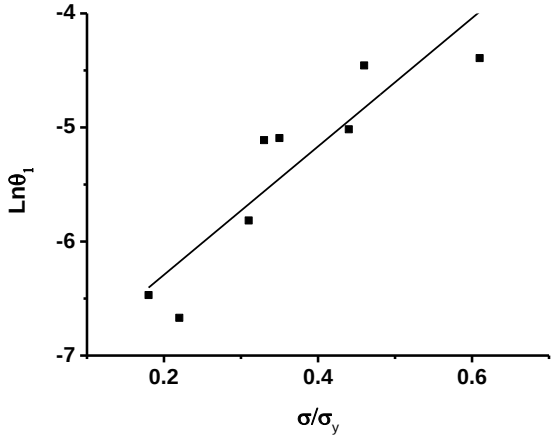

Fig. 84. The relationships of Ln θ_1 and σ/σ_y

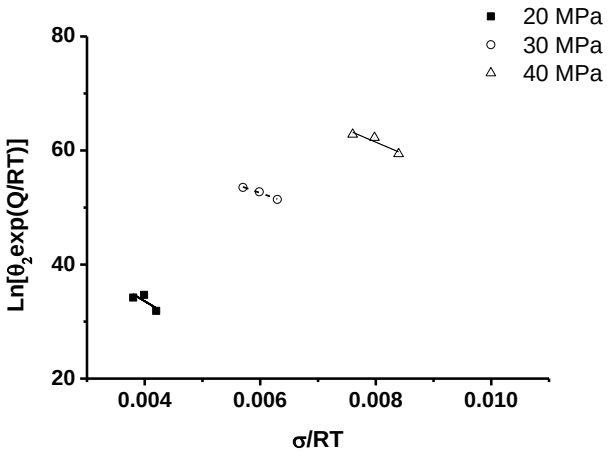

Fig. 85. The relationships of σ/RT and Ln $\theta_2 exp(Q/RT)$

4.6.3 Calculation tertairy creep constitutive model parameters of semi-solid AC4C alloys

Using the nonlinear least squares fitting method, the value of θ_3 andθ_4 can be gotten. The results of experimental in Table 18. The equation above is taken the natural logarithm, then the equation is gotten.

$$\ln \theta_3 = \ln G_3 + H_3 \times \frac{\sigma}{\sigma_Y} \quad (44)$$

Using above equation, the Table 19 of values of σ/σ_y and ln θ_3 is obtained. The curve of the relationships of Ln θ_3 and σ/σ_y is obtained too in Fig. 86. The curve of the relationships of Ln θ_3 and σ/σ_y is obtained too in Fig. 86.

$$\ln[\theta_4\, esp(\frac{Q}{RT})] = \ln G_4 + H_4 \times \frac{\sigma}{RT} \quad (45)$$

Using above equation, the Table 20 of the values of Q and Ln $\theta_4$exp(Q/RT) is obtained. According the Fig. 86 and 87, the constitution equation of primary stage of creep behavior is obtained using the linear least squares. It is noted that the activity energy in this equation is not the creep activity energy and is associated the primary and tertiary stage to overcome obstacles. The creep activity energy depends on the minimum creep rate and calculated form the minimum creep rate. So, the different activity energy used for the constitution equation establishment.

$$\begin{cases} \varepsilon_2 = \theta_3\left(1 - e^{-\theta_4 t}\right) \\ \theta_3 = e^{\left[-10.81094+11.73962\times\left(\frac{\sigma}{\sigma_Y}\right)\right]} \\ 20\text{ MPa: } \theta_4 = e^{\left(68.27662-\frac{Q}{RT}+\frac{-9213.73778\sigma}{RT}\right)} \\ 30\text{ MPa: } \theta_4 = e^{\left(84.24532-\frac{Q}{RT}+\frac{-5563.57074\sigma}{RT}\right)} \\ 40\text{ MPa: } \theta_4 = e^{\left(95.43379-\frac{Q}{RT}+\frac{-4324.33221\sigma}{RT}\right)} \end{cases}$$

Table 18 The values of θ_3 andθ_4

Temperature	20MPa		30MPa		40MPa	
	θ3	θ4	θ3	θ4	θ3	θ4
573			0.00215	0.0000547	0.000319	0.00429
603	0.000821	0.0000907	0.00135	0.00397	0.0044	0.0239
633	0.000788	0.0005178	0.00504	0.00139	0.000669	0.13441

Table 19 The values of σ/σ_y and ln θ_3

Stress (MPa)	573K		603K		633K	
	σ/σy	In θ3	σ/σy	In θ3	σ/σy	In θ3
20	0.18		0.26	-7.10	0.35	-7.15
30	0.22	-6.14	0.33	-6.61	0.44	-5.29
40	0.31	-8.05	0.46	-5.43	0.61	-7.31

Table 20 The values of Ln $\theta_4$exp(Q/RT)

Stress (MPa)	Ln $\theta_2$exp(Q/RT)			
	573K	603K	633K	Average
20		176.72	178.47	177.59
30	273.47	277.75	276.70	275.97
40	325.98	327.70	329.42	327.70

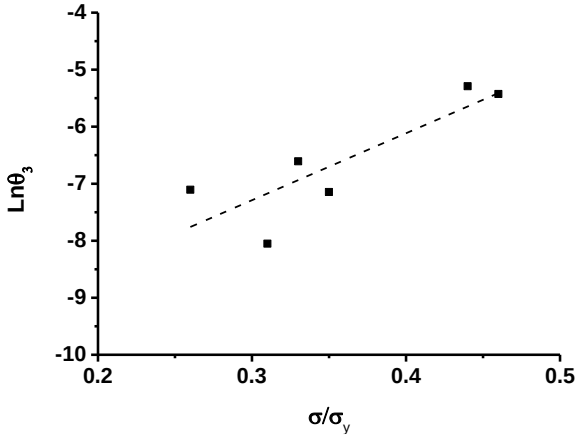

Fig. 86. The relationships of Ln θ_3 and σ/σ_y

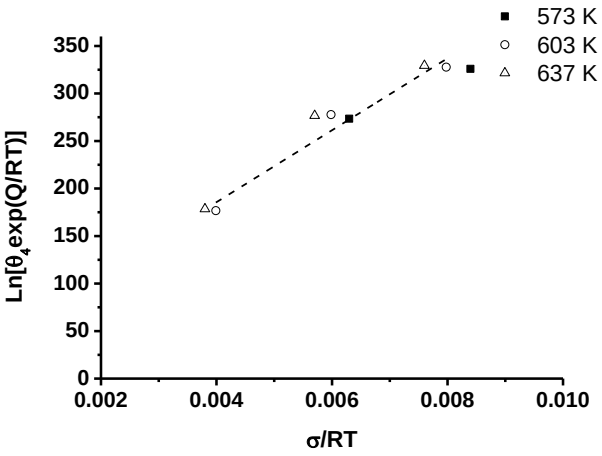

Fig. 87. The relationships of σ/RT and Ln $\theta_4$exp(Q/RT)

From the theta project equation and creep curves in Fig. 88, when the t = 0 at the tertiary stage, that creep rate should be equal to the minimum creep rate. Using the theta project equation, when t = 0, the equation will be changed into:

$$\dot{\varepsilon} = \theta_4\theta_3$$

So:

$$\dot{\varepsilon}_{ss} \cong \theta_4\theta_3$$

The θ_3 and θ_4 will get from the tertiary stage of creep and the minimum creep rates were gotten from the steady stage of creep curves. The Fig. 89 shows the relation of this two values. The data of this value should be linear due to the theta project method, however, the yield stresses come from the prediction and the activity energy

of tertiary is not steady during the tertiary because the states of beginning and rupture from different applied stress and temperature are not similar. The results of these are acceptable.

$$\theta_3 = G_3 exp H_3(\frac{\sigma}{\sigma_Y})$$

$$\theta_4 = G_4 exp\left[-\frac{Q - H_4\left(\frac{\sigma}{\sigma_Y}\right)}{RT}\right]$$

$$\theta_4 \times \theta_3 = G_4 exp\left[-\frac{Q - H_4\left(\frac{\sigma}{\sigma_Y}\right)}{RT}\right] \times G_3 exp H_3(\frac{\sigma}{\sigma_Y})$$

$$\theta_4 \times \theta_3 = G_4 G_3 exp\left[-\frac{Q - H_4\left(\frac{\sigma}{\sigma_Y}\right)}{RT} + H_3(\frac{\sigma}{\sigma_Y})\right]$$

$$ln[\theta_4\theta_3\, esp(\frac{Q}{RT})] = ln(G_4G_3) + \left(\frac{H_4}{RT} + H_4\right) \times (\frac{\sigma}{\sigma_Y})$$

$$ln[\theta_4\theta_3\, esp(\frac{Q}{RT})] = ln(G_4G_3) + \left(\frac{H_4}{RT} + H_4\right) \times (\frac{\sigma}{\sigma_Y})$$

From above formula derivation, the relation between $ln[\theta_4\theta_3\, esp(\frac{Q}{RT})]$ and normal stress should be linear. The relation is shown in Fig. 90. From this figure, this relation is also not linear. The reason of this is same as the relation between θ_3 and θ_4 from the tertiary stage of creep and the minimum creep rates from the steady stage.

$$\dot{\varepsilon}_{ss} \times t_r = k$$

$$\dot{\varepsilon}_{ss} \cong \theta_4\theta_3$$

$$ln[\dot{\varepsilon}_{ss} \times esp(\frac{Q}{RT})] = ln(G_4G_3) + \left(\frac{H_4}{RT} + H_4\right) \times (\frac{\sigma}{\sigma_Y})$$

$$ln[\frac{k}{t_r} \times esp(\frac{Q}{RT})] = ln(G_4G_3) + \left(\frac{H_4}{RT} + H_4\right) \times (\frac{\sigma}{\sigma_Y})$$

So, if the temperature is constant, the equation can be changed into:

$$ln\left(\frac{1}{t_r}\right) = A + D \times (\frac{\sigma}{\sigma_Y}) \quad (46)$$

After this, the curves of $1/t_r$ vs. σ/σ_Y can be drawn in Fig. 91. From Fig. 91, the value A and D were obtained. The equation between the rupture time and the

normal stress is established to predict the creep behavior. That means if temperature and stress is known, the rupture time or the life of creep will be predicted. The prediction equation of rupture time from normal stress is shown as follows:

$$\begin{cases} at\ 300\ ℃, ln\left(\frac{1}{t_r}\right) = -18.6 + 30.4 \times (\frac{\sigma}{\sigma_Y}) \\ at\ 330\ ℃, ln\left(\frac{1}{t_r}\right) = -16.3 + 20.4 \times (\frac{\sigma}{\sigma_Y}) \\ at\ 360\ ℃, ln\left(\frac{1}{t_r}\right) = -15.6 + 18.6 \times (\frac{\sigma}{\sigma_Y}) \end{cases}$$

The same equation between minimum creep rate and normal stress was gotten, that will explain the creep exponent are not constant at different stress, because the relationship of $\ln\ \dot{\varepsilon}_{ss}$ vs ln σ is not linear, the relation between minimum creep rate and normal stress is linear shown in Fig. 92. This will be perfect to explain the problem of prediction to long term creep life.

$$ln(\dot{\varepsilon}_{ss}) = E + H \times (\frac{\sigma}{\sigma_Y}) \tag{47}$$

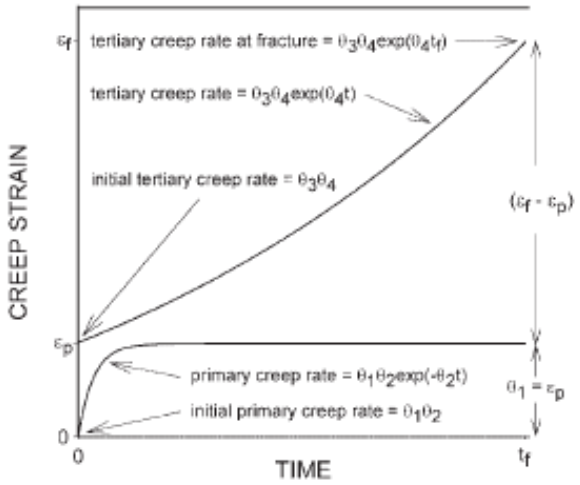

Fig. 88. Schematic representation of the physical significance of the primary and tertiary stages.

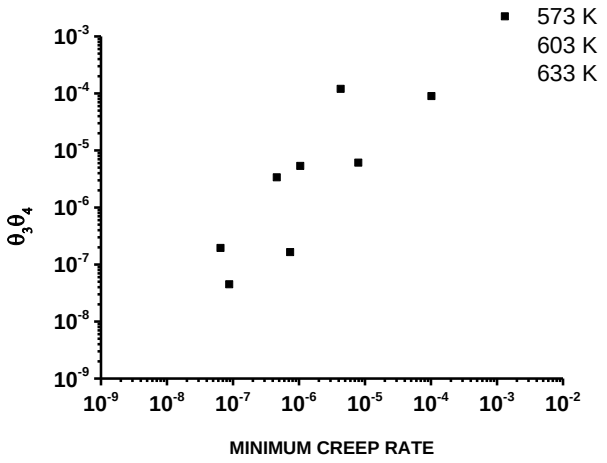

Fig. 89. The relationships of minimum creep rate and θ_3 θ_4.

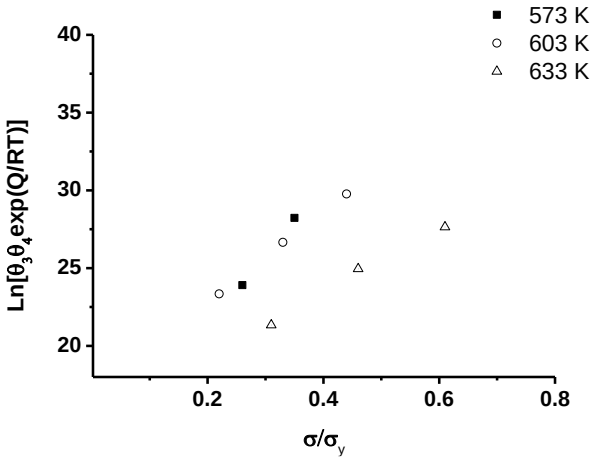

Fig. 90**.** The relationships of normal stresses and Ln $\theta_3\theta_4$exp(Q/RT)

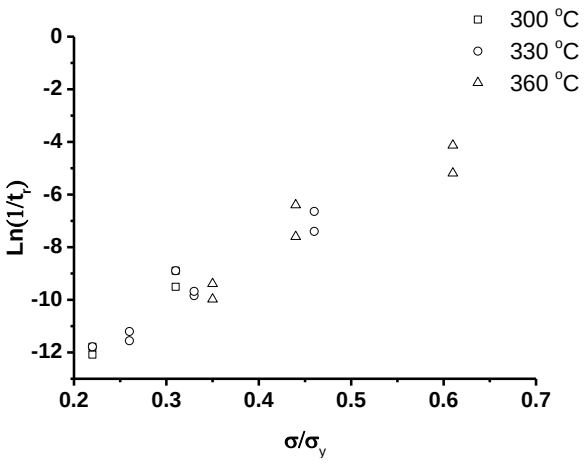

Fig. 91. The relationships of Ln($1/t_r$) and σ/σ_y

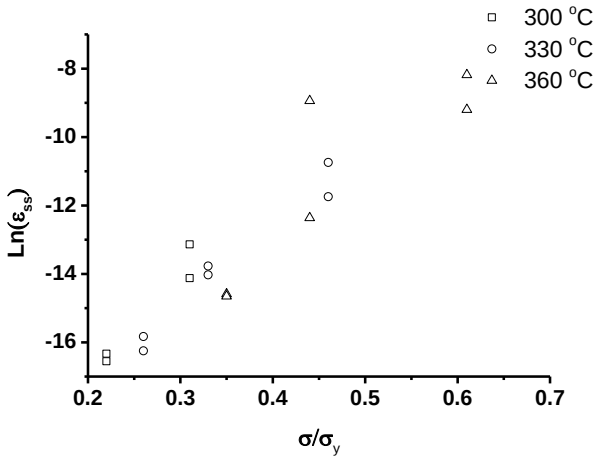

Fig. 92. The relationships of $Ln(1/t_r)$ and σ/σ_y

4.6.4 The creep damage tolerance

The strain in or after the rupture is important for creep behavior. The concentrations of stains will occur the concentrations of stress[159]. During this process, the ability of a material to resistant the damage or rupture should depend on the plastic and rupture strain[169]. The Monkman-Grant relationship will be show the ability of creep behavior. The very useful measure may be introduced by the creep damage tolerance parameter defined as[170, 171]:

$$\lambda = \frac{(\varepsilon_f - \varepsilon_p)}{\dot{\varepsilon}_{ss} \times t_r} \quad (48)$$

When values between 1 to 2.5, the fracture of creep should be attributable to cavitation. If the value is higher than 2.5, the fracture of creep should begin as necking. If the value is higher than 5, the fracture of creep should begin as precipitate coarsening[170].

From Fig. 93, the rupture at 300 °C should be attributable to cavitation due to the creep damage tolerance between 1 to 2.5. This fracture mechanism has already confirmed by previous work. But except at 40 MPa at 330 °C, all others should begin with necking. In previous work the necking is found in fracture surfaces at those conditions. But the almost of those are higher than 5. The precipitation during creep should be studied. Unfortunately, nothing can be observed in these Al alloys due to quickly disappeared dislocation during the preparation of specimen for TEM.

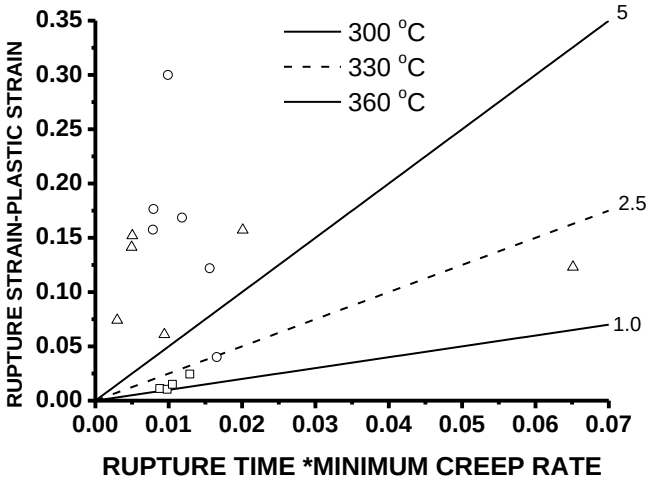

Fig. 93. The curve of creep damage tolerance parameter

.

4.6.5 Conclusions

The creep behavior of GISS die cast AC4C Al alloys and CLC die cast AC4C Al alloys were studied by the constant stress creep tests at the temperatures of 573, 603 and 633K. Using the theta projection method established the constitutive models to describe the creep behavior. The relations between minimum creep rate or creep life and normal stress are linear. The creep damage tolerance parameter is studied, the results are similar as previous work. The results show that experimental data is associated with predicted assumption which can provide an accurate and precise estimate of the creep behavior constitutive models in this works.

4.7 The stress-change creep

In previous part, the power law and theta projection were used to describe the creep behavior in the elevated temperatures. In this work the stress-dip test is used to describe the creep behavior due to the constant structure during the minimum creep rate and stress change. The creep exponent is about 3-5 in the previous work after deduction of threshold stress. The creep exponent from the creep-dip and increase test should be at values of 3-5 without any mathematical process.

4.7.1 Stress change creep at room temperature and 220, 250, 280 and 300°C

The constant structure are difficult to exist in different specimens due to the different cast processing and different heat treatment suffering. So the sensitivity of materials for creep behavior can be obtained using two ways. One is the strain rate change test, most of which are increase strain rate tests [23, 28, 148]. Other is the stress change test, most of which are decrease stain, also say, stress-drop [173][173] or dip stress test [174-176].

The stress change creep test originated by Gibbs and nix 40 years ago [173]. Recently, some researcher still focus on it.[173-175]. There are two kinds of this test, one is large stress used. Firstly the elastic and inelastic reduce quickly, then inelastic part reduce slowly gradually. Next the inelastic increase slowly like some kinds of backflow [151] . However, the very small stress reductions work during creep test. After the elastic and inelastic reduce quickly, then inelastic part increase slowly gradually. This results of stress-dip test partially should be responsible for action of the internal stress of inter backstress. If the stress reduction is very small, the internal backstress will quickly be equal to the applied stress in the balance situation, that shows like normal creep curve shapes [175]. But if the stress reduction is too large to change the microstructure too quickly into balance situation. So, the back flow and internal back stress are associated the microstructure defect such as dislocation or subgrain. Recently, some researcher focus on the internal stresses using modern analysis methods including the X-ray diffraction[176] or convergent bean electron diffraction (CBED)[177] and electron back-scattered diffraction (EBSD)[178, 179] to try to find some relationship between the internal stress and microstructure defects. Unfortunately most results of these works could not fit commonly for all materials and less strong math constitution equations or others powerful evidences were obtain to clearly explain the mechanism of affection of microstructure defects.

In previous work, the power law and theta projection were used to describe the creep behavior in the elevated temperatures. In present work the stress-dip test is used to describe the creep behavior due to the constant structure during the minimum creep rate and stress change. The creep exponent is about 3-5 in the previous

work after deduction of threshold stress. The creep exponent from the creep-dip and increase test should be at values of 3-5 without any mathematical process.

In Fig. 94 and 95, the creep increase and creep dip test were shown at the same interval time under the same applied stress change steps using GISS-DC-AC4C-T6 Al alloy at 25°C. The results showed that the strain of creep increase after stress changed like the normal creep curves. The stress change is not too large to show the balance between the applied stress and internal stress. The calculation of minimum creep rate carefully avoids to use the beginning of stress change areas. Although the minimum creep rate at room temperature is too small to calculate from the curves. So the data of minimum creep rate at room temperature can be used. In Fig. 96 and 97, the creep increase and creep dip test were shown at the same interval time under the same applied stress change steps using CL-DC-AC4C-T6 Al alloy at 25°C. As shown in Fig. 98, the data of minimum creep rate to calculate exponents of creep at room temperature from the stress increase and stress-dip test is linear with the applied stress. However, the exponent at room temperature is about 1-3, according the mechanism of creep theory, at 0.4-0.7 Tm and low stress should be diffusional creep (coble creep); at 0.4-0.7 Tm and intermediate and high stress should be dislocation creep. In Fig. 98, the transition in the n values at different applied stressed is observed from 1 to 3.

The same trend of creep increase and creep dip test of GISS-T6 AC4C Al alloy is shown at 250°C in Fig. 99 and 100 at the same interval time and applied stress-changes. The results showed that the strain of creep increase after stress changed. The stress change is main reason to show the balance change between the applied stress and internal stress. The calculation of minimum creep rate avoids to use the beginning of stress change areas too. So, the data of minimum creep rate at 250°C can be used. In Fig. 101 and 102, the creep increase and creep dip test were shown at the same interval time under the same applied stress change steps using CL-DC-AC4C-T6 Al alloy at 250°C. In Fig. 103, the data of minimum creep rate to calculate creep exponents from the stress change test is linear with the applied stress in the low stress. However, the exponent of GISS-T6 AC4C Al alloy is about 1 below 70 MPa in the increase test and 2.4 below 70 MPa in the dip test; the exponent of CL-DC-AC4C-T6 Al alloy is about 1.3 below 70 MPa in the increase test and 2.65 below 70 MPa in the dip test. According the mechanism of creep theory, at 0.4-0.7 Tm and low stress should be diffusional creep

(coble creep); at 0.4-0.7 Tm and intermediate and high stress should be dislocation creep, so in Fig. 103, the transition in the n values is observed at different applied stress. The exponent of CL-DC-AC4C-T6 Al alloy is high than the exponent of GISS-T6 AC4C Al alloy at 250°C in both of increase and dip test. The creep nature of CL-DC-AC4C-T6 Al alloy is better than GISS-T6 AC4C Al alloy at 250°C.

In the increase test, the balance of applied stress and the internal stress is recovered in the dip test, however in the increase test the state of applied stress and the internal stress begin to reach to the balance. The exponent of creep is used to describe the state of applied stress and the internal stress to reach to the balance not recovery. So the increase test is repeated at 220°C, 280°C and 300°C. The results of CL-DC and GISS-DC AC4C Al alloys at 220°C and 280°C are showed in Fig. 104, 105, 106 and 107. The exponent of GISS-T6 AC4C Al alloy is about 1 at 220°C in the increase test and 2.85 at 280°C; the exponent of CL-DC-AC4C-T6 Al alloy is 1.15 at 220°C in the increase test and 2.46 at 280°C. The results show the transformation of the mechanism of creep theory from the low temperature to the higher temperature and from diffusional creep (coble creep) to dislocation creep.

The increase test and dip test of CL-DC and GISS-DC AC4C Al alloys are carried out at 300°C shown in the Fig. 112, 113, 114 and 115 for the comparison of the creep results. The exponent of GISS-T6 AC4C Al alloy is 3.58 at 300°C in the increase test and 3.52 in creep test; the exponent of CL-DC-AC4C-T6 Al alloy is 3.65 at 300°C in the increase test and 3.96 in creep test in Fig. 113. The results show that the exponents of increase test almost equal to the creep exponents in previous experiments in Table 21. The increase test is more quick and simple than the creep test and used only one sample which means a more reliable and stable sample system.

In table 21, the results of stress change test and creep test shows that the exponents are change from 1 to 3, then to 5. According the creep theory, the creep exponents associated with different creep mechanisms, so the diffusional creep at 25°C, 220°C and 250°C is changed to the dislocation creep at 280°C, 300°C and 330°C, then the dislocation creep is carried out at 360°C. This trend is shown in the Fig. 114.

There are two kinds of this test, one is large stress used. Firstly the elastic and inelastic reduce quickly, then inelastic part reduce slowly gradually. Next the inelastic increase slowly like some kinds of backflow [151]. In the Fig. 115 and 116,

the very small stress reductions work during stress dip test. After the elastic and inelastic reduce quickly, then inelastic part increase slowly gradually. This results of stress-dip test partially should be responsible for action of the internal stress of inter backstress. If the stress reduction is very small, the internal backstress will quickly be equal to the applied stress in the balance situation, that shows like normal creep curve shapes [175]. In our result, the responsible is too quick to observe. In the Fig. 115 and 116, the large change stress dip test is carried out. The stress reduction is too large to change the microstructure too quickly into balance situation. So, the back flow and internal back stress are associated the microstructure defect such as dislocation or subgrain.

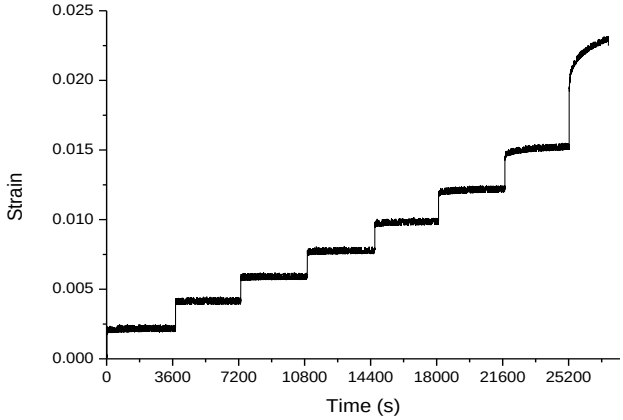

Fig. 94. The stress increase change creep curve of GISS-DC-T6 at 25°C

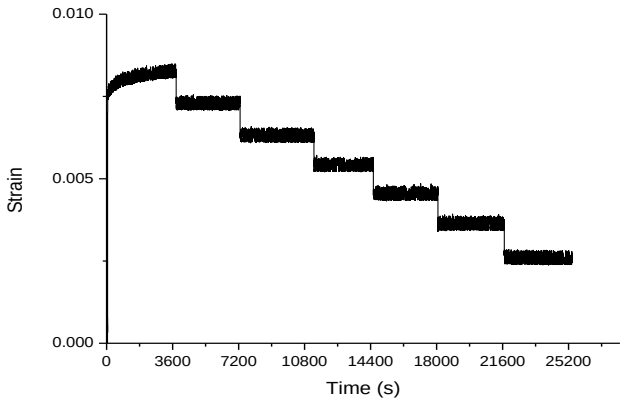

Fig. 95. The stress-dip change creep curve of GISS-DC-T6 at 25°C

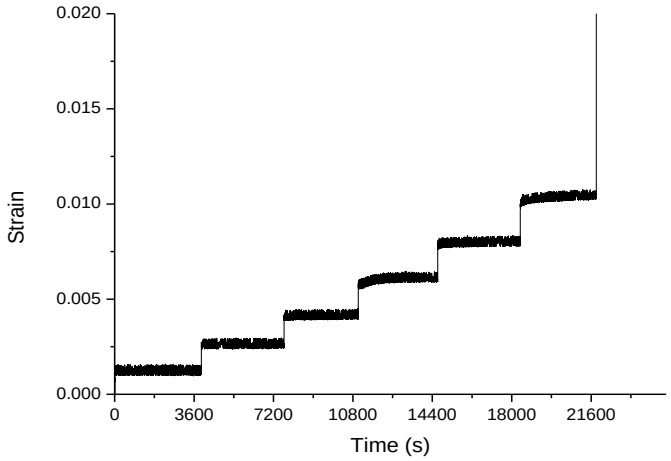

Fig. 96. The stress increase change creep curve of CL-DC-T6 at 25°C

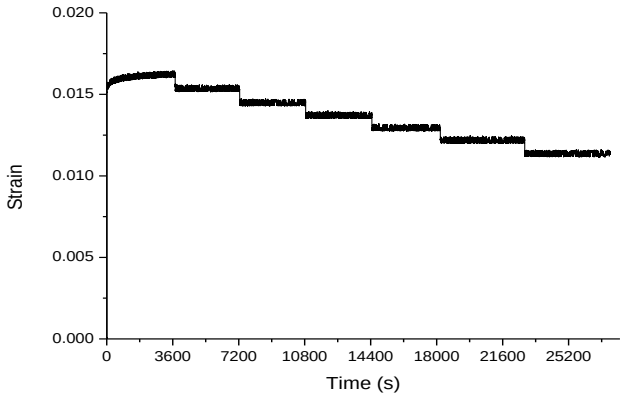

Fig. 97. The stress-dip change creep curve of CL-DC-T6 at 25°C

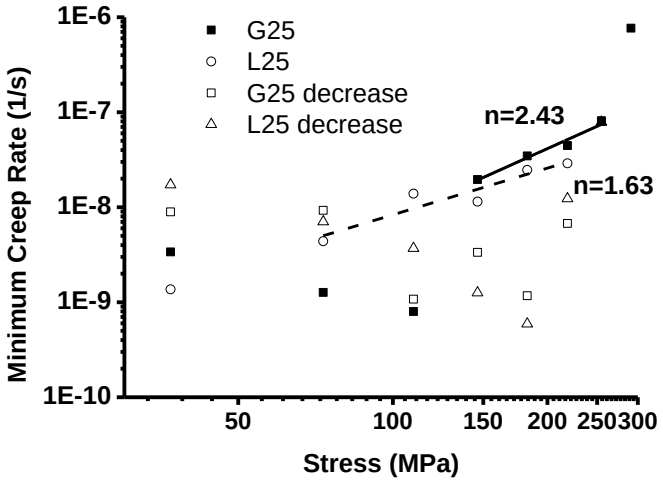

Fig. 98. Minimum creep rate versus stress of CL-DC and GISS-DC AC4C Al alloys, at temperature of 25 °C.

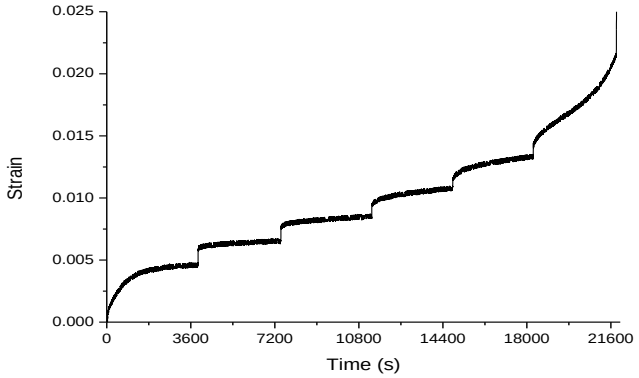

Fig. 99. The stress increase change creep curve of GISS-DC-T6 at 250°C

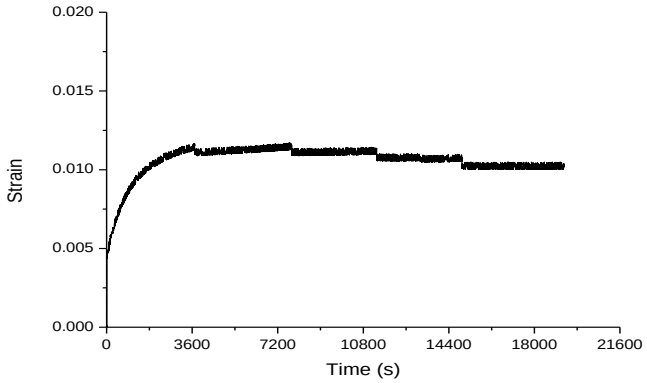

Fig. 100. The stress change-dip creep curve of DC-DC-T6 at 250°C

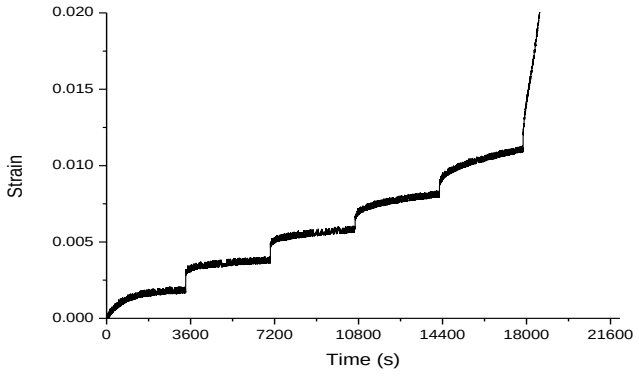

Fig. 101. The stress change increase creep curve of DC-DC-T6 at 250°C

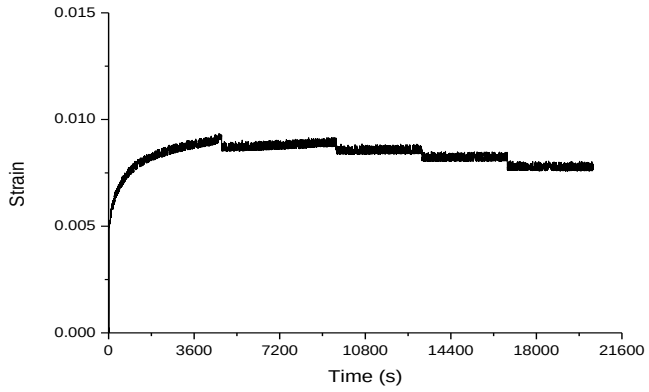

Fig. 102. The stress change-dip creep curve of DC-DC-T6 at 250°C

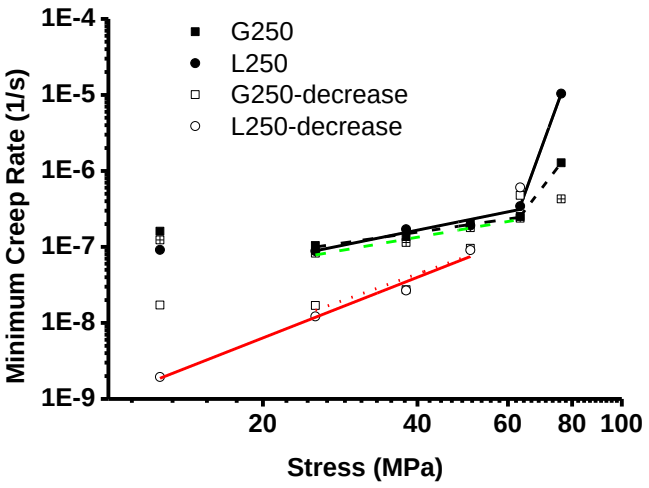

Fig. 103. Minimum creep rate versus stress of CL-DC and GISS-DC AC4C Al alloys, at temperature of 250 °C.

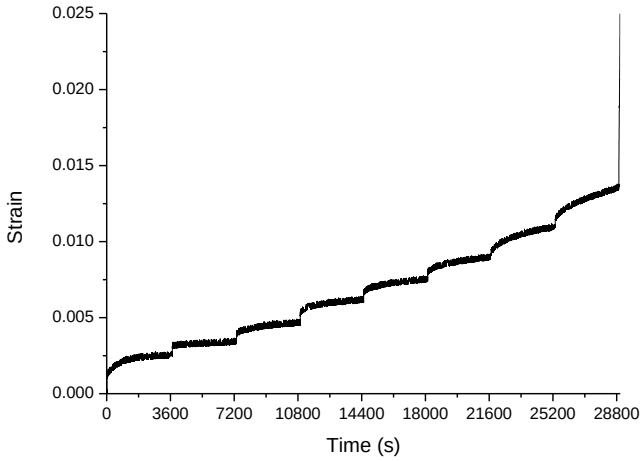

Fig. 104. The stress-increase change creep curve of GISS-DC-T6 at 220°C

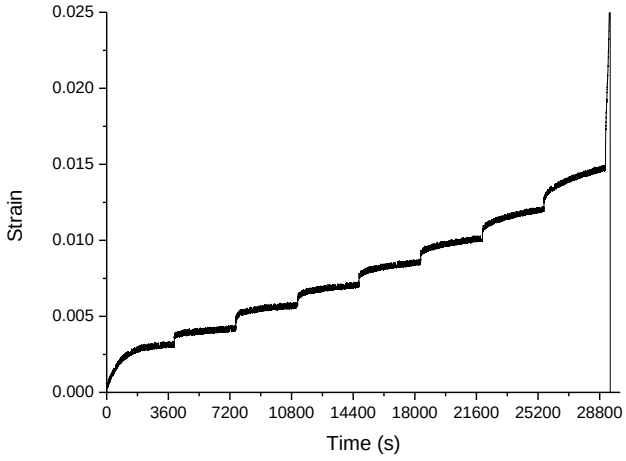

Fig. 105. The stress-increase change creep curve of CL-DC-T6 at 220°C

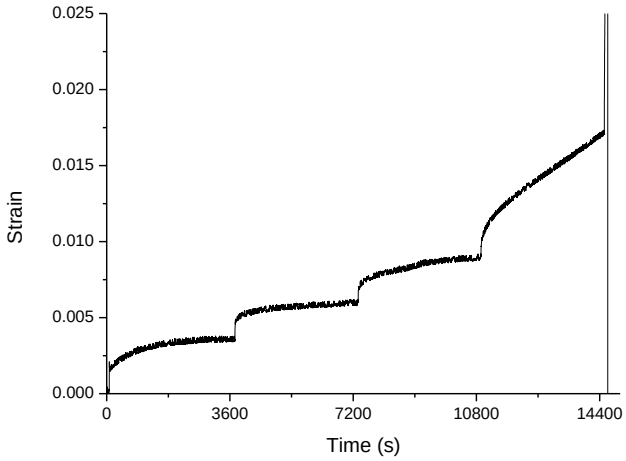

Fig. 106. The stress-increase change creep curve of GISS-DC-T6 at 280°C

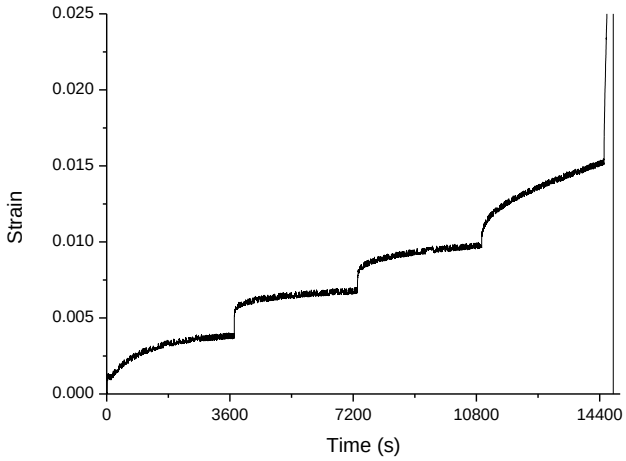

Fig. 107. The stress-increase change creep curve of CL-DC-T6 at 280°C

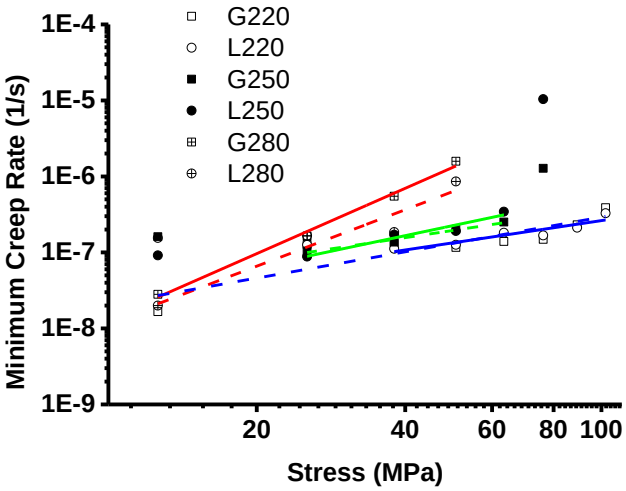

Fig. 108. Minimum creep rate versus stress of CL-DC and GISS-DC AC4C Al alloys, at temperature of 220 °C, 250 °C and 280 °C.

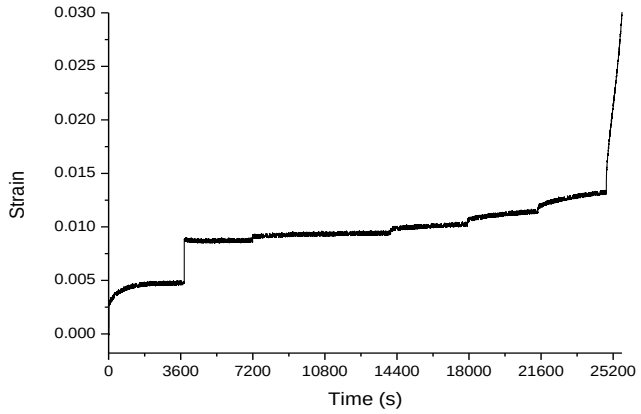

Fig. 109. The stress increase change creep curve of GISS-DC-T6 at 300°C

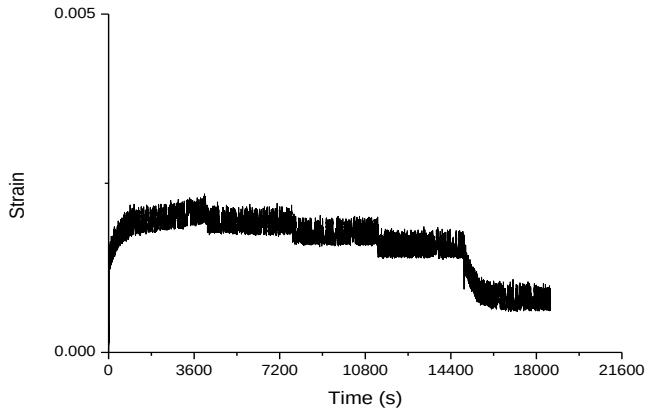

Fig. 110. The stress-dip change creep curve of GISS-DC-T6 at 300°C

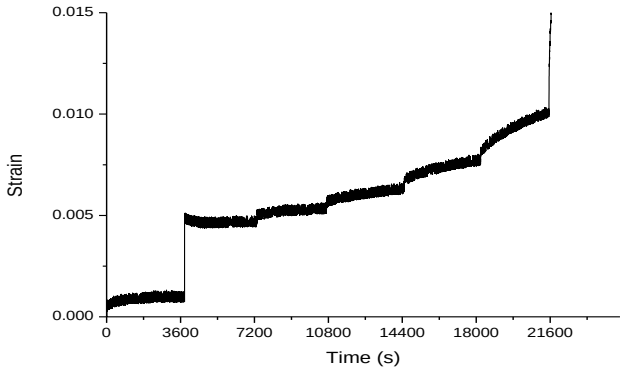

Fig. 111. The stress-increase change creep curve of CL-DC-T6 at 300°C

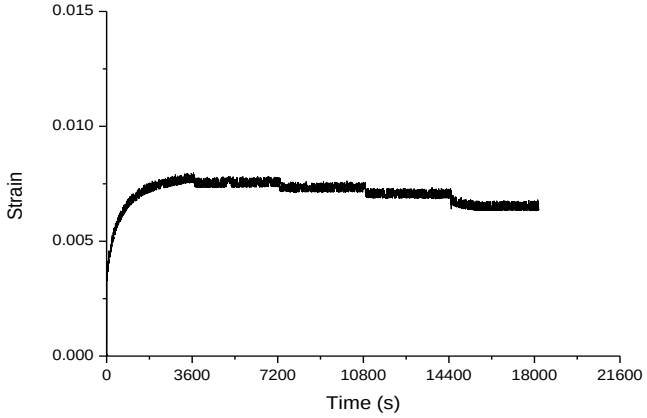

Fig. 112. The stress-dip change creep curve of CL-DC-T6 at 300°C

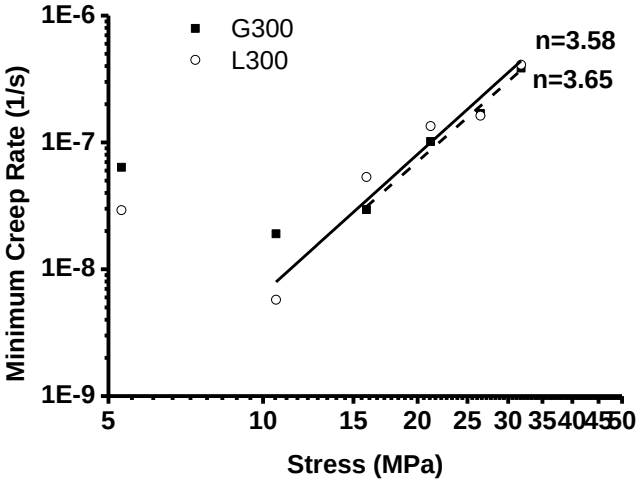

Fig. 113. Minimum creep rate versus stress of CL-DC and GISS-DC AC4C Al alloys, at temperature of 300 °C.

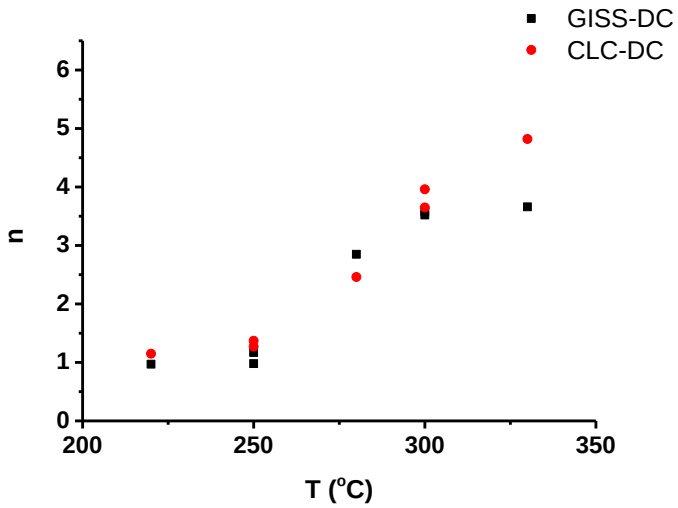

Fig. 114. Exponents of CL-DC and GISS-DC AC4C Al alloys versus temperatures.

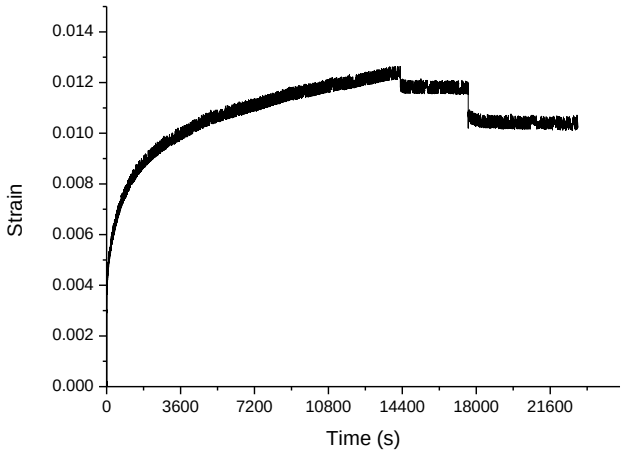

Fig. 115. The stress-dip change creep curve of CL-DC-T6 at 300°C with small stress and large stress deduction.

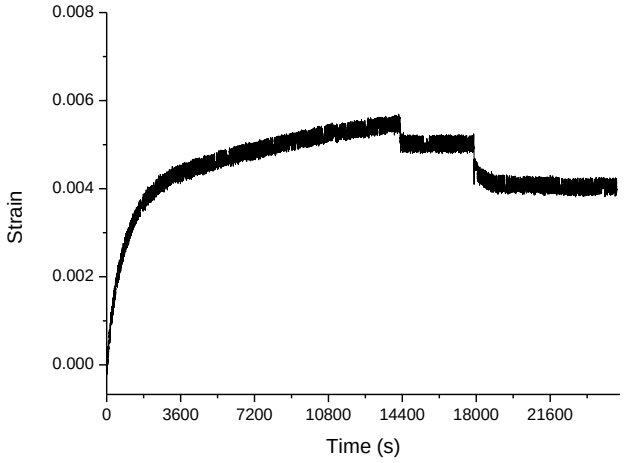

Fig. 116. The stress-dip change creep curve of GISS-DC-T6 at 300°C small stress and large stress deduction.

Table 21 The exponents of increase test, dip test and creep test

	Stress change creep						Constant stress creep		
		25°C	220°C	250°C	280°C	300°C	300°C	330°C	360°C
GISS-DC	Increase	2.43(4)	0.97	0.98 /1.17	2.85	3.58	3.52	3.66	4.94
	Decrease	Random		2.40		No			
CLC-DC	Increase	1.63(5)	1.15	1.37 /1.27	2.46	3.65	3.96	4.82	5.74
	Decrease	Random		2.65		No			

4.7.2 Fracture of stress change creep

The macroscopic observation of the tensile test fracture by naked eyes reveals the brittle nature features of these alloys at 25, 250 and 280 °C for both alloys. However, at the temperature of 300 °C, the GISS-DC AC4C Al alloy is still brittle and the CL-DC-AC4C-T6 Al alloy is ductile. From observations of SEM in Fig. 117 and 118, it is showed that the fracture surfaces of AC4C aluminum alloy tensile samples at different temperatures display a clearly brittle or ductile fracture, and the quasi-cleavage feature can be observed. The fracture surfaces of GISS-DC AC4C Al alloy and the CL-DC-AC4C-T6 Al alloy samples don't show a dimple-like morphology at room temperature. The dimple-like fracture surfaces reveal the ductile characteristics of the samples and show the micro-necking crack around dimples at higher temperatures.

Moreover, the more shrinkage defects and micro voids can also be observed at lower temperature and for GISS-DC AC4C Al alloy, as shown in Fig. 118, due to some defects such as shrinkages during the die cast process or gas babbles during the GISS process. The shrinkage pore is easy to cluster and harmful to mechanical properties in die casting components at higher temperature, so the GISS-DC AC4C Al alloy is more brittle than CL-DC-AC4C-T6 Al alloy. It is also confirmed that the clustering characteristics of pores and the eutectics are higher in higher temperatures. The fracture path preferentially goes through the shrinkage porosity in the case of the existence of excessive shrinkage defects, which results in the significant decrease of mechanical properties. In addition, there are no pores which are found to exist in the edge region of all alloys.

Necking as the local cross section area (CSA) decrease and constriction begins along the gage section after yield point. From this point, inhomogeneity between strain hardening and area decrease arises. As a result, the load required for further progression decreases. This means that load carrying capacity of this alloys decreases. After necking point, practically all plastic deformation is concentrated in the small necked region. Finally failure occurs in the necked region. Regard as the die cast semi-solid AC4C alloy was heat treated by T6, it is expected to exhibit work hardening and the secondary phases which is Si spherical precipitate particles excised where the

fracture surface comprised of cracking of Si particles on clearage planes. The broken particles were found on the fracture surface of the alloys to limit the plasticity of this alloy in Fig. 117 and 118. The existing of the brittle intermetallic precipitants and Si particles lead to fracture which were found that fracture of Si particles was the dominant feature at the temperature range between room and 250 °C (seen in the Fig. 120 and 121). The single dominant cleavage crack observed at low temperature which is seen in Fig. 118. At 25 °C for both alloys and 250 °C for GISS-DC AC4C Al alloy,, it is noted that the brittle cleavage fracture with small plastic deformation areas. At 250 °C, the fracture is ductile and it is observed where there are ductile dimples due to multiple between the reinforcing intermetallic particles and matrix plastic relaxation and the intermetallic particles dispersed in the small, ductile dimples. The brittle cleavage fracture dominant and the surfaces of fracture with some microvoid reveal the transition from brittleness to ductility from low temperature to high temperatures.

The effect of broken Si and intermetallic particles in Al-Si-Mg alloys have been widely studied in some literatures [1, 2, 128, 180] From above, the mode of fractures in both CL-DC and GISS AC4C-T6 alloys during the tensile test is transgranular with quasi-cleavage fracture along grain boundaries.

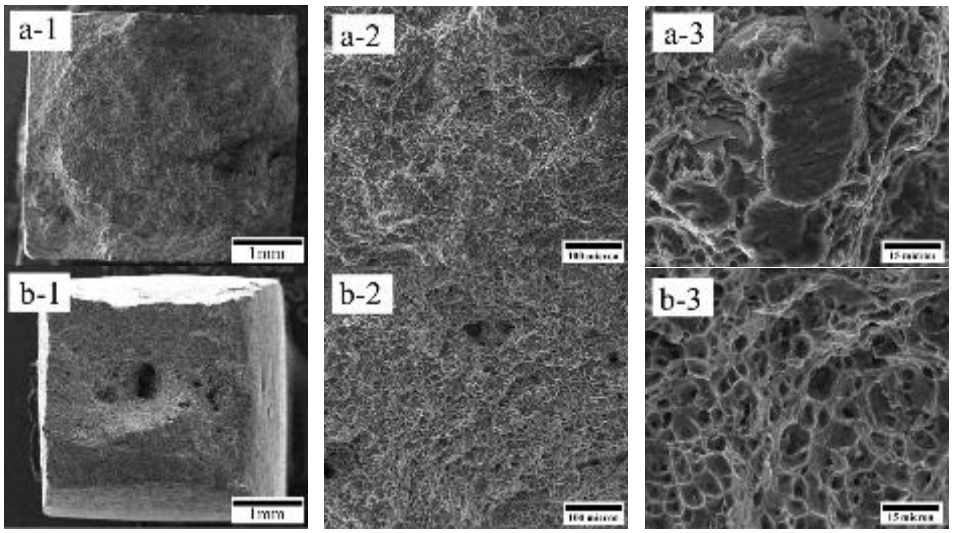

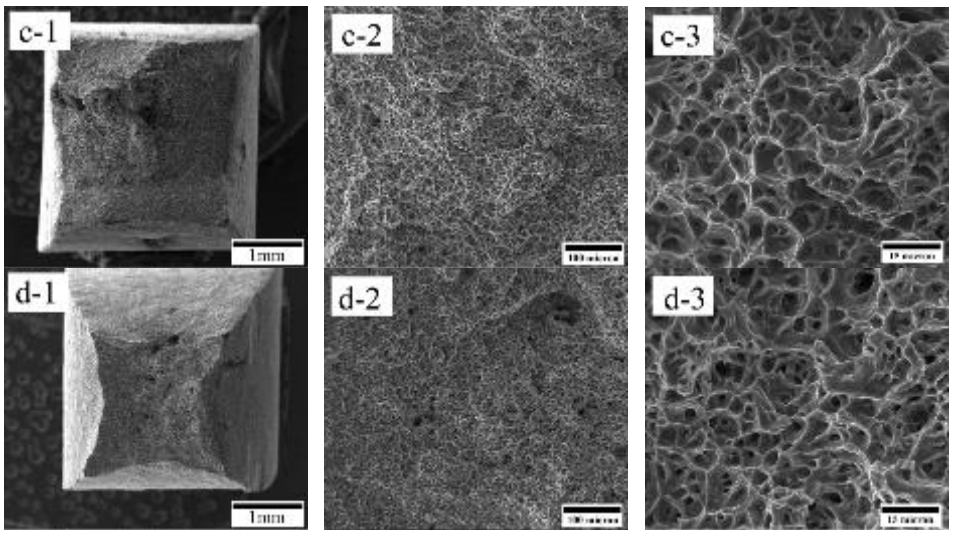

Fig. 117. Rupture surface for the CL-DC AC4C Al alloy (a) at 25 °C, (b) 250 °C, (c) at 280 °C and (d) at 300 °C.

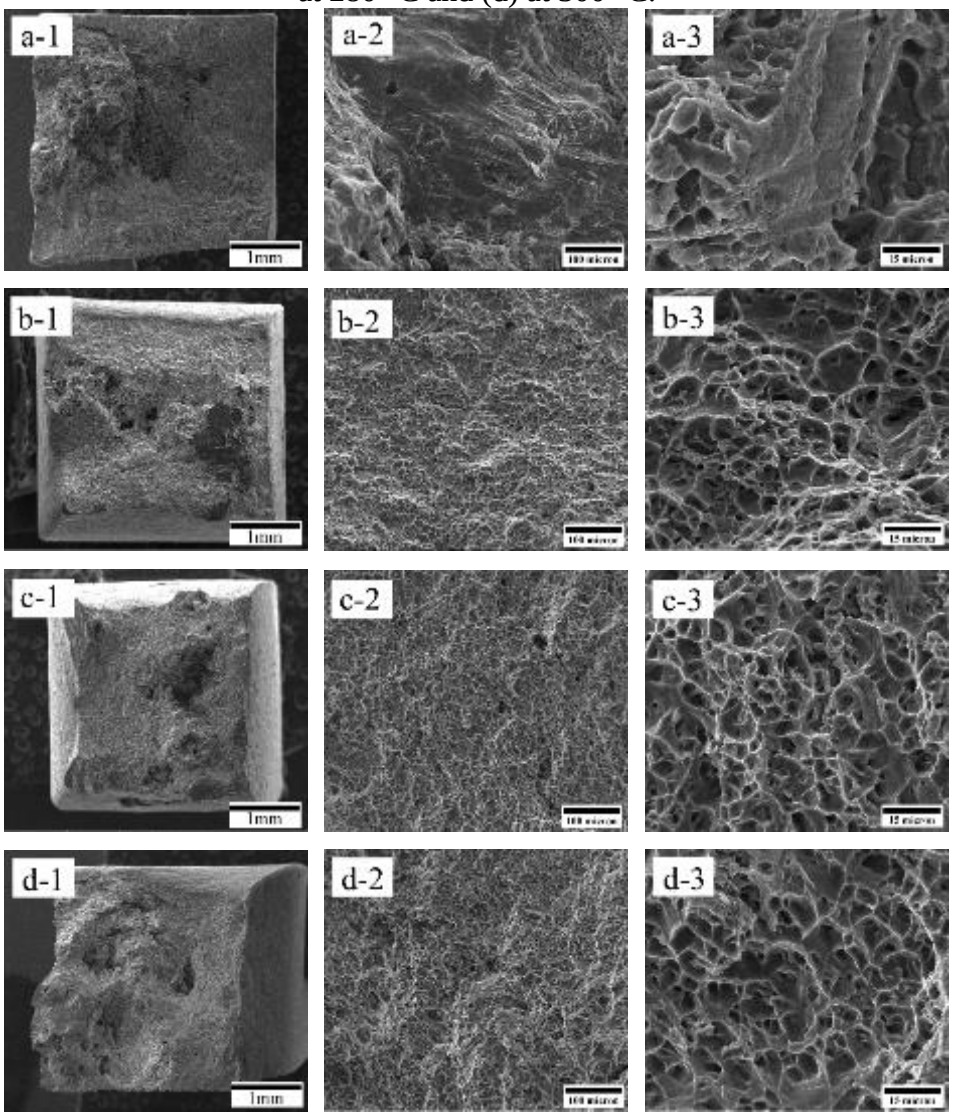

Fig. 118. Rupture surface for the GISS-DC AC4C Al alloy (a) at 25 °C, (b) 250 °C, (c) at 280 °C and (d) at 300 °C.

4.7.3 Conclusions

The creep behavior of GISS die cast AC4C Al alloys and CLC die cast AC4C Al alloys were studied by the change stress creep tests at the temperatures of 25, 250, 280 and 300°C. This results of stress-dip test partially should be responsible for action of the internal stress of inter backstress. If the stress reduction is very small, the internal backstress will quickly be equal to the applied stress in the balance situation, that shows like normal creep curve shapes. In our result, the responsible is too quick to observe. The large change stress dip test is carried out. The stress reduction is too large to change the microstructure too quickly into balance situation. So, the back flow and internal back stress are associated the microstructure defect such as dislocation or subgrain. The fractures of stress change test sample is also studied.

CHAPTER 5. CONCLUSIONS AND SUGGESTIONS

5.1 Conclusions

The GISS-DC AC4C aluminum alloy was investigated for microstructures and mechanical properties, including tensile test, creep rupture test and stress-change creep test. The results can be summerized as follows:

1. The primary α-Al grain size and its quantity of as-cast GISS-DC AC4C specimens from location 4 at the top part of die cast plates are larger than those from location 1 near the gate section. This may be due to the slower cooling rate and the turbulent flow behavior at location 4 during die casting. Between the primary α-Al grains contain a number of elements: Fe, Mg, Mn and Si which constitute the intermetallic and eutectic Al-Si particles. The compositions of Fe-rich intermetallic particles include FeSiMn, SiFeMg, and FeSiMgMn. At room tempearature, the average UTS and elongation of specimens from location 4 of the die cast plates are lower than those from the other locations. The average YS of specimens from all 4 locations are almost the same value of 100 MPa. The average UTS and elongation greatly decreases from about 200 MPa and 11.8 % at location 1 to about 140 MPa and 6.7 % at location 4, respectively. The location of specimens has more impact on the UTS than on the YS and elongation. The strain hardening of specimens from location 4 is significantly higher than those from the other locations. The mechanical properties of GISS-DC specimens are competitive with those of normal die casting (CL-DC). The UTS of GISS-DC AC4C alloy in this study is higher than that of CL-DC A356 alloy. The UTS of GISS-DC AC4C alloy from the present casting conditions is nearly highest when compared with those from the previous studies. The quasi-cleavage fractures of GISS-DC AC4C alloy are typically observed. The shrinkage porosities and micro voids at location 4 of the die cast plates are significantly higher than those found at location 1. In addition, in the edge region of die cast plates, porosities and cracks are not generally observed. The cracks and fractures are originated from the shrinkage defects which resulted in the decrease of strength and ductility of GISS-DC AC4C alloy.

2. The spheroidization of eutectic-Si particles occurred after T6 heat

treatment. In the as-cast GISS-DC and CL-DC alloys, there are some π-Chinese script phase and β phase. But after T6 heat treatment, only β phase can be found in both alloys. The percentage of Mg in both GISS-DC and CL-DC alloys increased after T6 heat treatment. The percentage of Si in CL-DC alloy increased after T6 heat treatment, however, the percentage of Si in GISS-DC alloy decreased. At elevated temperatures, tensile properties such as UTS, YS and elongation of GISS-DC and CL-DC AC4C alloys after T6 heat treatment were decreased with increasing of temperatures. At room temperature, the GISS-DC-AC4C-T6 alloy gained UTS and YS of 300.9 MPa and 244.5 MPa, respectively. The UTS of GISS-DC-AC4C-T6 alloy was higher than that of sand cast AC4C-AC4C-T6 alloy. Elongation of GISS-DC-AC4C-T6 alloy was lower than that of GISS-DC-A356-T6 alloy due to the Fe-contained intermetallic particles. Cracking of intermetallic phases and Si particles may control the failure of GISS-DC-AC4C-T6 alloy. At temperatures of 25, 100 and 175 °C, the GISS-DC-AC4C-T6 alloy exhibits brittle fracture before reaching to the maximum strength. Work hardening exponent (*n*) of GISS-DC-AC4C-T6 alloy decreases with increasing strain. When the necking occurs, *n* tends to be zero. At 250 °C, *n* decreases to a negative value before necking occurs due to superplastic deformation. The microstructures of GISS-DC-AC4C-T6 compared with CL-DC-AC4C-T6 alloys showed different distributions of Si and intermetallic particles at different temperatures. Fractographs of both alloys showed fracture surfaces changing from brittle to ductile behavior with increasing temperature. At 250 °C, work softening and typical ductile dimples on fracture surfaces were observed. The transition from brittle to ductile fracture was observed in both GISS-DC-AC4C-T6 and CL-DC-AC4C-T6 alloys. The less cracked intermetallic particles and less micro voids would be responsible for the better tensile properties of CL-DC alloy compared with those of GISS-DC alloy.

3. The microstructures and creep behavior of GISS-DC-AC4C-T6 alloy were investigated at temperature range of 300-360 °C and stress range of 20-40 MPa and compared with those of CL-DC-AC4C-T6 alloy. The intermetallic particles of both alloys comprise elements: Fe, Mg and Si. The spheroidization and coarsening of eutictic-Si particles occured after T6 heat treatment. Shapes of primary α-Al phases in GISS-DC-AC4C-T6 alloy are rosette while those in CL-DC-AC4C-T6 alloy are dendritic. The sizes of primary α-Al phases in GISS-DC-AC4C-T6 alloy are larger than

those in the CL-DC-AC4C-T6 alloy. Creep stress exponents (n) and apparent activity energy for creep (Q_c) of GISS-DC-AC4C-T6 and CL-DC-AC4C-T6 alloys were evaluated. The stress exponents n of CL-DC-AC4C-T6 alloy at 300 °C, 330 °C and 360 °C are 3.95, 3.66 and 4.94, while n of GISS-DC-AC4C-T6 are 3.52, 4.82 and 5.74, respectively. These stress exponents are closed to those of dislocation glide-climb control creep that are usually found in class M metal alloys or pure mtetals. The activity energy for creep increased with increasing stress in both CL-DC-AC4C-T6 and GISS-DC-AC4C-T6 alloys.

4. The minimum creep rate and rupture time from creep rupture tests demonstrated a linear relationship and well fitted to the Monkman-Grant model. The creep damage tolerance parameter was analyzed for predicting creep life and creep fracture mechanisms. The theta projection method based on shape of creep curves was also used to establish a constitutive model to predict creep behavior. The creep curve data of GISS-DC-AC4C-T6 alloy at temperatures of 300, 330 and 360 °C and stresses of 20, 30 and 40 MPa were used for establishing for the theta projection constitutive equations. The experimental creep data were associated with the predicted assumption, which may provide an accurate estimate of creep constitutive model for GISS-DC-AC4C-T6 alloy.

5. Creep behavior of GISS-DC-AC4C and CL-DC AC4C alloys after T6 heat treatment were studied using stress-change tests at temperatures of 25, 250, 280 and 300 °C. The result of stress-dip (or stress decrease) tests is responsible for an action of the internal backstress. If the stress reduction is very small, the internal backstress will quickly be equal to the applied stress, leading to a balance situation. This situation gives a normal creep curve. In the present study, the responds of stress-dip are too fast to be detected. For a large stress-dip test, the stress reduction is too large to change microstructures quickly into a balance situation. So, the back flow and internal backstress are associated with microstructure defects such as dislocations or subgrains.

5.2 Suggestions

The following could be studied in detail in the future work:

1. The subgrains formation of GISS-DC AC4C aluminum alloy during creep tests should be studied by using TEM.

2. The creep mechanisms of GISS-DC AC4C aluminum alloy at high temperatures should be examined.

3. The creep aging of GISS-DC AC4C aluminum alloy at high temperatures shoud be further studied.

REFERENCES

[1] Q. G. Wang, C. H. Caceres, and J. R. Griffiths, "Damage by eutectic particle cracking in aluminum casting alloys A356/357," *Metallurgical And Materials Transactions A-physical Metallurgy And Material,* vol. 34A, pp. 2901-2912, Dec 2003.

[2] G. Ran, J. E. Zhou, and Q. G. Wang, "Precipitates and tensile fracture mechanism in a sand cast A356 aluminum alloy," *Journal of Materials Processing Technology,* vol. 207, pp. 46-52, 2008.

[3] D. H. Kirkwood, M. Suéry, P. Kapranos, H. V. Atkinson, and K. P. Young, *Semi-solid processing of alloys*: Springer, 2010.

[4] R. Burapa, S. Janudom, T. Chucheep, R. Canyook, and J. Wannasin, "Effects of primary phase morphology on mechanical properties of Al-Si-Mg-Fe alloy in semi-solid slurry casting process," *Transactions Of Nonferrous Metals Society Of China,* vol. 20, pp. S857-S861, Sep 2010.

[5] S. Tahamtan, M. A. Golozar, F. Karimadeh, and B. Niroumand, "Microstructure and tensile properties of thixoformed A356 alloy," *Materials Characterization,* vol. 59, pp. 223-228, Mar 2008.

[6] S. Nafisi and R. Ghomashchi, "Semi-solid metal processing routes: an overview," *Canadian metallurgical quarterly,* vol. 44, pp. 289-304, 2005.

[7] S. Wisutmethangoon, S. Thongjan, N. Mahathaninwong, T. Plookphol, and J. Wannasin, "Precipitation hardening of A356 Al alloy produced by gas induced semi-solid process," *Materials Science And Engineering a-Structural Materials Properties Microstructure And Processing,* vol. 532, pp. 610-615, Jan 15 2012.

[8] Y. C. Lee, A. K. Dahle, D. H. StJohn, and J. E. C. Hutt, "The effect of grain refinement and silicon content on grain formation in hypoeutectic Al–Si alloys," *Materials Science and Engineering A,* vol. 259, pp. 43-52, 1999.

[9] P. R. Goulart, J. E. Spinelli, W. R. Osório, and A. Garcia, "Mechanical properties as a function of microstructure and solidification thermal variables of Al–Si castings," *Materials Science And Engineering A,* vol. 421, pp. 245-253, 2006.

[10] Z. W. Chen, C. Y. Ma, and P. Chen, "Eutectic modification of A356 alloy with Li addition through DSC and Miedema model," *Transactions Of Nonferrous Metals Society Of China,* vol. 22, pp. 42-46, Jan 2012.

[11] S. Imurai, J. Kajornchaiyakul, C. Thanachayanont, J. T. H. Pearce, and T. Chairuangsri, "Age Hardening and Precipitation Behavior of an Experimental Cast Al-Mg-Si Alloy Treated by T6 and T6I6 Heat Treatments," *Chiang Mai Journal Of Science,* vol. 37, pp. 269-281, May 2010.

[12] H. Möller, G. Govender, and W. E. Stumpf, "Natural and artificial aging response of semisolid metal processed Al–Si–Mg alloy A356," *International Journal of Cast Metals Research,* vol. 20, pp. 340-346, 2007.

[13] H. Möller, G. Govender, and W. E. Stumpf, "The T6 Heat Treatment of Semi-Solid Metal Processed Alloy A356," pp. 6-10, 2008.

[14] B. A. Esgandari, B. Nami, M. Shahmiri, and A. Abedi, "Effect of Mg and semi solid processing on microstructure and impression creep properties of A356 alloy," *Transactions Of Nonferrous Metals Society Of China,* vol. 23, pp. 2518-2523, Sep 2013.

[15] T. Jaglinski and R. Lakes, "Creep behavior of Al-Si die-cast alloys," *Journal Of Engineering Materials And Technology-Transactions Of the Asme,* vol. 126, pp. 378-383, Oct 2004.
[16] R. W. Evans and B. Wilshire, *Introduction to creep*: Institute of Materials London, 1993.
[17] C. Phaniraj, B. K. Choudhary, K. Bhanu Sankara Rao, and B. Raj, "Relationship between time to reach Monkman–Grant ductility and rupture life," *Scripta Materialia,* vol. 48, pp. 1313-1318, 2003.
[18] X. Y. Liu, Q. L. Pan, X. L. Zhang, S. X. Liang, F. Gao, L. Y. Zheng, *et al.*, "Creep behavior and microstructural evolution of deformed Al–Cu–Mg–Ag heat resistant alloy," *Materials Science and Engineering: A,* vol. 599, pp. 160-165, 2014.
[19] A. K. Mukherjee, "An examination of the constitutive equation for elevated temperature plasticity," *Materials Science And Engineering A,* vol. 322, pp. 1-22, Jan 15 2002.
[20] M. T. Abdu, M. S. Soliman, E. A. El-Danaf, A. A. Almajid, and F. A. Mohamed, "Creep characteristics and microstructure in nano-particle strengthened AA6082," *Materials Science And Engineering A,* vol. 531, pp. 35-44, Jan 1 2012.
[21] V. Srivastava, J. P. Williams, K. R. McNee, G. W. Greenwood, and H. Jones, "Low stress creep behaviour of 7075 high strength aluminium alloy," *Materials Science And Engineering A,* vol. 382, pp. 50-56, Sep 25 2004.
[22] N. Mahathaninwong, Y. Zhou, S. E. Babcock, T. Plookphol, J. Wannasin, and S. Wisutmethangoon, "Creep rupture behavior of semi-solid cast 7075-T6 Al alloy," *Materials Science And Engineering A,* vol. 556, pp. 107-113, Oct 30 2012.
[23] N. Q. Vo, C. H. Liebscher, M. J. S. Rawlings, M. Asta, and D. C. Dunand, "Creep properties and microstructure of a precipitation-strengthened ferritic Fe–Al–Ni–Cr alloy," *Acta Materialia,* vol. 71, pp. 89-99, 2014.
[24] P. Kumar, M. E. Kassner, W. Blum, P. Eisenlohr, and T. G. Langdon, "New observations on high-temperature creep at very low stresses," *Materials Science And Engineering A,* vol. 510-11, pp. 20-24, Jun 15 2009.
[25] A. A. Almajid, "High temperature deformation of solution treated 7010 Al-alloy," *Journal of King Saud University - Engineering Sciences,* vol. 23, pp. 21-25, 2011.
[26] B. Wilshire and P. J. Scharning, "Creep and creep fracture of commercial aluminium alloys," *Journal Of Materials Science,* vol. 43, pp. 3992-4000, Jun 2008.
[27] A. C. Fowler, "Weertman, Lliboutry and the development of sliding theory," *Journal Of Glaciology,* vol. 56, pp. 965-972, 2010.
[28] G. Liu, Y. C. Lin, X.-C. Zhang, and Y.-Q. Jiang, "Effects of two-stage creep-aging on precipitates of an Al–Cu–Mg alloy," *Materials Science and Engineering: A,* vol. 614, pp. 45-53, 2014.
[29] Y. C. Lin, Q.-F. Li, Y.-C. Xia, and L.-T. Li, "A phenomenological constitutive model for high temperature flow stress prediction of Al–Cu–Mg alloy," *Materials Science and Engineering: A,* vol. 534, pp. 654-662, 2012.
[30] Y. C. Lin, Y. C. Xia, X. M. Chen, and M. S. Chen, "Constitutive descriptions

for hot compressed 2124-T851 aluminum alloy over a wide range of temperature and strain rate," *Computational Materials Science,* vol. 50, pp. 227-233, Nov 2010.

[31] Z. W. Du, G. J. Wang, X. L. Han, Z. H. Li, B. H. Zhu, X. Fu, *et al.*, "Microstructural evolution after creep in aluminum alloy 2618," *Journal of Materials Science,* vol. 47, pp. 2541-2547, 2011.

[32] C. Yu-qiang, Y. I. Dan-qing, P. A. N. Su-ping, H. Xia, and Z. Ming-zhe, "Effect of temperature on creep behavior of 2024 aluminum alloy," *The Chinese Journal of Nonferrous Metals,* vol. 20, pp. 632-639, 2010.

[33] X.-f. Wan, H.-j. Ni, M.-y. Huang, H.-l. Zhang, and J.-h. Sun, "Microstructure, mechanical properties and creep resistance of Mg–(8%–12%)Zn–(2%–6%)Al alloys," *Transactions of Nonferrous Metals Society of China,* vol. 23, pp. 896-903, 2013.

[34] Y. H. Zhu, "Microstructure dependence of the creep behavior of a Zn-Al based alloy," *Journal Of Materials Processing Technology,* vol. 73, pp. 18-24, Jan 1998.

[35] Y. Terada, Y. Murata, and T. Sato, "Life assessment of die-cast Mg–5Al–1.7Ca alloys under creep service conditions," *Materials Science and Engineering: A,* vol. 613, pp. 136-140, 2014.

[36] Y. Terada, Y. Murata, and T. Sato, "Creep life assessment of a die-cast Mg–5Al–0.3Mn alloy," *Materials Science and Engineering: A,* vol. 584, pp. 63-66, 2013.

[37] L. T. Li, Y. C. Lin, H. M. Zhou, and Y. Q. Jiang, "Modeling the high-temperature creep behaviors of 7075 and 2124 aluminum alloys by continuum damage mechanics model," *Computational Materials Science,* vol. 73, pp. 72-78, Jun 2013.

[38] B. Z. Shakhashiri, "Chemical of the Week: Aluminum," *Science is Fun. Retrieved on,* pp. 08-28, 2007.

[39] J. R. Davis and J. R. Davis, *Aluminum and aluminum alloys*: ASM international, 1993.

[40] J. R. Davis, *Aluminum and aluminum alloys*: ASM international, 1993.

[41] I. Polmear, *Light alloys: from traditional alloys to nanocrystals*: Butterworth-Heinemann, 2005.

[42] M. Kral, H. McIntyre, and M. Smillie, "Identification of intermetallic phases in a eutectic Al–Si casting alloy using electron backscatter diffraction pattern analysis," *Scripta materialia,* vol. 51, pp. 215-219, 2004.

[43] I. Polmear, "Aluminium Alloys-A Century of Age Hardening," in *Materials forum*, 2004, pp. 1-14.

[44] J. W. Martin, *Precipitation hardening: theory and applications*: Butterworth-Heinemann, 2012.

[45] L. Rogal, J. Dutkiewicz, H. V. Atkinson, L. Litynska-Dobrzynska, T. Czeppe, and M. Modigell, "Characterization of semi-solid processing of aluminium alloy 7075 with Sc and Zr additions," *Materials Science And Engineering a-Structural Materials Properties Microstructure And Processing,* vol. 580, pp. 362-373, Sep 15 2013.

[46] M. Cabibbo, S. Spigarelli, and E. Evangelista, "A TEM investigation on the effect of semisolid forming on precipitation processes in an Al–Mg–Si Alloy," *Materials Characterization,* vol. 49, pp. 193-202, 2002.

[47] D. V. S. Rao, K. Muraleedharan, and C. J. Humphreys, "TEM specimen preparation techniques," pp. 1232-1244, 2010.
[48] H. Möller, G. Govender, W. E. Stumpf, and P. C. Pistorius, "Comparison of heat treatment response of semisolid metal processed alloys A356 and F357," *International Journal of Cast Metals Research,* vol. 23, pp. 37-43, 2010.
[49] D. Askeland and P. Fulay, *The Science & Engineering of Materials*: Cengage Learning, 2005.
[50] J. S. Association, "JIS H 5202:2010 Aluminium alloy castings," ed. Japan: Japanese Standards Association, 2010.
[51] K. R. Shi, S. Wisutmethangoon, J. Wannasin, and T. Plookphol, "Tensile Properties of Semi-Solid Die Cast AC4C Aluminum Alloy," *Applied Mechanics and Materials,* vol. 680, pp. 11-14, 2014.
[52] S. Janudom, J. Wannasin, J. Basem, and S. Wisutmethangoon, "Characterization of flow behavior of semi-solid slurries containing low solid fractions in high-pressure die casting," *Acta Materialia,* vol. 61, pp. 6267-6275, Sep 2013.
[53] T. Chucheep, J. Wannasin, R. Canyook, T. Rattanochaikul, S. Janudom, S. Wisutmethangoon, *et al.*, "Characterization of Flow Behavior of Semi-Solid Slurries with Low Solid Fractions," *Metallurgical And Materials Transactions a-Physical Metallurgy And Materials Science,* vol. 44A, pp. 4754-4763, Oct 2013.
[54] Y. C. Chen, A. Gholinia, and P. B. Prangnell, "Interface structure and bonding in abrasion circle friction stir spot welding: A novel approach for rapid welding aluminium alloy to steel automotive sheet," *Materials Chemistry And Physics,* vol. 134, pp. 459-463, May 15 2012.
[55] Y. Harada, S. Tamura, and S. Kumai, "Effects of High-Temperature Solutionizing on Microstructure and Tear Toughness of A356 Cast Aluminum Alloy," *Materials Transactions,* vol. 52, pp. 848-855, May 2011.
[56] T. Rattanochaikul, S. Janudom, N. Memongkol, and J. Wannasin, "Development of aluminum rheo-extrusion process using semi-solid slurry at low solid fraction," *Transactions Of Nonferrous Metals Society Of China,* vol. 20, pp. 1763-1768, Sep 2010.
[57] D. H. Choi, B. W. Ahn, C. Y. Lee, Y. M. Yeon, K. Song, and S. B. Jung, "Formation of intermetallic compounds in Al and Mg alloy interface during friction stir spot welding," *Intermetallics,* vol. 19, pp. 125-130, Feb 2011.
[58] R. Chiba, T. Nakamura, and M. Kuroda, "Solid-state recycling of aluminium alloy swarf through cold profile extrusion and cold rolling," *Journal Of Materials Processing Technology,* vol. 211, pp. 1878-1887, Nov 2011.
[59] S. Koyanaka and K. Kobayashi, "Automatic sorting of lightweight metal scrap by sensing apparent density and three-dimensional shape," *Resources Conservation And Recycling,* vol. 54, pp. 571-578, Jul 2010.
[60] W. Khalifa, Y. Tsunekawa, and M. Okumiya, "Effect of ultrasonic treatment on the Fe-intermetallic phases in ADC12 die cast alloy," *Journal Of Materials Processing Technology,* vol. 210, pp. 2178-2187, Nov 19 2010.
[61] L. Geng, L. N. Guan, and K. M. Lu, "Effects of whisker surface treatment on microstructure and properties of Al18B4O33w/6061Al composites," *Transactions Of Nonferrous Metals Society Of China,* vol. 20, pp. 349-354, Mar 2010.

[62] S. X. Dong, Y. Iwata, H. Hohjo, H. Iwahori, T. Yamashita, and H. Hirano, "Shell Mold Cracking and Its Prediction during Casting of AC4C Aluminum Alloy," *Materials Transactions,* vol. 51, pp. 1420-1427, Aug 2010.

[63] T. Chucheep, R. Burapa, S. Janudom, S. Wisutmethangoon, and J. Wannasin, "Semi-solid gravity sand casting using gas induced semi-solid process," *Transactions Of Nonferrous Metals Society Of China,* vol. 20, pp. S981-S987, Sep 2010.

[64] N. Omura, Y. Murakami, M. J. Li, T. Tamura, K. Miwa, H. Furukawa, *et al.*, "Effects of Mechanical Vibration on Macrostructure and Mechanical Properties of AC4C Aluminum Alloy Castings," *Materials Transactions,* vol. 50, pp. 2578-2583, Nov 2009.

[65] N. Omura, Y. Murakami, M. J. Li, T. Tamura, K. Miwa, H. Furukawa, *et al.*, "Effects of Mechanical Vibration on Cooling Rate and DAS of AC4C Aluminum Alloy Gravity Die Castings," *Materials Transactions,* vol. 50, pp. 2604-2608, Nov 2009.

[66] T. Chucheep, R. Canyook, T. Rattanochaikul, S. Janudom, S. Wisutmethangoon, and J. Wannasin, "A Fluidity Study of Semi-Solid Rheo-Slurry of AC4C Aluminum Alloy in Gravity Sand Casting," *Advanced Materials Research,* vol. 337, pp. 439-442, 2011.

[67] H. Yamagata, W. Kasprzak, M. Aniolek, H. Kurita, and J. H. Sokolowski, "The effect of average cooling rates on the microstructure of the Al–20% Si high pressure die casting alloy used for monolithic cylinder blocks," *Journal of Materials Processing Technology,* vol. 203, pp. 333-341, 2008.

[68] A. Ma, M. Takagi, N. Saito, H. Iwata, Y. Nishida, K. Suzuki, *et al.*, "Tensile properties of an Al–11mass%Si alloy at elevated temperatures processed by rotary-die equal-channel angular pressing," *Materials Science and Engineering: A,* vol. 408, pp. 147-153, 2005.

[69] Y. Nishida, H. Arima, and J.-c. Kim, "Rotary-die equal-channel angular pressing of an Al ± 7 mass % Si ± 0 . 35 mass % Mg alloy," vol. 45, pp. 261-266, 2001.

[70] H. D. Zhao, I. Ohnaka, and J. D. Zhu, "Modeling of mold filling of Al gravity casting and validation with X-ray in-situ observation," *Applied Mathematical Modelling,* vol. 32, pp. 185-194, Feb 2008.

[71] H. D. Zhao, F. Wang, Y. Y. Li, and W. Xia, "Experimental and numerical analysis of gas entrapment defects in plate ADC12 die castings," *Journal Of Materials Processing Technology,* vol. 209, pp. 4537-4542, May 1 2009.

[72] J.-C. Kim, Y. Nishida, H. Arima, and T. Ando, "Microstructure of Al–Si–Mg alloy processed by rotary-die equal channel angular pressing," *Materials Letters,* vol. 57, pp. 1689-1695, 2003.

[73] J. Pan, M. Yoshida, G. Sasaki, H. Fukunaga, H. Fujimura, and M. Matsuura, "Ultrasonic insert casting of aluminum alloy," *Scripta Materialia,* vol. 43, pp. 155-159, 2000.

[74] R. Kimura, M. Yoshida, G. Sasaki, J. Pan, and H. Fukunaga, "Influence of abnormal structure on the reliability of squeeze castings," *Journal Of Materials Processing Technology,* vol. 130, pp. 299-303, Dec 20 2002.

[75] N. Nicom and H. Nomura, "Melt infiltration of SiCp reinforced Al matrix composite by newly designed pressure infiltration technique," *Materials*

Science And Engineering a-Structural Materials Properties Microstructure And Processing, vol. 441, pp. 97-105, Dec 15 2006.

[76] J. P. Tu, "The solid particle erosion behavior of Al 18 B 4 O 33 whisker-reinforced AC4C al alloy matrix composites," pp. 22-30, 1998.

[77] J. P. Tu, J. Pan, H. X. Zhao, and H. Fukunaga, "Slurry erosion resistance of Al 18 B 4 O 33 whisker-reinforced AC4C Al alloy matrix composites," vol. 263, pp. 32-41, 1999.

[78] J. H. Lee, K. S. Kim, J. B. Lee, Y. S. Yang, and M. J. Yoo, "A numerical simulation model of cyclic hardening behavior of AC4C-T6 for LNG cargo pump using finite element analysis," *Journal Of Loss Prevention In the Process Industries,* vol. 22, pp. 889-896, Nov 2009.

[79] T. Miyazaki, H. Kang, H. Noguchi, and K. Ogi, "Prediction of high-cycle fatigue life reliability of aluminum cast alloy from statistical characteristics of defects at meso-scale," *International Journal Of Mechanical Sciences,* vol. 50, pp. 152-162, Feb 2008.

[80] A. J. McEvily, S. Ishihara, M. Endo, H. Sakai, and H. Matsunaga, "On one- and two-parameter analyses of short fatigue crack growth," *International Journal Of Fatigue,* vol. 29, pp. 2237-2245, Dec 2007.

[81] Y. C. Chen and K. Nakata, "Friction stir lap joining aluminum and magnesium alloys," *Scripta Materialia,* vol. 58, pp. 433-436, Mar 2008.

[82] Y. C. Chen, T. Komazaki, Y. G. Kim, T. Tsumura, and K. Nakata, "Interface microstructure study of friction stir lap joint of AC4C cast aluminum alloy and zinc-coated steel," *Materials Chemistry And Physics,* vol. 111, pp. 375-380, Oct 15 2008.

[83] S. Benke, S. Dziallach, G. Laschet, U. Prahl, and W. Bleck, "Modeling of the uniaxial tensile and compression behavior of semi-solid A356 alloys," *Computational Materials Science,* vol. 45, pp. 633-637, May 2009.

[84] C. M. Estey, S. L. Cockcroft, D. M. Maijer, and C. Hermesmann, "Constitutive behaviour of A356 during the quenching operation," *Materials Science And Engineering a-Structural Materials Properties Microstructure And Processing,* vol. 383, pp. 245-251, Oct 15 2004.

[85] M. J. Roy, D. M. Maijer, and L. Dancoine, "Constitutive behavior of as-cast A356," *Materials Science And Engineering a-Structural Materials Properties Microstructure And Processing,* vol. 548, pp. 195-205, Jun 30 2012.

[86] D. H. Kirkwood, M. Suéry, and P. Kapranos, *Semi-solid processing of alloys* vol. 124. Verlag Berlin Heidelberg: Springer, 2010.

[87] K. K. Wang, H. Peng, N. Wang, and S.-P. Wang, "Method and apparatus for injection molding of semi-solid metals," 1996.

[88] H. Jung and C. Kang, "A study on a thixoforming process using the thixotropic behavior of an aluminum alloy with an equiaxed microstructure," *Journal of materials engineering and performance,* vol. 9, pp. 530-535, 2000.

[89] J. Wannasin, R. A. Martinez, and M. C. Flemings, "Grain refinement of an aluminum alloy by introducing gas bubbles during solidification," *Scripta Materialia,* vol. 55, pp. 115-118, Jul 2006.

[90] T. Motegi and F. Tanabe, "New semi-solid casting of copper alloys using an inclined cooling plate," in *Proc. of 8th Int. Conf. on Semi-solid Processing of Alloys and Composites, Limmasol, Cyprus*, 2004.

[91] R. Canyook, S. Petsut, S. Wisutmethangoon, M. C. Flemings, and J. Wannasin, "Evolution of microstructure in semi-solid slurries of rheocast aluminum alloy," *Transactions Of Nonferrous Metals Society Of China,* vol. 20, pp. 1649-1655, Sep 2010.

[92] M. C. Flemings, "Behavior of metal alloys in the semisolid state," *Metallurgical transactions B,* vol. 22, pp. 269-293, 1991.

[93] J. Wannasin and S. Thanabumrungkul, "Development of a semi-solid metal processing technique for aluminium casting applications," *Songklanakarin Journal of Science Technology,* vol. 30, pp. 215-220, 2008.

[94] Y. Birol, "Semi-solid processing of the primary aluminium die casting alloy A365," *Journal Of Alloys And Compounds,* vol. 473, pp. 133-138, Apr 3 2009.

[95] L. BoChao, P. YoungKoo, and D. HongSheng, "Effects of rheocasting and heat treatment on microstructure and mechanical properties of A356 alloy," *Materials Science and Engineering: A,* vol. 528, pp. 986-995, 2011.

[96] G. H. Yan, S. D. Zhao, S. Q. Ma, and H. T. Shou, "Microstructural evolution of A356.2 alloy prepared by the SIMA process," *Materials Characterization,* vol. 69, pp. 45-51, Jul 2012.

[97] D. Abolhasani, H. R. Ezatpour, S. A. Sajjadi, and Q. Abolhasani, "Microstructure and mechanical properties evolution of 6061 aluminum alloy formed by forward thixoextrusion process," *Materials & Design,* vol. 49, pp. 784-790, Aug 2013.

[98] D. Ruvalcaba, R. Mathiesen, D. Eskin, L. Arnberg, and L. Katgerman, "In situ observations of dendritic fragmentation due to local solute-enrichment during directional solidification of an aluminum alloy," *Acta Materialia,* vol. 55, pp. 4287-4292, 2007.

[99] N. Iqbal, N. Van Dijk, S. Offerman, M. Moret, L. Katgerman, and G. Kearley, "Real-time observation of grain nucleation and growth during solidification of aluminium alloys," *Acta Materialia,* vol. 53, pp. 2875-2880, 2005.

[100] J. Wannasin, R. Canyook, R. Burapa, L. Sikong, and M. C. Flemings, "Evaluation of solid fraction in a rheocast aluminum die casting alloy by a rapid quenching method," *Scripta Materialia,* vol. 59, pp. 1091-1094, Nov 2008.

[101] R. Canyook, J. Wannasin, S. Wisuthmethangkul, and M. C. Flemings, "Characterization of the microstructure evolution of a semi-solid metal slurry during the early stages," *Acta Materialia,* vol. 60, pp. 3501-3510, May 2012.

[102] N. Mahathaninwong, S. Wisutmethangoon, T. Plookphol, J. Wannasin, and S. Chantaramanee, "Elevated Temperature Tensile Behavior of Rheo-Cast 7075-T6 Al Alloy Produced by GISS Technique," *Advanced Materials Research,* vol. 881-883, pp. 1597-1600, 2014.

[103] E. Giraud, M. Suery, and M. Coret, "High temperature compression behavior of the solid phase resulting from drained compression of a semi-solid 6061 alloy," *Materials Science And Engineering a-Structural Materials Properties Microstructure And Processing,* vol. 532, pp. 37-43, Jan 15 2012.

[104] A. B. Elshalakany, T. A. Osman, A. Khattab, B. Azzam, and M. Zaki, "Microstructure and Mechanical Properties of MWCNTs Reinforced A356 Aluminum Alloys Cast Nanocomposites Fabricated by Using a Combination of Rheocasting and Squeeze Casting Techniques," *Journal Of Nanomaterials,* vol. 2014, pp. 1-14, 2014.

[105] J. Jorstad, M. Thieman, and R. Kamm, "Fundamental Requirements for Slurry Generation in the Sub Liquidus Casting Process & The Economics of SLC™ Processing," in *Eighth International Conference on Semi-Solid Processing of Alloys and Composites,(Limassol, Cyprus)*, 2004.

[106] K. Young and P. Eisen, "SSM (semi-solid metal) technological alternatives for different applications," *Metallurgical Science and Tecnology,* vol. 18, 2013.

[107] S. Janudom, T. Rattanochaikul, R. Burapa, S. Wisutmethangoon, and J. Wannasin, "Feasibility of semi-solid die casting of ADC12 aluminum alloy," *Transactions Of Nonferrous Metals Society Of China,* vol. 20, pp. 1756-1762, Sep 2010.

[108] S. Thanabumrungkul, S. Janudom, R. Burapa, P. Dulyapraphant, and J. Wannasin, "Industrial development of gas induced semi-solid process," *Transactions of Nonferrous Metals Society of China,* vol. 20, pp. s1016-s1021, 2010.

[109] J. Wannasin, S. Janudom, T. Rattanochaikul, R. Canyook, R. Burapa, T. Chucheep, *et al.*, "Research and development of gas induced semi-solid process for industrial applications," *Transactions Of Nonferrous Metals Society Of China,* vol. 20, pp. S1010-S1015, Sep 2010.

[110] J. Wannasin, R. Canyook, S. Wisutmethangoon, and M. C. Flemings, "Grain refinement behavior of an aluminum alloy by inoculation and dynamic nucleation," *Acta Materialia,* vol. 61, pp. 3897-3903, Jun 2013.

[111] S. Kuntongkum, S. Wisutmethangoon, T. Plookphol, and J. Wannasin, "Influence of Heat Treatment Processing Parameters on the Hardness and the Microstructure of Semi-Solid Aluminum Alloy A356," *Journal of Metals, Materials and Minerals,* vol. 18, pp. 93-97, 2008.

[112] E. De Freitas, M. Ferrante, V. F. Da Silva, W. Bose Filho, and D. Spinelli, "Thixoextrusion of an A356 alloy: microstructural studies and high temperature fatigue behaviour," *Journal of Materials Processing Technology,* vol. 155-156, pp. 1629-1633, 2004.

[113] D. G. Eskin, Suyitno, and L. Katgerman, "Mechanical properties in the semi-solid state and hot tearing of aluminium alloys," *Progress In Materials Science,* vol. 49, pp. 629-711, 2004.

[114] N. Mahathaninwong, T. Plookphol, J. Wannasin, and S. Wisutmethangoon, "T6 heat treatment of rheocasting 7075 Al alloy," *Materials Science And Engineering a-Structural Materials Properties Microstructure And Processing,* vol. 532, pp. 91-99, Jan 15 2012.

[115] C. Xu, M. Furukawa, Z. Horita, and T. G. Langdon, "Using ECAP to achieve grain refinement, precipitate fragmentation and high strain rate superplasticity in a spray-cast aluminum alloy," *Acta Materialia,* vol. 51, pp. 6139-6149, 2003.

[116] O. Lashkari and R. Ghomashchi, "The implication of rheology in semi-solid metal processes: An overview," *Journal Of Materials Processing Technology,* vol. 182, pp. 229-240, Feb 2 2007.

[117] C. M. Dinnis, J. A. Taylor, and A. K. Dahle, "As-cast morphology of iron-intermetallics in Al–Si foundry alloys," *Scripta Materialia,* vol. 53, pp. 955-958, 2005.

[118] A. M. Gokhale and G. R. Patel, "Analysis of variability in tensile ductility of a semi-solid metal cast A356 Al-alloy," *Materials Science And Engineering a-*

Structural Materials Properties Microstructure And Processing, vol. 392, pp. 184-190, Feb 15 2005.

[119] L. Ceschini, A. Morri, and G. Sambogna, "The effect of hot isostatic pressing on the fatigue behaviour of sand-cast A356-T6 and A204-T6 aluminum alloys," *Journal Of Materials Processing Technology,* vol. 204, pp. 231-238, Aug 11 2008.

[120] H. MÖLler, G. Govender, and W. E. Stumpf, "Application of shortened heat treatment cycles on A356 automotive brake calipers with respective globular and dendritic microstructures," *Transactions of Nonferrous Metals Society of China,* vol. 20, pp. 1780-1785, 2010.

[121] P. Cavaliere, E. Cerri, and P. Leo, "Effect of heat treatments on mechanical properties and damage evolution of thixoformed aluminium alloys," *Materials Characterization,* vol. 55, pp. 35-42, Jul 2005.

[122] J. Sieniawski and M. Wierzbińska, "Analysis of intermetallic particles in AlSi1MgMn aluminium alloy," *Journal of Achievements in Materials and Manufacturing Engineering,* vol. 20, pp. 7-8, 2007.

[123] H. V. Atkinson and D. Liu, "Microstructural coarsening of semi-solid aluminium alloys," *Materials Science And Engineering a-Structural Materials Properties Microstructure And Processing,* vol. 496, pp. 439-446, Nov 25 2008.

[124] Z. Ma, A. M. Samuel, F. H. Samuel, H. W. Doty, and S. Valtierra, "A study of tensile properties in Al–Si–Cu and Al–Si–Mg alloys: Effect of β-iron intermetallics and porosity," *Materials Science and Engineering: A,* vol. 490, pp. 36-51, 2008.

[125] Y. C. Yu, W. Q. Chen, and H. G. Zheng, "Effects of Ti-Ce refiners on solidification structure and hot ductility of Fe-36Ni invar alloy," *Journal Of Rare Earths,* vol. 31, pp. 927-932, Sep 2013.

[126] S. G. Shabestari, "The effect of iron and manganese on the formation of intermetallic compounds in aluminum–silicon alloys," *Materials Science and Engineering: A,* vol. 383, pp. 289-298, 2004.

[127] D. Meccanica and U. Ancona-italy, "Metallography of Aluminium alloys Metallography of Aluminium alloys," 1999.

[128] G. Ran, J. G. Zhou, and Q. G. Wang, "The effect of hot isostatic pressing on the microstructure and tensile properties of an unmodified A356-T6 cast aluminum alloy," *Journal Of Alloys And Compounds,* vol. 421, pp. 80-86, Sep 14 2006.

[129] R. Akhter, L. Ivanchev, and H. P. Burger, "Effect of pre/post T6 heat treatment on the mechanical properties of laser welded SSM cast A356 aluminium alloy," *Materials Science And Engineering a-Structural Materials Properties Microstructure And Processing,* vol. 447, pp. 192-196, Feb 25 2007.

[130] H. C. Long, J. H. Chen, C. H. Liu, D. Z. Li, and Y. Y. Li, "The negative effect of solution treatment on the age hardening of A356 alloy," *Materials Science And Engineering a-Structural Materials Properties Microstructure And Processing,* vol. 566, pp. 112-118, Mar 20 2013.

[131] H. Möller, G. Govender, and W. E. Stumpf, "Investigation of the T4 and T6 Heat Treatment Cycles of Semi-Solid Processed Aluminium Alloy A356," pp. 11-18, 2008.

[132] H. Möller, G. Govender, and W. E. Stumpf, "The Natural and Artificial Aging Response of Semi-solid Metal Processed Alloy A356," vol. 143, pp. 737-742,

2008.
[133] C. H. Caceres, J. R. Griffiths, and P. Reiner, "The influence of microstructure on the Bauschinger effect in an Al-Si-Mg casting alloy," *Acta Materialia,* vol. 44, pp. 15-23, Jan 1996.
[134] G. B. Burger, A. K. Gupta, P. W. Jeffrey, and D. J. Lloyd, "Microstructural Control Of Aluminum Sheet Used In Automotive Applications," *Materials Characterization,* vol. 35, pp. 23-39, Jul 1995.
[135] G. A. Edwards, K. Stiller, G. L. Dunlop, and M. J. Couper, "The precipitation sequence in Al-Mg-Si alloys," *Acta Materialia,* vol. 46, pp. 3893-3904, Jul 1 1998.
[136] Y. B. Yu, P. Y. Song, S. S. Kim, and J. H. Lee, "Semi-Solid processed A356 Alloy by a post heat treatment at an extremently high temperature," *Scripta Materialia,* vol. 41, pp. 767-771, 1999.
[137] E. Ogris, A. Wahlen, H. Lüchinger, and P. J. Uggowitzer, "On the silicon spheroidization in Al–Si alloys," *Journal of Light Metals,* vol. 2, pp. 263-269, 2002.
[138] W. M. Jiang, Z. T. Fan, and D. J. Liu, "Microstructure, tensile properties and fractography of A356 alloy under as-cast and T6 obtained with expendable pattern shell casting process," *Transactions Of Nonferrous Metals Society Of China,* vol. 22, pp. S7-S13, Oct 2012.
[139] H. Liao, Y. Wu, and K. Ding, "Hardening response and precipitation behavior of Al–7%Si–0.3%Mg alloy in a pre-aging process," *Materials Science and Engineering: A,* vol. 560, pp. 811-816, 2013.
[140] Y. Zhou, T. Plookphol, and S. Wisutmethangoon, "HIGH-TEMPERATURE TENSILE PROPERTIES OF SEMI-SOLID ALUMINIUM ALLOY A356-T6 PRODUCED BY THE GISS PROCESS," *infor.eng.psu.ac.th,* pp. 4-7.
[141] E.-S. Y. El-Kady, T. S. Mahmoud, and M. A.-A. Sayed, "Elevated Temperatures Tensile Characteristics of Cast A356/Al₂O₃ Nanocomposites Fabricated Using a Combination of Rheocasting and Squeeze Casting Techniques," *Materials Sciences and Applications,* vol. 02, pp. 390-398, 2011.
[142] T. A. Khalifa and T. S. Mahmoud, "Elevated Temperature Mechanical Properties of Al Alloy AA6063 / SiC p MMCs," vol. II, pp. 1-6, 2009.
[143] S. Wilson, "Effect of temperature on the sliding wear performance of A1 alloys and A1 matrix composites," vol. 196, pp. 270-278, 1996.
[144] S. P. Midson, "Advanced Technology Minimizing Blistering During T6 Heat Treating of Semi-Solid Castings," pp. 40-43, 2011.
[145] S. W. Youn and C. G. Kang, "Characterization of age-hardening behavior of eutectic surface on rheo-cast A356-T5 alloy by using nano/micro-indentation, scratching and atomic force microscopy," *Materials Chemistry And Physics,* vol. 100, pp. 117-123, Nov 10 2006.
[146] T. G. Induced, "SSM / Squeeze Casting Semi-solid Die Casting using the Gas Induced Semi-Solid (GISS) Technique," pp. 36-40, 2012.
[147] Y. C. Lin, Y.-C. Xia, X.-S. Ma, Y.-Q. Jiang, and M.-S. Chen, "High-temperature creep behavior of Al–Cu–Mg alloy," *Materials Science and Engineering: A,* vol. 550, pp. 125-130, 2012.

[148] M. T. Whittaker, M. Evans, and B. Wilshire, "Long-term creep data prediction for type 316H stainless steel," *Materials Science And Engineering a-Structural Materials Properties Microstructure And Processing,* vol. 552, pp. 145-150, Aug 30 2012.

[149] T. Lecture and F. A. Level, "Creep of Aluminium and Aluminium Alloys," 1999.

[150] S. V. Raj and A. D. Freed, "A phenomenological description of primary creep in class M materials," *Materials Science and Engineering: A,* vol. 283, pp. 196-202, 2000.

[151] A. Yousefiani, F. A. Mohamed, and J. C. Earthman, "Creep Rupture Mechanisms in Annealed and Overheated 7075 Al under Multiaxial Stress States," vol. 31, pp. 2807-2821, 2000.

[152] B. Wilshire and A. J. Battenbough, "Creep and creep fracture of polycrystalline copper," *Materials Science And Engineering A,* vol. 443, pp. 156-166, Jan 15 2007.

[153] C. G. Panait, T. Koziel, A. Czyrska-filemonowicz, and W. Bendick, "Evolution of dislocation density , size of subgrains and MX-type precipitates in a P91 steel during creep and during thermal ageing at 600 ◦ C for more," vol. 527, pp. 4062-4069, 2010.

[154] C. G. Panait, A. Zielińska-Lipiec, T. Koziel, A. Czyrska-Filemonowicz, A.-F. Gourgues-Lorenzon, and W. Bendick, "Evolution of dislocation density, size of subgrains and MX-type precipitates in a P91 steel during creep and during thermal ageing at 600C for more than 100,000h," *Materials Science and Engineering: A,* vol. 527, pp. 4062-4069, 2010.

[155] K. Nogita and A. K. Dahle, "Eutectic solidification in hypoeutectic Al–Si alloys: electron backscatter diffraction analysis," *Materials Characterization,* vol. 46, pp. 305-310, 2001.

[156] Y. Hammi and M. F. Horstemeyer, "A physically motivated anisotropic tensorial representation of damage with separate functions for void nucleation, growth, and coalescence," *International Journal Of Plasticity,* vol. 23, pp. 1641-1678, 2007.

[157] F. A. Mohamed, "On creep behavior in powder metallurgy 6061 Al," *Scripta Materialia,* vol. 38, pp. 457-463, Jan 6 1998.

[158] B. F. Dyson, "Creep And Fracture Of Metals - Mechanisms And Mechanics," *Revue De Physique Appliquee,* vol. 23, pp. 605-613, Apr 1988.

[159] R. Evans and P. Scharning, "The θ projection method applied to small strain creep of commercial aluminium alloy," *Materials science and technology,* vol. 17, pp. 487-493, 2001.

[160] F. R. N. Nabarro and F. De Villiers, *Physics of creep and creep-resistant alloys*: CRC press, 1995.

[161] H. Uchida and T. Shinya, "Estimation of creep deformation behavior in Mg-Al alloys by using theta projection method," *Journal of Japan Institute of Light Metals(Japan),* vol. 45, pp. 572-577, 1995.

[162] J. Weertman, "Steady-State Creep through Dislocation Climb," *Journal of Applied Physics,* vol. 28, pp. 362-364, 1957.

[163] T. Gladman, "Precipitation hardening in metals," *Materials Science And Technology,* vol. 15, pp. 30-36, Jan 1999.

[164] J. Weertman, "Theory of Steady-State Creep Based on Dislocation Climb,"

Journal of Applied Physics, vol. 26, pp. 1213-1217, 1955.
[165] A. Usui, H. Sunakawa, A. Sakai, and A. A. Yamaguchi, "Thick GaN epitaxial growth with low dislocation density by hydride vapor phase epitaxy," *Japanese Journal Of Applied Physics Part 2-Letters*, vol. 36, pp. L899-L902, Jul 15 1997.
[166] Y. C. Lin, Y. C. Xia, M. S. Chen, Y. Q. Jiang, and L. T. Li, "Modeling the creep behavior of 2024-T3 Al alloy," *Computational Materials Science*, vol. 67, pp. 243-248, Feb 2013.
[167] C. M. Omprakash, A. Kumar, B. Srivathsa, and D. V. V. Satyanarayana, "Prediction of Creep Curves of High Temperature Alloys using θ -Projection Concept," *Procedia Engineering*, vol. 55, pp. 756-759, 2013.
[168] D. L. McDowell and F. P. E. Dunne, "Microstructure-sensitive computational modeling of fatigue crack formation," *International Journal Of Fatigue*, vol. 32, pp. 1521-1542, Sep 2010.
[169] Evans, "A constitutive model for the high-temperature creep of particle-hardened the theta projection.," 2000.
[170] H. Burt and B. Wilshire, "Theoretical and practical implications of creep curve shape analyses for 2124 and 2419," *Metallurgical and Materials Transactions A*, vol. 35, pp. 1691-1701, 2004.
[171] H. Burt and B. Wilshire, "Theoretical and practical implications of creep curve shape analyses for 8090," *Metallurgical and Materials Transactions A*, vol. 36, pp. 1219-1227, 2005.
[172] S.-M. Zhu, J. Nie, and B. Mordike, "Creep and rupture properties of a squeeze-cast Mg-Al-Ca alloy," *Metallurgical and Materials Transactions A*, vol. 37, pp. 1221-1229, 2006.
[173] Y. Estrin and A. Vinogradov, "Extreme grain refinement by severe plastic deformation: A wealth of challenging science," *Acta Materialia*, vol. 61, pp. 782-817, Feb 2013.
[174] L. Proville, D. Rodney, and M. C. Marinica, "Quantum effect on thermally activated glide of dislocations," *Nat Mater*, vol. 11, pp. 845-9, Oct 2012.
[175] P. Leo, S. Spigarelli, E. Cerri, and M. El Mehtedi, "High temperature mechanical properties of an aluminum alloy containing Zn and Mg," *Materials Science And Engineering a-Structural Materials Properties Microstructure And Processing*, vol. 550, pp. 206-213, Jul 30 2012.
[176] J. Almer and S. Stock, "Internal strains and stresses measured in cortical bone via high-energy X-ray diffraction," *Journal of structural biology*, vol. 152, pp. 14-27, 2005.
[177] S. Straub, W. Blum, H. J. Majer, T. Ungar, A. Borbely, and H. Renner, "Long-range internal stresses in cell and subgrain structures of copper during deformation at constant stress," *Acta Materialia*, vol. 44, pp. 4337-4350, Nov 1996.
[178] L. Brewer, M. Othon, L. Young, and T. Angeliu, "Misorientation mapping for visualization of plastic deformation via electron back-scattered diffraction," *Microscopy and Microanalysis*, vol. 12, pp. 85-91, 2006.
[179] D. Mainprice, J. Bascou, P. Cordier, and A. Tommasi, "Crystal preferred orientations of garnet: comparison between numerical simulations and electron back-scattered diffraction (EBSD) measurements in naturally deformed eclogites," *Journal of Structural Geology*, vol. 26, pp. 2089-2102, 2004.

[180] Q. G. Wang, "Microstructural effects on the tensile and fracture behavior of aluminum casting alloys A356/357," *Metallurgical And Materials Transactions A-physical Metallurgy And Material,* vol. 34A, pp. 2887-2899, Dec 2003.
[181] C. H. Caceres, C. J. Davidson, and J. R. Griffiths, "The deformation and fracture behaviour of an Al-Si-Mg casting alloy," *Materials Science and Engineering A,* vol. 197, pp. 171-179, Jul 1 1995.
[182] M. Hitchcock, Y. Wang, and Z. Fan, "Secondary solidification behaviour of the Al–Si–Mg alloy prepared by the rheo-diecasting process," *Acta Materialia,* vol. 55, pp. 1589-1598, 2007.
[183] X. Fang, M. Song, K. Li, and Y. Du, "Precipitation Sequence Of an Aged Al-Mg-Si Alloy," *Journal Of Mining And Metallurgy Section B,* vol. 46, pp. 171-180, 2010.
[184] N. Maruyama, R. Uemori, N. Hashimoto, M. Saga, and M. Kikuchi, "Effect of Silicon addition on the composition stiructure of fine -scale precipitation in Al-Mg-Si Alloys," *Scripta Materialia,* vol. 36, pp. 89-93, 1997.
[185] A. K. Gupta, D. J. Lloyd, and S. A. Court, "Precipitation hardening in Al–Mg–Si alloys with and without excess Si," *Materials Science and Engineering A,* vol. 316, pp. 11-17, 2001.
[186] M. M. Makhlouf and H. V. Guthy, "The aluminum-silicon eutectic reaction : mechanisms and crystallography," *Journal of Light Metals,* vol. 1, pp. 199-218, 2002.
[187] L. T. Jiang, G. H. Wu, W. S. Yang, Y. G. Zhao, and S. S. Liu, "Effect of heat treatment on microstructure and dimensional stability of ZL114A aluminum alloy," *Transactions Of Nonferrous Metals Society Of China,* vol. 20, pp. 2124-2128, Nov 2010.
[188] G. Rajaram, S. Kumaran, and T. S. Rao, "High temperature tensile and wear behaviour of aluminum silicon alloy," *Materials Science and Engineering A,* vol. 528, pp. 247-253, Nov 25 2010.
[189] M. E. Kassner and M. T. Pérez-Prado, "Five-power-law creep in single phase metals and alloys," *Progress in Materials Science,* vol. 45, pp. 1-102, 2000.
[190] J. C. Dandrea and R. Lakes, "Creep and creep recovery of cast aluminum alloys," *Mechanics Of Time-Dependent Materials,* vol. 13, pp. 303-315, Nov 2009.
[191] A. Orozco-Caballero, S. K. Menon, C. M. Cepeda-Jiménez, P. Hidalgo-Manrique, T. R. McNelley, O. A. Ruano, *et al.*, "Influence of microstructural stability on the creep mechanism of Al–7wt% Si alloy processed by equal channel angular pressing," *Materials Science and Engineering: A,* vol. 612, pp. 162-171, 2014.
[192] H. J. McQueen and W. Blum, "Dynamic recovery: sufficient mechanism in the hot deformation of Al (<99.99)," *Materials Science and Engineering A,* vol. 290, pp. 95-107, 2000.
[193] Y. D. Chen, D. Q. Yi, S. P. Pan, H. Xia, and Z. X. Huang, "Effect of temperature on creep behavior of 2024 aluminum alloy," *The Chinese Journal of Nonferrous Metals,* vol. 20, pp. 632-639, 2010.

APPENDIX A

Applied Mechanics and Materials
ISSN: 1662-7482, Vol. 680, pp 11-14
doi:10.4028/www.scientific.net/AMM.680.11
© 2014 Trans Tech Publications, Switzerland

Submitted: 2014-07-08
Accepted: 2014-07-09
Online: 2014-10-20

Tensile Properties of Semi-Solid Die Cast AC4C Aluminum Alloy

Keren Shi[1,2,a], Sirikul Wisutmethangoon[3,b], Jessada Wannasin[2,c] and Thawatchai Plookphol[2,d]

[1]State Key Laboratory Cultivation Base of Natural Gas Conversion, Ningxia University, Yinchuan 750021, China

[2]Department of Mining and Materials Engineering, Faculty of Engineering, Prince of Songkla University, Hat Yai 90112, Thailand

[3]Department of Mechanical Engineering, Faculty of Engineering, Prince of Songkla University, Hat Yai 90112, Thailand

[a]shikeren@163.com, [b]sirikul@me.psu.ac.th, [c]jessada@alum.mit.edu, [d]thawatchai.p@psu.ac.th

Keywords: AC4C; tensile properties; fracture; GISS; die casting.

Abstract. In this study, semi-solid Al-Mg-Si alloy (AC4C) was produced by using the Gas Induced Semi-Solid (GISS) die casting process. The tensile strength and ductility of the semi-solid die cast Al alloy (GISS-DC) after T6 heat treatment were investigated and compared with those of the conventional liquid die casting (CLDC). The microstructures of GISS-DC and CLDC observed by an optical microscopy were presented. The ultimate tensile strength (UTS) and yield strength (0.2% YS) of GISS-DC are compatible with those of the CLDC. However, the GISS-DC has better ductility than the CLDC, this may be due to the smaller and more globular primary α-Al phase and rounder shaped-Si particle microstructures presented in the GISS-DC. Common shrinkage pores and defects were also observed by SEM from the fracture surfaces of both alloys.

Introduction

Semi-solid metal (SSM) technology has been continuously developed to produce Al alloys with uniform microstructures and better mechanical properties for the automotive industry. There are two major processing types of SSM: thixocasting and rheocasting [1]. A lot of research works have been focused on SSM processing as a way to cast near-net-shape products [2]. Gas Induced Semi-Solid (GISS) technique which was invented by the Innovative Metal Technology (IMT) team at Prince of Songkla University, Thailand is a novel, simple, economical and efficient rheocasting process which has succeeded to produce globular structure in many alloys [3,4]. Although many previous research works were focused on the properties of GISS squeeze cast alloys [5,6], only a few on the properties of SSM alloy produced by using GISS die casting process. So, the purpose of this work was to investigate the tensile property and microstructures of the SSM Al-Mg-Si alloy (AC4C) produced by the GISS die casting.

Experiment

Materials. The chemical composition of AC4C aluminum alloy produced by the GISS die casting (GISS-DC) and the conventional liquid die casting (CLDC) was shown in Table 1. During the GISS-DC, the aluminum alloy was melted in a graphite crucible in an electric furnace at 680 °C before casting. Approximately 200 g of the melt was taken out from the crucible using a ladle cup. Then, the nitrogen gas was injected through a graphite diffuser into the ladle when the rheocasting temperature (RCT) of the melt was about 616 °C, for about 10 seconds to create a semi-solid slurry with a low solid fraction of about 10% [1]. The schematic diagram of the GISS process was shown in Fig. 1. The SSM slurry was transferred to the die casting machine and then poured into the shot sleeve for die casting. The temperature of shot sleep and die was kept at 200 °C. The schematic diagram of

All rights reserved. No part of contents of this paper may be reproduced or transmitted in any form or by any means without the written permission of Trans Tech Publications, www.ttp.net. (#74607479-21/02/17,06:36:04)

the GISS-DC process was illustrated in Fig. 2. For the CLDC process, the ingot of AC4C Al alloy was melted at 680 °C, then the melt was poured into shot sleeve for die casting.

Table 1 Chemical composition of GISS-DC and CLDC aluminum alloys

Elements	Si	Fe	Cu	Mn	Mg	Zn	Ti	Cr	Ni	Pb	Al
CLDC	7.543	0.456	0.063	0.063	0.381	0.088	0.016	0.014	0.010	0.004	Bal.
GISS-DC	7.996	0.488	0.063	0.039	0.364	0.089	0.014	0.014	0.009	0.003	Bal.

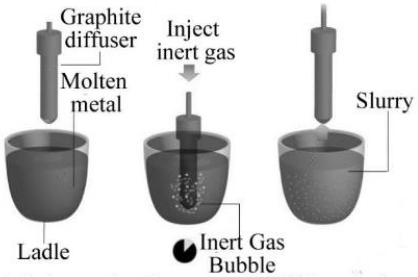

Fig. 1 Schematic diagram of GISS technique [7].

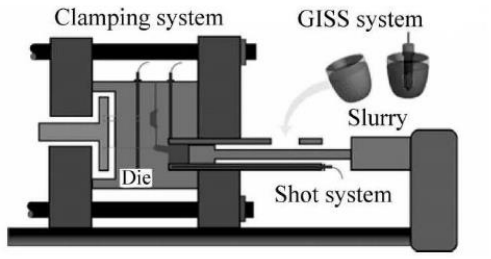

Fig. 2 Schematic diagram of GISS die casting process [8].

Tensile test. AC4C Al alloy produced by GISS-DC and CLDC were heat treated to T6 designation by a solution treatment at 540 °C for 4 h and artificially aged at 195 °C for 3 h after [3]. Tensile test was followed the ASTM E8-08 standard. Tensile specimens were prepared from GISS-DC and CLDC AC4C-T6 bars by machining. The dimensions of specimen were shown in Fig. 3. Tensile tests were performed in a universal testing machine, HOUNSFILELD Model H100KS, Serial No. 0068, using a constant cross-head speed of 1.5 mm/min, corresponding to a strain rate of 1×10^{-3} s^{-1}.

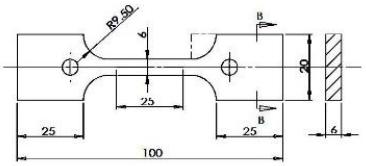

Fig. 3 Dimensions of tensile test specimen.

Results and Discussion

Microstructures. The microstructures of CLDC AC4C-T6 aluminum alloy (Fig. 4b) were composed of α-aluminum dendrites, eutectic silicon particles and Fe-bearing intermetallic compounds. While the rosaceous and globular primary α-aluminum phase and rounder shaped silicon particles were found in the GISS-DC AC4C-T6 (Fig. 4a).

Tensile test. The ultimate tensile strength (UTS), yield strength (0.2%YS) and eloangation of the GISS-DC AC4C-T6 were compared with those of CLDC AC4C-T6 in Fig. 5, and listed in Table 2. At room temperature, the GISS-DC gained the UTS and 0.2% YS of 294.4 MPa and 241.5 MPa while the CLDC gained 298.2 MPa and 251.6 MPa, reperatively. The averaged UTS and 0.2% YS of CLDC are slightly higher than those of GISS-DC. The elongation of GISS-DC and CLDC are 5.9% and

4.8%, respectively. The result shows that GISS-DC is more ductile than CLDC. This may be resulted from the fact that the GISS-DC microstructures are composed of smaller and more globular primary α-Al phase and rounder shaped-silicon particles when compared with the CLDC.

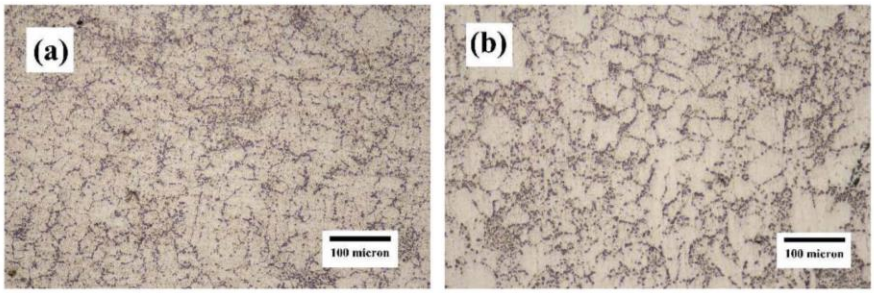

Fig. 4 Optical micrographs of (a) GISS-DC AC4C-T6 Al alloy and (b) CLDC AC4C-T6 Al alloy.

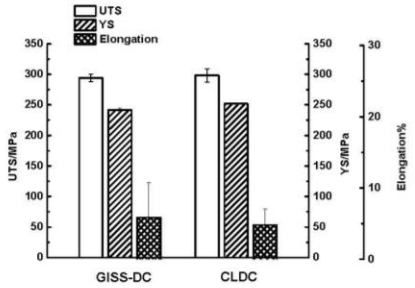

Fig. 5 Comparison of ultimate tensile strength (UTS), yeild stress (0.2% YS) and elongation of GISS-DC and CLDC AC4C-T6 aluminum alloys.

Table 2 Ultimate tensile strength (UTS), yield strength (0.2% YS) and elongation of GISS-DC and CLDC AC4C-T6 aluminum alloys.

Materials	UTS (MPa)	0.2%YS (MPa)	Elongation (%)
GISS-DC AC4C-T6	294.4±6.1	241.5±2.9	5.9±4.9
CLDCAC4C-T6	298.2±10.8	251.6±1.1	4.8±2.2

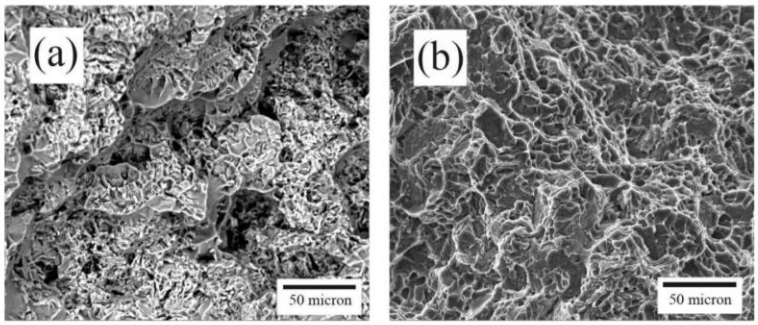

Fig. 6 SEM micrographs of fractured surfaces of (a) GISS-DC AC4C-T6 and (b) CLDC AC4C–T6 after tensile tests.

Fractography. The fractured surfaces of specimens after tensile tests were shown in Fig 6. At room temperaure, both GISS-DC and CLDC AC4C-T6 were fractured in the brittle mode of quasi-cleavage form. The GISS-DC was more dimple structure. When the applied stress was increased, the internal stress was developed at Si particle and approached to its fracture stress, crack was initiated at the Si particle as observed on the fractured surface. Some common shrinkage pores and defects were also found in the fractures in both types of specimens.

Summary

1. The semi-solid AC4C aluminum alloy can be produced by using the GISS die casting process.
2. The UTS and 0.2% YS of both GISS-DC and CLDC are almost the same.
3. The GISS-DC gains more ductility than the CLDC. This may be resulted from the microstructures of GISS-DC, which are composed of smaller and more globular primary α-Al phase and rounder shaped-silicon particles.
4. Both GISS-DC and CLDC are fractrued in the brittle mode of quasi- cleavage at room temperature.

Acknowledgement

The authors would like to thank the Department of Mining and Materials Engineering, Faculty of Engineering, Prince of Songkla University. The authors acknowledge the president scholarship from the President Office of Prince of Songkla University. This work was supported by the Higher Education Research Promotion and National Research University Project of Thailand, Office of the Higher Education Commission.

References

[1] R. Burapa, S. Janudom, T. Chucheep, R. Canyook, J. Wannasin, Effects of primary phase morphology on mechanical properties of Al-Si-Mg-Fe alloy in semi-solid slurry casting process, T. Nonferr. Metal. Soc. 20 (2010) 857-861.

[2] S. Tahamtan, M.A. Golozar, F. Karimzadeh, B. Niroumand, Microstructure and tensile properties of thixoformed A356 alloy, Mater. Charact. 59 (2008) 223-228.

[3] J. Wannasin, R. Martinez, M. Flemings, Grain refinement of an aluminum alloy by introducing gas bubbles during solidification, Scripta Mater. 55 (2006) 115-118.

[4] S. Wisutmethangoon, S. Thongjan, N. Mahathaninwong, T.Plookphol, J. Wannasin, Precipitation hardening of A356 Al alloy produced by gas induced semi-solid process, Mat. Sci. Eng. A 532 (2012) 610-615.

[5] Q.G. Wang, Microstructural Effects on the Tensile and Fracture Behavior of Aluminum Casting Alloys A356/357, Metall. Mater. Trans. A 34 (2003) 2887-2899.

[6] G. Ran, J.E. Zhou, Q.G. Wang, Precipitates and tensile fracture mechanism in a sand cast A356 aluminum alloy, J. Mater. Process. Technol. 207 (2008) 46-52.

[7] T. Rattanochaikul, S. Janudom, N. Memongkol, J. Wannasin, Development of aluminum rheo-extrusion process using semi-solid slurry at low solid fraction, T. Nonferr. Metal. Soc. 20 (2010) 1763-1768.

[8] J. Wannasin, S. Thanabumrungkul, Development of a semi-solid metal processing technique for aluminum casting applications, Songklanakarin J. Sci. Technol. 30 (2008) 215-220.

APPENDIX B

INTERNATIONAL JOURNAL OF CAST METALS RESEARCH, 2017
VOL. 30, NO. 3, 180–190
https://doi.org/10.1080/13640461.2017.1286551

Taylor & Francis
Taylor & Francis Group

Variation of microstructure and mechanical property of slurry die cast Al-Si-Mg-Fe alloy

Keren Shi[a,b], Sirikul Wisutmethangoon[c], Somjai Janudom[b] and Thawatchai Plookphol[b]

[a]State Key Laboratory Cultivation Base of Natural Gas Conversion, Ningxia University, Yinchuan, China; [b]Faculty of Engineering, Department of Mining and Materials Engineering, Prince of Songkla University, Hat Yai, Thailand; [c]Faculty of Engineering, Department of Mechanical Engineering, Prince of Songkla University, Hat Yai, Thailand

ABSTRACT

Semi-solid metal processing technologies have been intensively studied in recent years. Gas Induced Semi-Solid (GISS) is a slurry preparation technique for producing non-dendritic or globular structures for cast alloys. In the present study, GISS technique was used in conjunction with conventional die cast process for casting Al–Si–Mg–Fe alloy. The shape of die cast specimen was designed as a simple flat plate. The variation of microstructures and tensile properties of specimens from different locations of cast plates was studied. The results show that the specimens from bottom location, near the gate section and the middle location of cast plates are stronger and more ductility than those from the top location. The microstructural examination reveals that the specimens from top location of cast plates contain more defects, such as shrinkage pores than those from the other locations. These defects are resulted in lower strength and ductility of the cast product.

ARTICLE HISTORY
Received 29 December 2015
Accepted 18 January 2017

KEYWORDS
Semi-solid; SSM; GISS; die casting; Al alloys; AC4C

1. Introduction

Light structural metal, Al–Si–Mg–Fe alloy (AC4C, JIS standard) has some advantages such as good fluidity and mechanical properties. AC4C plays an important role in the metal casting industry [1–7]. It is widely used in automotive industries. There are good wear resistance and castability in the eutectic Al–Si alloys [6]. Mg is added into Al–Si alloys because of its good solubility to improve strength of the alloy [5]. Fe is also added into Al–Si alloys to form intermetallic phases with Al and Si, or Mg to reduce defects such as erosion and shrinkage during the die casting process [6].

For commercial castings, the formation of finer equiaxed grain structure in a semi-solid metal (SSM) alloy improves fluidity and produces less porosity and hot tearing in the cast products, which leads to better physical properties than coarse dendritic structure [8]. It has been reported that finer equiaxed grain structure can be formed by using gas bubbles to agitate a molten metal during the solidification process. This slurry forming technique was called Gas Induced Semi-Solid, or GISS [8]. In recent years, many GISS researches have been focused on forming metal slurry with low solid fraction ($f_s < 0.25$). After a minor modification, GISS technique was successfully used in conjunction with standard casting processes such as gravity casting, squeeze casting, die casting, and rheo-extrusion processes. Many SSM aluminium alloys and zinc alloy, including A356, A380, A383, 5052, 6061, 2024, 7075, and ZAMAK-3, can be produced using GISS technology [9–14]. Moreover, several application products have been manufactured by using GISS with die casting process (GISS-DC), such as an automotive rotor cover, a prosthesis tube adaptor, and a prosthesis foot adaptor [9–14].

Although it is known that process parameters, such as die design, plunger speed, die temperature and pressure, have to be strictly controlled in the die casting process. The products from the die cast process still exhibit non-uniform structures and low mechanical properties. The die casting process is widely used because of its low production cost. It was previously reported that the production cost of GISS-DC process could be lower than that of the conventional die casting [9]. Since GISS-DC process operates at lower temperature, consumes less heat, and uses shorter cycle time. Moreover, GISS-DC process is able to cast thicker and larger components [10]. Many researches on GISS processing have been focused on die casting applications [14]. Recently, flow behavior of GISS-DC was studied for AC4C alloy at different rheocasting times and plunger velocities. The flow behavior of the slurry depends on the initial solid fraction (f_s) and the gate velocity (V_g) of the slurry. With an appropriate control the ratio of V_g/f_s, it is able to reduce the defects, such as gas and shrinkage porosities in the GISS-DC product

CONTACT Thawatchai Plookphol thawatchai.p@psu.ac.th

© 2017 Informa UK Limited, trading as Taylor & Francis Group

Table 1. Chemical compositions of AC4C alloy.

Elements	Si	Fe	Cu	Mn	Mg	Zn	Ti	Cr	Ni	Pb	Al
wt-%	8.0	0.49	0.06	0.04	0.36	0.09	0.01	0.01	0.01	0.0031	Bal.

[15]. However, experimental data, such as microstructure homogeneity which has impact on the GISS-DC product for aluminium alloys are very little known [10]. Therefore, it is important to understand microstructural defects which are formed in the GISS-DC product. The purpose of this work is to investigate the impact of microstructures with respected to the location of die-cast parts on tensile properties of AC4C alloy.

2. Experimental

2.1. Materials

Commercial AC4C aluminium alloy used in this study was obtained from Daiki Aluminium Industry (Thailand) Co., Ltd., Chonburi, Thailand. The chemical compositions of alloy are shown in Table 1.

2.2. Casting

Aluminium alloy ingots were first melted in a graphite crucible using an electric furnace at temperature of 700 °C. The molten alloy in the amount of about 200 g was taken from the graphite crucible using a steel ladle cup. The nitrogen gas bubbles were injected into the melt at temperature of 616 °C through a graphite diffusor for 10 s. The schematic diagram of GISS process is shown in Figure 1. After nitrogen gas bubbling, the alloy slurry was then transferred and poured into the shot sleeve. The slurry was pushed into the die cavity at a plunger speed of 0.2 mm/s. After complete solidification, the cast specimen was ejected from the die. The schematic diagram of GISS-DC process is illustrated in Figure 2. The capacity of die casting machine was about 80 tons. The shot sleeve and die were preheated to temperatures of 250 and 200 °C, respectively. The size of die-cast plate specimen was 70 mm wide, 100 mm long and 8 mm thick as shown in Figure 3. After casting, all specimens were checked by visual inspection for macrosegregation which might take place in the as cast specimens. Only complete specimens without macrosegregation were used for microstructural examination and mechanical tests.

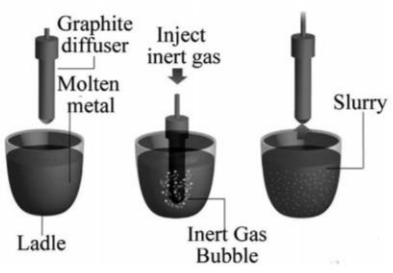

Figure 1. Schematic diagram of GISS technique [11].

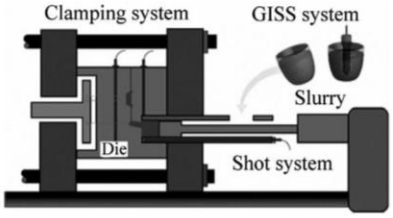

Figure 2. Schematic diagram of GISS die casting process [11].

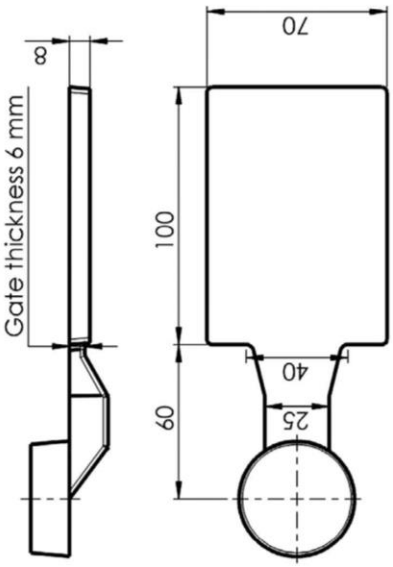

Figure 3. Drawing of die cast specimen.
Note: All dimensions are in mm.

2.3. Tensile test

The tensile test machine, HOUNSFILELD Model H100KS, Serial No. 0068 was used in this study. The tensile tests were performed at a constant crosshead speed of 1.5 mm/min, which is approximately equal to a strain rate of 1×10^{-3} 1/s, at room temperature. The tensile specimens were machined from 4 different locations of the die-cast plates, location 1 at the bottom near the gate, locations 2 and 3 at the middle and location 4 at the top, as shown in Figure 4. The dimensions of tensile specimen was 4 mm × 4 mm cross section and 25 mm gauge length as shown in Figure 5.

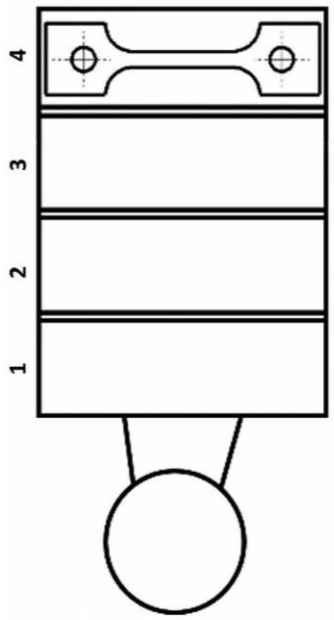

Figure 4. Designation of tensile specimens prepared from different locations of die cast plate.

2.4. Microstructure analysis

The specimens for optical microscopy (OM) and scanning electron microscopy (SEM) analysis were mounted using plastic mounting materials, cured at room temperature and grinded by a standard method using silicon carbide (SiC) abrasive paper (from 180p to 2000p grit) at rotation speed of 300 r/min manually. Then the two-steps polishing using a medium-nap cloth with an alumina abrasive suspension with particle sizes of 5 and 1 microns was performed at rotation speed of 150 r/min. Keller's reagent was used to reveal microstructure of the polished specimens by OM and SEM. The energy dispersive spectroscopy (EDS) technique was used to examine an elemental composition of microstructural phases containing in the specimens. The fracture surfaces of tested specimens were observed by SEM to reveal the microscopic failure mode of the material.

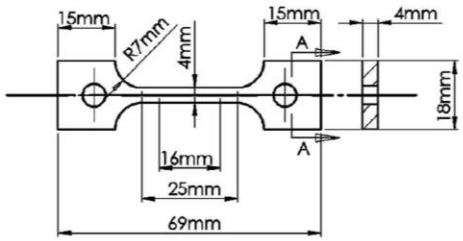

Figure 5. Dimensions of tensile specimen.

3. Results and discussion

3.1. Microstructure

The as cast microstructure of Al–Si–Mg–Fe alloys (AC4C) is usually consisted of dendritic primary Al grains and eutectic Al–Si and Fe-bearing intermetallic phases [16]. Figure 6 shows a representative microstructure of as cast GISS-DC AC4C alloy. Typically, it comprised globular or rosette primary Al grains, eutectic Al–Si particles and intermetallic phases. It was previously reported that the precipitates are distributed among the primary Al grains and large rod-shaped Mg_2Si compounds and intermetallic phases are around the primary Al grains [5]. As shown in Figure 6, it is evident that the primary Al grains and its quantity at location 4 of as cast specimen are larger and higher than those at location 1. This may be due to a slower cooling rate and different flow behavior at location 4. It was previously reported that in slurry die cast process, there are two kinds of flow behaviors, turbulence flow and laminar flow. The flow behaviors depend on viscosity (or the initial solid fraction in the slurry) and velocity of the slurry. At location 1 the slurry with an initial solid fraction solidified first and the flow at location 1 is laminar. The slurry moved upward to location 4 at top part of the die. The slurry at location 4 may contain lower solid fraction than that at location 1 and the flow behavior at location 4 might change from laminar flow to turbulent flow. The turbulent flow may cause gas and shrinkage porosities at top part of the cast specimen. Moreover, the slurry at location 4 solidified last with a slower cooling rate than that at location 1. This may be

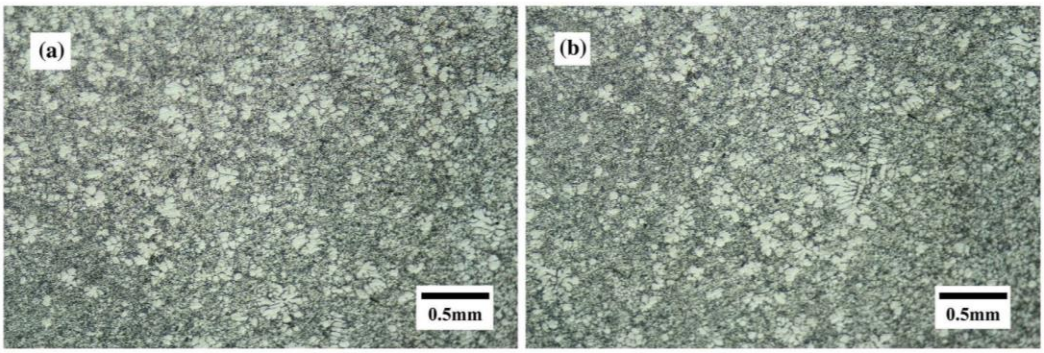

Figure 6. Optical micrographs showing microstructures of AC4C alloy prepared from (a) location 1 (bottom) and (b) location 4 (top) of die cast plate.

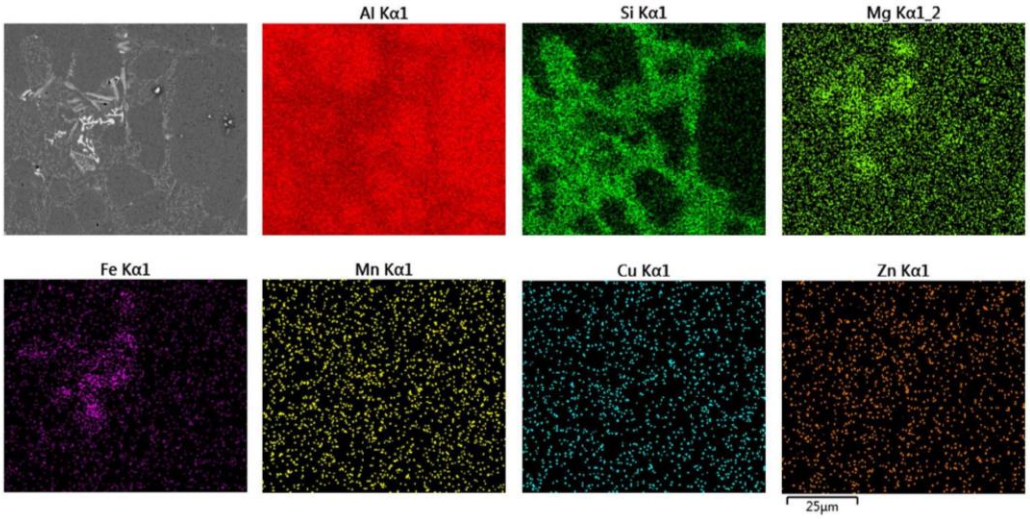

Figure 7. Elemental mapping of a polished section of GISS-DC AC4C alloy.

resulted in microstructure with coarser and higher quantity of primary Al grains at location 4 [11,15].

Figure 7 shows result of elemental area mapping of microstructure of GISS-DC AC4C alloy using EDS. It demonstrates that the primary Al grains compose mainly of Al element. While the large rod-shaped particles uniformly distribute around the primary Al grains. The large particles contain multi alloying elements: Fe, Mg, Mn and Si which formed eutectic Al–Si particles and intrmetallic phases. The microstrures are consistent with the previous report [17].

Figure 8 shows SEM micrograph of GISS-DC AC4C alloy and the EDS point mapping of intermetallic phases at three different points or particles. The EDS spectra of particles at point 1, 2, and 3 are the intermetallic compounds of FeSiMn, SiFeMg, and FeSiMgMn, respectively. However the specific composition and crystal structure of the intermetallic phases in the Al–Si–Mg–Fe alloy is still a hot research topic since it is very difficult to obtain an accurate determination [6].

3.2. Mechanical properties

Figure 9 shows stress-strain curves of specimens from 4 different locations. The specimens from all locations show a similar trend of deformation but they are different in strain hardening behavior. The specimens from location 4 show a lower strain hardening rate compared to those from the others. In addition, strain at fracture, or elongation of specimens from location 4 is lower than those from the others due to reasons of strain hardening and defects such as the arrangement of micro porosities and shrinkages in the specimens.

Yielding point and necking were not obviously observed during tensile test. Therefore, the method of 0.2% offset strain was used for determination of yield strength. The ultimate tensile strength (UTS) and yield strength (YS) plotted against the locations of specimens are shown in Figure 10(a) and (b), respectively. The average UTS of specimens from locations 1, 2 and 3 are almost the same value of about 200 MPa. The average UST of specimens from location 4 significantly decreases to 140 MPa. The average YS are almost the same value of about 100 MPa for all 4 locations. Typically, the YS is dependent on two factors, the strain rate of deformation and the temperature. The YS increases with increasing strain rate and decreases with increasing temperature. In the present work, all tensile tests were performed using the same strain rate and at the same temperature. Hence, the YS of specimens from different locations are reasonably the same value. Figure 10(c) shows the variation of average elongation or ductility of specimens. The average elongations of specimens from locations 1, 2 and 3 are almost the same value of about 11.8%. However, the average elongation of specimens from location 4 has lowest value of 6.7%. The defects such as gas and shrinkage porosities in the cast specimens would be the main causes of low UTS and ductility of materials.

The average UTS of specimens from locations 1, 2 and 3 from the present study is compared with the data of A356 alloy prepared by conventional die casting (Liquid-DC) and GISS die casting (GISS-DC) from the literature as shown in Figure 11. The UTS of GISS-DC AC4C alloy from the present work is higher than that of Liquid-DC A356. This may be resulted from the microstructure of GISS-DC AC4C alloy has finer globular grains and less casting defects. However, the UTS of the present work is slightly lower than that of GISS-DC A356. This may be due to the different chemical compositions of AC4C and A356 alloys. The AC4C alloy contains Fe about 0.49 wt-% while the A356 alloy contains Fe less than 0.2 wt-%.

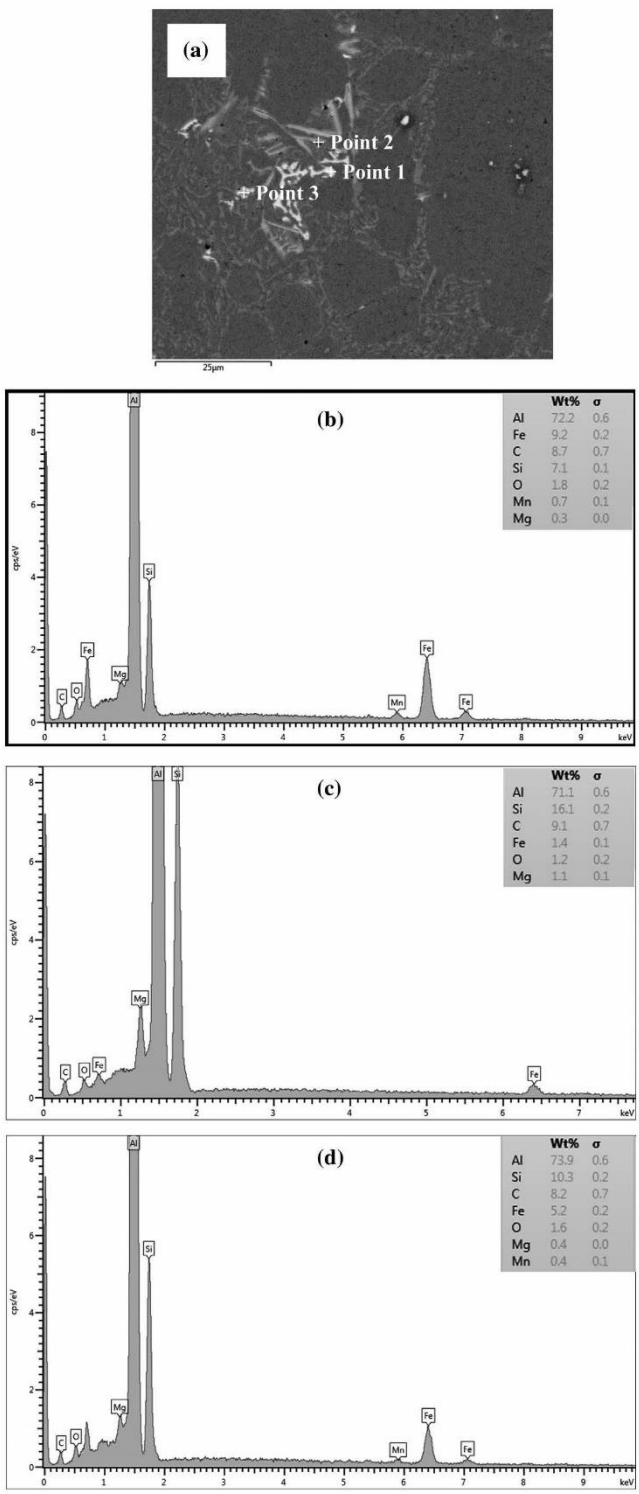

Figure 8. (a) SEM micrograph of GISS-DC AC4C alloy, (b), (c) and (d) are EDS spectra from point scan corresponding to points 1, 2 and 3 marked in (a), respectively.

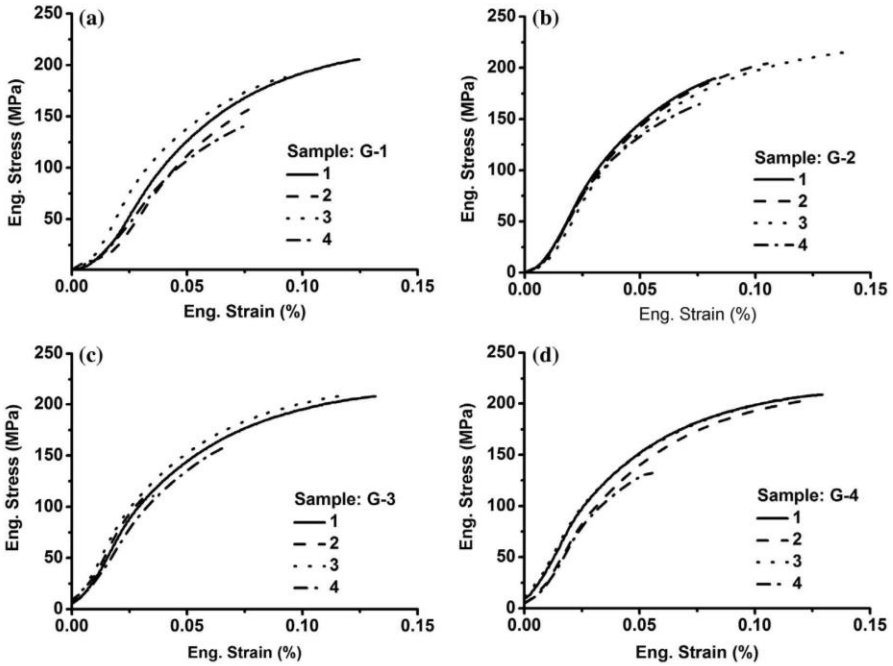

Figure 9. Stress-strain curves of tensile tests from 4 die cast plates (a), (b), (c) and (d), The numbers are corresponding locations 1, 2, 3, and 4 of each die cast plate.

However, the AC4C alloy has better castability and less die erosion and shrinkage [6].

The UTS of GISS-DC AC4C alloy from the present study is compared with the data of GISS squeeze casting AC4C alloy processed using different rheocasting temperatures 650, 635 and 620 °C and initial solid fraction 10 and 25% as shown in Figure 12. The UTS data from the present work is higher than those from the literature [14] from which the alloy was produced by GISS technique, using rheocasting temperatures 650, 635 and 620 °C and 10% solid fraction. However, the UTS data of the present study is slightly lower than that of AC4C alloy prepared by GISS squeeze casting, using the rheocasting temperature 620 °C and solid fraction 25%. It is noted that in the present study our GISS die casting was operated by using the rheocasting temperature 616 °C and the initial solid fraction of about 11% [15].

3.3. Fractures

Fracture surfaces of GISS-DC AC4C alloy after tensile tests were examined by SEM and OM. The macroscopic observation of fracture surfaces by naked eyes reveals a brittle fracture. Figure 13 shows SEM micrographs of fracture surfaces of specimens prepared from locations 1 and 4. It is observed that the fracture surface of specimen from location 4 shows a brittle fracture while the location 1 shows quasi-cleavage feature indicating more ductility which is consistent with results of elongation data shown in Table 2. The fracture surfaces do not show a dimple-like morphology which is the characteristic of high ductility material.

Figure 14(a) and (b) shows SEM fractographs of specimens from locations 1 and 4 of die cast plate, respectively. The micro voids and shrinkage pores can be clearly observed. The decrease in UTS and elongation may be resulted from the defects such as gas and shrinkage porosities. The shrinkage pores are easy to cluster and harmful to die casting components. The clustering of shrinkage porosities at location 4 is higher than that at the other locations. The fracture path preferentially goes through the shrinkage porosities in case of the existence of excessive shrinkage defects, which results in the significant decrease of mechanical properties. Figure 15 shows SEM fractograph of specimen from location 4 of die cast plate. Internal or embedded cracks were observed which are responsible for the reduction of tensile properties of specimens from location 4. It is noted that the surface cracks in the die cast parts may be easily observed, however the internal cracks such as porosities are more difficult to found. The gas and shrinkage defects are the origin of internal cracks which might cause failure of die cast components during service time.

Figures 16 and 17 show SEM fractographs with EDS analysis of GISS-DC AC4C specimens from locations 1 and 4, respectively. The silicon distributions at different locations were observed using EDS line and point scanning. Some silicon particles embedded in a eutectic

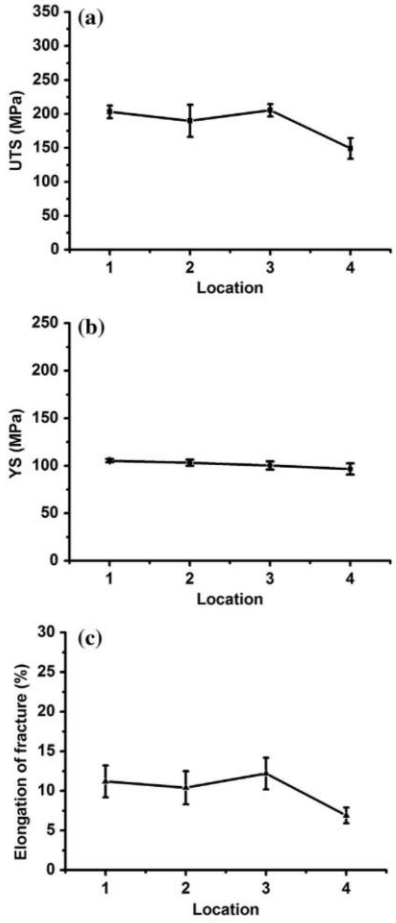

Figure 10. (a) Ultimate tensile strength (UTS), (b) Yield strength (YS) and (c) Elongation of specimens prepared from different locations of die cast plate.

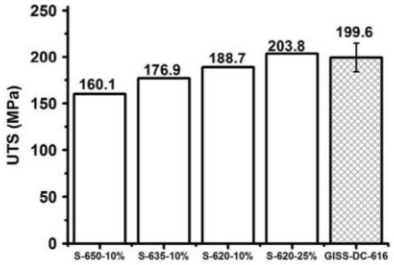

Figure 12. Comparison of UTS of GISS-DC AC4C alloy from this study (meshed pattern) with those of GISS-DC AC4C (blank) [14].

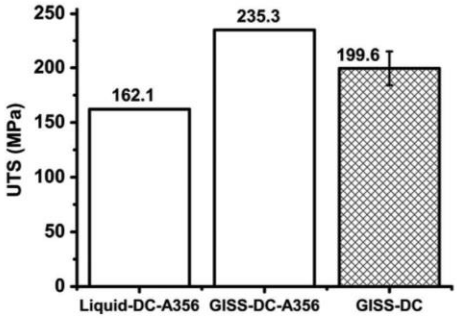

Figure 11. Comparison of UTS of GISS-DC AC4C alloy from this study (meshed pattern) with those from the literatures (blank) [12].

Table 2. Tensile properties of GISS-DC AC4C specimens prepared from different locations of die cast plate.

Location No.	YS 0.2% (MPa)	UTS (MPa)	Elongation (%)
1	105.4 ± 1.9	203.2 ± 9.4	11.2 ± 2.0
2	103.1 ± 3.3	189.9 ± 23.8	10.4 ± 2.1
3	100.3 ± 4.3	205.6 ± 9.2	12.2 ± 2.0
4	96.6 ± 5.8	149.1 ± 15.3	6.9 ± 1.0

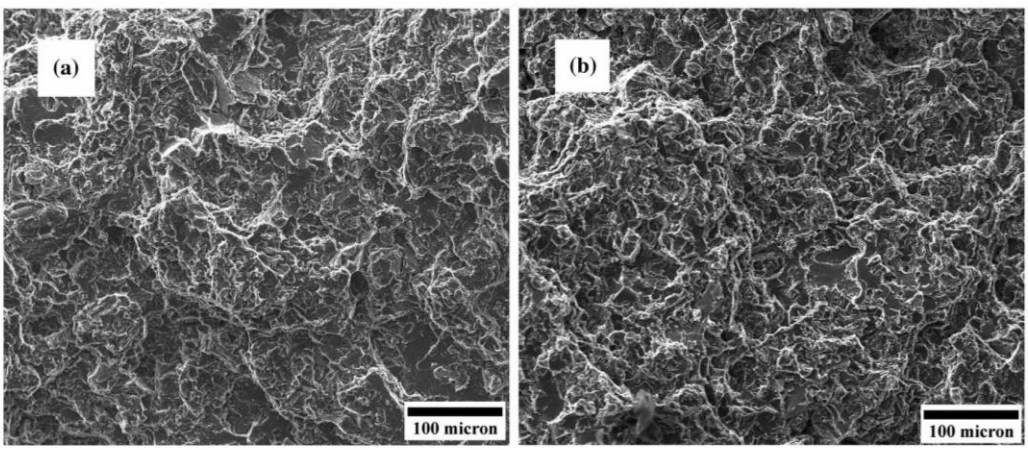

Figure 13. SEM fractographs of specimens after tensile tests. (a) and (b) corresponding to specimens prepared from locations 1 and 4 of die cast plate, respectively.

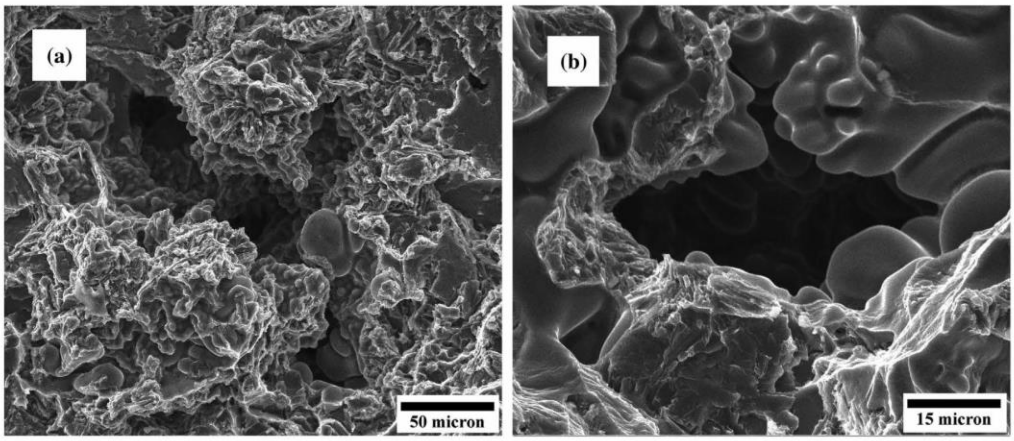

Figure 14. SEM fractographs of specimens after tensile tests, showing shrinkage pores and micro voids. (a) and (b) corresponding to specimens prepared from locations 1 and 4 of die cast plate, respectively.

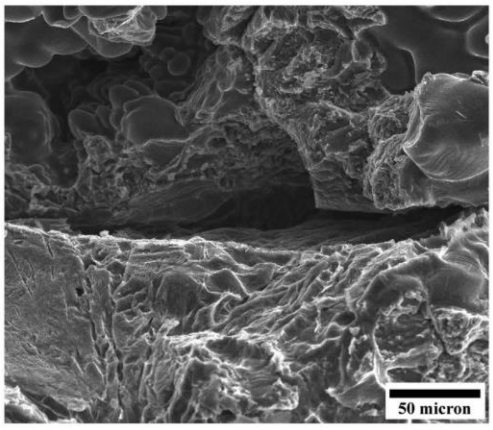

Figure 15. SEM fractograph of specimen after tensile test, prepared from location 4 of die cast plate.

matrix consisting of continuous Al and Si. The shrinkage in specimen from the location 1 was observed along the grain boundary which is silicon particles as shown at the center of Figure 16. The fractures of specimens are brittle and intra-granular. Cavity coalescence and crack growth may be deduced as the failure mechanism. In Figure 17, the same trend was also observed but the EDS point scanning was used instead. The porosities could be resulted in crack propagations and reduced the material mechanical properties. When the tensile stress was applied, porosities might be concentrated by internal stresses, and then the fracture would be started from these areas. The propagation of cracks could lead to speed up to failure, which reduces the mechanical properties, especially a loss of ductility.

Figure 18 shows optical micrographs of microstructures from the area near fracture surface of specimens after tensile tests, (a) and (c) are specimens from location 1, (b) and (d) are specimens from location 4. The arrows in the figures indicate the direction of tensile stress. It was observed that the primary Al phases elongated along the stress direction. Some secondary phases coarsened because the larger primary Al phase might be broken and generated a new secondary phase during tensile test. There might be three mechanisms in the damage process: particle cracking and debonding, micro crack formation and growth and debonding, and local linkage of microcracks as previously reported [18]. Moreover, OM fractograph reveals that cracks are observed along the grain boundaries and stopped by the eutectic particles or clusters of eutectic phase. The existence of silicon

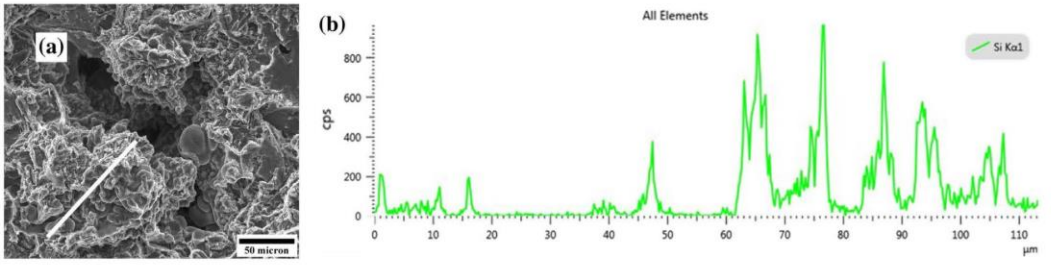

Figure 16. (a) SEM fractograph of specimen after tensile test, prepared from location 1 of die cast plate and (b) EDX spectrum along the line marked in (a).

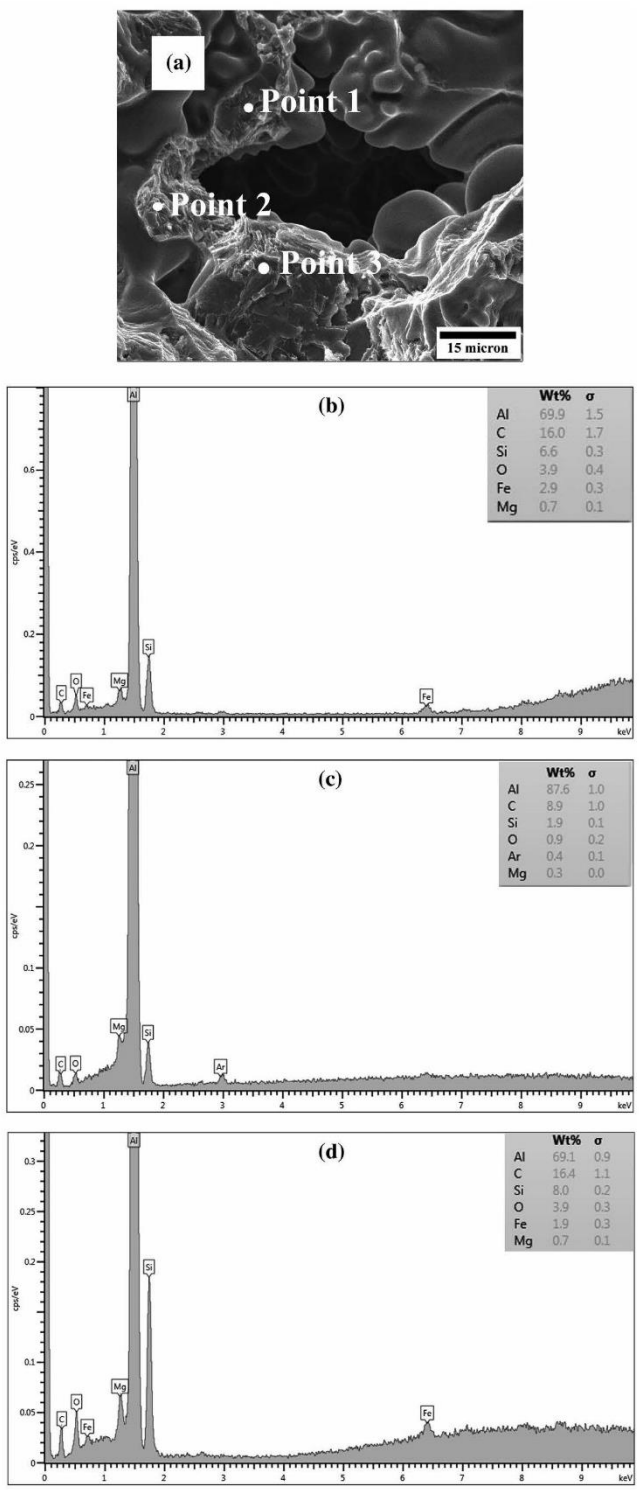

Figure 17. (a) SEM fractograph of specimen prepared from location 4 of die cast plate, (b), (c) and (d) are EDS spectra from point scan corresponding to points 1, 2 and 3 marked in (a), respectively.

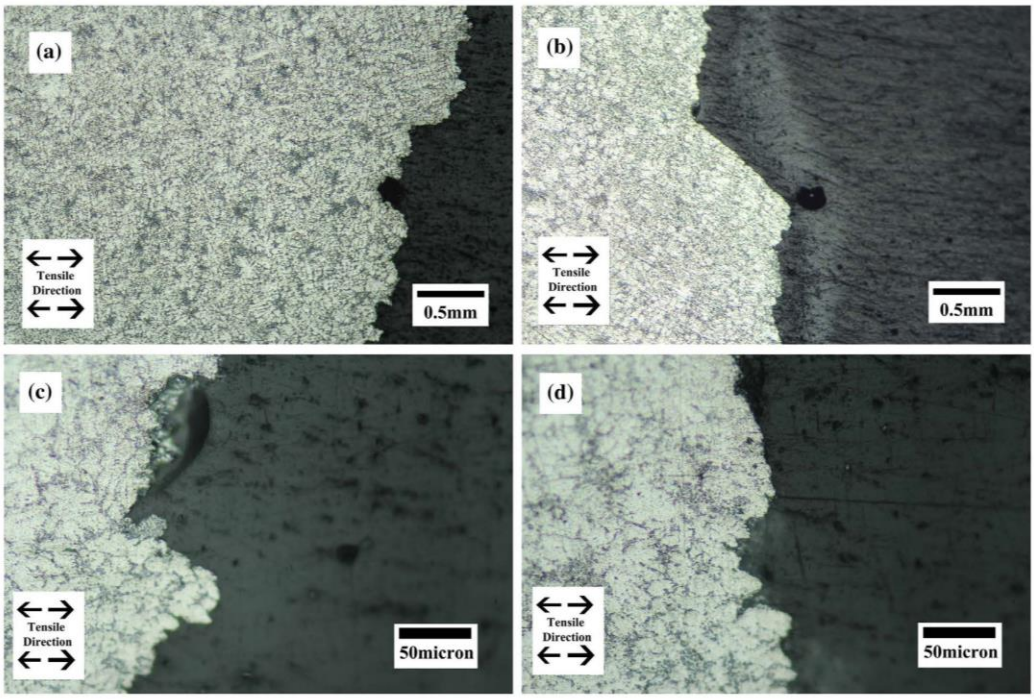

Figure 18. Optical micrographs showing microstructures near fracture surface of specimens after tensile tests. (a) and (c) specimen prepared from location 1, and (b) and (d) from location 4 of die cast plate.

particles, especially in the presence of other defects, would increasingly degrade tensile properties. The fracture path mainly goes through the eutectic region.

The eutectic of AC4C was characterized by phases containing Si, Fe and Mg embedded in Al. The primary silicon particles can be correlated to the tensile performance. The shapes of eutectic particles are elongated and irregular. The elongated and irregular eutectic particles are more brittle and can be fractured faster than the round particles which can be generated by the T6 heat treatment, but the as cast GISS-DC shows more brittle behavior. The analysis of micrographs of samples after tensile test revealed that the fractures were susceptible to brittle fracture. In Al alloys, silicon is added to increase the hardness and improve wear resistance and castability. However, the rupture of silicon particles damaged the formability of these alloys. The defects are pre-existing and grown during tensile test, which cause fracture, reduce the ductility and more difficult to predict the strains. The tensile properties could be increased through refinement of the primary silicon particles. Creep resistance was degraded with increasing silicon particle sizes as previously repoted in the literature [19]. The fracture and debonding of eutectic Si particles play an important role. In general, the formation of the microcracks in the eutectic silicon particles is mainly normal to the applied stress which is consistent with results earlier reported [7]. In Figures 14–17, multiple cracks were observed on the fracture surface of tested specimens. During tensile test, the deformation of eutectic Al–Si and Fe-bearing intermetallic phases could induce internal stresses. When the internal stresses approach the critical value of fracture stress, the crack will be occurred. Therefore, the fracture of particles depends on the stress and microstructure features such as the size and shape [18].

4. Conclusions

In the present study, impact on tensile test results was presented and explained for the GISS-DC AC4C alloy. The microstructures of this alloy were studied by OM, SEM and EDS. The fractures of alloy were characterized by OM, SEM and EDS. The complex defects of different geometries of microstructural features were non-uniform, however, they had some spatial correlations between locations. The features which have different spatial arrangement, size distribution and shape caused different fracture mechanisms and strongly affected the fracture path and mechanical properties. The results illustrate the location impact on the microstructures and mechanical properties. The fracture mechanisms were also discussed. Some evidences which can be concluded from the present study are follows:

(1) The primary Al grain size and its quantity of specimens from location 4 of the die cast plate are larger than those from the location 1. This may be due to the slower cooling rate and the

turbulent flow behavior at location 4 region during GISS-DC processing.

(2) Between the primary Al grains contain a large number of elements: Fe, Mg, Mn and Si which constitute the intermetallic particles and eutectic Al–Si. The compositions of rich Fe intermetallic particles include FeSiMn, SiFeMg, and FeSiMgMn.

(3) The average UTS and elongation of specimens from location 4 are lower than those from the other 3 locations. The average YS of specimens from all 4 locations are almost the same value of 100 MPa. The average UTS and elongation enormously decreases from about 200 MPa and 11.8% at location 1 to about 140 MPa and 6.7% at location 4, respectively. The location of specimens has more impact on the UTS than on the YS and elongation. The strain hardening of specimens from location 4 is significantly higher than those from the other locations.

(4) The mechanical properties of GISS-DC are competitive with those of normal die casting. The UTS value of GISS-DC AC4C is higher than that of CLDC A356. However, it is slightly lower than GISS-DC A356. The UTS of GISS-DC AC4C in the present casting conditions is nearly highest when compared with the previous results.

(5) The quasi-cleavage fractures of GISS-DC AC4C alloy are typically observed. The shrinkage porosities and micro voids at location 4 are significantly higher than those found at location 1. In addition, in the edge region of the die cast plate there are no porosities and the big cracks are generally observed in the location 4.

(6) The cracks and fractures are originated from the shrinkage defects which resulted in the decreasing of mechanical properties and ductility of GISS-DC AC4C alloy.

Acknowledgment

I would like to thank the PSU Department of Mining and Materials Engineering.

Disclosure statement

No potential conflict of interest was reported by the authors.

Funding

This work was funded by the Prince of Songkla University for President Scholarship and the National Research University Project of Thailand's Office of Higher Education Commission [grant number ENG540551c].

References

[1] Möller H, Govender G, Stumpf WE. Natural and artificial aging response of semisolid metal processed Al–Si–Mg alloy A356. Int J Cast Metal Res. 2007;20:340–346.
[2] Möller H, Govender G, Stumpf WE, et al. Influence of temper condition on microstructure and mechanical properties of semisolid metal processed Al–Si–Mg alloy A356. Int J Cast Metal Res. 2009;22:417–421.
[3] Okayasu M, Yoshifuji S, Mizuno M, et al. Comparison of mechanical properties of die cast aluminium alloys: cold v. hot chamber die casting and high v. low speed filling die casting. Int J Cast Metal Res. 2009;22:374–381.
[4] Möller H, Govender G, Stumpf WE, et al. Comparison of heat treatment response of semisolid metal processed alloys A356 and F357. Int J Cast Metal Res. 2010;23:37–43.
[5] Jiang WM, Fan ZT, Liu DJ, et al. Influence of process parameters on filling ability of A356 aluminium alloy in expendable pattern shell casting with vacuum and low pressure. Int J Cast Metal Res. 2012;25:47–52.
[6] Samuel E, Samuel AM, Doty HW, et al. Intermetallic phases in Al–Si based cast alloys: new perspective. Int J Cast Metal Res. 2014;27:107–114.
[7] Singh SK, Chattopadhyay K, Phanikumar G, et al. Experimental and numerical studies on friction welding of thixocast A356 aluminum alloy. Acta Mater. 2014;73:177–185.
[8] Wannasin J, Martinez RA, Flemings MC. Grain refinement of an aluminum alloy by introducing gas bubbles during solidification. Scripta Mater. 2006;55:115–118.
[9] Wannasin J, Thanabumrungkul S. Development of a semi-solid metal processing technique for aluminium casting applications. Songklanakarin J Sci Tech. 2008;30:215–220.
[10] Rattanochaikul T, Janudom S, Memongkol N, et al. Development of aluminum rheo-extrusion process using semi-solid slurry at low solid fraction. Trans Nonferrous Metal Soc. 2010;20:1763–1768.
[11] Janudom S, Rattanochaikul T, Burapa R, et al. Feasibility of semi-solid die casting of ADC12 aluminum alloy. Trans Nonferrous Metal Soc. 2010;20:1756–1762.
[12] Thanabumrungkul S, Janudom S, Burapa R, et al. Industrial development of gas induced semi-solid process. Trans Nonferrous Metal Soc. 2010;20:s1016–s1021.
[13] Wisutmethangoon S, Thongjan S, Mahathaninwong N, et al. Precipitation hardening of A356 Al alloy produced by gas induced semi-solid process. Mater Sci Eng A Struct Mater Prop Microstruct Process. 2012;532:610–615.
[14] Burapa R, Janudom S, Chucheep T, et al. Effects of primary phase morphology on mechanical properties of Al-Si-Mg-Fe alloy in semi-solid slurry casting process. Trans Nonferrous Metal Soc. 2010;20:S857–S861.
[15] Janudom S, Wannasin J, Basem J, et al. Characterization of flow behavior of semi-solid slurries containing low solid fractions in high-pressure die casting. Acta Mater. 2013;61:6267–6275.
[16] Wang QG. Microstructural effects on the tensile and fracture behavior of aluminum casting alloys A356/357. Metall Mater Trans A. 2003;34:2887–2899.
[17] Ran G, Zhou JE, Wang QG. Precipitates and tensile fracture mechanism in a sand cast A356 aluminum alloy. J Mater Process Tech. 2008;207:46–52.
[18] Wang QG, Caceres CH, Griffiths JR. Damage by eutectic particle cracking in aluminum casting alloys A356/357. Metall Mater Trans A. 2003;34:2901–2912.
[19] Jaglinski T, Lakes R. Creep behavior of Al–Si die-cast alloys. J Eng Mater-T ASME. 2004;126:378–383.

VITAE

Name Keren Shi

Student ID 5510130004

Educational Attainment

Degree	Name of Institution	Year of Graduation
B. Eng.	Beijing University of Chemical Technology	2002
M. Eng.	Beijing University of Chemical Technology	2008

Scholarship Awards during Enrolment

-The President Scholarship from Prince of Songkla University

Work – Position and Address

-Lecturer at Ningxia University, Yinchuan, Ningxia, 750021 China

List of Publication and Proceeding

1. Ke Ren Shi, Sirikul Wisutmethangoon, Jessada Wannasin, and Thawatchai Plookphol, 'Tensile Properties of Semi-Solid Die Cast Ac4c Aluminum Alloy', *Applied Mechanics and Materials,* 680 (2014), 11-14.
2. Keren Shi, Sirikul Wisutmethangoon, Somjai Janudom, and Thawatchai Plookphol, 'Variation of Microstructure and Mechanical Property of Slurry Die Cast Al-Si-Mg-Fe Alloy', International Journal of Cast Metals Research, 30 (2017), 180-190.